UNIVERSITY OF SOUTHAMPTON

Ti:sapphire waveguide laser by the thermal diffusion of Ti into sapphire

Louise Mary Brendan Hickey

A thesis submitted for the degree of Doctor of Philosophy

Department of Electronics and Computer Science
and
Optoelectronics Research Centre

May 1998

UNIVERSITY OF SOUTHAMPTON

ABSTRACT

FACULTY OF ENGINEERING AND APPLIED SCIENCE
DEPARTMENT OF ELECTRONICS AND COMPUTER SCIENCE

Doctor of Philosophy

TI:SAPPHIRE WAVEGUIDE LASER BY THERMAL DIFFUSION OF TITANIUM INTO SAPPHIRE

by Louise Mary Brendan Hickey

This thesis reports the first realisation of a Ti:sapphire channel waveguide laser by the thermal diffusion of titanium(Ti) into a sapphire wafer. The Ti-diffused region provides both the optical gain medium and the optical waveguide. These results comprise the first realisation of Ti^{3+} diffusion in sapphire and the first realisation of optical waveguides in sapphire by diffusion doping. The attraction of the Ti:sapphire laser in a planar waveguide configuration is its potential as a compact, broadly tunable source over 400nm in the near infra-red, which would provide a versatile radiation source for sensing or spectroscopy.

The basis for the Ti:sapphire laser formed in a waveguide geometry by diffusion doping is discussed, and a simple model indicates that pump power thresholds less than 100mW are achievable. Previous work on the diffusion of metals into sapphire is reviewed, indicating that temperatures as high as 1950°C are appropriate for initial experimental work.

Processes, equipment and characterisation techniques are presented that enable the investigation of Ti diffusion in sapphire. Spectroscopic characterisation of the diffused material indicates that fluorescent Ti^{3+} ions are incorporated, appropriate for use as an optical gain medium. The diffused Ti distribution is investigated following diffusion at temperatures between 1480°C and 1950°C over diffusion times between 0.2 and 8 hours, achieving depths in excess of 50μm and peak Ti^{3+} concentrations greater than 0.4wt%Ti_2O_3 in Al_2O_3. Following diffusion from a series of stripe sources, a fast lateral diffusion is observed.

Slab and channel waveguides are formed in the Ti-diffused sapphire and trends in the effective refractive index, mode intensity profiles and spectral attenuation are reported. Channel waveguides appropriate for the realisation of a miniature laser are identified.

Ti:sapphire waveguide lasers are reported for two cavity configurations, with operation at wavelengths between 770nm and 810nm. With 7% output coupling, a pump power threshold of 1.2±0.4W and slope efficiency of 0.5% is achieved. This first realisation of a waveguide laser by the thermal diffusion of titanium into sapphire clearly demonstrates the feasibility of this approach to the realisation of a miniature broadly tunable Ti:sapphire waveguide laser.

TABLE OF CONTENTS

ACKNOWLEDGEMENTS

I would like to thank James Wilkinson for all the discussion, guidance, encouragement and patience throughout.

Many thanks to Brian Ault and Dave Sager for all the clean room expertise, experience and advice. Thanks to Ping Hua for the hours and hours of polishing. I would like to thank Eliette Moya and Fernand Moya for sharing their insight to diffusion in sapphire. Andy Anderson and Rob Eason have also featured highly during the course of this work and I would like to thank them for the useful discussions, fresh point of view and that added bit of pressure!

Many others also have contributed to life at the ORC - particular thanks to all the planar and IOMG members, past and present, who were always ready to help or as last resort, share a swift half etc.

Outside the ORC are friends and family that have given enormous support throughout as well as have plotted and schemed the many, many adventures. GOTP tour '98 is starting and should be as eventful as ever.

I acknowledge the support of the University of Southampton and the Optoelectronics Research Centre in providing the studentship. The Optoelectronics Research Centre is a UK EPSRC Interdisciplinary Research Centre.

CHAPTER 1

INTRODUCTION

1.1 Introduction

A miniature Ti:sapphire laser, continuously tunable between 660-1050nm would have significant impact as a versatile radiation source for applications in spectroscopy, sensing and remote instrumentation. By exploiting the planar integrated optic configuration such a laser could be realised on a single sapphire chip, to form a compact device with an output compatible with optical fibre technology. Essential parts of achieving this aim are to realise a gain medium and optical waveguides in a sapphire wafer. Both of these are reported here for the first time, by the thermal diffusion of titanium, and lead to the first realisation of a Ti:sapphire channel waveguide laser.

The work described in this thesis charts progress made towards realising the miniature Ti:sapphire laser. In this chapter, the attractive properties of the well-known bulk Ti:sapphire laser are highlighted and the motivation behind miniaturising the laser to an integrated optic format is outlined. Recent interest in the application of an Al_2O_3 host to active waveguide devices is briefly reviewed, highlighting activity in the realisation of an Er:Al_2O_3 amplifier and interest in the realisation of a Ti:sapphire waveguide laser. Thermal diffusion is identified as an appropriate fabrication technique for this work and a synopsis of the thesis is given in §1.5.

1.2 Application and miniaturisation of the Ti:sapphire laser

In the bulk configuration, the Ti:sapphire laser was first demonstrated in 1982[1] and rapidly became commercially viable. Its success may be attributed to the broad gain band, the lack of low lying energy levels for excited state absorption, the availability of high quality crystals and the existence of a high power pump source. Whilst providing a versatile source, application is generally limited to research and development environments, with significant

investment required to support the high power pump source. For example, water cooling and a three phase power supply are needed to support an argon ion laser suitable for pumping a commercial Ti:sapphire laser.

The broad Ti:sapphire emission band also lends itself to the generation of short pulses, for which the phenomena of 'self-modelocking' was first demonstrated in 1990[2]. At high pump power densities, the combination of thermal lensing and gain saturation contributes to changes of refractive index in the gain medium, leading to self-starting mode-locked operation. The optimum performance of the laser, in either continuous or pulsed operation requires cooling of the Ti:sapphire crystal.

Miniaturisation of the Ti:sapphire laser and the associated optical components presents an ambitious task. Starting with a commercial sapphire wafer, processes need to be developed for introducing the Ti^{3+} active ion and for forming optical waveguides in sapphire. Combining the two technologies, a waveguide laser may be realised, forming a cavity by directly butting plane mirrors onto the waveguide endfaces. Advantages of the waveguide geometry over the bulk laser include the potential for a significant reduction in pump power threshold, the potential for integration of tuning components and the compact, robust geometry. In the future, the potential for a mode locked Ti:sapphire waveguide laser may be addressed; this is not the aim of the current work.

Selectively introducing the active ion, for example by thermal diffusion, offers flexibility in the design of the gain medium, allowing it to be tailored for optimum performance. The confinement of radiation to a waveguide geometry ensures that high optical intensities are maintained throughout the region of gain. Laser operation may ensue with appropriate feedback into the waveguide, for example using high reflectivity dielectric coatings deposited on the waveguide endface. The threshold power for lasing may be significantly reduced compared to a bulk system with low waveguide propagation losses, leading to a wider choice of pump sources. For example, when they become available, an electrically pumped blue-green diode could be directly butt-coupled to the Ti:sapphire laser.

Following the realisation of a Ti:sapphire waveguide laser, the planar configuration may be further exploited with schemes to integrate tuning and wavelength selection components on the same chip. For example, a waveguide circuit may be designed with a spectrally dependent loss, which may be tuned externally. Such control over the intracavity waveguide

characteristics would dominate the laser properties, determining the wavelength of operation. The compact miniature laser would be versatile and easy to use with no intracavity components sensitive to optical alignment. Applications would be as a source for sensing and diagnostic equipment, which requires a tunable radiation source.

Whilst one of the attractions of the Ti:sapphire laser is the broad tunability, the wavelength range, 650nm to 1050nm, may attract competition from the semiconductor diode laser market. Diodes are cheap, readily available and present an area of significant commercial investment. However, diodes exhibit emission over discrete wavelength ranges and are limited in output power. Diode arrays lead to higher output powers, although this solution is not ideal, as the laser output beam is highly asymmetric and is not diffraction limited. In addition, the diodes are not available over a continuous spectral range. The Ti:sapphire miniature laser in comparison, has the potential for continuous tunability and a diffraction limited output, compatible with other integrated optic devices.

1.3 Al_2O_3 as a material for integrated optics

Interest in aluminium oxide as a material for integrated optics has been increasing over recent years. Recent advances include the realisation of amplification in an Er:Al_2O_3 waveguide formed on an oxidised silicon substrate (Si/SiO_2)[3] and the realisation of a Ti:sapphire slab waveguide laser in a Ti:sapphire thin film formed by laser pulsed laser deposition on a sapphire substrate[4]. In a different vein, the realisation of small diameter single crystal fibres (about 350μm) has also led to the demonstration of a miniature Ti:sapphire laser[5].

These achievements demonstrate the diversity of approaches taken to exploit Al_2O_3 as a host material. The motivation for realising rare earth and transition metal ion doped devices differs significantly and recent activity in these areas is reviewed briefly in turn below.

1.3.1 Rare-earth doped Al_2O_3 devices

Much of the recent interest in developing rare-earth doped Al_2O_3 films is motivated by the potential for incorporating high concentrations of impurity ions, such as Er^{3+}, in the Al_2O_3 matrix. The development of rare-earth doped Al_2O_3 films follows the realisation of high quality passive waveguides in Al_2O_3 films deposited on lower index substrates[6-8].

The optical properties of the rare-earth ion are based on transitions of an f-shell electron, whose energy level structure is well shielded from the local electric field provided by the host material. In these devices, the Al_2O_3 film does not have to be in single crystal form, and so a range of fabrication techniques is available. For example, gain was observed in sputtered Al_2O_3 film, subsequently doped with Er by ion implantation[3], with the spectroscopic properties of these films summarised in a review by Polman[9]. Other techniques that have been explored, and allow the growth of Al_2O_3 films doped in situ Er-doped Al_2O_3 films, are chemical vapour deposition(CVD)[10,11] and pulsed laser deposition[12]. The composition and structure of the film are controlled by the deposition conditions.

The Al_2O_3 film may readily form an optical waveguide if a substrate of lower refractive index is used. For example, much work has been done using an oxidised silicon substrate (Si/SiO_2), on which waveguides are formed in the higher index deposited Al_2O_3 thin films, which may be over-clad with a further thin film of SiO_2. Channel waveguides have been developed by patterning and etching either the Al_2O_3 waveguide layer[3] or the SiO_2 cladding layer[11].

CVD deposited films, sputtered films and those doped by ion implantation require a post annealing procedure. The post annealing changes the defect structure of the Al_2O_3 host, reducing waveguide losses[6] and for Er^{3+} doped sputtered Al_2O_3 enhances the spectroscopy by reducing the density of non-radiative decay routes[13]. However, with increasing temperature, the Er^{3+} mobility becomes sufficient for short range diffusion to occur, promoting the formation of Er pairs or clusters. Pairs or clusters of Er^{3+} affect the spectroscopy of the material[14], so that optimum annealing conditions may be found. During the course of several studies, the annealing of defects in Al_2O_3 has been studied for doped[15] and ion implanted[16-18] Al_2O_3, considering the use of a conventional furnace annealing and rapid thermal annealing process using a pulsed laser source[19,20]. The rapid thermal annealing is a promising technique as it allows defects in the Al_2O_3 to anneal without promoting the formation of clusters in the structure.

1.3.2 Transition metal doped Al_2O_3 devices

The proven success of lasers in Cr doped and Ti doped sapphire (ruby and Ti:sapphire lasers), has led to interest in the formation of Al_2O_3 waveguides doped with the transition metals Cr and Ti. However, the electronic transitions responsible for the optical gain in Cr

and Ti doped systems involve electrons in the outermost d-shell, rather than shielded f-shells of the rare earth ions. In consequence, careful control over the structure of the Al_2O_3 host is necessary to maintain the attractive properties of the transition metal ion dopant.

Approaches to the fabrication of transition metal ion doped Al_2O_3 include film deposition techniques such as electron beam evaporation[15,21-23] and pulsed laser deposition[24,25]. With careful control over the fabrication conditions, appropriate films of Al_2O_3 may be formed, and doped in situ. The use of a sapphire substrate in combination with a thermal annealing process promotes the formation of epitaxial single crystal Al_2O_3 films, in which the dopant may exhibit the appropriate spectroscopic properties.

To the best of my knowledge, the only report of direct growth of an epitaxial Ti^{3+}-doped Al_2O_3 film is formed by pulsed laser deposition on a sapphire substrate[25]. This work has been carried out in Southampton, in parallel to the work reported in this thesis. In sufficiently thick layers, the doped single crystal film may form an optical waveguide as the Ti^{3+} doping has been found to increase the refractive index of the sapphire host[26]. By this method, a slab Ti:sapphire waveguide laser has been recently demonstrated[4]. The waveguide was 12.3μm thick, 3.8mm long and doped at about 0.1wt%. With about 2% output coupling from the cavity, the lowest absorbed pump power threshold reported was 0.56W. The maximum output power observed was 357mW for 3.44W absorbed pump power, for a 35% output coupler.

An alternative route to forming integrated optical devices in sapphire is by ion implantation of a light ion such as He, to form a waveguide, and an active medium, by introducing an impurity ion. In sapphire, the formation of waveguides by ion implantation is limited to a brief report[27] and it is believed that the extent of the structural damage in the implanted region leads to high waveguide losses.

The direct implantation of numerous transition metal ions, including Ti, into sapphire substrate has been studied[16-18,28,29]. However, the application of implanted regions to active devices is hindered by the structural damage introduced during implantation, which affects the spectroscopy of the implanted ion. Post annealing in a conventional furnace allows the recovery of the Al_2O_3 lattice structure, but can also lead to the formation of impurity clusters, or new crystalline phases[17,18,28]. The realisation of an active waveguide device fabricated by ion implantation of a transition metal ion in sapphire has yet to be demonstrated. An

attractive route may be to utilise rapid thermal annealing to recover the structure of the implanted sapphire whilst maintaining the attractive spectroscopy of the implanted ion.

In a contrasting geometry, a Ti:sapphire laser has been reported in a single crystal fibre pulled from a melt using the laser heated pedestal method[5,30,31]. The laser was formed in a fibre 11.2mm long, with a diameter of about 350μm. This geometry does not offer all of the advantages of the integrated optic format although, with further reduction in the fibre diameter, some of the advantages of the waveguide confinement may be realised.

In summary, there is increasing interest in the realisation of active integrated optical devices in Al_2O_3. Numerous techniques have been explored for the deposition of thin films and the incorporation of active ions into the lattice. Active devices have been demonstrated in epitaxially grown Ti-doped α-Al_2O_3 film and in Er doped Al_2O_3. However, excepting the work described in this thesis, there are no reports of integrated optic devices made by the thermal diffusion of impurity ions in sapphire, to the best of my knowledge.

1.4 Ti:sapphire waveguide laser by thermal indiffusion of Ti^{3+}.

The aim of the work reported in this thesis is to realise a Ti:sapphire waveguide laser by locally doping sapphire with Ti by thermal diffusion. Thermal diffusion is a technique that offers the potential for introducing an impurity into a lattice without significantly affecting the crystal structure. The distribution of the impurity may be controlled by the fabrication conditions, although the maximum concentrations incorporated and the diffusion rate will be a characteristic of the diffusant and the host.

The route to an integrated optic device in sapphire by thermal diffusion of impurities has not previously been investigated. A reason for this may be that previous reports of lattice diffusion rates for transition metals (for example Cr, Ni and Fe) in sapphire indicate that prohibitively high temperatures are needed to attain appropriate diffusion rates[32]. However, little direct work has been carried out to establish the diffusion characteristics of Ti in sapphire.

In contrast, thermal diffusion has been used to realise numerous active[33-36] and passive[37] integrated optic devices in other materials such as $LiNbO_3$. For example, active ions, such as Er^{3+} and Nd^{3+} may be introduced by thermal diffusion and low loss passive waveguides can

be routinely fabricated by thermal diffusion from a Ti source[38]. By diffusing both the waveguide and the active ion, and utilising the electro-optic properties of the host material, devices such as tunable[39] and Q-switched[40] lasers have been realised.

Motivated by the success of the application of thermal diffusion to the development of $LiNbO_3$ devices, the thermal diffusion of titanium into sapphire is proposed as a method for fabricating a versatile Ti:sapphire waveguide laser. To achieve this aim, this thesis reports a method that has been developed for introducing Ti^{3+} into a commercially available sapphire wafer. The doped region forms both a gain medium and an optical waveguide, leading to the realisation of a Ti:sapphire channel waveguide laser. These results comprise the first demonstration of Ti^{3+} diffusion into sapphire[41], the first realisation of diffused waveguides in sapphire[42] and the first Ti:sapphire waveguide laser[43].

1.5 Synopsis of thesis

In chapter 2, an overview of the attractive mechanical and optical properties of sapphire and Ti^{3+} doped sapphire are presented. The spectroscopy of Ti:sapphire and the basis of a Ti:sapphire laser are discussed. A simple model describing the operation of a 4-level laser in a waveguide geometry is presented and used to investigate the potential performance of a Ti:sapphire waveguide laser. The effects of intracavity losses at the pump and signal wavelengths are considered for a range of average titanium concentrations and sample lengths.

Chapter 3 considers the diffusion doping of sapphire. Solutions to the diffusion equation are presented for a range of fabrication conditions and possible deviations from ideal kinetics are discussed. Previous studies related to the movement of metal ions in sapphire are reviewed. The aim of the literature review is to identify appropriate conditions for preliminary experimental work and to identify the various mechanisms that may apply to the movement of titanium in sapphire.

Chapter 4 presents the experimental study of titanium diffusion into sapphire for a broad range of fabrication conditions. The fabrication procedure is discussed in detail and the experimental methods used for the characterisation of the diffused Ti concentration are described. Characteristics of diffusion from a continuous thin film source and a patterned

thin film source are discussed in turn. Suitable fabrication conditions are identified for the realisation of a localised gain medium, appropriate for use in a miniature Ti:sapphire laser.

Chapter 5 presents the characteristics of optical waveguides formed by the diffusion of Ti into sapphire. The experimental procedures used to analyse the optical properties of both slab and channel waveguides are outlined. Trends in the characteristics of the waveguides are observed for a range of fabrication conditions, which are related to the progression of the diffusion. Interpretation of the optical properties in comparison with the known Ti distribution enables an estimate of the relationship between refractive index and titanium concentration to be made. The properties of selected waveguides diffused from a patterned source are investigated in greater depth to identify channel waveguides that exhibit attractive properties for the realisation of a channel waveguide Ti:sapphire laser.

The first Ti:sapphire waveguide lasers are discussed in chapter 6. The experimental method is outlined and the characteristics of the laser presented for two cavity configurations. The power, spectral and temporal properties of the Ti:sapphire laser in the waveguide configuration are presented.

Chapter 7 draws conclusions from the research presented in this thesis. Further work to exploit the first demonstration of the Ti:sapphire laser in the integrated optic configuration is proposed.

In summary, this thesis records the successful realisation of a method for selectively doping a sapphire wafer with titanium to form a localised gain medium and an optical waveguide. This has led to the realisation of a Ti:sapphire waveguide laser that may present a versatile source for a range of novel applications in integrated optics.

1.6 References to Chapter 1

1. P F Moulton, *XXII Int. Quant. Electron. Conf., Munich, Germany, June 1982*
2. D E Spence, P N Kean, W Sibbett; *Proc. CLEO, 1990, paper CPDP10, p 619* and *Opt. Lett.*, ***16*** *(1991), pp 42-44*

3. G N van den Hoven, E Snoeks, A Polman, C van Dam, J W M van Uffelen, M K Smit, "**Optical gain in erbium-implanted Al_2O_3 waveguides**"; *Proc. 7th Europ. Conf. Int. Opt., 3-6 April 1995, Delft, Holland, pp 229-232*
4. A A Anderson, R W Eason, L M B Hickey, M Jelinek, C Grivas, D S Gill, N A Vainos "**A Ti:sapphire planar waveguide laser grown by pulsed laser deposition**"; *Opt. Lett., **22** (1997), pp 1556-1558*
5. L Wu, A Wang, J Wu, L Wei, G Zhu, S Ying "**Growth and laser properties of Ti:sapphire single crystal fibres**"; *Electron. Lett., **14** (1995), pp 1151-1152*
6. M K Smit, G A Acket, C J van der Laan, "**Al_2O_3 films for integrated optics**"; *Thin Solid Films, **138** (1986), pp 171-181*
7. B J Stadler, M Oliveria, L O Bouthillette, "**Alumina thin films as optical waveguides**"; *J. Am. Ceram. Soc., **78** (1995), pp 3336-3344*
8. G Este, W D Westwood, "**Reactive deposition of low loss Al_2O_3 optical waveguides by modified dc planar magnetron sputtering**"; *J Vac. Sci. Technol. A, **2** (1984), pp 1238-1247*
9. A Polman, "**Erbium implanted thin photonic films**"; *J. Appl. Phys., **82** (1997), pp 1-39*
10. O Blume, M Mahnke, D Sander, J Muller, "**Rare-earth doped Al_2O_3 thin film waveguides deposited by MO-PECVD and MO-LPCVD on silicon substrates**"; *Proc. CLEO/Europe, 8-13 Sept. 1996, Hamburg, Germany, paper CTuG5 p77*
11. M Mahnke, O Blume, J Reininger, J Muller, "**In situ erbium doped Al_2O_3 MO-PECVD and MO-LPCVD thin film waveguides on silicon substrates**"; *Proc. 8th Europ. Conf. Int. Opt., 2-4 Apr. 1997, Stockholm, Sweden, paper EThH28, p 404*
12. R Serna, C N Afonso, "**In situ growth of optically active erbium doped Al_2O_3 thin films by pulsed laser deposition**"; *Appl. Phys. Lett., **69** (1996), pp 1541-1543*
13. G N van den Hoven, E Snoeks, A Polman, J W M van Uffelen, Y S Oei, M K Smit, "**Photoluminescence characterisation of Er-implanted Al_2O_3 films**"; *Appl. Phys. Lett., **62** (1993), pp 3065-3067*
14. G N van den Hoven, E snoeks, A Polman, C van Dam, J W M van Uffelen, M K Smit, "**Upconversion in Er-implanted Al_2O_3 waveguides**"; *J. Appl. Phys., **79** (1996), pp 1258-1266*

15. N Yu, T W Simpson, P C McIntyre, M Nastasi, I V Mitchell, "**Doping effects on the kinetics of solid-phase epitaxial growth of amorphous alumina thin films on sapphire**"; *Appl. Phys. Lett., **67** (1995), pp 924-926*
16. C W White, G C Farlow, C J McHaragues, P S Sklad, M P Angelini, B R Appleton, "**Formation of amorphous layers in Al_2O_3 by ion implantation**"; *Nucl. Inst. Meth. Phys. Res., **B7/8** (1985), pp 473-478*
17. G C Farlow, C W White, C J McHaragues, P S Sklad, B R Appleton, "**Thermal annealing of Fe implanted Al_2O_3 in an oxidising and reducing environment**"; *Nucl. Instr. Meth. Phys. Res., **B7/8** (1985), pp 541-546*
18. H Naramoto, C W White, J M Williams, C J McHaragues, O W Holland, M M Abraham, B R Appleton, "**Ion implantation and thermal annealing of α-Al_2O_3 single crystals**"; *J. Appl. Phys., **54** (1993), pp 683-698*
19. N Can, P D Townsend, D E Hole, C N Afonso, "**High intensity luminescence from pulsed laser annealed europium implanted sapphire**"; *Appl. Phys. Lett., **65** (1994), pp 1871-1873*
20. N Can, P D Townsend, D E Hole, H V Snelling, J M Ballesteros, C N Afonso, "**Enhancement of luminescence by pulsed laser annealing of ion-implanted europium in sapphire and silica**"; *J. Appl. Phys. 78 (1995), pp 6737-6744*
21. N Yu, M Nastasi, "**Epitaxial growth of Fe-doped sapphire thin films from amorphous Al oxide layers deposited on sapphire substrates**"; *Appl. Phys. Lett., **62** (1994), pp 180-182*
22. Q Wen, D R Clarke, N Yu, M Nastasi, "**Epitaxial regrowth of ruby on sapphire for an integrated thin film stress sensor**"; *Appl. Phys. Lett., **66** (1995), pp 293-295*
23. N Yu, Q Wen, D R Clarke, P C McIntyre, H Kung, M Nastasi, T W Simpson, I V Mitchell, D Li, "**Formation of iron or chromium doped epitaxial sapphire thin films on sapphire substrates**"; *J. Appl. Phys. Lett., 78 (1995), pp 5413-5420*
24. P E Dyer, S R Jackson, P H Key, W J Metheringham, M J J Schmidt, "**Excimer laser ablation and film deposition of Ti:sapphire**"; *Appl. Surf. Sci., **96-98** (1996), pp 849-854*
25. A A Anderson, R W Eason, M Jelinek, C Grivas, D Lane, K Rogers, L M B Hickey, C Fotakis, "**Growth of Ti:sapphire single crystal thin films by pulsed laser deposition**"; *Thin Solid Films, **300** (1997), pp 68-71*

26. A A Anderson, R W Eason, M Jelinek, L M B Hickey, C Grivas, C Fotakis, K Rogers, D Lane, "**Waveguiding and crystallographic properties of single crystal Ti:sapphire layers produced by pulsed laser deposition**"; *Proc. CLEO/Europe, 8-13th Sept. 1996, Hamburg, Germany, paper CTuG8 p79*
27. P D Townsend, P J Chandler, R A Wood, L Zhang, J McCallum, C W McHarague, "**Chemically stabilised ion implanted waveguides in sapphire**"; *Electron. Lett., **26** (1990), pp 1193-1194*
28. A P Mouritz, D K Sood, D H St John, M V Swain, J S Williams, "**Ion implantation of low melting point metals into sapphire**"; *Nucl. Instr. Meth. Phys. Res., **B19** (1987), pp 805-808*
29. M Rahmani, P D Townsend, "**Ag^+ implantation in Al_2O_3, $LiNbO_3$ and quartz**"; *Vacuum, **39** (1989), pp 1157-1162*
30. J H Sharp, T J P Han, B Henderson, R Illingworth "**Instability in the growth of Ti:Al_2O_3 single-crystal fibres**"; *J. Crys. Grow., **140** (1994), pp 79-83*
31. B M Tissue, L Lu, L Ma, W Jia, M L Norton, W M Yen, "**Laser-heated pedestal growth of laser and IR-upconverting materials**"; *J. Crys. Grow., **109** (1991), pp 323-328*
32. B Lesage, A M Huntz, G Petot-Ervase, "**Transport phenomena in undoped and chromium or yttrium doped-alumina**"; *Radiation Effects, 75 (1983), pp 283-299*
33. J P de Sandro, J K Jones, D P Shepherd, M Hempstead, J Wang, "**Non-photorefractive CW Tm-indiffused Ti-$LiNbO_3$ waveguide laser, operating at room-temperature**"; *IEEE Photon. Tech. Lett., 8 (1996), pp 209-211*
34. R Brinkman, W Sohler, H Suche, "**Continuous-wave Er-diffused $LiNbO_3$ waveguide laser**"; *Electron. Lett., 27 (1991) pp 415*
35. J Amin, M Hempstead, J E Roman, J S Wilkinson, "**Tunable, coupled-cavity waveguide laser at room temperature in Nd-diffused $LiNbO_3$**"; *Opt. Lett., 9 (1994) pp 1541-1543*
36. J K Jones, J P de Sandro, M Hempstead, DP Shepherd, A C Large, J S Wilkinson, "**Channel waveguide laser at 1μm in Yb-indiffused $LiNbO_3$**"; *Opt. Lett., **20** (1995), pp 1477-1479*
37. M Kondo, "**$LiNbO_3$ waveguide devices**"; *J. Ceram. Soc. Jpn., **101** (1993), pp 38-42*

38. J Amin, "**Integrated optical devices in rare-earth-doped $LiNbO_3$**"; *PhD Thesis, University of Southampton, November 1996*
39. H Suche, L Bauman, D Hiller, W Sohler, "**Modelocked Er:Ti $LiNbO_3$ waveguide laser**"*; Electron. Lett., **29** (1993), pp 1111-1112*
40. J Amin, W H Loh, M Hempstead, J S Wilkinson, "**Multiple function waveguide laser in Nd-diffused Ti:$LiNbO_3$** "*; Proc. 7th Europ. Conf. Int. Opt., 3-6 April, 1995, Delft, Holland, paper ThA4, pp 575-579*
41. L M B Hickey, E Martins, J E Roman, W S Brocklesby, J S Wilkinson, "**Fluorescence of Ti^{3+} ions thermally diffused into sapphire**"*; Opt. Lett., **21** (1996), pp 597-599*
42. L M B Hickey, J S Wilkinson, "**Titanium diffused waveguides in sapphire**"*; Electron. Lett., **32** (1996), pp 2238-2239*
43. L M B Hickey, A A Anderson, J S Wilkinson, "**Ti:sapphire channel waveguide laser by thermal diffusion of titanium into sapphire**"*; Addendum to Proc. 8th Europ. Conf. Int. Opt., 2-4 Apr. (1997), Stockholm, Sweden, paper PD6*

CHAPTER 2

PROSPECTS FOR A TI:SAPPHIRE WAVEGUIDE LASER

2.1 Introduction

The physical and spectral properties of sapphire and Ti-doped sapphire make it an attractive optoelectronic material. The single crystal is extremely hard, chemically inert and has excellent thermal conductivity and high electrical resistivity. Sapphire may be synthetically grown, with the process well advanced owing to its demand as an electrically insulating substrate for microelectronic devices. Therefore, high quality, low cost wafers are readily available.

With the advent of the Ti:sapphire laser, the growth of high quality Ti-doped material and its spectroscopic properties were investigated to the extent that the laser rapidly became commercially viable. For a high quality bulk doped crystal, control over the growth conditions is needed to ensure the Ti is included substitutionally on the Al lattice, in the 3+ valence state. The inclusion of Ti^{4+} leads to absorption at the laser wavelength, which reduces the efficiency of the laser medium.

In the realisation of the Ti:sapphire waveguide laser, the aim is to dope a commercially available sapphire wafer with Ti^{3+} to form a gain medium and an optical waveguide. Since sapphire has not been extensively investigated as a substrate for integrated optics, the aim of this chapter is to highlight its attractive properties as a substrate material and to discuss the properties of titanium doped sapphire. A simple model of a four-level laser system is presented to illustrate the potential performance of the Ti:sapphire laser in a waveguide geometry.

2.2 Material characteristics of sapphire and Ti-doped sapphire

The properties of sapphire and titanium doped sapphire are reviewed in this section, with particular attention given to characteristics that have a direct bearing on the fabrication or

performance of a Ti:sapphire laser. The intention is that the review is focussed on the application without being exhaustive.

2.2.1 Structure of sapphire and Ti-doped sapphire

Sapphire is one of many oxides of aluminium. The chemical formula is Al_2O_3 and is also known as α-Al_2O_3 or α-alumina. The lattice consists of layers of closely packed oxygen ions with aluminium sites between each layer, as shown in Figure 2.1(a). Only two out of every three aluminium sites are filled, to maintain overall charge neutrality. The symmetry of the lattice is described, to a close approximation by the C_{3v} classification[2], which describes an octahedral structure with both cubic and trigonal components. Deviations from the C_{3v} symmetry include a discrete shift in the aluminium ion towards the vacant site along the c-axis and a discrete rotation of each layer of oxygen ions[3]. The orientations of the common crystal planes are shown in Figure 2.1(b), together with the corresponding crystallographic axes, defined in a direction perpendicular to the planes.

High quality sapphire crystals are routinely grown and are readily available in wafer form, with one surface polished to high quality. The wafers used in this work are 300μm thick, 2" in diameter, oriented with the polished face parallel to the c-plane, costing about £100 each.

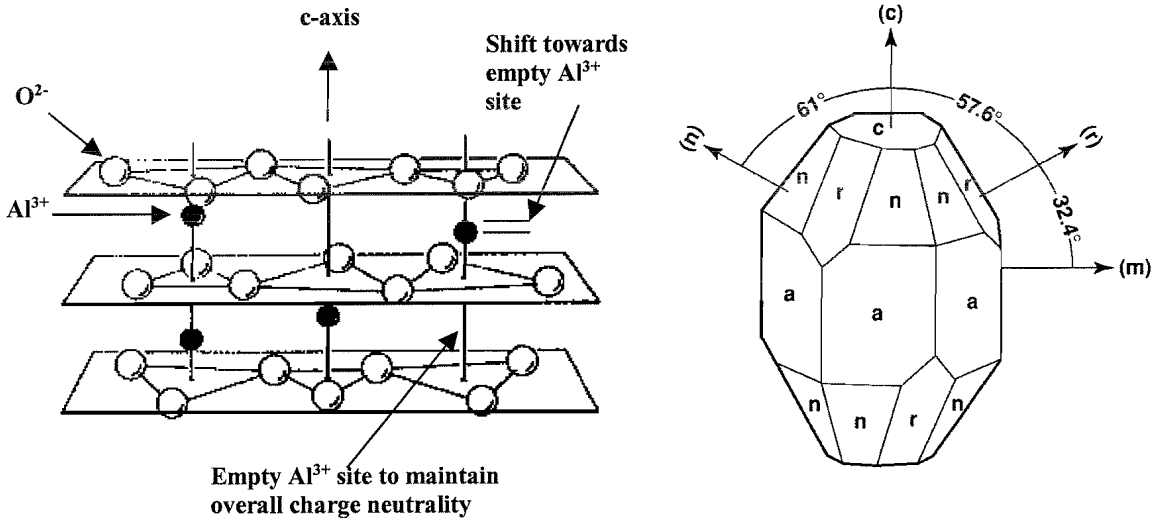

Figure 2.1:- (a) 3-D view of the structure of sapphire[2]; between each layer of close packed oxygen ions, are aluminium sites, although only two out of every three are occupied. (b) Diagram of the common crystal planes in the sapphire lattice[1].

Ti-doped sapphire crystals (referred to as "bulk-doped Ti:sapphire") are formed by introducing Ti_2O_3 into the melt during crystal growth. The Ti^{3+} impurities are incorporated on the Al lattice, in place of an Al^{3+} ion. The Ti^{3+} impurity will cause some local distortion of the lattice due to the difference in size, since the ionic radius of Al^{3+} is about $^2/_3$ that of Ti^{3+}. Incorporating other valence states of Ti, will require a mechanism to compensate for the local imbalance of charge and correspondingly, the solubility of Ti^{3+} is significantly greater than that of Ti^{4+} in sapphire[4].

2.2.2 Physical properties of sapphire and Ti-doped sapphire

Sapphire is an attractive material for use in a broad range of environments. The single crystal has good chemical stability, being resistant to attack by acids, moisture and solvents at room temperature. The crystal is extremely hard, rating 9 on the Moh scale, in comparison to diamond which rates 15, or $LiNbO_3$, which rates 4.5[5]. A device fabricated in a sapphire substrate would be robust and scratch resistant, although the hardness necessitates the use of high specification cutting and polishing equipment during fabrication.

The ordinary refractive index of sapphire is about 1.8 at visible wavelengths and varies with wavelength as graphed in Figure 2.2[6]. The crystal has a negative birefringence, with the extraordinary ordinary index about 0.008 lower than the ordinary index at a wavelength of 633nm. Some variation in refractive index has been observed for crystals grown by different methods, which is attributed to variations in defect structure and impurity content[7].

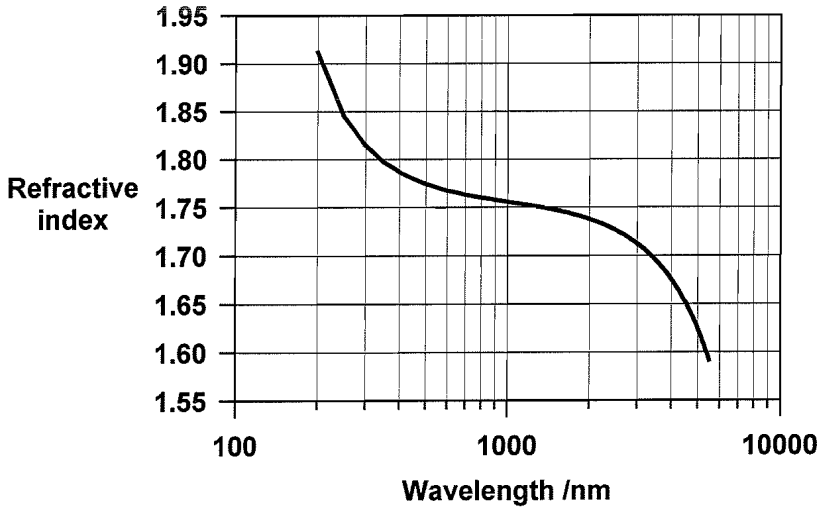

Figure 2.2:- Ordinary refractive index of sapphire at 24 °C over the region of optical transparency 0.2 – 5μm[6].

The refractive index of sapphire increases on heating[8,9], which can lead to thermal lensing in a laser crystal. In addition, the refractive index of Ti-doped sapphire increases under intense illumination with wavelengths in the blue-green[10,11], which corresponds to an absorption of the Ti^{3+} ion (discussed further in §2.2.3). These properties are significant in the operation of a Ti:sapphire laser as they contribute to instabilities in the laser properties as a function of pump power. For example, the early demonstrations of a Ti:sapphire laser relied on liquid nitrogen to cool the crystal and later results indicate that the maximum output power may be increased by about 200 times if operated at a temperature of 77K rather than room temperature[12].

In a waveguide laser system, local changes in the refractive index due to heating would affect the properties of the waveguide. However, the planar geometry also offers the potential for efficient heat extraction due to the proximity of the waveguide to the substrate surface.

2.2.3 Spectroscopy of sapphire and Ti^{3+}-doped sapphire

Pure single crystal sapphire has a high transparency to wavelengths between 0.2μm to about 5μm in the infra-red, as shown in Figure 2.3.

The presence of defects and impurities in the lattice will affect the electronic structure and may allow optical transitions to occur. For example, optical absorption at wavelengths in the ultra-violet accompany electron transitions that are related to the presence of defects in the Al_2O_3 lattice. Impurities, particularly transition metal ions, give rise to characteristic absorption and often yield brightly coloured crystals. In naturally occurring forms, the doped sapphires are well known gemstones, for example ruby is Cr^{3+} doped sapphire and 'star' sapphire contains Ti^{4+} and Fe^{2+} impurities[14].

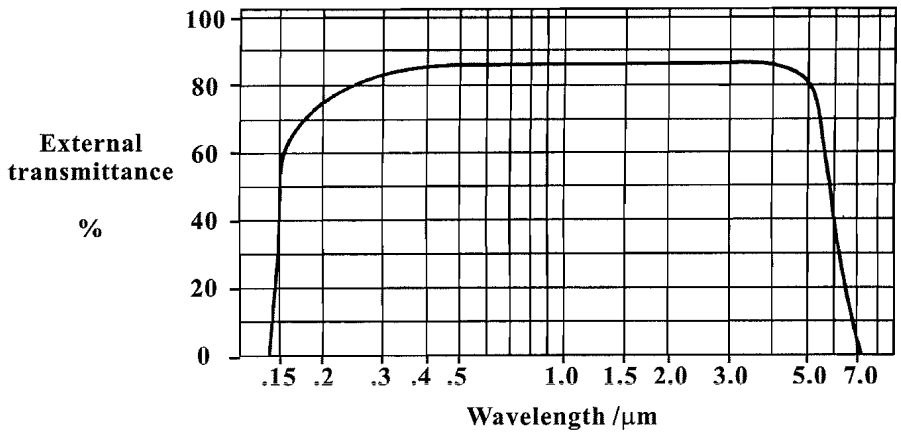

Figure 2.3:- Transmission of a 1mm thick sapphire wafer, uncorrected for Fresnel loss.[13]

For Ti^{3+}-doped sapphire, optical absorption and fluorescence are related to electronic transitions of the Ti^{3+} ion incorporated substitutionally on the Al lattice. The origin of the optical transitions has been extensively studied, with recent interest motivated by the advent of the Ti:sapphire laser and the need for high quality crystals[2,3,15-19]. In the 3+ valence state, the Ti ion has the electron configuration $Ar]4s^2\ 3d^1$, with one electron in the outer most d-electron energy level. In an isolated environment, the d-electron energy level would have a 10-fold degeneracy, with no low lying electron energy levels available for optical transitions. However, when incorporated in the sapphire lattice, the degeneracy is lifted such that the d-shell electron may undergo optical transitions in the visible and near infra-red. A schematic of the splitting is shown in Figure 2.4, considering that the local crystal field is approximated by the sum of cubic and trigonal fields with additional perturbations yielding characteristic fine structure[18,19]. The nomenclature of the energy levels is discussed elsewhere[2]. At room temperature, each electron energy level is coupled to vibrations in the lattice, leading to significant broadening of the transition bands. Electron transitions between the lower group and upper group are allowed with the absorption or emission of a photon.

The characteristic absorption illustrated in Figure 2.5(a) extends from 400 to 600nm, peaking at around 490nm. The peak absorption cross section is of the order of $10^{-24}m^2$ for the π-polarisation[21], which exhibits a stronger absorption than the σ-polarisation. In a Ti:sapphire laser system, the pump source is usually an argon ion laser, aligned with the π-polarisation and operating on all lines, with emission at wavelengths between 450 and 515nm.

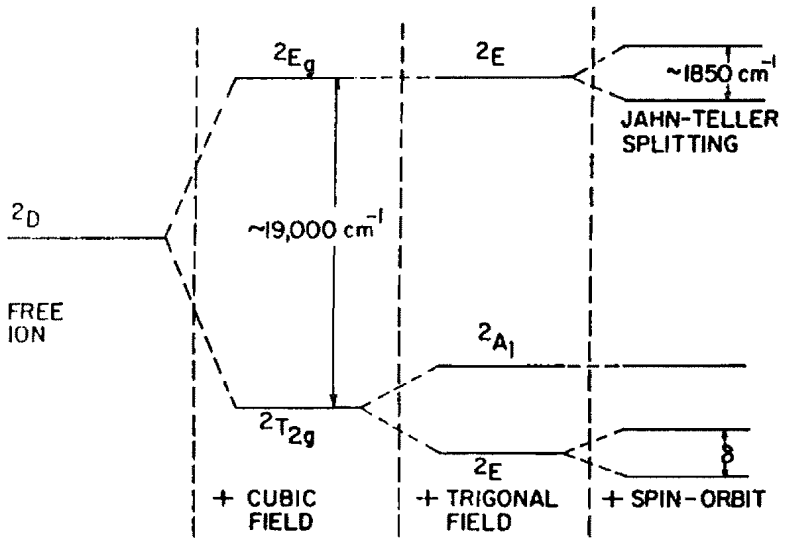

Figure 2.4:- Schematic showing the influence of the local crystal field on the d-shell energy levels of the Ti^{3+} ion in sapphire[20]

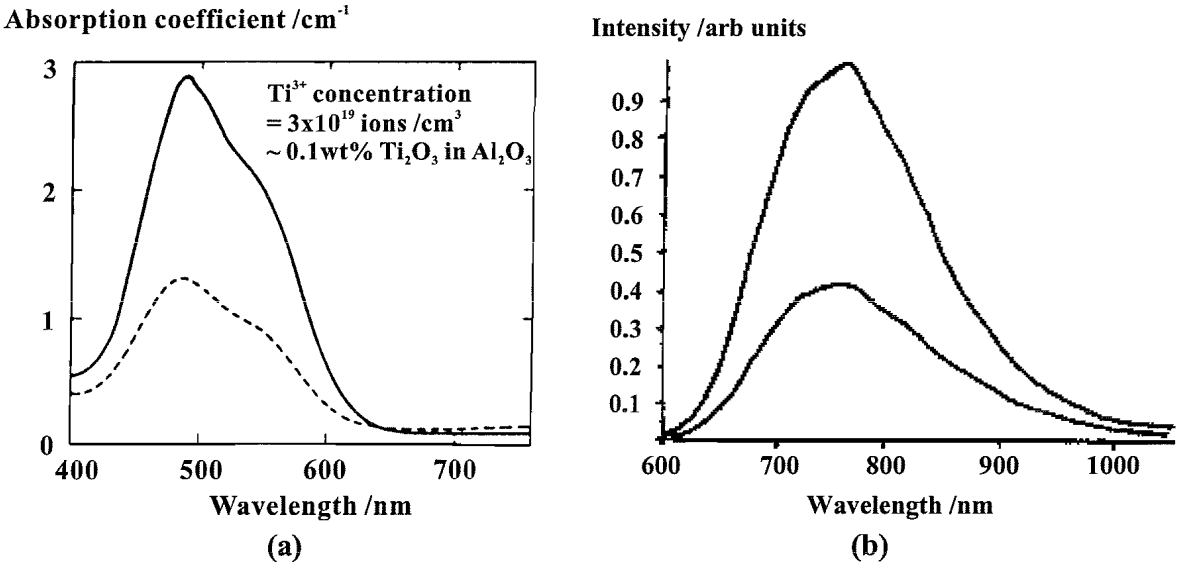

Figure 2.5:- (a) Absorption spectra of the Ti^{3+} ion in sapphire at wavelengths in the visible[27] and (b) emission spectra at wavelengths in the near infra-red region[22].

The broad fluorescence band that results from relaxation to the lower level is illustrated in Figure 2.5(b). The emission lineshape is a close approximation to a Gaussian distribution in the frequency domain, peaking at 396×10^{12} Hz (760nm), with a full width at half maximum of approximately 91×10^{12} Hz (175nm). The breadth of this single transition and the lack of additional low lying empty electron energy levels make the Ti:sapphire material an extremely attractive medium for a broadly tunable laser.

The fluorescence lifetime of the upper laser level is of the order of μs, and decreases with increasing temperature, as illustrated in Figure 2.6[23]. The decrease in observed lifetime is attributed to an increase in the non-radiative decay rate as the temperature increases[23]. At room temperature, the lifetime is reported to be 3.2μs. In a more recent study, a second component in the fluorescence lifetime has been identified with decay times as great as 8μs[24].

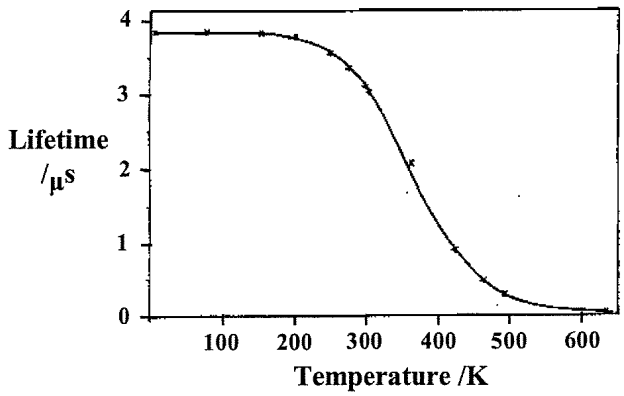

Figure 2.6:- Fluorescence lifetime as a function of temperature[23].

The origin of this longer lifetime is thought to be related to the presence of titanium in either alternative sites or valence states within the crystal.

2.2.4 Influence of Ti^{4+} and defects on Ti:sapphire spectroscopy

Although Ti^{3+} is significantly more soluble in sapphire than Ti^{4+}, trace quantities of Ti^{4+} may be included in the sapphire lattice. The inclusion of Ti^{4+} is detrimental to laser performance as the resulting distortions to the lattice and the inclusion of associated defects causes a shift in the absorption of a near by Ti^{3+} ion from the blue-green to the near infra-red[25]. The shift to longer wavelengths is attributed to a weakened local crystal field as a result of interaction with a nearby Al vacancy[26] and/or Ti^{4+} ion[25,27].

The absorption shown in Figure 2.7 overlaps the fluorescence band associated with the laser emission. In a laser configuration, this would increase the round-trip cavity losses and limit the laser performance. The absorption band peaks at around 800nm and extends well into the infra-red. The polarisation dependence is in contrast with the absorption characteristic of the Ti^{3+} ion, with the σ-polarised absorption greater than the π-polarised absorption.

The proportion of Ti^{4+} included in a laser crystal is characterised by a Figure of Merit (FOM), which quantifies the ratio of peak absorption at the useful, pump wavelength to that at 800nm, due to the inclusion of Ti^{3+}-Ti^{4+} pairs. Currently crystals with Figures of Merit in excess of 100 may be routinely grown.

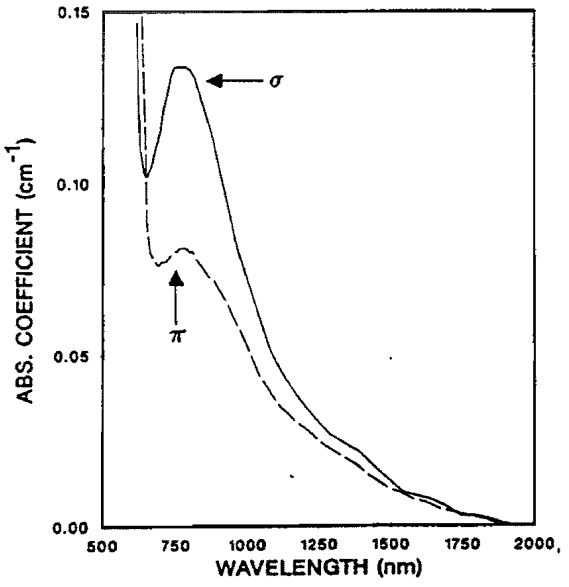

Figure 2.7:- Absorption at wavelengths in the near infra-red due to so-called Ti^{3+}-Ti^{4+} pairs.[15]

2.2.5 Summary of material characteristics

Sapphire is a robust, readily available material, with attractive properties for integrated optic devices. When doped with Ti^{3+}, electronic transitions may occur between electron energy levels of the d-shell which are split, under the influence of the local crystal field. The optical transitions are broadened by strong coupling to vibrations in the lattice. The incorporation of Ti^{4+} promotes the inclusion of defects, for example Al vacancies, which in combination affect the spectroscopy of nearby Ti^{3+} ions.

Therefore, in the preparation of a localised gain medium in a sapphire substrate, the aim is to selectively introduce Ti^{3+} in a substitutional lattice site, whilst minimising the inclusion of Ti^{4+} and associated defects in the lattice.

2.3 Ti:sapphire laser operation

Confining the pump and signal wavelengths to a waveguide configuration through the length of the gain medium leads to the potential for significant improvement in laser performance in comparison with a bulk, commercially available laser. For low input powers, high optical intensities and hence a large excited state population may be achieved within a waveguide, as radiation is confined to a modal area of the order of square microns. The waveguide modes at the pump and signal wavelengths are maintained through the length of the gain medium, which ensures efficient extraction of gain along the axis of the cavity. Under conditions of low propagation loss, there is potential for forming a waveguide laser with a launched pump power threshold orders of magnitude lower than may be achieved in a bulk configuration. The optimum cavity design and the performance of a bulk Ti:sapphire laser have been previously reported[28-30].

Aside from the difference in performance, the planar geometry also offers the advantage of a robust, compact configuration with the potential for the colinear integration of intracavity control components. In addition, by controllably doping a pure sapphire substrate with the Ti^{3+} to form the active medium, the distribution of gain in the waveguide may be optimised according to the waveguide geometry and application.

Considering that the thermal diffusion of ions in sapphire was not developed prior to this work, the potential performance of a waveguide laser is considered here for idealised conditions. The model is based on that presented for a 4-level Nd-doped waveguide laser in

glass by Mwarania[31], with the addition of a term describing the FOM of the gain medium. Other publications that present models describing optical gain and lasing in a waveguide geometry may be found in the literature[32-34]. Further development of the model is anticipated once the characteristics of titanium diffusion and the realisation of passive waveguides in sapphire are fully understood.

2.3.1 Ti:sapphire laser transitions

The combination of optical and vibrational transitions between the d-shell electron energy levels presents a close approximation to a 4-level laser system, as shown in Figure 2.8. In the presence of radiation at a wavelength in the blue-green, $I_p(x,y,z)$, electrons in the lowest vibrational state of the $^2T_2$ level are excited to an excited vibrational state of the ^2E level, from which they undergo a rapid non-radiative decay to occupy the lowest vibrational state of the same energy band. This comprises the upper laser level, which may decay radiatively either by spontaneous emission, or by stimulated emission of a photon. The lower laser level comprises of an excited vibrational state of the $^2T_2$ electron energy level, which rapidly decays, non radiatively, to the lowest vibrational state of the same energy band.

The population of the upper laser level may be solved for a given pump power by considering that the rate of excitation equals the rate of decay under conditions of thermal equilibrium. The rate of excitation from level 1 to 3 is given by the product of the incident photon density (Intensity, $I_p(x,y,z)$ / photon energy, $h\upsilon_p$), the absorption cross section (σ_p), the population of

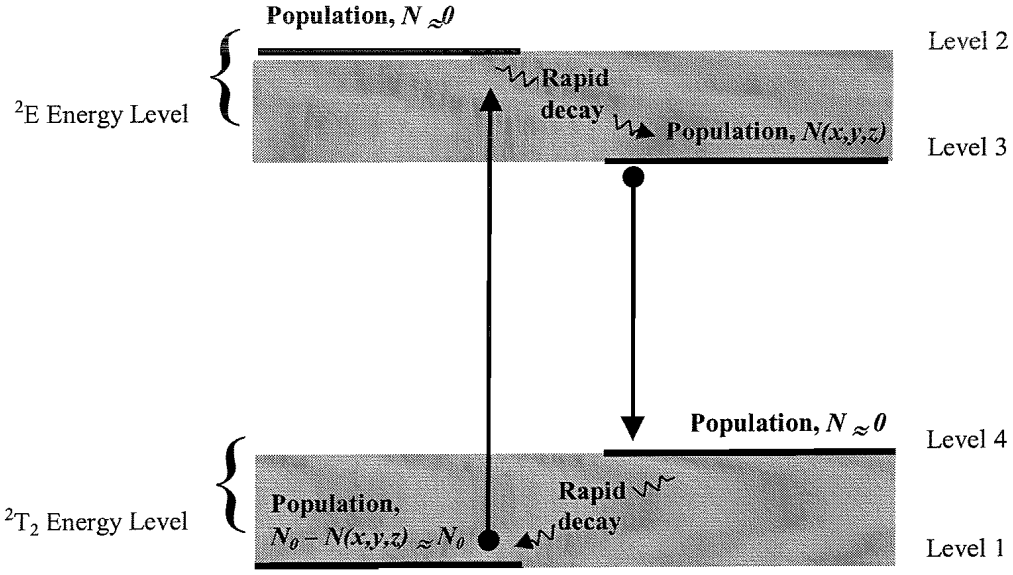

Figure 2.8:- Schematic showing the 4-level pumping scheme for the Ti:sapphire laser.

the lower laser level and the quantum efficiency of transfer from levels 2 to 3 (η). In a four level system, at low pump powers, the population of level 1 may be approximated to the concentration of the Ti^{3+} ion, N_0. This is summarised in *Eqn. 2-1*.

$$\left(\frac{dN}{dt}\right)_{1\to 3} = \frac{I_p(x,y,z)}{h\upsilon_p}\sigma_p \eta N_0 \qquad \textit{Eqn. 2-1}$$

The rate of radiative decay from the level 3 to 1 is given by the sum of the spontaneous emission rate and the stimulated emission rate; between levels 4 and 1, the electron undergoes a non-radiative decay with a lifetime fast compared to the fluorescence lifetime. In thermal equilibrium the rate of stimulated decay is very small in comparison with the spontaneous decay rate. Under these conditions, the decay from the upper laser level (3) to the ground state may be approximated to the spontaneous decay rate, given in *Eqn. 2-2*. *N(x,y,z)* is the population of the upper laser level and τ is the fluorescence lifetime.

$$\left(\frac{dN}{dt}\right)_{3\to 1} = \frac{N(x,y,z)}{\tau} \qquad \textit{Eqn. 2-2}$$

*Eqn. 2-1*and *Eqn. 2-2* are equivalent under thermal equilibrium and may be solved to find the population of the upper laser level, *N(x,y,z)*, given by *Eqn. 2-3*.

$$N(x,y,z) = \frac{I_p(x,y,z)}{h\nu_p}\sigma_p \eta N_0 \tau \qquad \textit{Eqn. 2-3}$$

The population of the exited state is therefore related to the distribution of the pump radiation, the material characteristics of the gain medium, and the concentration of active ion. This analysis uses the approximation that the population of level 1 is much greater than the population of the upper laser level, level 3.

2.3.2 Threshold and slope efficiency of a 4-level waveguide laser

An example of a waveguide laser cavity configuration is shown in Figure 2.9. The waveguide confines the pump along the length of the gain medium, providing a defined region of excited state population. Fluorescence emitted within the numerical aperture of the waveguide will be collected and will stimulate further emission along the axis of the waveguide. Plane mirrors, directly butted to the waveguide endfaces provide feedback of the

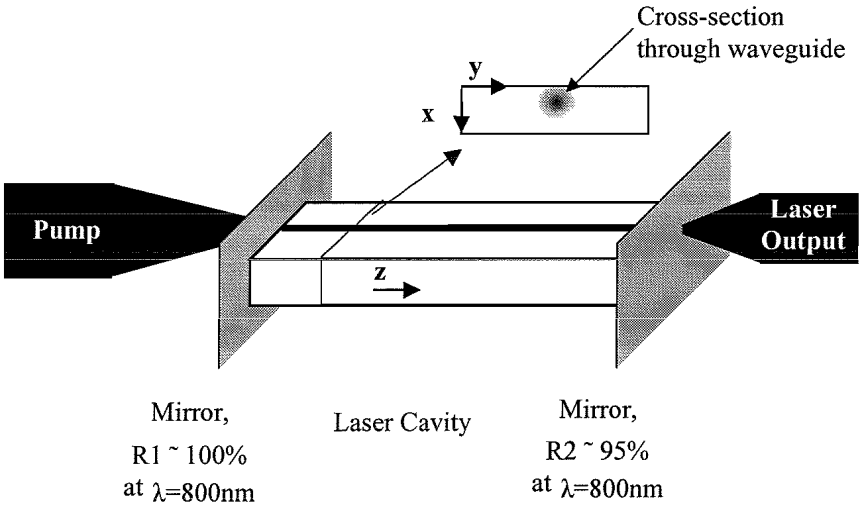

Figure 2.9:- Configuration of a laser in a channel waveguide geometry

signal wavelength into the excited region, and once the total gain is equal to the round trip cavity losses, laser oscillation will occur.

Propagation in the waveguide is assumed to be in the z-direction. The intensity of radiation in the waveguide at the pump and signal wavelengths, $I_p(x,y,z)$ and $I_s(x,y,z)$, may be represented as a product of the total power, $P(z)$ and its modal distribution $S(x,y)$ within the waveguide for the pump and signal modes respectively; $P_p(z)S_p(x,y)$ and $P_s(z)\ S_s(x,y)$.

Substituting I_p in *Eqn. 2-3*, the population of the excited state is proportional to the pump power according to *Eqn. 2-4*.

$$N(x,y,z) = \frac{\tau N_0 \sigma_p \eta}{h\upsilon_p} S_p(x,y) P_p(z) \qquad \textit{Eqn. 2-4}$$

The pump power (P_p) will decrease as a function of z, due to absorption and waveguide propagation losses according to *Eqn. 2-5*. The absorption coefficient is given by the product of the absorption cross section, σ_p and the population in the ground state (level 1), N_0. The distributed loss coefficient that describes the waveguide propagation loss at the pump wavelength is β_p.

$$P_p(z) = P(0)\exp\left[-(N_0\sigma_p + \beta_p)z\right] \qquad \textit{Eqn. 2-5}$$

At the signal wavelength, the power in the waveguide depends on the gain, waveguide propagation losses and intracavity losses. At any point in the gain medium, the fractional change in power will depend on the stimulated emission power, the waveguide propagation loss, and any absorption at the signal wavelength. For Ti:sapphire, reabsorption at the lasing

wavelength is given by the Figure of Merit (*FOM*) which is the ratio between the absorption at the pump and signal wavelengths. The level of stimulated emission depends on the stimulated emission cross section, σ_s and the interaction between the incident signal, $I_s(x,y,z)$ and the population inversion $N(x,y,z)$.

$$\frac{dP_s(z)}{dz} = \iint N(x,y,z) I_s(x,y,z) \sigma_s dxdy - \left[\beta_s + \frac{N_0 \sigma_p}{FOM} \right] P_s(z) \qquad \textit{Eqn. 2-6}$$

Substituting for $N(x,y,z)$ and $I_s(x,y,z)$ in *Eqn. 2-6* the total gain, G, as a result of a single pass through the gain medium of length, L is given by *Eqn. 2-7*.

$$\int_{P(0)}^{P(L)} \frac{1}{P_s(z)} dP_s(z) = \frac{\tau N_0 \sigma_p \eta \sigma_s}{h\upsilon_p} \int_0^L P_p(z) dz \iint S_s(x,y) S_p(x,y) dxdy - \int_0^L (\beta_s + \frac{N_0 \sigma_p}{FOM}) dz \qquad \textit{Eqn. 2-7}$$

The laser threshold occurs when the total losses equal the gain in a round trip of the cavity. Mirrors of a power reflectivity R_1 and R_2 would contribute a loss coefficient of $ln(R_1)$ and $ln(R_2)$, so that the threshold will occur for a pump power threshold which satisfies *Eqn. 2-8*

$$2G = \ln(R_1 R_2) \qquad \textit{Eqn. 2-8}$$

The pump power threshold of the waveguide laser is therefore given by *Eqn. 2-9*. The equation is grouped to show terms describing loss at the signal wavelength, terms describing the absorption of the pump power, a term characterising the waveguide modes and a term containing the spectroscopic characteristics of the gain medium.

$$P_{th} = \left[(\beta_s + \frac{N_0 \sigma_p}{FOM}) L - \frac{\ln(R_1 R_2)}{2} \right] \frac{N_0 \sigma_p + \beta_p}{N_0 \sigma_p (1 - e^{-(N_0 \sigma_p + \beta_p) L})} \frac{1}{\iint S_s(x,y) S_p(x,y) dxdy} \frac{h\upsilon_p}{\tau \eta \sigma_s} \qquad \textit{Eqn. 2-9}$$

Above threshold, the laser output power will increase with increasing pump power according to the slope efficiency of the system. The output power is related to the oscillating intracavity power by the transmission of the output mirror (T). The ratio of power at the signal wavelength compared to the pump wavelength is related to the energy difference between the pump and signal wavelengths, to the quantum efficiency and to the total round trip cavity loss, *RTL*. The slope efficiency (*SE*) is given by *Eqn. 2-10*.

$$SE = \frac{\lambda_p}{\lambda_s} \eta \frac{T}{RTL} \qquad \textit{Eqn. 2-10}$$

The total round trip cavity loss, *RTL* is given by the sum of the intracavity round trip loss, described by the coefficient, 2α, and the loss through the cavity mirrors, $(2\alpha L - ln(R_1R_2))$.

2.4 Potential performance of a Ti:sapphire waveguide laser

Features of a Ti:sapphire waveguide laser may be explored using the model described in §2.3. According to *Eqn. 2-9*, the pump power threshold is dependent on;

- the material parameters, σ_s, σ_p, η and τ
- the cavity configuration, R_1 and R_2
- the waveguide length, L
- the waveguide geometry, $S_s(x,y)$ and $S_p(x,y)$
- the propagation losses at the pump and signal wavelengths, β_p, β_s
- the pump absorption, $N_0\sigma_p$

According to *Eqn. 2-10*, the laser slope efficiency is dependent on the ratio of the transmission of the output coupler to the total round trip cavity losses.

In the following calculations, it is assumed that the gain region is homogeneously doped with Ti^{3+}, and the properties of the waveguide and gain medium can be independently manipulated.

2.4.1 Influence of material parameters and cavity configuration on pump power threshold

The material parameters σ_s, σ_p, η, τ have been experimentally determined by several authors in the course of investigation of bulk Ti:sapphire laser systems and spectroscopic studies[15-17,21-27,35,36]. In the following calculations, the values used are given in Table 2.1 and are assumed constant under the conditions stated. The reported values of the quantum efficiency exhibit the greatest variation, ranging from 0.42[35] to figures close to unity[15,16]. In general the higher values are reported for lower Ti^{3+} concentrations and for Ti:sapphire lasers operating in pulsed mode. A value of 0.5 is taken for the purposes of the following calculations. Since the pump power threshold is inversely proportional to the quantum efficiency, a greater value of η would decrease the projected pump power threshold.

Parameter	Value used in modelling
Stimulated emission cross section, σ_s (π-polarisation)[22]	$3.5 \cdot 10^{-23}$ m^{-2}
Absorption cross section, σ_p (π-polarisation)[21]	$9.3 \cdot 10^{-24}$ m^{-2}
Quantum efficiency, η	0.5
Lifetime[15]***, τ***	$3.2 \cdot 10^{-6}$ s

Table 2.1:- Material parameters used in the modelling of the waveguide laser performance

The reflectivities of the mirrors that form the laser cavity have a direct bearing on the pump power threshold and laser efficiency. According to *Eqn. 2-9*, the lowest pump power threshold would be achieved with high reflectivity mirrors. However, this configuration would also lead to a low slope efficiency, considering *Eqn. 2-10*; this is discussed further in §2.4.5. In the following calculations, the power reflectivity of the cavity mirrors is assumed to be 100% and 95% at the signal wavelength. The laser output is directed through the 95% reflectivity mirror, which is referred to as the output coupler. The output coupling is therefore 5%, given by the power transmission of the mirror.

2.4.2 Effect of waveguide mode size on the laser threshold

The factor $\iint S_s(x,y)S_p(x,y)dxdy$ in *Eqn. 2-7* describes the overlap of the pump and signal modes in the waveguide. In a diffused channel waveguide, the mode profiles are defined by the graded refractive index distribution provided by the diffusion doping. However, in the absence of data for diffused Ti:sapphire refractive index profiles, trends in the characteristics of a Ti:sapphire waveguide laser may be illustrated by approximating the mode profiles to circularly symmetric Gaussian distributions. The mode profiles are characterised by full width at 1/e of the peak intensity (w_p and w_s for the pump and signal widths respectively) and follow the form of *Eqn. 2-11,* which is normalised to unit area according to *Eqn. 2-12.* For these mode profiles, the overlap integral can be solved analytically, as shown in *Eqn. 2-13.*

$$S(x,y) = \frac{1}{\pi w^2} \exp\left[-\frac{x^2+y^2}{w^2}\right] \qquad \textit{Eqn. 2-11}$$

$$\int S(x,y)dxdy = 1 \qquad \textit{Eqn. 2-12}$$

$$\iint S_s(x,y)S_p(x,y)dxdy = \frac{1}{\pi(w_p{}^2 + w_s{}^2)} \qquad \textit{Eqn. 2-13}$$

Since the pump power threshold is inversely proportional to the overlap integral, the threshold will increase proportionally with $w_p^2 + w_s^2$. This relation is shown in Figure 2.10, where the pump power threshold is calculated for a range of mode sizes and waveguide lengths. In this calculation, the width of the mode at the signal wavelength is assumed to be slightly greater (w_s=1.2w_p) than at the pump wavelength, to reflect the lesser degree of confinement at longer wavelengths; the choice of this relation between the pump and signal mode sizes is entirely speculative. The waveguide propagation losses are assumed to be negligible and the waveguide region homogeneously doped at 0.1wt% Ti_2O_3.

Figure 2.10 shows the pump power threshold decreasing with increasing sample length, for mode sizes of 1, 3 and 10μm at the pump wavelength. The threshold tends towards the limiting value of $1.4 \cdot 10^{-3}$ w_p^2 W as L→∞, according to *Eqn. 2-9*. This is the lowest pump power threshold that may be achieved with complete absorption of the pump, a 5% output coupler and no intracavity losses. For the 1, 3 and 10μm pump mode sizes, the limiting thresholds are 1.4, 13 and 140 mW respectively.

Although these calculations are based on simple Gaussian modal distributions, they allow an estimate of the potential laser characteristics to be made and trends in the pump power

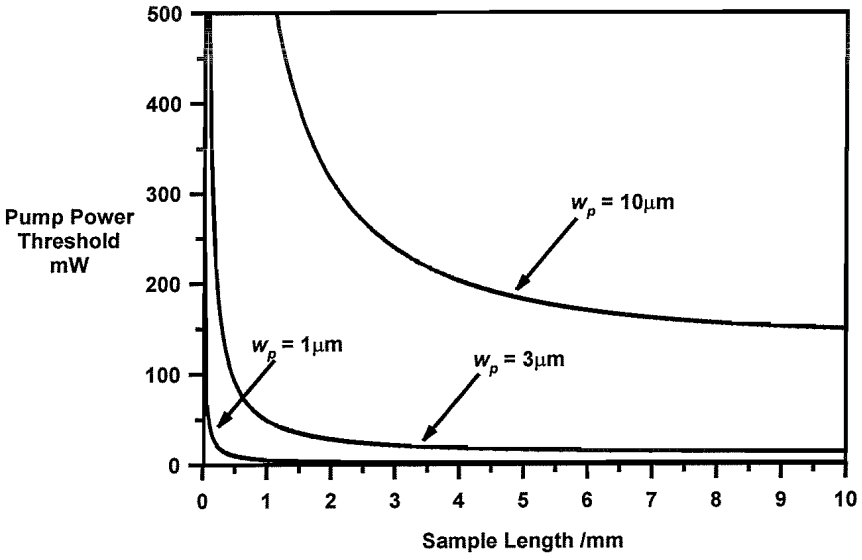

Figure 2.10:- Variation in pump power threshold with waveguide length for waveguide mode sizes of 1, 3 and 10μm at the pump wavelength.

threshold to be observed for a range of modal spot sizes and sample lengths. In the following sections, the mode intensity distribution is assumed to be Gaussian, with $w_s = 1.2w_p = 3\mu m$.

2.4.3 Effect of loss at the signal wavelength on the threshold of a Ti:sapphire waveguide laser

Losses in the laser cavity at the signal wavelength will increase the pump power threshold, as a greater level of stimulated emission is needed to increase the round trip gain. Losses include scattering from the waveguide, given by the loss coefficient β_s and absorption due to Ti^{3+}-Ti^{4+} pairs, characterised by the Figure of Merit, *FOM*. The effect of these losses on the pump power threshold are shown in Figure 2.11, for a 5% output coupler, a 3μm mode size at the pump wavelength and a uniform Ti^{3+} concentration of 0.1wt%.

Curve (a) presents the laser performance in the absence of any material losses in the cavity; as discussed in §2.4.2, the threshold decreases with sample length, tending towards the limiting value of about 13mW. Curve (b) shows that with a finite propagation loss of 1dB/cm at the signal wavelength, the threshold is higher and a minimum pump power threshold is observed for a sample length of 2.4mm. The minimum threshold is 78mW, 6 times greater than the limiting threshold with no loss at the signal wavelength.

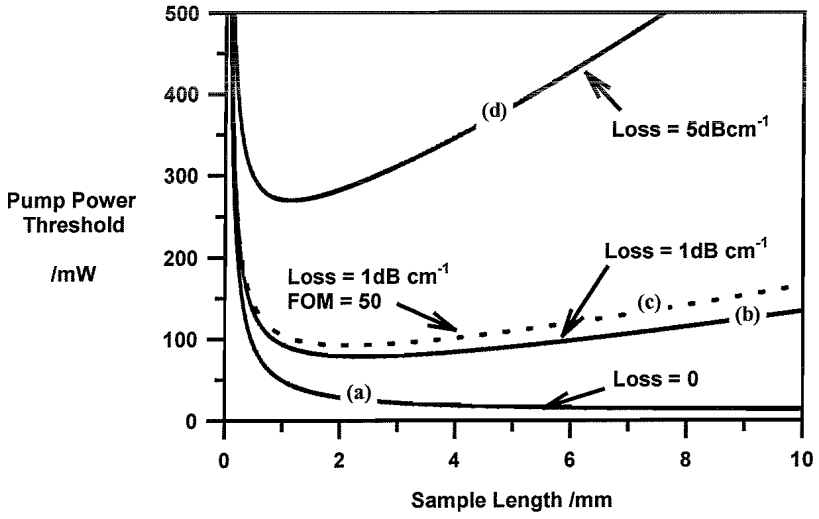

Figure 2.11:- Pump power threshold of Ti:sapphire waveguide laser as a function of sample length, for a range of intracavity losses at the signal wavelength; (a) no propagation loss, (b) 1dB/cm propagation loss, (c) 1dB/cm propagation loss and reabsorption due to FOM of 50, and (d) 5dB/cm propagation loss.

Curve (c) shows the affect of absorption at the signal wavelength, for material with a figure of merit of 50 and a propagation loss of 1dB/cm. The absorption increases the minimum pump power threshold from 78mW to 92mW and slightly decreases the optimum sample length. Material with figure of merit of 50 is equivalent to an additional intracavity loss of 0.3dB/cm.

Curve (d) further illustrates the effect of increasing cavity losses on the pump power threshold. For an intracavity loss of 5dB/cm, the minimum threshold is about 270mW for a device length of just under 1mm. This is 20 times the limiting threshold with no loss at the signal wavelength.

In summary, losses at the signal wavelength increase the pump power threshold. An optimum sample length is found, which decreases as the losses increase.

2.4.4 Effect of Ti^{3+} concentration on the threshold of a Ti:sapphire waveguide laser

The effect of the Ti^{3+} concentration on the pump power threshold is shown in Figure 2.12, considering a 1dB/cm loss at the signal wavelength, 5% output coupler and 3μm mode size at the pump wavelength. With decreasing absorption length (equivalent to an increasing Ti^{3+} concentration for a given propagation loss), the minimum pump power threshold decreases and the optimum sample length decreases.

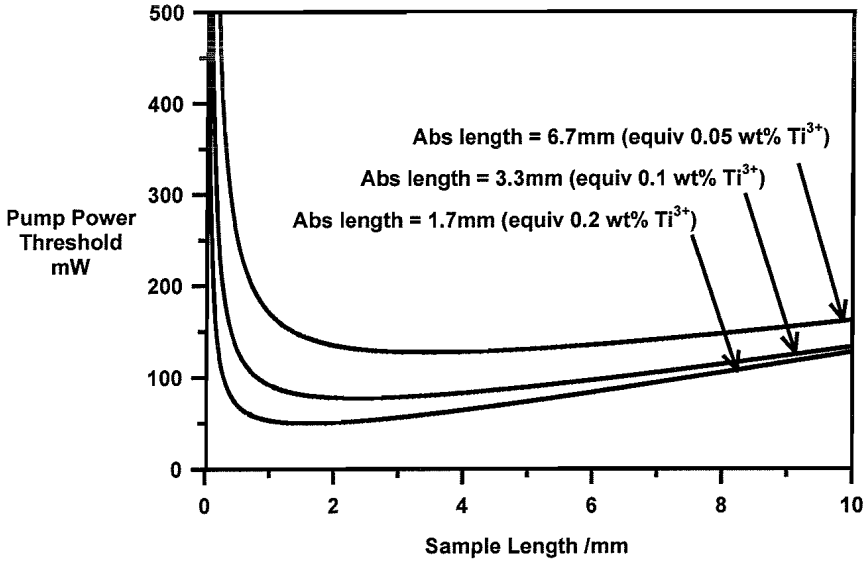

Figure 2.12:- Pump power threshold as a function of sample length for a range of absorption lengths, assuming a total loss of 1dB/cm at the signal wavelength

2.4.5 Efficiency of waveguide laser above threshold

Referring back to *Eqn. 2-10,* the slope efficiency is related to the ratio of the output coupling and total round trip loss in the cavity. Figure 2.13 presents the laser output power characteristics for the waveguide lasers described in Figure 2.11, optimised in length for lowest threshold operation. Curve (a) shows the power characteristics for a laser operating with 5% output coupling, a 3μm mode size at the pump wavelength, doped at 0.1wt% with Ti^{3+} and with no propagation losses at the signal wavelength. Under these conditions, a lowest threshold of 13mW may be achieved and a slope efficiency of 30%. For the same laser, except for a1dB/cm propagation loss at the signal wavelength, the power characteristics are shown by curve (b). A minimum threshold of 78mW is achieved for a sample length of 2.4mm (as discussed in §2.4.3), and a slope efficiency of 9.5%. Curves (c) and (d) present the power characteristics for lasers with a further increase in loss at the signal wavelength. For a 1dB/cm propagation loss and a FOM of 50, a slope efficiency of 8.5% is achieved. For a 5dB/cm propagation loss, the slope efficiency decreases further to 6.5%. In conclusion, as the loss at the signal wavelength increases, the slope efficiency decreases.

For these results, the transmission of the output coupler was set at 5%; greater slope efficiencies may be obtained by increasing the transmission although the threshold would also increase. For a particular launched pump power an optimum cavity configuration may be found for optimum overall power conversion, for the given characteristics of the waveguide and gain medium.

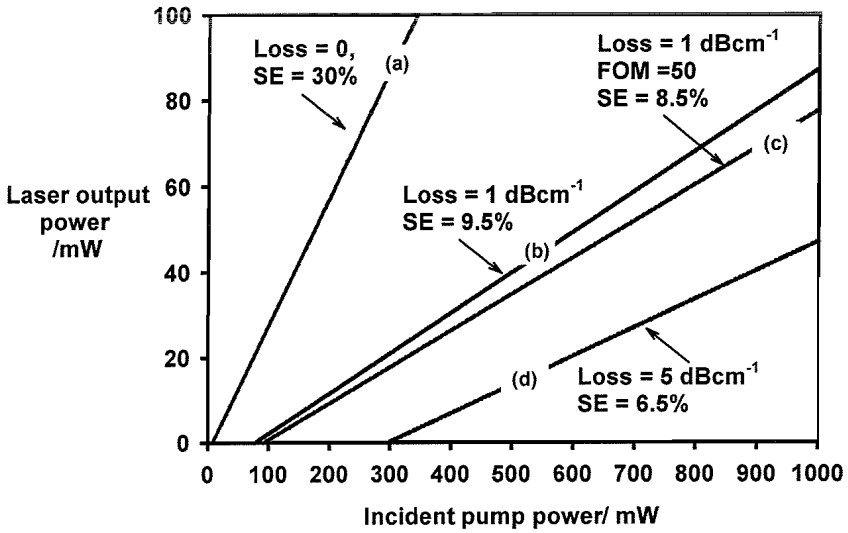

Figure 2.13:- Laser output power characteristics, for a range of intracavity losses at the signal wavelength. (a) No propagation loss, (b) 1dB/cm propagation loss, (c) 1dB/cm propagation loss and FOM of 50 and (d) 5dB/cm propagation loss

2.4.6 Discussion of Ti:sapphire waveguide laser model

Using a simple model of a four level laser, expected trends in the characteristics of a Ti:sapphire waveguide laser have been explored. Under appropriate conditions, there is potential for realising a laser with a pump power threshold of less than 100mW. In the model, the waveguide modes were approximated to Gaussian power distribution, with the mode size slightly increased for the signal wavelength compared to the bulk and the Ti^{3+} distribution is assumed to be homogeneously distributed throughout the waveguide. In the proposed Ti:sapphire laser, deviations from this configuration will occur as both the gain medium and the waveguide are fabricated by thermal diffusion. These features may be included with further development of the model, once the characteristics of the diffused material are known.

The pump power threshold is inversely proportional to the overlap of the waveguide modes at the pump and signal wavelengths, and with mode sizes of the order 3μm, the minimum pump power threshold is 13mW for 5% output coupling. Losses within the cavity at the signal wavelength will increase the threshold and lead to an optimum sample length. For example, the occurrence of a 1dB/cm propagation loss at the signal wavelength, will increase the minimum pump power threshold from 13mW to 78mW. Therefore, to design a laser with a low threshold, the aim is to achieve tight confinement of the waveguide modes, and low losses at the signal wavelength. Then, according to this model, once the losses in the waveguide system are minimised, the Ti^{3+} concentration should be maximised and the sample length minimised.

These conclusions, however, are limited since some of the characteristics of the Ti:sapphire medium have been simplified in this model. For example, the *FOM* is reported to increase with Ti concentration[22], and in practice, the waveguide propagation losses may be related to the Ti concentration. In addition, considering that the difference in the absorption and fluorescence wavelengths (approximately 500nm and 800nm respectively), it is apparent that 40% of the absorbed energy is not re-emitted as photons at the signal wavelength. This energy may be dissipated by heating of the active medium. Temperature changes will reduce the excited state lifetime, reduce the quantum efficiency and increase the local refractive index, affecting the waveguide properties. Therefore, once losses in the waveguide are minimised, an optimum Ti^{3+} doping level and sample length may be expected for a given mode size.

In the Ti:sapphire waveguide laser reported in this thesis, both the waveguide and the gain medium are formed by the thermal diffusion of Ti into sapphire so that the Ti^{3+} concentration and the waveguide characteristics are closely tied. In future devices, the introduction of a second ion to form a passive waveguide, independent of the gain medium would significantly enhance the flexibility of waveguide laser design.

2.5 Summary of chapter

Sapphire is a robust, inert single crystal, with high transparency at wavelengths in the visible and near infra-red regions. However, when Ti^{3+} is incorporated substitutionally for an Al^{3+} ion, a broad absorption appears in the blue-green with a corresponding broad emission band centred at 760nm in the near infra-red. The absorption and emission bands are due to a transition of the outer most electron of the Ti^{3+} ion between d-shell energy levels, which are split by the sapphire crystal field. In combination with rapid non radiative decays between excited vibrational states, the dynamics of a 4-level laser system are set up.

Assuming that the realisation of appropriate waveguides is possible, it is expected that a Ti:sapphire laser may be realised with a pump power threshold less than 100mW. A simple model indicates that once the losses at the signal wavelength have been minimised, the Ti^{3+} concentration should be maximised and the sample length optimised for low threshold operation. However in practice, it is expected that an optimum Ti^{3+} doping level will exist for a given waveguide configuration. Further development of the model is anticipated once diffused waveguides in sapphire are realised for the first time and the characteristics of diffused Ti^{3+} gain medium are investigated. The diffusion doping of sapphire is discussed in the following chapter.

2.6 References to chapter

1. **"Properties of Sapphire"**; *Sapphire information and data booklet, Crystal products, Union Carbide Chemicals and Plastics Co. Inc., pub. 1993*
2. B Henderson, G F Imbusch, **"Optical Spectroscopy of Inorganic Solids"**, *Clarendon Press, 1989*
3. D S McClure, **"Optical Spectra of Transition-Metal Ions in Corundum"**; *J. Chem. Phys., **36** (1962), pp 2757-2779*

4. S K Roy, R L Coble, **"Solubilities of magnesia, titania and magnesium titanate in aluminium oxide"**; *J. Am. Ceram. Soc., **51** (1968), pp 1-6*
5. C W Fynn, W J A Powell, "**Cutting and polishing optical and electronic materials**"; *Adam Hilger imprint for IOP Publishing Ltd, 2nd Ed. 1988*
6. I H Malitson, "**Refraction and dispersion of synthetic sapphire**"; *J. Opt. Soc. Am., **52** (1962), pp 1377-1379*
7. A C DeFranco, B G Pazol, "**Index of refraction measurement on sapphire at low temperatures and visible wavelengths**"; *Appl. Opt., **32** (1993), pp 2224-2234*
8. M A Jeppeson, **"Some optical, thermo-optical, and piezo-optical properties of synthetic sapphire"**; *J. Opt. Soc. Am., **48** (1958), pp 629-632*
9. J Tapping, M L Reilly, "**Index of refraction of sapphire between 24 and 1060°C for wavelengths of 633 and 799nm**"; *J. Opt. Soc. Am. A, **3** (1986), pp 610-616*
10. K F Wall, R L Aggarwal, M D Sciacca, H J Zeiger, R E Fahey, A J Strauss, "**Optically induced non-resonant changes in the refractive index of Ti:Al_2O_3**"; *Opt. Lett., **14** (1989), pp 180-182*
11. H Eilers, E Strauss, W M Yen, "**Photoelastic effect in Ti^{3+}-doped sapphire**"; *Phys. Rev. B, **45** (1992), pp 9604-9610*
12. P A Schulz, S R Henion, "**Liquid-nitrogen-cooled Ti:Al_2O_3 laser**"; *IEEE J. Quant. Electron., **27** (1991), pp 1039-1047*
13. **"Optical properties and applications of Linde Cz Sapphire"**; *Technical bulletin, Union Carbide crystal products, 1988*
14. A R Moon, M R Phillips, "**Defect clustering and color in Fe, Ti:α-Al_2O_3**"; *J. Am. Ceram. Soc., 77 (1994), pp 356-367*
15. P F Moulton, **"Spectroscopic and laser characteristics of Ti:Al_2O_3"**; *J. Opt. Soc. Am. B, **3** (1986), pp 125-133*
16. G F Albrecht, J M Eccleston, J J Ewing, "**Measurements of Ti^{3+}:Al_2O_3 as a lasing material**"; *Opt. Comm., **52** (1985), pp 401-404*
17. P Lacovara, L Esterowitz, M Kokta, "**Growth, spectroscopy and lasing of titanium-doped sapphire**"; *IEEE J. Quantum. Electron., **QE-21** (1985), pp 1614-1618*
18. B F Gachter, J A Koningstein, "**Zero phonon transitions and interacting Jahn-Teller phonon energies from the fluorescence spectrum of α-Al_2O_3 :Ti^{3+}**"; *J. Chem. Phys., **60** (1974), pp 2003-2006*

19. R M McFarlane, J Y Wong, M D Sturge, **"Dynamic Jahn-Teller effect in octahedrally coordinated d^1 impurity systems"**; *Phys. Rev., **166** (1968), pp 250-258*
20. E D Nelson, J Y Wong, A L Schawlow, **"Far infra-red spectra of $Al_2O_3:Cr^{3+}$ and $Al_2O_3:Ti^{3+}$"**; in **"Optical properties of ions in crystals"**, *Ed. H M Crosswhite, H W Moos, Interscience publishers, John Wiley & Sons, 1966, pp 375-381*
21. R L Aggarwal, A Sanchez, R E Fahey, A J Strauss, **"Magnetic and optical measurements on Ti:Al_2O_3 crystal for laser applications: Concentration and absorption cross section of Ti^{3+} ions"**; *Appl. Phys. Lett., **48** (1986), pp 1345-1347*
22. W R Rapoport, C P Khattak, **"Titanium sapphire laser characteristics"**; *Appl. Opt., **27** (1988), pp 2677-2684*
23. P Albers, E Stark, G Huber, **"Continuous wave laser operation and quantum efficiency of titanium-doped sapphire"**; *J. Opt. Soc. Am. B, **3** (1986), pp 134-139*
24. B Gu, M Birnhaum, B Leong, M Bass, **"Material characteristics of titanium: sapphire"**; *J. Opt. Soc. Am. B, **6** (1989), pp 2338-2341*
25. R L Aggarwal, A Sanchez, M M Stuppi, R E Fahey, A J Strauss, W R Rapoport, C P Khattak, **"Residual infra-red absorption in as-grown and annealed crystals of Ti:Al_2O_3"**; *IEEE J. Quant. Electron. **24** (1988), pp 1003-1008*
26. M Yamaga, T Yosida, S Hara, N Kodama, B Henderson, **"Optical and electron spin resonance spectroscopy of Ti^{3+} and Ti^{4+}"**; *J. Appl. Phys., **75** (1994), pp 1111-1117*
27. A Sanchez, A J Strauss, R L Aggarwal, R E Fahey, **"Crystal growth, spectroscopy and laser characteristics of Ti:Al_2O_3"**; *IEEE J. Quantum. Electron., **24** (1988), pp 995-1002*
28. Model 3900, CW Ti:sapphire Laser, Instruction Manual, Spectra-Physics, October 1989
29. D M Kane, **"Ti:sapphire laser cavity mode and pump-laser mode calculations"**; *Appl. Opt., **33** (1994), pp 3849-3856*
30. A J Alfrey, **"Modelling of longitudinally pumped CW Ti:sapphire laser oscillators"**; *IEEE J. Quant. Electron., **25** (1989), pp 760-766*
31. E K Mwarania, **"Planar ion-exchanged waveguide lasers in glass"**; *PhD thesis, University of Southampton, April 1992*
32. M J F Digonnet, **"Closed-form expressions for the gain in three-and four-level laser fibers"**; *IEEE J. Quant. Electron. **26** (1990), pp 1788-1796*

33. M J F Digonnet, **"Theory of operation of three- and four-level fiber amplifiers and sources"**; *SPIE, 1171 (1989), pp 8-26*

34. M J F Digonnet, C J Gaeta, **"Theoretical analysis of optical fiber laser amplifiers and oscillators"**; *Appl. Opt. 24 (1985), pp 333-342*

35. R Moncourge, G Boulon, D Vivien, R Collongues, V Djevahirdjian, K Djevahirdjian, R Cagnard, "**Optical properties and tunable laser action of Verneuil-grown single crystals of $Al_2O_3:Ti^{3+}$**"; *IEEE J. Quant. Electron., 24 (1988), pp 1049-1051*

36. A Mandelis, J Vanniasinkam, S Budhudu, A Othonos, M Kokta, **"Absolute nonradiative energy-conversion-efficiency spectra in $Ti^{3+}:Al_2O_3$ crystals measured by noncontact quadrature photopyroelectric spectroscopy"**; *Phys. Rev. B, 48 (1993), pp 6808-6821*

CHAPTER 3

REVIEW OF DIFFUSION IN SAPPHIRE

3.1 Introduction

To realise the Ti:sapphire waveguide laser, it is proposed that Ti^{3+} is introduced into a nominally pure sapphire wafer by thermal diffusion. Thermal diffusion presents an appropriate fabrication technique, since it offers control over the depth, concentration and spatial distribution of the diffusant, and hence gain medium and waveguide properties.

In this chapter, the basis for the diffusion experiments is established by reviewing simple diffusion theory and published work on the interaction of impurities with sapphire. Ideal solutions to the diffusion equation are presented in order to illustrate the diffusion profiles expected for ideal diffusion conditions. Mechanisms that may cause deviation from the ideal conditions are outlined, in anticipation of the experimental results presented in chapter 4. The discussion is followed by a review of previous studies in sapphire for the metals Al (self-diffusion), Cr, Ni, Fe, Ag and Cu, which serves to highlight the range of diffusivities and diffusion mechanisms that may occur in sapphire. These reviews lead to a discussion of conditions appropriate for the experimental study of Ti diffusion in sapphire. The aim of this chapter is to determine the basis for the experimental diffusion studies that are reported in chapter 4 and lead to the realisation of a waveguide laser.

3.2 Diffusion Dynamics[1]

The original model describing the diffusion of particulants was proposed by Fick in 1855, by comparing mass transport to that of heat flow through a medium. Just as heat flows in a temperature gradient, a particle flux will exist under conditions of a concentration gradient. Quantitatively, the flux is proportional to the concentration gradient, with the constant of proportionality described by a diffusion coefficient. In one dimension, this is summarised by

Eqn. 3-1, where J is the flux, D the diffusion coefficient and $C(x)$ the concentration, defined in the x-ordinate as indicated by the subscript.

$$J_x = -D_x \frac{dC(x)}{dx} \qquad \textit{Eqn. 3-1}$$

The rate of change of concentration in any discrete volume is given by the differential flux through the volume according to *Eqn. 3-2*, a relation that constitutes the condition of mass conservation.

$$\frac{dJ_x}{dx} = -\frac{dC(x)}{dt} \qquad \textit{Eqn. 3-2}$$

Substituting for J, a relation describing the concentration distribution as a function of time for given diffusion rate is forthcoming. Assuming the diffusion coefficient is independent of concentration, the diffusion equation reduces to *Eqn. 3-3*, which may be solved for a range of practical geometries to identify the distribution of the diffused species, $C(x,t)$.

$$\frac{dC(x)}{dt} = D_x \frac{d^2C(x)}{dx^2} \qquad \textit{Eqn. 3-3}$$

The diffusion coefficient describes the rate of movement through the lattice and is a function of temperature following the thermodynamic relation given in *Eqn. 3-4*. Q is the activation energy of the movement, R is the universal gas constant and D_o a constant of proportionality. Both Q and D_o may be modelled in terms of the fundamental thermodynamic properties of the lattice[1], although are more usually determined experimentally, by considering changes in the diffusion coefficient as a function of temperature.

$$D = D_o \exp\left(-\frac{Q}{RT}\right) \qquad \textit{Eqn. 3-4}$$

The relation described in *Eqn. 3-3* gives one of the least complex diffusion relations that may be observed in a practical system. Solutions to this relation are presented in the following section for two sets of boundary conditions that may occur between an ideal planar diffusion source and a substrate.

3.3 Solutions to the diffusion equation

Eqn. 3-3 may be solved for diffusion between a thin film source and substrate, infinite in extent in two dimensions, with the diffusion progressing in the third dimension (x-direction), as shown in Figure 3.1. This is solved in the following sections for the case, (i) when the source is unlimited in thickness and (ii) when the source is instantaneously depleted. In practice for the fabrication of integrated optic devices, the geometry will fall between these two extremes, with the thin film depleted during the diffusion anneal.

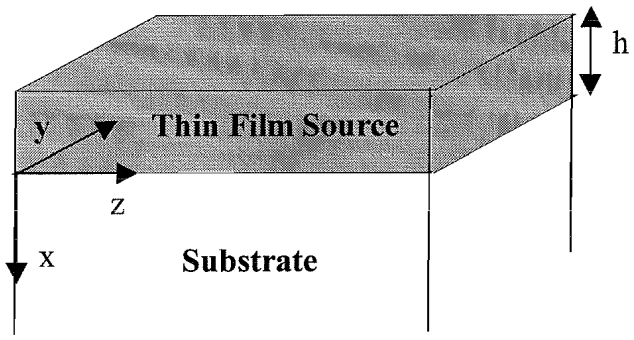

(i) Unlimited diffusion source
$h \rightarrow \infty$
$y \rightarrow \infty$
$z \rightarrow \infty$

(ii) Instantaneous diffusion source
$h \rightarrow 0$
$y \rightarrow \infty$
$z \rightarrow \infty$

Figure 3.1:- Formation of a diffusion couple between a diffusion source and a substrate

3.3.1 Solution for an unlimited diffusion source

When the diffusion source is sufficiently thick, the diffusion may be considered to be unlimited in extent so that the supply to the surface is constant throughout the diffusion anneal. At the interface between the source and the substrate, the diffusant concentration will be maintained at the maximum solubility at the diffusion temperature, C_s. Applying these boundary conditions, the diffusion equation may be solved in terms of the complementary error function (*erfc*), as given in *Eqn. 3-5* below. D is the diffusion coefficient and t, the diffusion time.

Boundary Conditions:
Initially at t = 0, C(x,t) is
C(0,0) = C_s and C(>0,0) =0

Then at t = t, C(x,t) is
C(0,t) = Cs and C(>0,t) = C(x,t)

$$C(x,t) = C_s\left[1 - \int_0^x \exp\left(-\frac{x^2}{4Dt}\right)\right] = C_s erfc\left(\frac{x}{2\sqrt{Dt}}\right) \qquad \textit{Eqn. 3-5}$$

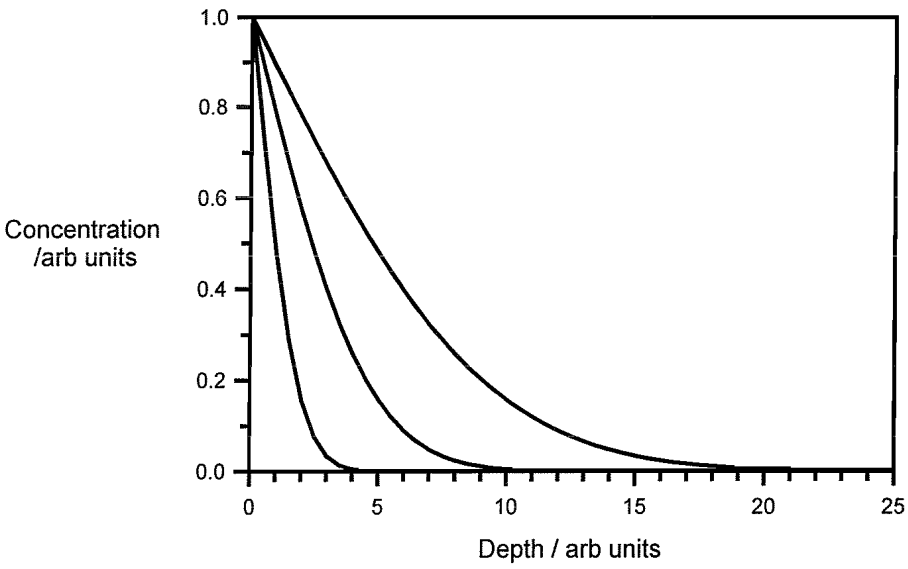

Figure 3.2:- Solutions to the diffusion equation for an unlimited diffusion source, for effective diffusion depths of 2,5 and 10 units.

The solution is characterised by the maximum surface concentration, C_s, and the factor $2\sqrt{Dt}$. The factor $2\sqrt{Dt}$ is referred to as the effective diffusion depth, characterising the depth at which the concentration has fallen to *erfc(1)* (= 0.157) of the peak value at the surface. Examples of the diffusion profile, calculated for effective diffusion depths of 2, 5 and 10 units are shown in Figure 3.2. Under these conditions, the total amount of dopant incorporated increases with time, which is expected considering that the diffusion source has infinite thickness. For the purpose of this illustration, the surface concentration, C_s has been normalised to 1. In a practical system, the surface concentration will be given by the maximum solid solubility of Ti in sapphire, which increases with temperature[2].

3.3.2 Solution for an instantaneous diffusion source

A thin film deposited on a substrate may be rapidly depleted by diffusion into the substrate. Under these conditions, the diffusion may be approximated to have occurred from a diffusion source that is instantaneously depleted. Applying the corresponding boundary conditions, the diffusion equation may be solved analytically to yield the concentration, *C(x,t)*, as a function of depth, *x*, and diffusion time, *t*, given in *Eqn. 3-6*. *Q* is the total number of diffusant atoms supplied per unit area of the surface and *D* is the diffusion rate.

Boundary conditions:

Initially at t = 0,

$\int C(0,0)dx = Q$ *and* $C(x,0) = 0$

$$C(x,t) = \frac{Q}{2\sqrt{\pi Dt}} \exp\left(-\frac{x^2}{4Dt}\right) \qquad \textit{Eqn. 3-6}$$

Then, at t = t, $\int_0^\infty C(x,t)dx = Q$

The solution is characterised by a Gaussian profile for which the concentration falls to 1/e of the peak value at a depth of $2\sqrt{Dt}$, the effective diffusion depth. At all times, the peak concentration is located at the surface, $x=0$, although the peak concentration decreases with time. The total number of particles included in the substrate remains constant, given by the initial number of atoms supplied per unit area of surface, Q. These features are illustrated in Figure 3.3, which shows the diffusion profile for effective diffusion depths of 2, 5 and 10 units.

3.3.3 Summary of ideal diffusion dynamics

By thermal diffusion from a thin film diffusion source, an impurity may be controllably introduced into a substrate. For a source that is unlimited in extent the diffused profile will follow an *erfc* form. The concentration at the surface will be equal to the solid solubility of the diffusant in the substrate, which is a function of temperature. With increasing diffusion time, greater diffusion depths are achieved, whilst the surface concentration remains constant. If the diffusion source is instantaneously depleted at the diffusion temperature, the diffused concentration profile will follow a Gaussian form. With increasing diffusion time, the depth

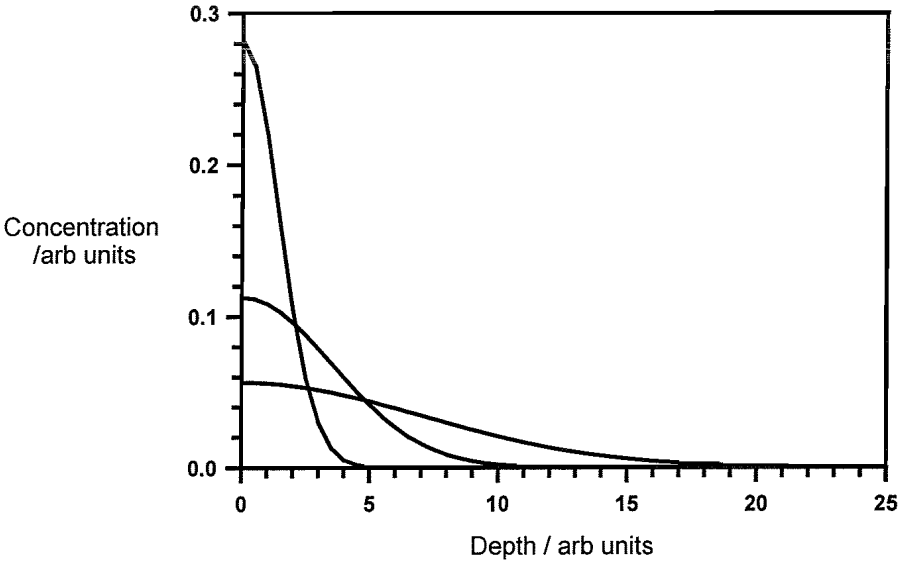

Figure 3.3:- Solutions to the diffusion equation for an instantaneous diffusion source, for effective diffusion depths of 2, 5 and 10 units.

of incorporation increases and the maximum surface concentration decreases. The diffusion coefficient increases exponentially with temperature. Therefore, this ideal model indicates that the diffusion depth, the form of the profile and the concentration may be controlled by varying the diffusion time, the source thickness and the diffusion temperature.

3.4 Deviations from the simplest diffusion conditions

The solutions to the diffusion discussed in §3.3 present the extremes of the most practical diffusion experiments designed to realise materials for integrated optical devices. Typically, a thin film source of finite thickness is deposited on the substrate surface, which is consumed during the diffusion. Therefore, the diffused profile will contain character of the two solutions. For times before the source is depleted, the profile will approximate to the *erfc* solution. For longer times, the surface concentration will decrease and the profile will tend towards that of a Gaussian distribution.

Further deviations from the ideal dynamics described in §3.3 may arise depending on the combination of substrate, source and experimental conditions. For example:-

- more than one diffusion mechanism may exist
- more than one species may be diffusing in the lattice
- diffusion rates may vary with direction in the lattice
- inhomogeneities in the lattice may lead to a spatially dependent diffusion rate
- evaporation of material may occur from the exposed surface
- a chemical reaction may occur between the diffusion source and substrate

The potential for these mechanisms affecting the diffusion of Ti into sapphire is discussed in §3.6. However, the effect of more than one diffusion rate is elaborated further in the following section, in anticipation of the review of diffusion studies of metals in sapphire. In the main, these studies were motivated by the need to independently identify lattice and dislocation diffusion rates in sapphire.

3.4.1 Competitive diffusion routes

The solutions to the diffusion equation presented in *Eqn. 3-5* and *Eqn. 3-6* assume the diffusion uses sites which are homogeneously distributed throughout the lattice. This may be achieved if the diffusion occurs by interstitial sites or by point defects that exist under

conditions of thermal equilibrium. However, a crystal structure will also contain a network of extended defects such as dislocations or grain boundaries. These extended defects may provide an alternative diffusion route (a "short-circuit" diffusion route), which is faster than the lattice diffusion rate. The presence of a faster diffusion route in addition to the lattice diffusion can lead to significant deviations in the measured diffused profile from the ideal diffusion scheme presented in §3.2. The characteristics of the diffusion profile under these conditions have been extensively discussed in published work [1,3-6], and so only brief qualitative description is presented here. The features are highlighted in anticipation of the review of literature discussing the diffusion of metals into sapphire.

3.4.2 Effect of an additional fast-diffusion route on the diffused profile

Qualitatively, Figure 3.4 shows the effect of a fast diffusion rate (D_d) along extended defects and a slower lattice diffusion rate (D_l) on the distribution of a diffusant. In this diagram, the extended defects, such as dislocations, or grain boundaries, are assumed to be oriented perpendicular to the surface. The effective diffusion depths corresponding to the respective diffusion rates are described by d_d and d_l.

Three distinctive diffused profiles are illustrated in Figure 3.4, identified as types A, B and C, with the difference between each type given by the relative rates of diffusion and the distribution of the extended defects. Type A corresponds to the case when the distance between extended defects is small compared to the effective lattice diffusion depth (d_l). Type B occurs when the effective lattice diffusion depth (d_d) is less than the average separation of extended defects. Type C occurs when the lattice diffusion rate is very small compared to the size of the extended defects.

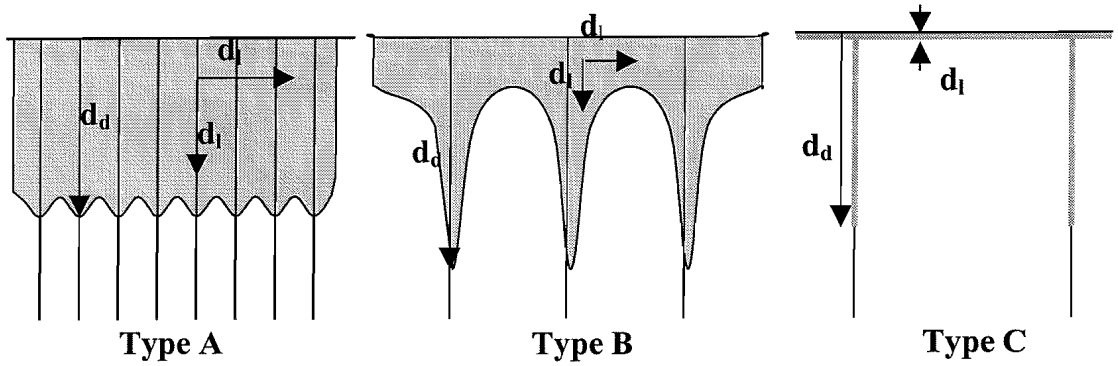

Figure 3.4:- Type A-C diffusion profiles following diffusion along both extended defects and through the lattice, with effective diffusion depths d_d and d_l respectively. The extended defects are oriented perpendicular to the surface, represented by solid lines.

In each of type A-C, the combination of diffusion mechanisms leads to a spatially dependent diffusion profile, with the greatest contrast observed for type C. The techniques available for analysing diffused profiles will normally sample a large area compared to the spatial fluctuations and so the measured concentration of a diffusant is averaged over a depth plane. This leads to distinctly different diffused profiles being measured for each of types A-C.

Type A kinetics lead to a diffused profile that can be characterised by an effective diffusion rate, which is greater than D_l. The enhancement of the effective diffusion coefficient relative to the lattice diffusion coefficient depends on the relative number of diffusion sites on the lattice compared to the extended defect. This system could provide a useful method of enhancing the apparent diffusion rate of dopants in sapphire, as long as the high defect density does not adversely affect the physical and spectroscopic properties of the diffused material.

In contrast, in type C kinetics the effect of the lattice diffusion is very small compared to the transport along the extended defects. In consequence, D_l and D_b can be distinguished, as the diffused profile would be a close approximation to a linear sum of the concentration contributed by the independent diffusion rates. Whilst attractive for identifying D_l and D_d independently, this system is rarely used in diffusion experiments, as it is demanding on the sample morphology and the sensitivity of the analysis technique.

Type B kinetics are often used in diffusion experiments, as the contributions from D_l and D_d can be distinguished from the measured diffused profile. Models describing the diffused profile for various types of extended defects, such as grain boundaries and dislocations are well advanced. An example of the diffused profile is shown in Figure 3.5, which has been published for the self-diffusion of Al in Al_2O_3. The shallowest region of the graph is dominated by the lattice diffusion kinetics and the deeper section is dominated by diffusion along the extended defects. Observing the behaviour of the diffusion profile as a function of time, the nature of the extended defects can be established and estimates made for D_d and D_l.

In summary, the influence of extended defects oriented parallel to the surface, on the diffused distribution has been illustrated qualitatively. Three regimes have been highlighted which are distinguished by D_d, D_l and the density of the extended defects. Each of type A-C leads to spatial inhomogeneities across a depth plane, on a scale comparable to the spacing of the extended defects.

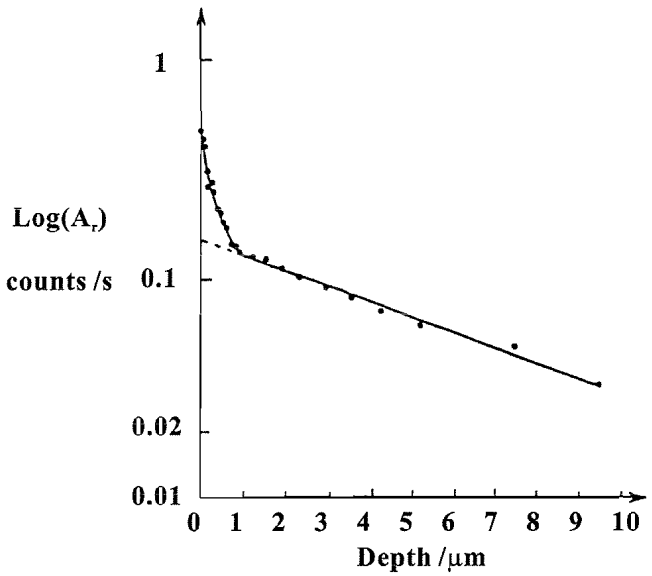

Figure 3.5: Semilogarithmic plot of the residual activity, A_r as a function of depth reported by Legall[7] for the diffusion of the radioisotope ^{26}Al into sapphire. A_r is proportional to the ^{26}Al concentration.

In the diffusion of Ti^{3+} into sapphire, fast diffusion routes along extended defects are expected to exist. If the diffused profiles tend towards that of type B or type C, the spatial inhomogeneities may affect the properties of a waveguide laser formed in the diffused region. Greater homogeneity and a faster effective diffusion rate may be achieved if type A kinetics are realised, although the higher density of defects may affect the properties of the gain medium.

3.5 Review of diffusion studies in sapphire

Interest in the incorporation of impurities in Al_2O_3 spans several decades. However, much of the research was motivated by the ceramics (sintered Al_2O_3) industry and there is only limited data available for diffusion in single crystal Al_2O_3, sapphire. The studies reviewed in this section discuss the movement of Al (self-diffusion), Ni, Cr, Fe, Ag and Cu in sapphire. In many of the studies, two components to the diffusion are observed, explained as diffusion through the lattice and a faster diffusion along short-circuit diffusion routes. None of the diffusion studies was carried out with a view to developing an integrated optic device.

The general experimental method involves the formation of a diffusion couple between a source and substrate, followed by a controlled heat treatment. Often, the sapphire substrates were pre-annealed at a temperature equal to or greater than the diffusion temperature to equilibrate the defect structure prior to the diffusion experiment. Information on the

diffusion rates and diffusion mechanisms was obtained by observing trends in the diffusion profile for a range of temperatures and diffusion times.

The form of the measured diffused profile and the subsequent interpretation of the diffusion coefficients rely on the resolution of the diffused profile. Early diffusion studies relied on the use of radioactive diffusion sources, for which the diffusion profiles were established by sequential sectioning of the diffused region and monitoring the radioactivity of both the removed material and the remaining substrate. This technique requires radioactive sources and relatively deep diffusion depths. More recently, the depth profiling technique, Secondary Ion Mass Spectrometry (SIMS) has been applied to sapphire. This technique removes the need of a radioactive isotope and has the potential for greater sensitivity to low concentrations and has a higher depth resolution. The use of SIMS to analyse a depth profile is discussed further in chapter 4.

The diffusants that are considered in the following sections are the radioisotopes ^{26}Al, ^{110}Ag, ^{63}Ni, ^{51}Cr, ^{59}Fe and the metals Ag and Cu. The diffusion of Ti in sapphire has not been directly studied, prior to the work reported in this thesis. By considering that Ti may exhibit diffusion rates similar to the other transition metal ions, an appropriate range of diffusion conditions may be established for the initial experimental studies.

3.5.1 Self-diffusion of aluminium

The movement of aluminium ions around the sapphire lattice has been investigated using a radioisotope of aluminium, ^{26}Al [7,8]. The isotope has a long half life (in excess of 10^7 years) and is not readily available. As a result, reports describing aluminium self diffusion are limited to include an early investigation by Palandino (1962)[8] in polycrystalline Al_2O_3 and more recent work by Legall (1994)[7] in sapphire. The diffusion coefficients were measured over the temperature range 1540°C-1905°C and span over approximately over 7 orders of magnitude for the various experimental conditions. These results are summarised in Figure 3.6.

In the early study by Palandino, polycrystalline alumina rather than single crystal sapphire, was used as the substrate material. Considering the large number of grain boundaries present in such a system, it is likely that the observed diffusion is due to movement through a combination of lattice and grain boundary sites. The later study by Legall considered self-diffusion in a preannealed single crystal over times up to 250hrs, analysing the diffused

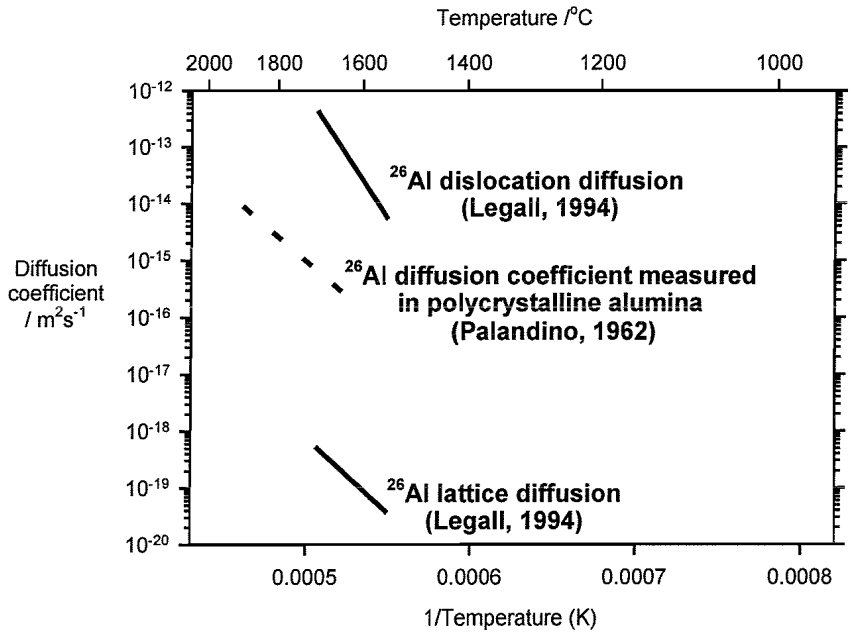

Figure 3.6:- Self diffusion coefficients reported for ^{26}Al in polycrystalline alumina and sapphire, after Palandino[8] and Legall[7].

profile up to depths of about 10μm. Two components to the diffusion were observed and interpreted assuming type B kinetics. From the initial section (depth <1μm) lattice diffusion rates were obtained, as shown in Figure 3.6. The diffusion rate corresponding to the faster diffusion route (described as subboundaries) was estimated to be about 10^6 times faster at a temperature of 1610°C.

The coefficients of Al self-diffusion in sapphire are of interest because the diffusion rate will indicate the mobility of defects in the lattice. For lattice diffusion rates, the aluminium self-diffusion will occur by movement to a neighbouring aluminium vacancy. The number of vacancies and the energy required to change sites will determine the rate of movement. For the crystals used in the Legall study, silicon is known to be an impurity and its presence will increase the density of aluminium vacancies by several orders over the intrinsic defect density at the diffusion temperature. The measured self-diffusion of Al in the lattice will correspond to the movement through extrinsic defects and may be described as an extrinsically controlled diffusion rate. Assuming the aluminium vacancies are not bound to the silicon impurity, the temperature dependence of the diffusion will indicate the activation energy of the migration of point defects in the lattice. The reported activation energy for ^{26}Al lattice self-diffusion, and hence the activation energy for point defect migration is 510 KJ mol^{-1}, which serves as a comparison for other impurities which diffuse by aluminium vacancies.

In summary, self-diffusion rates for ^{26}Al have been reported in the temperature range 1540-1905°C, spanning about 7 orders of magnitude. Diffusion rates corresponding to movement through the lattice and subboundaries have been identified, with the diffusion coefficient for subboundary diffusion about 10^6 greater at a temperature of 1610°C. The density of aluminium vacancies is related to the impurity content of the sapphire, leading to the measurement of an extrinsically controlled lattice diffusion rate. The activation energy of diffusion is 510 KJ mol^{-1} and corresponds to the activation energy for diffusion of aluminium vacancies.

3.5.2 Movement of chromium in sapphire

The results of studies of chromium lattice diffusion in sapphire by Lesage[9], Stubican[10], and Moya[11] are summarised in Figure 3.7, in comparison to the lattice self-diffusion rate for ^{26}Al. The diffusion rates observed for Cr in sapphire are interesting in comparison with aluminium self-diffusion, as Cr^{3+} is only about 20% bigger than Al^{3+} and has complete solubility in the Al_2O_3 lattice at elevated temperature.

The diffusions were carried out over the temperature range 1000-1700°C, using both radiotracer techniques[9,10] and Secondary Ion Mass Spectrometry[11] to identify the diffused profile. In each case, two components to the diffusion were identified and attributed to

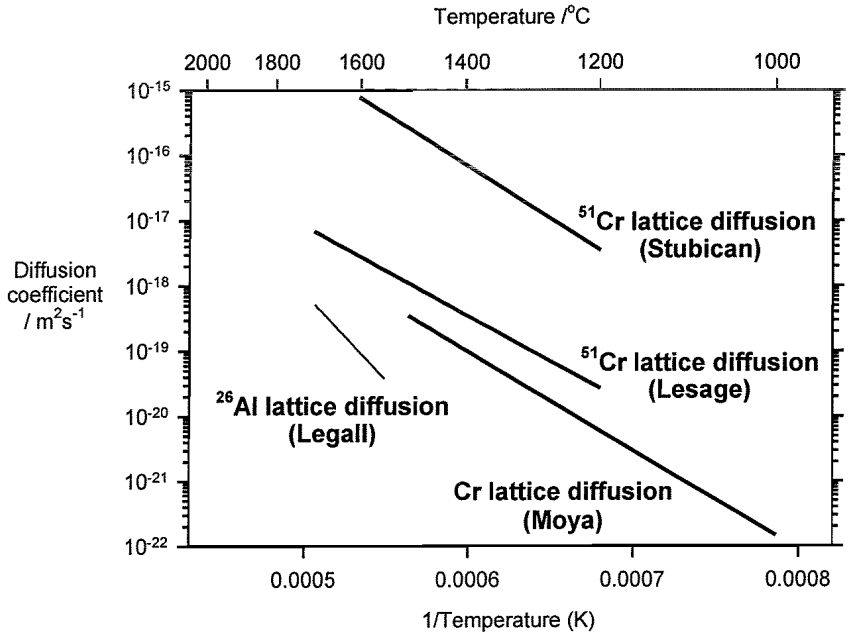

Figure 3.7:- Measured lattice diffusion rates for Cr in sapphire, after Lesage[9], Stubican[10] and Moya[11], with the lattice self-diffusion coefficient of ^{26}Al determined by Legall[7] shown for comparison.

movement through the lattice and to movement through short-circuit diffusion routes, such as grain boundaries and dislocations. The Arrhenius relations describing the lattice diffusion coefficients for the temperature range studied are given in *Eqn's 3-7, 3-8* and *3-9*; along short-circuits the diffusion rate was several orders of magnitude greater.

$$D(1200-1600°C)_{Stubican} = (2.58 \pm 1.5)\cdot 10^{-7} \exp(-\frac{(306 \pm 58)KJmol^{-1}}{RT}) \qquad \textit{Eqn. 3-7}$$

$$D(1000-1500°C)_{Moya} = 1.2\cdot 10^{-10} \exp(-\frac{(290 \pm 30)KJmol^{-1}}{RT}) \qquad \textit{Eqn. 3-8}$$

$$D(1200-1700°C)_{Lesage} = 6.9\cdot 10^{-11} \exp(-\frac{265KJmol^{-1}}{RT}) \qquad \textit{Eqn. 3-9}$$

The measured lattice diffusion rates shown in Figure 3.7 range over about 3 orders of magnitude and are very similar in slope. The similarity in slope indicates the activation energy for migration is similar in all three experimental studies. In each case, the activation energy is less than that of aluminium self-diffusion, implying the larger Cr^{3+} ion has greater mobility in the lattice than a native Al^{3+} ion. The range of diffusivities reported for Cr lattice diffusion may be explained by differences in the impurity content and defect density. For example, the crystals used by Stubican had a significantly greater impurity content than those used by Moya.

Along short-circuit diffusion routes, Moya and Stubican report an enhancement in the diffusion rate of $1.3\cdot 10^{6}$ and 10^{5}-10^{6} respectively. This estimate of fast diffusion along short-circuit routes is similar to that reported for ^{26}Al by Legall. In contrast, the enhancement of diffusion rate along short-circuits reported by Lesage is significantly lower at about a factor of 10.

Stubican also considered diffusion rates in different crystalline directions and concluded that the lattice diffusion rate exhibited no anisotropy.

In summary, Cr diffusion in sapphire has been studied in the temperature range 1000-1700°C. The measured activation energies of lattice diffusion rate are in close agreement and less than that reported for ^{26}Al self-diffusion, indicating the impurity ion has greater mobility than the Al^{3+} ion. The measured lattice diffusion rate varies between studies, a feature that is likely to be due to different trace impurity concentrations in the sapphire and hence a

different defect density. Diffusion rates along short-circuits are reported to be about 10^5-10^6 times greater than the lattice diffusion rates.

3.5.3 Diffusion of nickel in sapphire

The diffusion of nickel in sapphire was considered by Lesage[9] using the ^{63}Ni radioisotope. Nickel in a 3+ valence state, may be substitutionally incorporated on the aluminium lattice, with an ionic radius only slightly smaller than Cr^{3+}. Other valences of Ni may also exist in the sapphire lattice, although a local defect structure is required to compensate for the difference in charge. Oxidation and reduction of nickel in a sapphire lattice has been observed on annealing at temperatures of 800-900°C in the appropriate atmospheres[12]. In the diffusion study discussed here, diffusion was carried out at atmospheric oxygen pressure over the temperature range 1200-1700°C. The valence of the diffused Ni cannot be identified by the radiotracer technique used.

The diffusion coefficients measured by Lesage for nickel are shown in Figure 3.8 in comparison with the ^{26}Al lattice diffusion rate reported by Legall. Two diffusion rates were identified for the movement of nickel, one attributed to lattice diffusion, and the second attributed to a faster diffusion route. The Arrhenius relation describing the lattice diffusion is given in *Eqn. 3-10.*

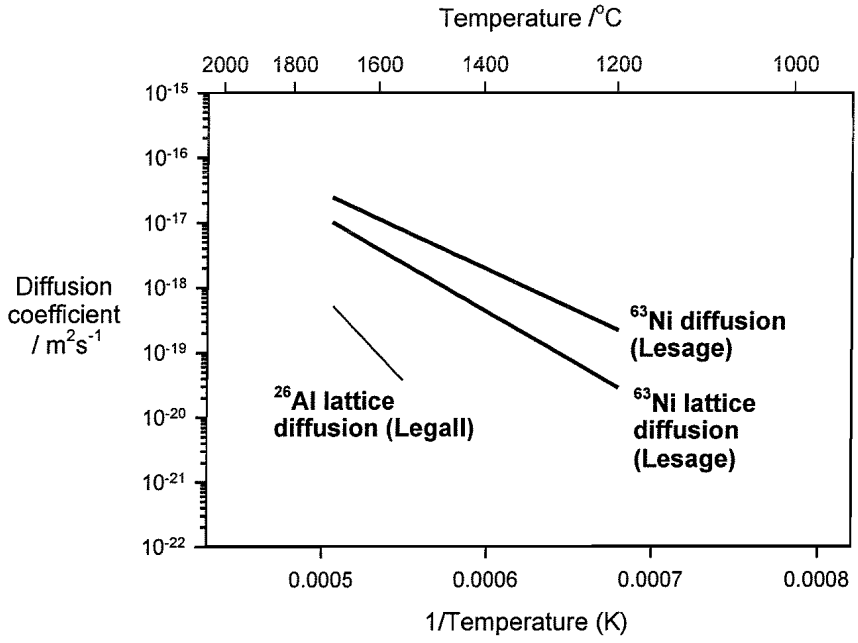

Figure 3.8:- Diffusion rates reported by Lesage[9] for the radiotracer ^{63}Ni, with the lattice self-diffusion coefficient of ^{26}Al determined by Legall[7] shown for comparison.

$$D(1220-1700°C)_{Ni} = 2.53 \cdot 10^{-10} \exp(-\frac{280KJmol^{-1}}{RT}) \qquad \textit{Eqn. 3-10}$$

The lattice and enhanced diffusion rates are similar in magnitude to those determined for chromium by the same author. This may be expected if the diffusion occurs by the same mechanism for Ni and Cr and if the impurity content and defect structure of the substrate are similar.

3.5.4 Diffusion of Iron in sapphire

The diffusion of iron in sapphire has been reported by Lesage[9] and Lloyd[13]. Iron is a transition metal ion that, in the 3+ valence, is similar in ionic size to both Cr^{3+} and Ni^{3+}. A range of possible oxidation states of Fe exists and has been observed in sapphire. Ionic states other than Fe^{3+} will require a local mechanism for compensating for charge, for example, in the form of a local defect structure or an associated impurity. Lloyd considers the occurrence of iron in states other than 3+, although concludes that under the conditions used, the concentrations may be expected to be lower than the background impurity concentration.

The diffusion coefficients measured by Lloyd and Lesage are shown in Figure 3.9, in comparison with the lattice diffusion coefficient for ^{26}Al self diffusion reported by Legall[7].

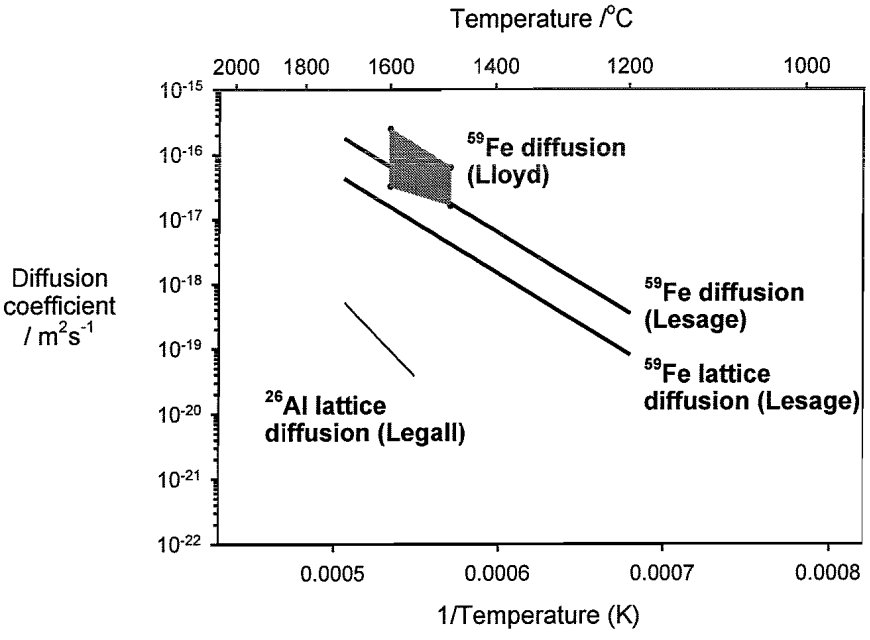

Figure 3.9:- Diffusion rates reported for iron in sapphire (Lesage[9] and Lloyd[13]), with the lattice self-diffusion coefficient of ^{26}Al determined by Legall[7] shown for comparison.

In the study by Lesage, the diffusions were carried out in the temperature range 1200-1700°C in an atmospheric oxygen pressure. Two components to the diffused profiles were identified and attributed to diffusion through lattice and dislocation routes. The Arrhenius equation for the lattice diffusion is given in *Eqn. 3-11*. The activation energy for the diffusion is slightly greater than the values reported by the same author for ^{51}Cr and ^{63}Ni and less than that reported for ^{26}Al by Legall.

$$D(1200-1700°C)_{Fe} = 3.6\cdot 10^{-9}\exp(-\frac{300KJmol^{-1}}{RT}) \qquad Eqn.\ 3\text{-}11$$

The effect of the impurity content of the sapphire on the Fe diffusivity was also investigated by Lesage. In sapphire crystals doped with 1000ppm and 8000ppm of Cr, the iron diffusivity increased. In a similar vein, the penetration of Fe along dislocation was greater for Y^{3+} doped sapphire compared to nominally pure sapphire. These observations would support the hypothesis that the diffusion rate is dependent upon the defect structure of the sapphire, which is controlled by the impurity content.

The diffusion study carried out by Lloyd covered a more discrete temperature range, 1480-1600°C, but considered the effect of differing oxygen partial pressures (10^{-4}-10^{2} Pa) and impurity concentrations (10-50ppm). The range of diffusivities measured under these conditions is included within the shaded region of Figure 3.9. In these studies, a single contribution to the diffusion rate was observed, with no faster component as typical of other diffusion studies. The detailed interpretation of results identified silicon as the dominating impurity that affects the defect structure of the sapphire. Lloyd's conclusions are as follows. At lower temperatures, little oxygen pressure dependence was observed and the iron diffusion occurred by point defects bound to an impurity (mainly silicon). At higher temperatures the diffusion occurs by vacancies which have become dissociated from the impurity. With further increase in temperature or oxygen pressure (T>1600°C and Po_2>10^2Pa) a change in diffusion mechanism is proposed in which interstitial sites play a role. Lloyd's study is one of the earliest to suggest a diffusion mechanism other than by Al^{3+} vacancies.

No anisotropy in the diffusion rate was observed by Lloyd for diffusion perpendicular and parallel to the r-axis (oriented about 60^{o} to the c-axis).

3.5.5 Diffusion of silver and copper

Using radiotracer and SIMS analysis techniques, the diffusion of silver[14-16] and copper[17,18] into sapphire has been investigated. Silver and copper are both metals with one electron in the outer most shell and as ions are most commonly found in the +1 valence state. The atomic radius of copper is similar to that of the atomic radius of chromium, whilst that of silver is about 15% greater.

The diffusion of silver and copper in sapphire has been studied in the temperature range 827-1400°C. Often two components to the diffusion were observed and the diffusion rates associated with the initial sections are shown in Figure 3.10, in comparison with the lattice self-diffusion rate of ^{26}Al. The Arrhenius equations for Ag and Cu diffusion are given in *Eqn. 3-12* and *Eqn. 3-13* respectively. For silver, the activation energy is only slightly higher than that characteristic of the transition metal ions, whilst for copper the activation energy is significantly higher.

$$D(827-1400°C)_{Ag} = 2\cdot 10^{-4}\exp\left(\frac{-331KJmol^{-1}}{RT}\right) \qquad \textit{Eqn. 3-12}$$

$$D(800-1100°C)_{Cu} = 0.11\cdot\exp\left(\frac{-411KJmol^{-1}}{RT}\right) \qquad \textit{Eqn. 3-13}$$

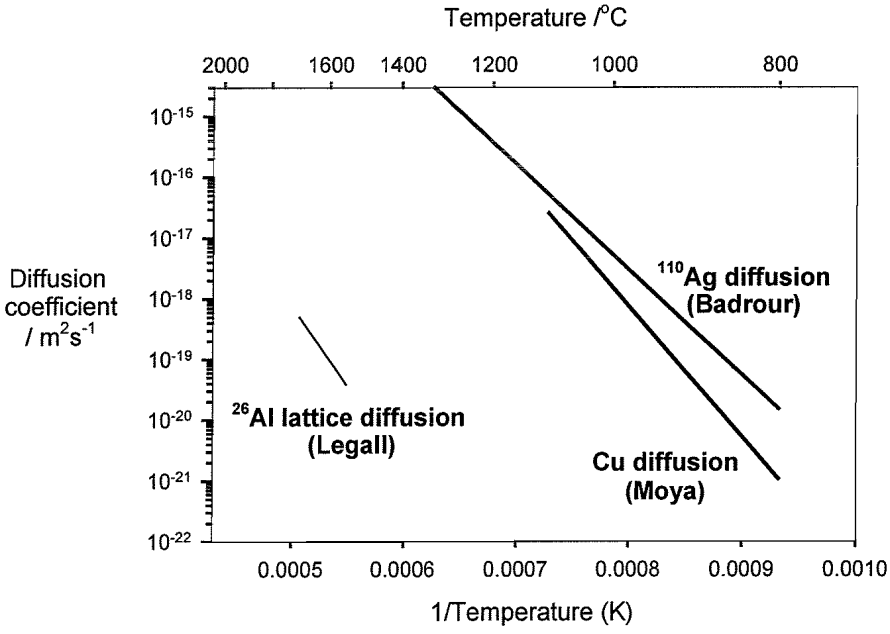

Figure 3.10:- Diffusion rates measured for Cu and Silver, after Moya and Badrour, with the lattice self-diffusion coefficient of ^{26}Al determined by Legall shown for comparison.

The observed diffusion rates are several orders of magnitude greater than the self-diffusion of ^{26}Al and the lattice diffusion rates of the transition metal ions Cr, Ni and Fe, if the data is extrapolated to equivalent temperatures. The diffusion rates observed for silver and copper are close to those attributed to the movement of Cr and Al along extended defects, which are typically 10^5-10^6 times greater than the lattice diffusion rate. Copper and silver are referred to as fast-ions and a different diffusion mechanism is proposed to account for the faster rate.

For silver, the diffusion rate is insensitive to the impurity concentration and independent of changes in oxygen partial pressure. This indicates that the diffusion mechanism does not involve aluminium vacancies. In support of this hypothesis is the observation that a monovalent ion such as Cu^+ or Ag^+ in an Al^{3+} site would repel a nearby aluminium vacancy. The diffusion mechanism that is proposed for these ions involves the use of the interstitial site which has a similar size to the Al lattice site, but is unoccupied to maintain overall charge neutrality. Whilst it is expected this interstitial site plays a role in the diffusion, the substitutional site remains the preferred location. For the movement of copper, Moya concludes that the measured diffusion rate would depend on the ratio of interstitial to substitutional impurity concentrations.

3.5.6 Summary of cation diffusion in sapphire

The reported characteristics of self-diffusion of Al and the diffusion of Cr, Ni, Fe, Ag and Cu in sapphire have been summarised. For diffusion through the lattice a large difference in diffusion rate is observed between the transition metal ions and the monovalent ions of silver and copper.

The transition metals, Cr, Ni and Fe are reported to diffuse by aluminium vacancies, whose concentration is related to the impurity content of the crystal. Lattice diffusion rates spanning several orders of magnitude were observed as the impurity content varied. In each case, the activation energy of movement of the transition metals ions was less than that of aluminium self diffusion, indicating the transition metals ions have greater mobility in the lattice. For iron, at the highest temperature of 1600°C and high oxygen partial pressure, a change in the diffusion mechanism, using interstitial sites is proposed by one author. No anisotropy in the lattice diffusion rate was observed in studies that considered diffusion in different crystal directions.

A second, faster component to the diffusion was observed in many instances and attributed to movement along extended defects such as dislocations and grain boundaries which provide short-circuit routes. Studies by Lesage for Cr, Ni and Fe indicate the enhancement in rate is only about an order of magnitude compared to the lattice diffusion route. However, in other detailed studies of ^{26}Al and Cr, the enhancement of diffusion rate is 5-6 orders of magnitude.

Although many of the transition metal ions may exist in many oxidation states, most diffusion studies assume the diffusant is incorporated in the trivalent state so that it may be directly substituted on the aluminium lattice. The analysis techniques used in the diffusion studies are insensitive to the electron configuration of the lattice constituents.

In contrast, the monovalent ions silver and copper are observed to diffuse significantly faster than the transition metal ions. For silver, the diffusion rate is insensitive to the impurity content and a diffusion mechanism involving interstitial sites is proposed.

3.6 Implications for the diffusion of titanium into sapphire

The diffusion of titanium in sapphire has not been directly studied to the best of my knowledge. However, by reference to diffusion studies reported for other metals in sapphire, some comment may be made on the range of diffusion rates that might be expected. The potential for deviations from simple diffusion theory are also discussed in this section by drawing on other published work.

3.6.1 Ti diffusion dymanics

Titanium is a transition metal with a range of possible oxidation states, although the most common are 4+ and 3+ valences. The ratio of Ti^{3+} and Ti^{4+} will depend on the oxygen partial pressure in the system, so that Ti^{3+} may be formed preferentially over Ti^{4+} if the proportion of oxygen in the ambient atmosphere is minimised[19]. In a practical system, this can be achieved using a reducing atmosphere. Introducing the Ti^{3+} on an Al^{3+} lattice site is central to the formation of the Ti:sapphire waveguide laser.

For the Ti^{3+} ion, the dynamics of the diffusion may be expected to be similar to that observed for Cr, considering that Cr is expected to diffuse as Cr^{3+} ion and the size of the Cr^{3+} and Ti^{3+} are similar. Under this assumption, the Ti^{3+} diffusion is expected to occur using Al^{3+} vacancies in the lattice, with lattice diffusion rate controlled by the impurity content. Along

extended defects, the diffusion rate may be up to 10^6 times greater than through the lattice. The diffusion rate in the bulk is expected to be isotropic, although, a non uniform distribution of defects may lead to local differences in diffusivity.

Figure 3.11 shows the diffusion time that would be required to achieve a 5μm diffusion depth for a range of diffusion temperatures, considering the lattice diffusion rate and the enhanced diffusion rate measured for Cr in sapphire by Moya[11]. The diffusion depth is defined by $2\sqrt{Dt}$, where t is the diffusion time and D is the lattice diffusion rate. The enhanced diffusion rate is taken to be $1.3 \cdot 10^6$ times greater than the lattice diffusion rate, following the conclusions of the author.

Figure 3.11 shows that if Ti is incorporated by the same lattice diffusion rate to that reported for Cr, a diffusion time of hundreds of hours would be needed to achieve a 5μm diffusion depth, at a temperature above 1800°C. However, if a significant density of extended defects is present, the effective diffusion rate could be increased by several orders of magnitude, following type A kinetics. These observations assume that the diffusion mechanism remains the same at higher temperatures than reported for Cr diffusion. On this basis, initial experimental investigation of Ti diffusion in sapphire is carried out at temperatures of 1750°C and 1950°C. At these temperatures, an oxide of titanium is used as a diffusion source.

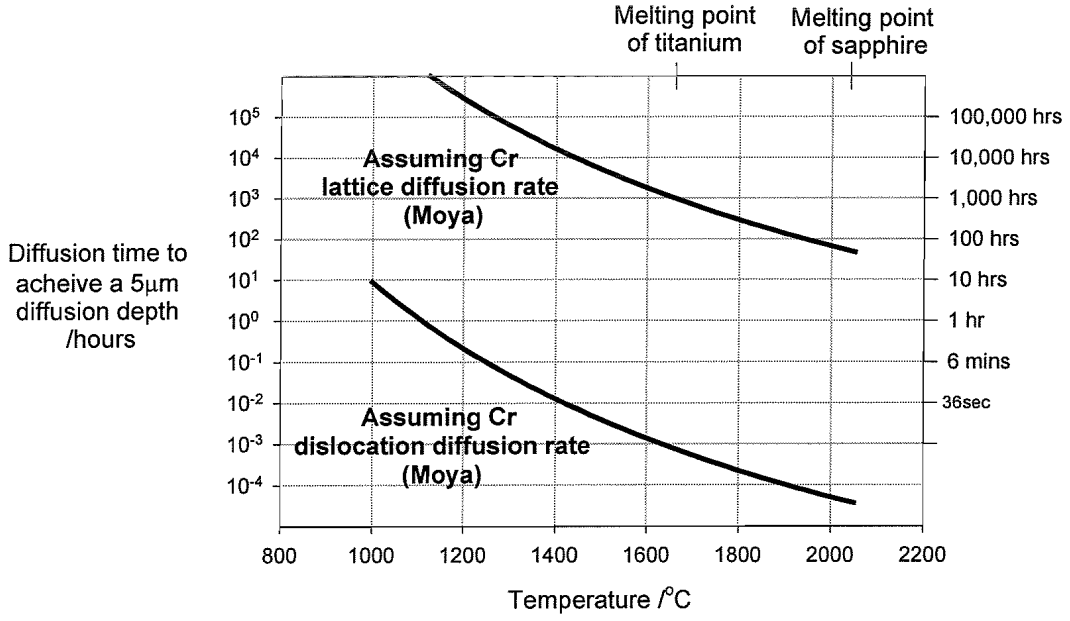

Figure 3.11:- Diffusion time required to achieve a 5μm diffusion depth if the dynamics of Ti^{3+} diffusion follow those of Cr as reported by Moya[11].

3.6.2 Influence of a preanneal

Many of the discussed diffusion studies report the annealing of samples prior to the diffusion experiments[7,10,11,13-18]. The preanneal is carried out at temperatures and for times equal to or greater than, those used for the diffusion experiments. The purpose of the preanneal is to reduce the density of defects in the near surface region which are introduced during the mechanical polishing of the surface[20]. The damage due to mechanical polishing is reported to extend about 1μm beneath the surface and may be removed by a 4 hr anneal at T>1500°C[21]. The preanneal is important to many of these studies, as the contributions to the diffused profile from lattice and short-circuit routes needs to be distinguished. In preannealed samples, type B kinetics were readily achieved.

For the diffusion of Ti into sapphire, the benefits of a preanneal are debatable. A high density of defects immediately below the surface may provide faster diffusion routes for the titanium into sapphire. This would lead to type A kinetics in which the diffused profile is described by an apparent diffusion rate containing a component of lattice and short-circuit diffusion rates. This would have advantages in enhancing the effective diffusion rate and leading to small spatial inhomogeneities. However, a high density of defects may compromise the spectroscopy of the Ti diffused region.

3.6.3 Reaction between source and substrate

At temperatures lower than the proposed diffusion temperature, Ti and TiO_2 are reported to react with sapphire[22-34]. The reaction product and the progression of the reaction are debated between authors and differences are likely to be due to the differences in experimental conditions for each study. Extrapolating this data to the diffusion temperatures proposed for initial experimental work, it is expected that the titanium oxide will rapidly react with the sapphire to form a mixed Ti:Al:O phase. The formation of the reaction product will influence the diffused Ti profile, particularly for short diffusion times. The amount of source supplied will also affect the dynamics of the reaction/diffusion and may lead to non-trivial relations between the diffused profile and the amount of source supplied. In addition, different phases of Ti:Al:O may exist at each diffusion temperature[35], leading to non-ideal trends in the diffused profile as a function of temperature.

3.6.4 Evaporation at high temperature

At temperatures close to the melting point of the diffusion source, some evaporation of Ti may occur. This would lead to a reduction in the total source available for diffusion, and lead to a more rapid depletion of the source than expected. Dissociation of impurities from the surface of a sapphire substrate has been previously observed[36,37] for the impurities Ca and Mg above temperatures of 1600°C and 1400°C respectively.

Once the surface concentration of Ti falls to below the maximum solubility at the diffusion temperature, evaporation of Ti from the surface during the diffusion process will affect the diffused profile. For example, once the source is depleted, the evaporation from the surface would lead to the peak Ti concentration occurring beneath the sample surface[1,38].

3.7 Conclusions

Thermal diffusion offers a flexible method for locally doping a substrate with an impurity ion. The distribution and concentration of the impurity may be controlled by varying the diffusion temperature, the diffusion time and the amount of source supplied. The diffused profile may be easily modelled in one dimension for conditions of an infinite diffusion source and an instantaneous diffusion source. In practice, deviations from this simple scheme will occur if more than one mechanism is affecting the movement of the diffusant. Contributing mechanisms may include more than one diffusion route, more than one diffusing species, anisotropic diffusion rates, spatially dependent diffusion rates, evaporation of the diffusant or a chemical reaction between the source and substrate. Identifying the contribution of some or all of these mechanisms requires significant experimental investigation.

Review of previous diffusion studies in sapphire indicates that a broad range of diffusivities have been observed in sapphire. For transition metal ions Cr, Ni and Fe, the lattice diffusion rates are dependent on the impurity content of the sapphire. The diffusion along extended defects may be up to 10^6 times greater than the diffusion rate through the lattice. The metals Cu and Ag, are identified as "fast-diffusants" in sapphire, and a diffusion mechanism involving interstitial sites is proposed. In all studies that considered diffusion along different crystal orientations, no anisotropy in the diffusion rate was observed.

The kinetics of Ti diffusion into sapphire has not been reported to date, so estimates of appropriate conditions for initial experimental work have been obtained by reference to

studies of similar metals. It is expected that the Ti^{3+} may follow similar kinetics to Cr^{3+}, diffusing using Al^{3+} vacancies, with a rate that is controlled by the impurity content and defect structure of the Al_2O_3 substrate. The diffusion is expected to occur both through the lattice and along any extended defects. The diffusion rate along the extended defects may be as much as 10^6 times greater than the diffusion rate through the lattice. Although preannealing of the substrate prior to diffusion is used in most reported diffusion studies, it is not proposed for initial experimental work. Appropriate temperatures for initial diffusion experiments are 1750°C and 1950°C, with an ambient atmosphere with a low partial oxygen pressure. The low partial oxygen pressure will ensure the Ti diffuses as the Ti^{3+} ion rather than the Ti^{4+} ion.

Deviations from the simple model of diffusion in one dimension may be observed for the Ti diffusion. It is expected that some extended defects will exist in the sapphire surface, which will provide a faster diffusion route. The diffused profile will depend on the distribution of the extended defects. It is expected that the diffusion source will rapidly react with the sapphire, so that the diffusion will occur from the reaction product. The form of the reaction product will depend on the temperature, and the time taken to consume the original diffusion source will depend on the amount of source provided. In addition, evaporation of Ti from the surface may occur at the proposed diffusion temperatures. Establishing influence of these mechanisms on the Ti diffusion in sapphire requires significant experimental investigation.

These ideas are pursued in the experimental work discussed in chapter 4 and lead to the realisation of a Ti-diffused region that is appropriate for a Ti:sapphire waveguide laser.

References to chapter 3

1. General references to this section: "**Atom movements. Diffusion and mass transport in solids**" *by J Philibert, translated by S J Rothman, pub. Les Editiones de Physique, 1991 and* "**The mathematics of diffusion**" *by J Crank, pub. Oxford University Press, 2nd Ed., 1997*
2. S K Roy, R L Coble, "**Solubilities of magnesia, titania and magnesium titanate in aluminium oxide**"; *J. Am. Ceram. Soc., 51 (1968), pp 1-6*

3. A D Leclaire, A Rabinovitch, "**A mathematical analysis of diffusion in dislocations: I. Application to concentration 'tails'**"; *J. Phys. C: Solid State Phys., **14** (1981), pp 3863-3879*
4. A D Leclaire, A Rabinovitch, "**A mathematical analysis of diffusion in dislocations: II. Influence at low densities on measured diffusion coefficients**"; *J. Phys. C: Solid State Phys., **15** (1982), pp 3455-3471*
5. A D Leclaire, A Rabinovitch, "**A mathematical analysis of diffusion in dislocations: III. Diffusion in a dislocation array with diffusion zone overlap**"; *J. Phys. C: Solid State Phys., **16** (1983), pp 2087-2104*
6. A D Leclaire, A Rabinovitch, "**A mathematical analysis of diffusion in dislocations: IV. Diffusion-controlled absorption or desorption for a solid containing dislocations**"; *J. Phys. C: Solid State Phys., 17 (1984), pp 991-1000*
7. M Legall, B Lesage, J Bernardini, "**Self diffusion in α-Al_2O_3 I. Aluminium diffusion in single crystals**"; *Phil. Mag. A, **70** (1994), pp 761-773*
8. A E Palandino, W D Kingery, "**Aluminium ion diffusion in aluminium oxide**"; *J. Chem. Phys., **37** (1962), pp 957-962*
9. B Lesage, A M Huntz, G Petot-Ervas, "**Transport phenomena in undoped and chromium or yttrium doped-alumina**"; *Radiation Effects, 75 (1983), pp 283-299*
10. V S Stubican, J W Osenbach, "**Grain-boundary and lattice diffusion of ^{51}Cr in alumina and spinel**"; *Advances in Ceramics, ed. Kingery, **10** (1984) pp 406-417*
11. E G Moya, F Moya, A Sami, D Juvé, D Tréheux, C Grattepain, **"Diffusion of chromium in alumina single crystals"**; *Phil. Mag. A 2(1995), pp 861-870*
12. R Muller, Hs H Gunthard, "**Spectroscopic study of the reduction of nickel and cobalt ions in sapphire**": *J. Chem. Phys. **44** (1966), pp 365-373*
13. I K Lloyd, H K Bowen, "**Iron tracer diffusion in aluminium oxide**"; *J. Am. Ceram. Soc., **64** (1981), pp 744-747*
14. L Badrour, E G Moya, J Bernadini, F Moya **"Fast diffusion of silver in single and polycrystals of α-alumina**"; *J. Phys. Chem. Solids, **50** (1989), pp 551-561*
15. B Sérier, A Berroug, D Juvé, D Tréheux, E G Moya, **"Silver-alumina solid state bonding: study of diffusion and toughness close to the interface**"*; J. Europ. Ceram. Soc. **12** (1993), pp 385-390*

16. L Badrour, E G Moya, J Bernardini, F Moya, **"Bulk diffusion of ^{110}Ag tracer in Al_2O_3"**; *Scripta Metall. Mater., **20** (1986), pp 1217-1222*

17. C Grattepain, E G Moya, D Juvé, D Tréheux, M Aucouturier, F Moya, **"Depth-profiling for copper diffusion in α-alumina single crystals"**; *SIMS VIII, pp 483-486*

18. F Moya, E G Moya, D Juvé, D Tréheux, C Grattepain, M Aucouturier, **"SIMS Study of copper diffusion into bulk alumina"**; *Scripta Metall. Mater., **28** (1993) pp 343-348*

19. S K Mohapatra, F A Kröger, **"Defect structure of α-Al_2O_3 doped with titanium"**; *J. Am. Ceram. Soc., **60** (1977), pp 381-387*

20. J D Cawley, A l'Hoir, D Schmaus, **"Characterisation of the near-surface region of single-crystal alumina diffusion samples using Rutherford backscattering and channeling"**; *J. Am. Ceram. Soc., **68** (1985), pp 663-667*

21. DJ Reed, B J Wuensch, **"Ion-Probe measurement of oxygen self-diffusion in single crystal Al_2O_3"**; *J. Am. Ceram. Soc., **63** (1980), pp 88-92*

22. F S Ohuchi, M Kohyama, **"Electronic structure and chemical reactions at metal-alumina and metal-aluminium nitride interfaces"**; *J. Am. Ceram. Soc., 74 (1991), pp 1163-1187*

23. R E Tressler, T L Moore, R L Crane, **"Reactivity and interface characteristics of titanium-alumina composites"**; *J. Mat. Sci., **8** (1973), pp 151-161*

24. M Koyama, S Arai, S Suenaga, M Nakahashi, **"Interfacial reactions between titanium thin film and single crystal α-Al_2O_3"**; *J. Mat. Sci., **28** (1993), pp 830-834*

25. L S Drake, R J Lad, **"Electronic and chemical interactions at aluminium/TiO_2(110) interfaces"**; *Surf. Sci., **239** (1993), pp 297-306*

26. M B Chamberlain, **"Solid-state reaction of Ti and sapphire"**; *J. Vac. Sci. Technol., **15** (1978), pp 240-242*

27. J H Seleverian, F S Ohuchi, M Bortz, M R Notis, **"Interface reactions between titanium thin films and (11$\underline{2}$) sapphire substrates"**; *J. Mat. Sci., **26** (1991), pp 6300-6308*

28. B Freudenberg, A Mocellin, **"Aluminium titanate formation by solid state reaction of Al_2O_3 and TiO_2 single crystals"**; *J. Mat. Sci., **25** (1990), pp 3701-3708*

29. B Freudenberg, A Mocellin, **"Aluminium titanate formation by solid state reaction of fine Al_2O_3 and TiO_2 powders"**; *J. Am. Ceram. Soc., **70** (1987), pp 33-38*

30. B Freudenberg, A Mocellin, "**Aluminium titanate formation by solid-state reaction of coarse Al_2O_3 and TiO_2 powders**"; *J. Am. Ceram. Soc., 71 (1988), pp 22-28*

31. M Nathan, C R Anderson, J S Ahearn, "**Interfacial reactions of thin titanium aluminide films with Al_2O_3 films and with sapphire**"; *Mat. Sci. Engin., A162 (1993), pp 107-113*

32. Y-H Kim, YS Chang, N J Chou, J Kim, "**Adhesion of titanium thin film to oxide substrates**"; *J. Vac. Sci. Technol. A, 5 (1987), pp 2890-2893*

33. X A Xhao, E Kolawa, M A Nicolet, "**Reaction of thin metal films with crystalline and amorphous Al_2O_3**"; *J. Vac. Sci. Technol. A, 4 (1986), pp 3139-3141*

34. X L Li, R Hillel, F Teyssandier, S K Choi, F J J van Loo, "**Reactions and phase relations in the Ti-Al-O system**"; *Acta Metall. Mater., 40 (1992), pp 3149-3157*

35. E Levin, "**Phase diagrams for ceramists**"; *2nd ed. Pub. Am. Ceram. Soc., 1964, fig. 316*

36. R C Mclune, W T Donlon, R C Ku, "**Yttrium segregation and YAG precipitation at surfaces of yttrium-doped α-Al_2O_3**"; *J. Am. Ceram. Soc., 69 (1986), pp C196-C199*

37. J D Cawley, J W Halloran, "**Dopant distribution in nominally yttrium-doped sapphire**"; *J. Am. Ceram. Soc. 69 (1986), pp C195-C196*

38. R J Tarento, "**Influence of evaporation and exchange reactions at the surface on the evolution of an arbitrary tracer distribution by diffusion**"; *Revue Phys. Appl., 24 (1989), pp 11-16*

CHAPTER 4

THE DIFFUSION OF TITANIUM INTO SAPPHIRE

4.1 Introduction

Realising a localised gain medium and optical waveguide by thermal diffusion of titanium into sapphire requires significant experimental investigation of the diffusion process. Limited information is available describing the movement of cations in sapphire and less is available discussing the movement of titanium in sapphire. By considering previous work, it is proposed that initial diffusion studies be carried out at temperatures 1750°C and 1950°C in a reducing atmosphere, using a titanium oxide diffusion source. At these temperatures, the diffusion source is expected to react with the sapphire in addition to diffusing into the lattice. Evaporation of the diffusion source may also occur. In the reducing atmosphere it is expected that the Ti will exist as the Ti^{3+} ion and will diffuse using vacant Al^{3+} lattice sites. In addition, a faster diffusion route is expected to exist, using extended defects in the lattice. The difference in diffusion rate by these two routes may be as much as 10^6 times. Establishing the dominance of each mechanism contributing to the transport process requires experimental investigation.

In this chapter, the experimental investigation of the diffusion of titanium into sapphire is discussed. To the best of my knowledge, these results comprise the first realisation of a sapphire wafer locally doped with titanium by thermal diffusion. The purpose of the experimental study is to identify whether the active ion Ti^{3+} may be incorporated in the lattice, to observe how fast the Ti may be introduced and how the diffused profile may be manipulated by varying the experimental conditions. These experiments are not designed to yield fundamental information about the diffusion mechanism or diffusion rate, but to lead to the realisation of a gain medium and an optical waveguide. The formation of optical waveguides in sapphire is the subject of chapter 5; this chapter discusses the spectroscopic properties of the diffused sapphire and the characteristics of the Ti transport process.

The chapter is structured as follows; §4.2 describes the processes developed for diffusing titanium into sapphire, §4.3 describes the experimental techniques used for investigating the spectroscopy and distribution of diffused Ti and §4.4 - 4.7 present the experimental results that characterise the Ti diffusion.

4.2 Fabrication; materials, equipment and processes

The study of titanium diffusion in sapphire was carried out by deposition of a thin film diffusion source onto a sapphire substrate and holding the diffusion couple at elevated temperature under controlled conditions. The following carbon resistance furnace and fabrication processes were developed during the course of this work

4.2.1 Substrate preparation

Commercially available, synthetic sapphire wafers were used as substrate material. These were typically 300μm thick and supplied with one face epi-polished[1] to high quality, oriented perpendicular to the c-, or optical-axis. The wafers were cut into multiple samples of maximum dimensions 10x10mm. If a patterned diffusion source was to be used, one edge of the sample, aligned perpendicular to the a-axis (<1120>), was polished to provide a reference.

The sapphire surface was degreased and cleaned in preparation for the deposition of a diffusion source using a sequence of organic solvents prior to an acid treatment. The organic solvents were used in an ultrasonic bath at temperatures up to 55°C. A typical sequence is 20 minutes in 1,1,1-trichloroethane followed by 20 minutes in acetone. The 1,1,1-trichloroethane removes residues of wax used to secure the sample during cutting and polishing stages, whilst acetone is an effective solvent for common organic compounds. Since the availability of 1,1,1-trichloroethane has become restricted due to environmental concerns, lotoxane or ecoclear[2] may present a preferred solvent for the removal of wax in future processing.

Following the sequence of organic solvents, the surface should be clean of organic impurities, but is usually still covered with a scattering of particulants. These may be removed in a mixture of hydrogen peroxide and sulphuric acid, known as piranha solution. The sample was immersed in a 4:1 mixture of concentrated sulphuric acid: hydrogen peroxide supported in a water bath at 80°C. After ten minutes, a second measure of peroxide

was added and the mixture left for a further ten minutes. The top-up with peroxide half way through the cleaning process compensates for loss of the original peroxide as it rapidly dissociates at the elevated temperature and ensures the mixture is active throughout the 20 minute process. Following immersion in the piranha solution, the sample is rinsed in de-ionised water, blown dry and baked in an oven at 120°C for at least half an hour to remove any remaining moisture from the surface.

4.2.2 Preparation of a photoresist mask by photolithography

When a patterned diffusion source rather than a continuous thin film diffusion source was required, a photoresist film was spun on the sapphire surface and photolithographically patterned to form a mask. The pattern was transferred to the thin film diffusion source using a standard lift-off technique.

The photoresist mask was fabricated in Shipley 1400-27 resist, spun onto the substrate to form a film approximately 1μm thick. Following a soft bake (30 minutes at 90°C), the sample was aligned with respect to a mask and exposed for between 7 and 7.5s. Prior to development of the photoresist, the sample was soaked in chlorobenzene for 5 minutes. The chlorobenzene diffuses into the surface of the photoresist layer and reduces the rate of development, allowing the profile of the photoresist mask to be optimised for the lift-off process. The exposed regions were developed for 3 minutes to leave a series of channels in the photoresist, which are partially filled during the subsequent deposition of a thin film. After deposition of a titanium oxide film, the process is completed by rinsing the sample in acetone, which removes the photoresist mask to leave a patterned thin film diffusion source. The Shipley 1400-27 resist has recently been discontinued and replaced with the 1813 series. Initial indications are that the same fabrication parameters may be used with the new series.

The mask used in this work consisted of a series of stripe openings in a chrome film on a glass substrate, prepared using direct-write electron beam technology. The stripes were grouped in sets of 14, with widths ranging from 3 to 16μm at 1μm increments and spaced by 100μm. To aid the identification of stripes across the sample, 100μm wide marker stripes separate every second group. An example of the small differences in the dimensions of the transferred pattern and the original mask are illustrated in Figure 4.1, with a 2μm increase in stripe size, compared to the original mask, typical of the fabrication parameters used. With refinement of the parameters used in the photolithography, the reproducibility of the mask

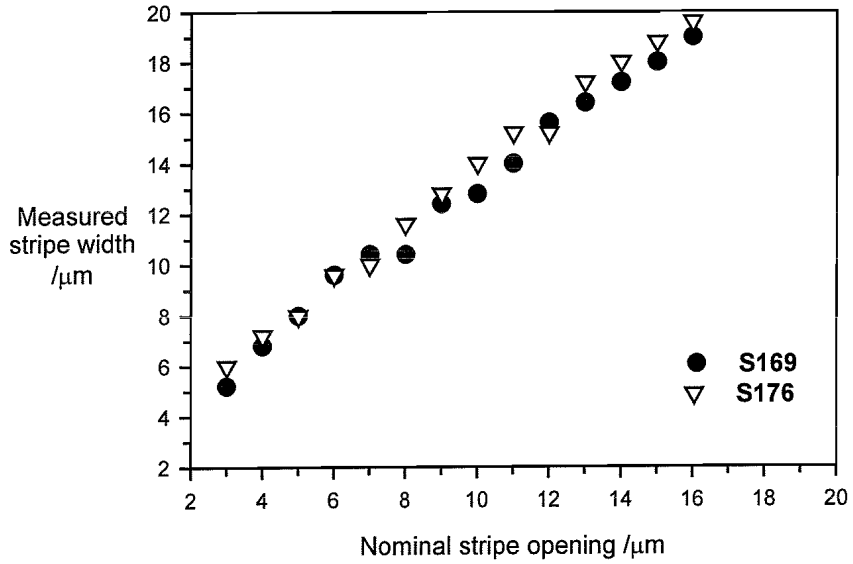

Figure 4.1:- Example of stripe blow-out as measured for samples S169 and S176. The defined stripes are typically between 2 and 4μm wider than the original mask opening, however, stripes are identified by reference to the width of the initial mask opening.

could be improved. Throughout this work, stripes are identified by reference to the dimensions of the original mask opening.

4.2.3 Deposition of thin film diffusion source

The diffusion source was deposited by thermal evaporation from a powdered titanium sesquioxide (Ti_2O_3) source in a partial oxygen pressure using an Edwards 306 evaporator. A maximum of 12 samples could be coated simultaneously, mounted on an aluminium block positioned directly above the evaporation source at a distance of approximately 30cm. The evaporation source was supported in a small tungsten boat that could be re-used for two or three runs, with the source topped up each time. Once loaded, the evaporator was evacuated to a pressure of the order of 10^{-6} mbar, before it was back filled with oxygen to a pressure of 10^{-4}mbar. The evaporation source was resistance heated over a period of about 3 minutes, before the shutter was opened, allowing the evaporated material to reach the samples and condense to form a thin film. The thickness and deposition rate of the film was monitored with a piezoelectric crystal monitor located close to the samples being coated. A typical deposition rate was around 1 nm s^{-1} and films of thickness between 15 and 270nm were deposited.

The film thickness was measured after deposition using a Tencor α-step profilometer. For samples patterned with stripes, the thickness measurement was recorded for the height of the

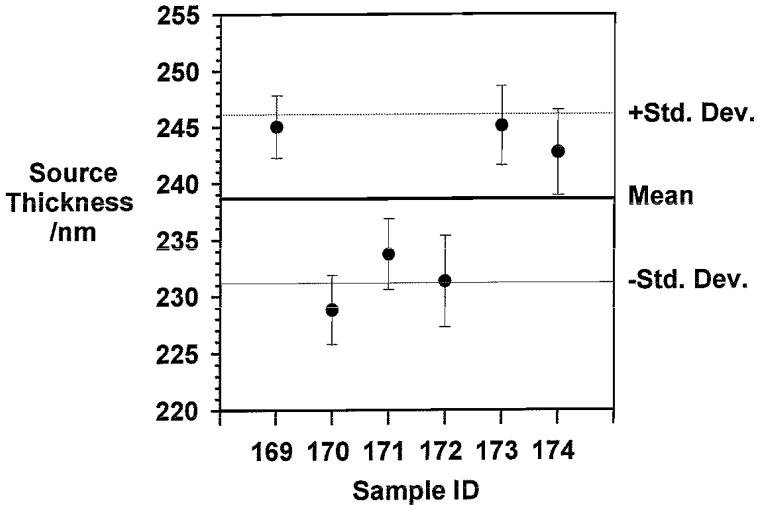

Figure 4.2:- Example of variation in source thickness obtained in the thermal evaporator for samples coated simultaneously.

16μm stripe after lift-off. For samples coated with a continuous thin film, the film thickness was taken to be that measured for a test sample patterned with a photoresist mask and included in the same evaporation run. The uniformity of film thickness across the sample mounting area in the evaporator is typically 10%, illustrated in Figure 4.2. The patterned films on samples S169-S174 were deposited simultaneously.

The deposited thin film is expected to contain Ti in a range of oxidation states, as the Ti_2O_3 source is reported to dissociate on heating[3]. In calculations that require the density and composition of the diffusion source, the film is assumed to be stoichiometric Ti_2O_3, however, to reflect the unknown composition of the film, the diffusion source is referred to as Ti(O).

4.2.4 Thermal diffusion

The thermal diffusion was carried out in a carbon resistance furnace operable between 1400°C and 2000°C. The furnace was mounted vertically and provided a hot zone of the order of a few millimetres in length, monitored in temperature pyrometrically. Laterally, the temperature profile was at a minimum at the centre of the cylindrical carbon elements and increased by about 30°C over the area occupied by the sample. Due to the exposed carbon heating elements, the ambient atmosphere was restricted to an inert gas, in this case argon.

For the diffusion experiments, the prepared sapphire sample was positioned in the furnace hot zone, supported on a thin tantalum foil covering a carbon support rod. The furnace was

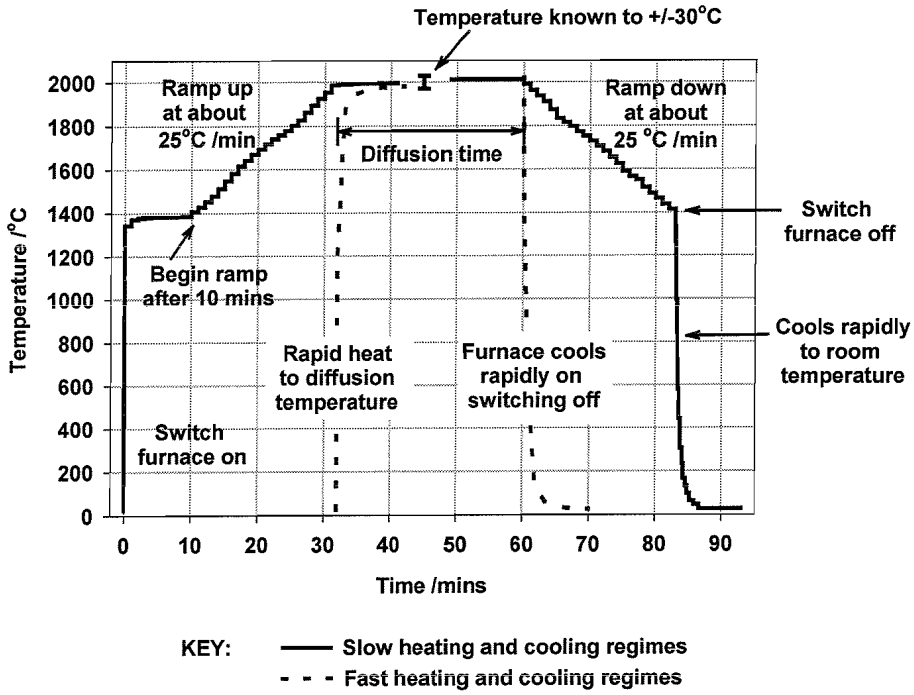

Figure 4.3:- Example of heating and cooling rates used in the diffusion of titanium into sapphire, measured using a Type W thermocouple.

heated and cooled around the sample according to the experimental conditions under investigation. Heating and cooling rates were either 'rapid' in that the furnace was switched directly between the required temperatures or 'slow', for which the ramp rate was controlled over a fixed period. The temperature profile accompanying these regimes is shown in Figure 4.3, measured with a type W thermocouple. The 'slow' heating rate is described by switching the furnace on close to the lowest controllable temperature, about 1400°C and leaving for 10 minutes before ramping to higher temperatures in about 25°C increments at minute intervals. This is reversed for the slow cool regime, as shown in the diagram. Thus for heating to or cooling from temperatures of 1950°C, the slow regime spans 32 minutes.

4.2.5 Preparation for characterisation

Following the diffusion, samples were prepared for characterisation. For optical techniques, 2mm sections were removed from opposing edges of the sample, before the exposed end faces were polished to high optical quality.

4.2.6 Sample referencing scheme

The fabrication process described is the result of continuous development over the course of the work. The fabrication conditions for individual samples are summarised in the text on

first introduction and are repeated in shorthand as a footnote whenever they are subsequently referred to. For example, sample S124 was fabricated with a 27nm diffusion source, diffused for a time of 8 hours at a temperature of 1950°C, and heated and cooled slowly. This would be summarised in a footnote by S124{slow heat, slow cool, 27nm, 8hrs, 1950°C}. If the source were patterned with stripes using the mask described above, the letter P would prefix the film thickness, for example {slow heat, slow cool, P27nm, 8 hrs, 1950°C}.

4.2.7 Summary of fabrication procedure

The fabrication technique and the characteristics of the equipment developed for diffusing titanium into sapphire have been described. The diffusion is carried out between a thin film of Ti(O), evaporated from a Ti_2O_3 powder in a partial oxygen pressure, and a cleaned sapphire substrate. The furnace used for the diffusion is a carbon resistance furnace that is operable between 1400°C and 2000°C, and is restricted to an inert argon atmosphere. The diffusion time is defined as the dwell time at the diffusion temperature and the substrate heating and cooling rates may be controlled. The fabrication conditions used for each sample are summarised in the text and repeated in shorthand as a footnote.

4.3 Experimental techniques for characterising diffused Ti.

The experimental techniques used to investigate the characteristics of the Ti-diffused region were developed to address two primary concerns. The first is whether the titanium has diffused into the sapphire as the Ti^{3+} ion, substitutionally incorporated on an Al^{3+} lattice site. This is necessary for the diffused region to have spectroscopic properties comparable to those of the bulk doped Ti:sapphire laser crystal. The second concern is whether the concentration, depth and spatial distribution of the Ti may be controlled by varying the fabrication conditions.

The experimental technique used to investigate the spectroscopic properties of the diffused region are considered first in §4.3.1, addressing the issue of titanium valency and lattice site. The basis for the experimental techniques implemented are well known and the equipment generally readily available. The experimental procedure is outlined briefly, with emphasis on issues specific to the analysis of the localised diffused region.

Effort to identify the depth, concentration and spatial distribution of the diffused titanium was concentrated around two experimental techniques. The first is an all-optical imaging

technique, developed during the course of this work and is referred to as 'fluorescence imaging'. This is based on resolving the spatial distribution of fluorescent Ti^{3+} ions through a cross section of the diffused sample. The second technique is an established surface analysis and depth profiling technique, Secondary Ion Mass Spectrometry (SIMS). SIMS involves the sputtering of material from the surface layer and subsequent identification by mass spectrometry. The fluorescence imaging technique and the application of SIMS to the analysis of titanium diffused sapphire, are discussed in §4.3.2 and §4.3.3.

4.3.1 Spectroscopic characterisation of fluorescence in the near infra-red

The spectroscopy of the laser-active Ti^{3+} ion incorporated substitutionally on the Al^{3+} lattice in sapphire is well known[4,5]. The degenerate electron energy levels of the one Ti^{3+} d-shell electron are split under the influence of the local crystal field, giving rise to an absorption in the blue-green and an emission in the near infra-red. The transition is broadened by strong electron-phonon coupling to yield the characteristic broad fluorescence spectrum that is responsible for one of the largest tuning ranges of solid state lasers.

The experimental configuration used to identify the presence, and investigate the spectral characteristics, of fluorescent Ti^{3+} ions in sapphire is shown in Figure 4.4. A portable air-cooled argon-ion laser was used as a radiation source, operating at a wavelength of 488nm with a maximum output of 20mW. For this radiation source, it is necessary to use a short

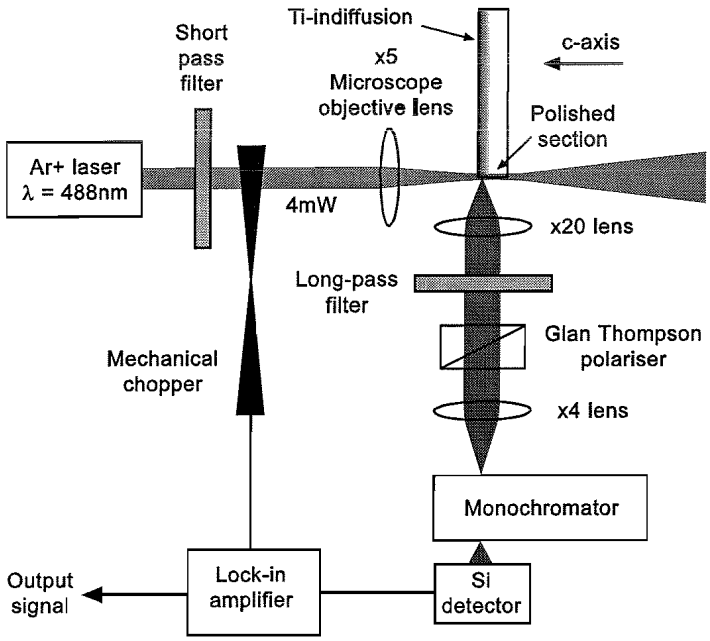

Figure 4.4:- Experimental configuration used to identify the presence of and investigate the spectral characteristics of fluorescent Ti^{3+}.

wave pass filter to remove a series of characteristic fluorescent wavelengths in the red and near infra-red regimes. The filtered radiation was directed through a mechanical chopper operating between 250 and 350Hz and was focussed at a polished cross section through the sample under investigation using a x5 microscope objective.

Fluorescence originating from the excited region was collected with a x20 microscope objective, oriented along an optical axis perpendicular to that of the excitation optics. The collected fluorescence was imaged onto the entrance slit of a monochromator, having passed through a series of optical components to enable polarisation selection and to remove any scattered pump radiation. A small area ($<2mm^2$) silicon detector was positioned behind the monochromator exit slit to measure the transmitted power. A good signal to noise ratio was achieved by using lock-in amplification and an electronic integration time of 300ms or 1s. The monochromator grating movement and data collection were controlled remotely.

The monochromator resolution was typically 4nm, which was sufficient considering the breadth of the Ti^{3+} fluorescence band under investigation. The measured fluorescence spectra were corrected for the non-linear system response by comparison with that measured for a tungsten lamp of known spectral luminosity.

An example of the fluorescence spectra obtained in the π- and σ-polarisations for a high quality, bulk doped $Ti:Al_2O_3$ sample is shown in Figure 4.5. In the frequency domain, the spectra present close approximations to a Gaussian distribution, peaking at $395\pm3 \times 10^{12}$Hz

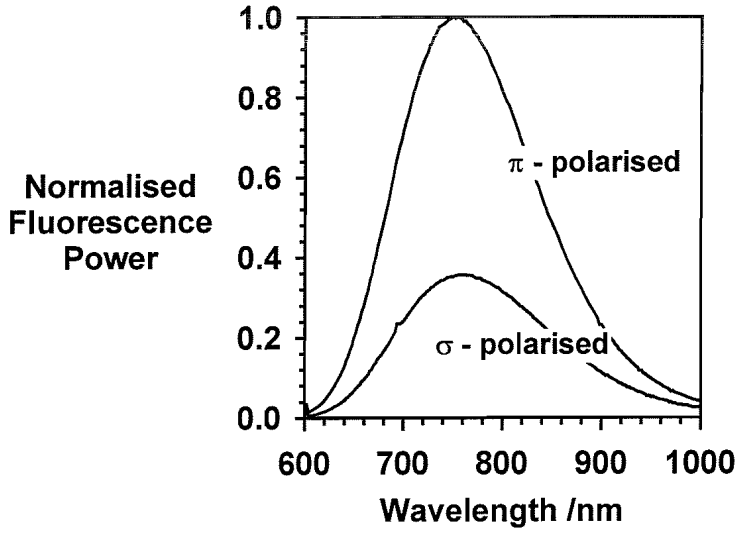

Figure 4.5:- Fluorescence spectra obtained for a high quality bulk doped $Ti:Al_2O_3$ crystal using the experimental conditions described.

(759±5 nm), with a full width 1/e intensity of 89±3 x10^{12} Hz (174±9 nm). The polarisation dependence is clear, with a ratio of peak fluorescence intensities of 0.37. These results are in close agreement with previously published spectra for high quality Ti:sapphire laser crystals[4].

For analysis of a diffused sample, the technique of imaging the polished cross section onto the monochromator ensures that the collected fluorescence arises from a diffused region rather than from background Ti^{3+} impurities.

4.3.2 Characterisation of diffused Ti^{3+} distribution by fluorescence imaging

During the spectral characterisation, the fluorescence originating from the excited region was focussed onto the monochromator entrance slit. Replacing the collection optics with an imaging system and a vidicon camera, the distribution of fluorescent Ti^{3+} ions may be resolved as a function of distance along a polished cross section through a sample.

A schematic of the experimental configuration is illustrated in Figure 4.6. The excitation optics and the sample orientation are similar to those in the spectroscopic characterisation. Fluorescence originating from the excited region was collected with a x20 microscope objective and imaged onto a silicon vidicon camera (Hamamatsu C1000-02). Either the whole image or a line profile through the image may be stored in a digital format, allowing

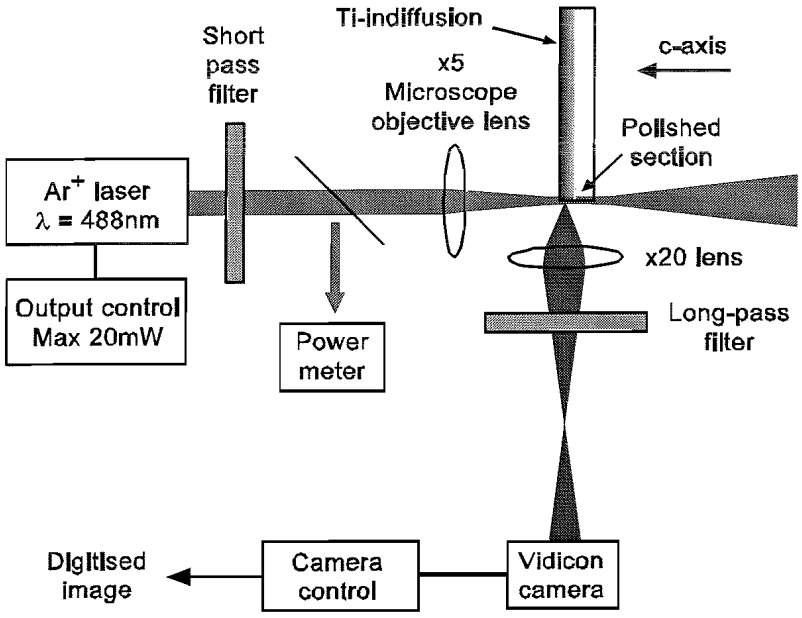

Figure 4.6:- Schematic illustrating the experimental configuration used to image the distribution of fluorescent Ti^{3+} ions after diffusion.

further analysis. A filter ensures that fluorescence wavelengths are detected rather than scattered radiation from the argon ion laser. Quantitative measurements are possible by monitoring the incident pump power and maintaining the optical alignment of the excitation and collection optics for each comparative measurement. Repeated measurements for a bulk doped Ti:Al_2O_3 sample provide a standard reference and indicate the accuracy of the quantitative analysis.

An example of a line profile taken along a central axis of the image obtained for a bulk doped Ti:Al_2O_3 sample, is shown in Figure 4.7. The location of the surface (defined at zero depth) is identified by prior illumination with a white light source and a series of repeated measurements indicate the surface may be identified to within ±2μm. Prior illumination with a white light source also enables accurate alignment of the image plane on the camera head. The depth scale is obtained by calibrating the magnification of the imaging system with commercial microscope graticule.

The titanium concentration in the bulk doped Ti:Al_2O_3 standard is known to be 0.11wt%. From a series of measurements, the fluorescence yield may be calibrated in terms of Ti concentration. The observed fluctuation reflects the accuracy with which each measurement is aligned, rather than the limitations of the equipment. The data illustrated in Figure 4.7 shows one of a series of measurements, for which the scatter in fluorescence yield corresponds to an error in the concentration scale of about 15%, shown by the error bar. This leads to an error of about 20% in the measurement of a diffused Ti^{3+} distribution.

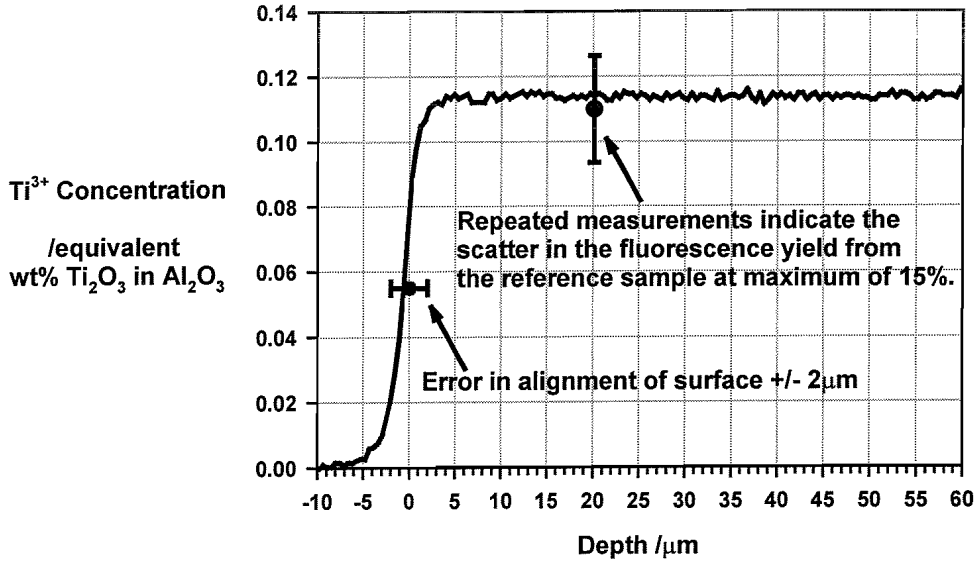

Figure 4.7:- Fluorescence image obtained for a bulk doped sample of Ti:Al_2O_3.

Whilst this error is not insignificant, the technique does allow a ready comparison between samples.

The form of the line profile shown in Figure 4.7 is close to the step function expected for a homogeneously doped Ti:Al_2O_3 crystal. Within ±5μm of the surface, the image is affected by the resolution of the optics. With further analysis, the system response could be filtered from the image, however the features characterised by this method are not, in general, limited by the resolution. For depths between 5 and 60μm, the fluorescence levels are approximately constant, indicating that absorption of the pump radiation and diffraction of the beam are not significant over this depth. If absorption or diffraction were significant, the fluorescence level would decrease with depth.

In summary, the fluorescence imaging technique provides a powerful method for evaluating the distribution of fluorescent Ti^{3+} ions along a polished cross section of a sample. Features greater than 5μm may be resolved and located to within ±2μm. Quantitative comparisons of fluorescent Ti^{3+} concentration made between samples within an error of about 20%. The technique uses readily available equipment in an optical research laboratory and is non-destructive.

4.3.3 Depth profiling by Secondary Ion Mass Spectrometry

Secondary Ion Mass Spectrometry (SIMS) is an established high resolution, destructive technique for analysing the composition of a surface. Under high vacuum conditions, a stream of high-energy ions, such as O_2^+, Ga^+ or Cs^+ is focussed at an oblique angle onto the surface under investigation. The incident ions become embedded in the lattice, transferring their kinetic energy as they come to rest. Material from the surface monolayer may be sputtered from the lattice as clusters or single species that may be either electrically neutral or charged. The positively charged ions can be selected by accelerating them towards an aperture held at a negative potential and identified by mass spectrometry. Depth profiling is possible by repeated rastering of the incident ion beam over an area to form a crater whilst measuring the mass spectrum of the sputtered positive ions. The sputtering rate is established by measuring the crater depth using a surface profilometer such as a Tencor alpha-step. Quantitative measurements are possible by comparing the yield to that of a standard of the same matrix.

The application of SIMS to depth profiling of sapphire is complicated by problems of sample charging and a low sputter rate. Sapphire, compared to other commonly analysed materials, such as silicon, is subject to charging due to its high electrical resistivity. For insulating samples, the charging may be controlled by depositing a thin layer of gold on the surface and flooding the surface with electrons. Over long periods (>1 hour) of analysis, the efficiency of the charge compensation may drift and lead to instabilities in the collection of the sputtered ions. The tendency for the sample to charge also limits the incident ion current, limiting the sputtering rate to between 1 and 2μm per hour. Despite these complications, SIMS has been previously used to analyse diffused or implanted impurities in sapphire[6,7].

An example of the data obtained for a 0.11wt% bulk doped Ti:sapphire crystal is shown in Figure 4.8. The yield of the ions $^{54}Al_2^+$, $^{50}Ti^+$, $^{48}Ti^+$, $^{46}Ti^+$ is measured as a function of time, for a central region of the etched crater. The isotopes $^{49}Ti^+$ and $^{47}Ti^+$ are also collected but are not shown in Figure 4.8 to preserve clarity. The depth scale is established later by measuring the depth of the crater. The initial section of the trace corresponds to etching though the gold film on the surface. The system will also require a finite depth to establish equilibrium energy transfer between the incident ions and the sputtered ions. For the data in Figure 4.8, the ion yield becomes quite stable after about 200s sputtering time. The measured ratio of the titanium isotopes can be compared to the natural isotope abundance to confirm the identity of the collected species. The $^{54}Al_2^+$ ion is monitored in preference to the $^{27}Al^+$ ion since the yield is lower and the detector is not saturated. In the analysis of

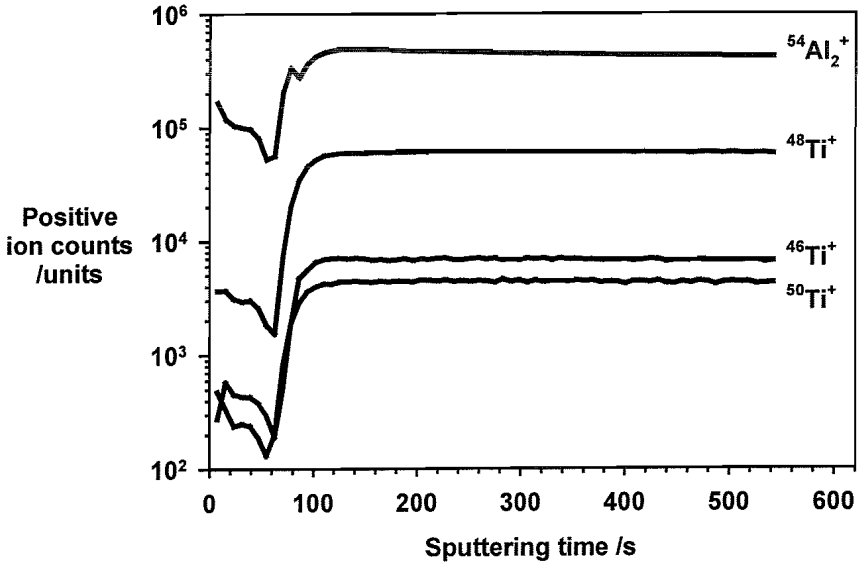

Figure 4.8:- Example of data obtained using SIMS to analyse the composition of a Ti:sapphire bulk doped sample.

sapphire, the yield of $^{54}Al_2^+$ should be constant; fluctuations or drifts in the signal give an indication of instabilities in the system, for example due to charging of the sample. For the bulk doped sample illustrated, the Ti concentration is known to be 0.11wt%, and so the ratio of $^{48}Ti/^{54}Al_2^+$ can be used to calibrate the Ti yield in terms of absolute concentration.

4.3.4 Summary of characterisation techniques

Methods for investigating the spectroscopic characteristics and the concentration profile of diffused Ti have been presented. The spectroscopic characterisation identifies the presence of Ti^{3+} in an Al^{3+} lattice site and has been demonstrated for a bulk doped Ti:sapphire crystal. The fluorescence imaging technique allows the distribution of fluorescent Ti^{3+} ions in an Al^{3+} lattice site to be identified along a polished section through a sample. This technique allows quantitative comparisons between samples, with an error of 20% and has been demonstrated for a bulk doped Ti:sapphire sample. Secondary Ion Mass Spectrometry (SIMS) provides an alternative route for measuring the total Ti concentration in sapphire. This technique is insensitive to the Ti valence state or lattice site, and so measures the total Ti concentration. The use of the fluorescence imaging technique and SIMS to analyse the Ti distribution in the same sample provide a detailed insight to the distribution of useful, fluorescent Ti^{3+} compared the total diffused Ti distribution.

4.4 Measured spectroscopic properties of Ti-diffused sapphire

The spectroscopic characteristics of the near surface region of a series of samples were investigated following diffusion at 1950°C, using the experimental technique described in §4.3.1. The aim of these investigations is to identify whether diffused Ti has been incorporated in a valence state and lattice site appropriate for use as a gain medium. If so, the spectroscopic properties of the diffused region will be similar to those measured for a bulk doped Ti:Al_2O_3 sample.

4.4.1 Fluorescence in the near infra-red

Figure 4.9 shows the fluorescence characteristics obtained for a Ti-diffused sample. In this case the sample, S131, was diffused from continuous thin film diffusion source 41±3nm thick at a temperature of 1950±30°C for eight hours. The fluorescence spectrum extends from 600nm over 400nm into the near infra-red and exhibits strong polarisation dependence. In the frequency domain, the spectra present good approximations to Gaussian distributions,

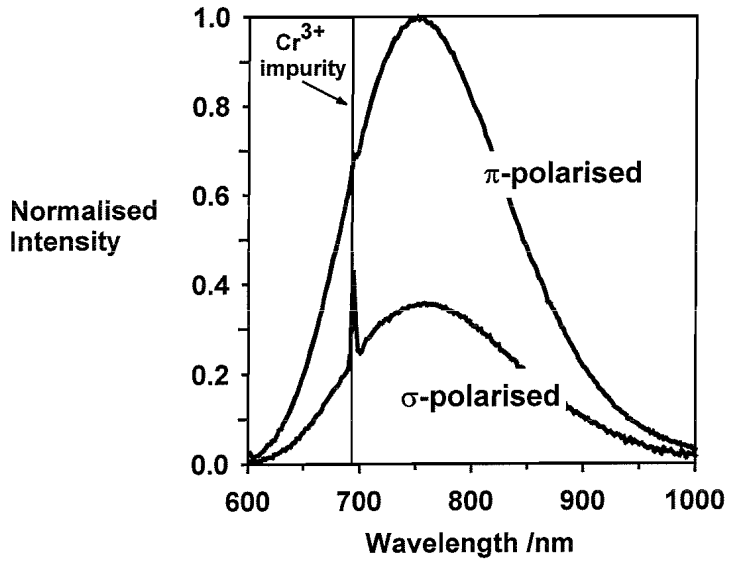

Figure 4.9:- Fluorescence spectra obtained for diffused Ti, excited with radiation at 488nm

peaking at $396x10^{12}$ Hz (758nm) with a full width at half maximum of $91x10^{12}$ Hz (175nm). The measured intensity ratio of peak π-polarised to σ-polarised radiation is 0.37. These results are typical of samples fabricated at a diffusion temperature of 1950°C over diffusion times of up to 8 hours from a continuous thin film source thickness up to 41nm thick and heated slowly to and from the diffusion temperature. The bandwidth, the peak wavelength, and the polarisation ratio are in excellent agreement with fluorescence characteristics measured for a high-quality 0.11wt% $Ti^{3+}:Al_2O_3$ bulk-doped crystal [see §4.3.1], and with published data[4] . The sharp peak in the region 692-695nm is attributed to the presence of trace amounts of Cr^{3+} impurity in the sapphire substrate.

The fluorescence lifetime was measured in a separate experiment by E Martins (ORC, Southampton) by rapidly switching the pump beam using an acousto-optic modulator and monitoring the fluorescence decay time. The fluorescence lifetime was measured to be 3.2±0.25μs at room temperature, which is in excellent agreement with previously published data for Ti^{3+} in sapphire at room temperature[4].

4.4.2 Summary of spectroscopic characteristics

In summary, the measured spectroscopic properties of the diffused region are in excellent agreement with those of a high quality bulk-doped $Ti^{3+}:Al_2O_3$ laser crystal. These results demonstrate that by thermal diffusion, Ti^{3+} has been incorporated in a lattice site and valence state appropriate for use as an optical gain medium.

4.5 Diffusion of Ti into sapphire at 1950°C and 1750°C from a continuous thin film source

Initial diffusion experiments were carried out at temperatures of 1950°C and 1750°C using a continuous thin film of Ti(O) as the diffusion source.

At 1950°C, trends in the diffused Ti^{3+} and total Ti distribution were investigated for increasing diffusion times for a 41nm thick diffusion source and slow cooling conditions. The experiment was repeated, with different samples and fast cooling conditions, so that the effect of the cooling rate on the diffused Ti^{3+} could be investigated. A further experiment at a temperature of 1950°C was carried out from a 27nm thick diffusion source, to consider the effect of reducing the source thickness on the diffused Ti^{3+} distribution.

At 1750°C, trends in the diffused Ti^{3+} distribution were investigated for diffusion from a 27nm thick diffusion source as a function of time. The results are compared to those obtained for similar conditions, except at the higher temperature of 1950°C.

These studies lead to greater understanding of the diffusion characteristics, and provide a basis for the investigation of diffusion from a patterned thin film source reported later in this chapter.

4.5.1 Diffusion at 1950°C from a 41nm source, with slow cooling

A series of Ti-diffused samples (S130, S131, S133, S134) were prepared with a 41nm thick diffusion source, evaporated from powdered Ti_2O_3, and diffused at a temperature of 1950°C for times between 1 and 8 hours. In each case the samples were heated to, and cooled from, the diffusion temperature over a period of 32 minutes, although the diffusion time was defined as dwell time at the diffusion temperature. Characteristics of the Ti^{3+} and the total Ti distribution were investigated quantitatively using the fluorescence imaging and SIMS techniques described in §4.3.

4.5.1.1 Diffused Ti^{3+} distribution

Figure 4.11 illustrates the Ti^{3+} distribution obtained for S130-134. For each sample, it is apparent that fluorescent Ti^{3+} ions have diffused to significant depths within the diffusion time. For example, after 8 hours at 1950°C, Ti^{3+} is present at depths greater than 50μm. In addition, the form of the Ti^{3+} profiles is not expected from standard diffusion theory, with the peak Ti^{3+} concentration located between 10μm and 20μm beneath the surface. This

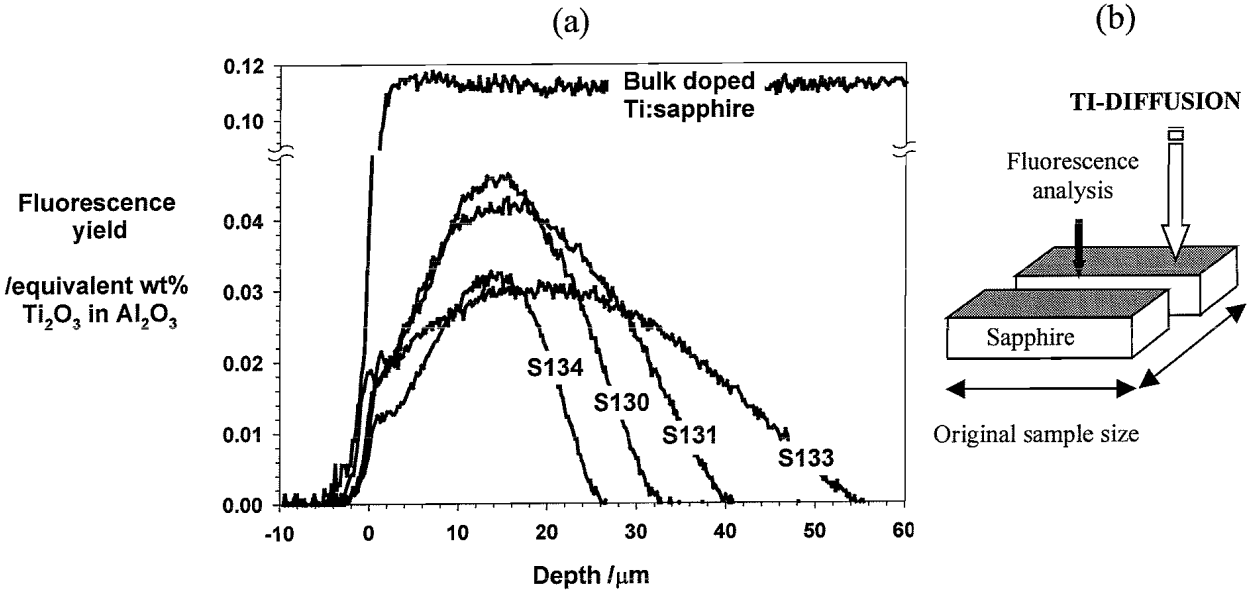

Figure 4.11:- (a) Distribution of fluorescent Ti^{3+} ions after diffusion at 1950°C or between 1 and 8 hours from a 41nm thick diffusion source and (b) illustration of the analysis orientation with respect to the initial sample configuration.

complicates the estimate of an overall diffusion rate, and may indicate that not all of the Ti is detected by this technique. The peak concentration of incorporated Ti^{3+} ranges between 0.03 and 0.05wt% and would be equivalent to that of a lightly doped Ti:Al_2O_3 laser crystal.

Integrating the area under the curves in Figure 4.11, the amount of detected Ti^{3+} can be compared to the amount supplied in the thin film diffusion source. This is shown in Figure 4.10. For each sample, the total Ti^{3+} detected is less than a third of that supplied for diffusion, with the fraction increasing with diffusion time.

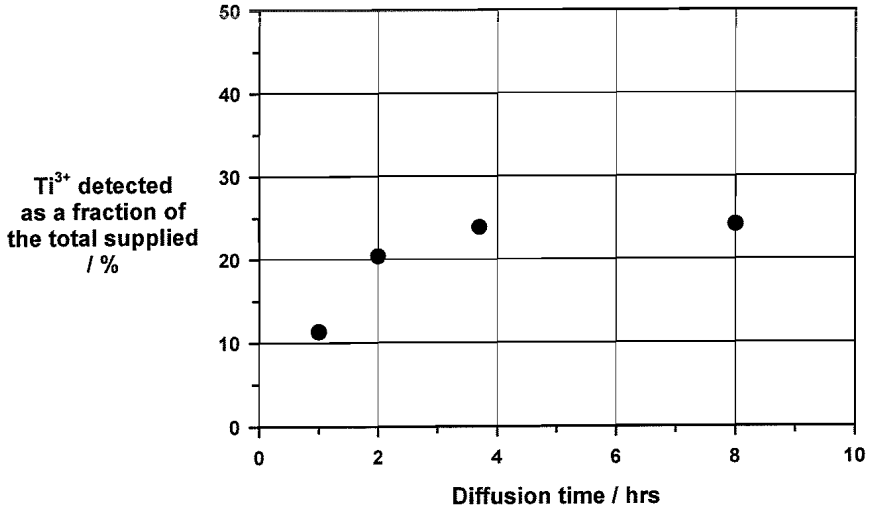

Figure 4.10:- Percentage of Ti detected by fluorescence imaging compared to the total amount of Ti supplied as the diffusion source

S134 {Slow heat, slow cool, 41nm, 1 hr, 1950°C} S130 {Slow heat, slow cool, 41nm, 2 hr, 1950°C}
S131 {Slow heat, slow cool, 41nm, 3.7hrs, 1950°C} S133 {Slow heat, slow cool, 41nm, 8 hrs, 1950°C}

The diffused Ti concentration was investigated further, using SIMS to analyse the surface concentration and the diffused total Ti distribution of S130.

4.5.1.2 Total Ti concentration distribution

For each of the samples S130-S134, SIMS was used to measure the Ti concentration, irrespective of spectroscopic properties (referred to as the 'total-Ti concentration'), at a shallow depth beneath the sapphire surface. The results are shown in Figure 4.12 and indicate that the total-Ti concentration at a depth of 70nm beneath the substrate surface decreases from about 0.08wt% to 0.01wt% as the diffusion time increases from 1 to 8 hours. For the shortest diffusion time, the measured total-Ti concentration is significantly greater than Ti^{3+} concentration measured by fluorescence imaging. This comparison gives the first indication that some non-fluorescent Ti may be present in the sapphire lattice after the shortest diffusion times.

The diffused total-Ti distribution of S130 was investigated further by carrying out a series of SIMS measurements at intervals along a 0.5° bevel polished through the diffused region. The bevel and series of analyses were necessary considering that the Ti^{3+} fluorescence has been recorded at depths up to 30μm, and the sputter rate of sapphire is less than 2μm per hour. The location of the analysis points beneath the original surface could be measured using a surface profilometer, to the accuracy indicated in Figure 4.13. The error in the concentration at each point is given by the yield of each titanium isotope in comparison with

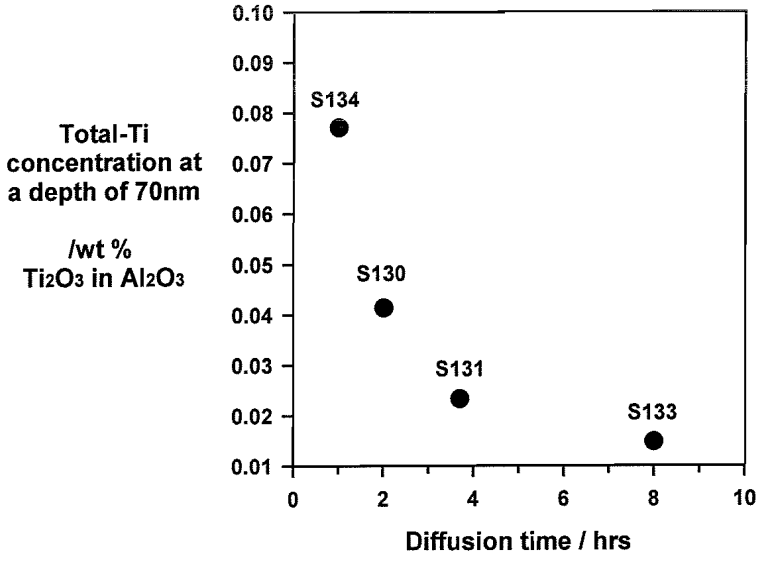

Figure 4.12:- Concentration of Ti present 70nm beneath the substrate surface after diffusion, measured by Secondary Ion Mass Spectrometry.

S134 {Slow heat, slow cool, 41nm, 1 hr, 1950°C} S130 {Slow heat, slow cool, 41nm, 2 hr, 1950°C}
S131 {Slow heat, slow cool, 41nm, 3.7hrs, 1950°C} S133 {Slow heat, slow cool, 41nm, 8 hrs, 1950°C}

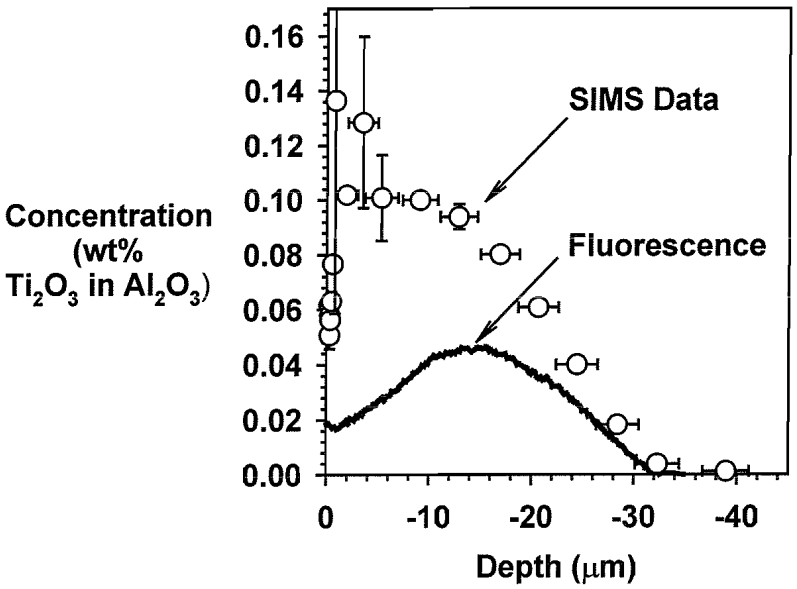

Figure 4.13:- Comparison of the titanium distribution measured by fluorescence imaging and SIMS, following a 2 hour anneal at 1950°C with a 41nm diffusion source.

that of a standard Ti:sapphire matrix. The results are shown in Figure 4.13 in comparison to the Ti^{3+} concentration profile measured by fluorescence imaging.

The SIMS measurements confirm the diffusion of the Ti into sapphire to depths of tens of microns within the time scale of 2 hours, but also reveal a significant difference between the total-Ti distribution and the Ti^{3+} distribution. The presence of non-fluorescent Ti may be related to the composition of a reaction product between the diffusion source and sapphire. In addition, considering the samples have been cooled slowly from the diffusion temperature, the non-fluorescent phase may form during the cooling process[10]. Although little information is available for the Ti^{3+} ion in sapphire, different phases of TiO_2 in Al_2O_3 are known to exist at different temperatures[8].

Integrating the area under each of the profiles, it seems that about half of the supplied Ti has been incorporated in the sapphire, and of that only a quarter is present as fluorescent Ti^{3+}. This indicates that a significant loss of the source has occurred during the 2 hour diffusion anneal.

Considering the SIMS data for depths greater than 2μm, the total-Ti concentration decreases with depth into the substrate as expected for a diffusion process. The form of the

concentration-depth profile is best described by a logistic function, given by *Eqn. 4-1*, with asymptotes at 0.1wt% and zero and a point of inflection at 22μm depth.

$$C(x) = \frac{0.1}{1 + e^{-26 \cdot 10^4 (22 \cdot 10^{-6} - x)}} \qquad \textit{Eqn. 4-1}$$

The function described by *Eqn. 4-1* is not a solution to the standard diffusion equation given in *Eqn. 3-3*. If the 1/e depth of the peak concentration is taken to be the effective diffusion depth (defined as $2\sqrt{Dt}$), an estimate of the overall transport rate would be $10^{-14}m^2s^{-1}$. Referring to chapter 3, this rate is several orders of magnitude greater than may be expected for the lattice diffusion of Ti in sapphire if it follows similar kinetics to Cr^{3+} (D_l at 1950°C for Cr^{3+} would be $4.10^{-17}m^2s^{-1}$, according to Moya[9]). This discrepancy indicates that either an alternative diffusion mechanism exists for Ti in sapphire, and/or that diffusion along extended defects contributes significantly to the transport process under the conditions used, or that $2\sqrt{Dt}$ is not an appropriate measure of the effective diffusion depth for this profile.

Immediately beneath the surface, the total-Ti concentration rises sharply from 0.05wt% to 0.1wt%, with this confirmed by a series of measurements at depths between 40nm and 2μm. In addition, the near surface measurement of 0.05wt% is in agreement with the total-Ti concentration measured at a depth of 70nm beneath the surface in the independent series of measurements presented in Figure 4.12. An explanation offered[10] is that the Ti diffuses rapidly to the surface during cooling to form a monolayer of titanium. The presence of a monolayer of Ti on the surface would be complicated to detect by SIMS, although other surface analysis techniques may be available. This has not been investigated further.

In summary, the diffusion of Ti into sapphire has been demonstrated for the first time, at a temperature of 1950°C. The observed profiles are not easily explained by standard diffusion theory and it seems that not all the Ti is incorporated as the fluorescent Ti^{3+} ion. It has been suggested that the incorporation of non-fluorescent Ti may be related to the changes that occur during the cooling period[10]. To investigate this further, a similar series of samples were fabricated, except that they were cooled rapidly following the diffusion anneal. These results are presented in the next section.

4.5.2 Diffusion at 1950°C from a 41nm source, with rapid cooling

Four samples, S135, S137, S138 and S139 were prepared to investigate the effect of the cooling rate on the diffused distribution of total-Ti and Ti^{3+}. The fabrication conditions were similar to those used for S130-S134, discussed in the previous section, except that rapid cooling conditions were invoked by switching power to the furnace off immediately after the diffusion (see §4.2.4 for further details). Following diffusion, the Ti^{3+} distribution was investigated for each sample using the fluorescence imaging technique. For S137, a 0.5° bevel was polished through the diffused region so that a series of SIMS measurements could be carried out at depths up to 30μm beneath the original surface.

4.5.2.1 Diffused Ti^{3+} distribution

Figure 4.14 shows the Ti^{3+} distribution for the rapidly cooled samples. With increasing diffusion time, the depth of Ti^{3+} increases as expected for a diffusion process. However, deviations from simple diffusion kinetics are apparent. For example, the peak Ti^{3+} concentration is located beneath the surface at depths increasing from about 5μm to 20μm. In addition the relation between the diffused forms of S135, S137 and S138 does not indicate a simple relationship with diffusion time. The form of the profiles for the shorter diffusion times differ significantly from those shown in Figure 4.11 for samples diffused under similar conditions, except for the slow cooling rate.

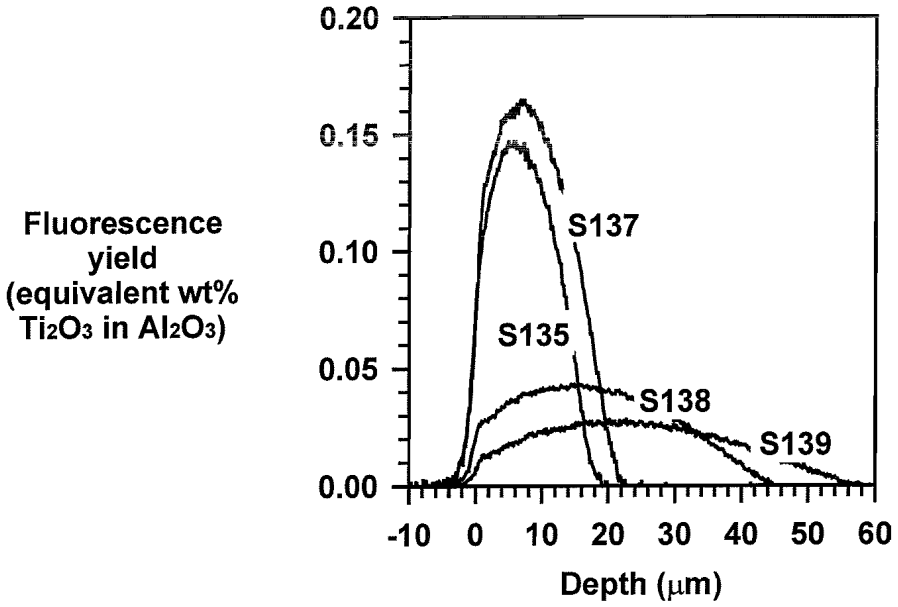

Figure 4.14:- Ti^{3+} distribution following diffusion from a 41nm continuous thin film source at a temperature of 1950°C for times between 1 and 8 hours and cooled rapidly following the diffusion anneal.

S135 {Slow heat, rapid cool, 41nm, 1 hr, 1950°C} S137 {Slow heat, rapid cool, 41nm, 2 hr, 1950°C} S138 {Slow heat, rapid cool, 41nm, 3.7hrs, 1950°C} S139 {Slow heat, rapid cool, 41nm, 8 hrs, 1950°C}

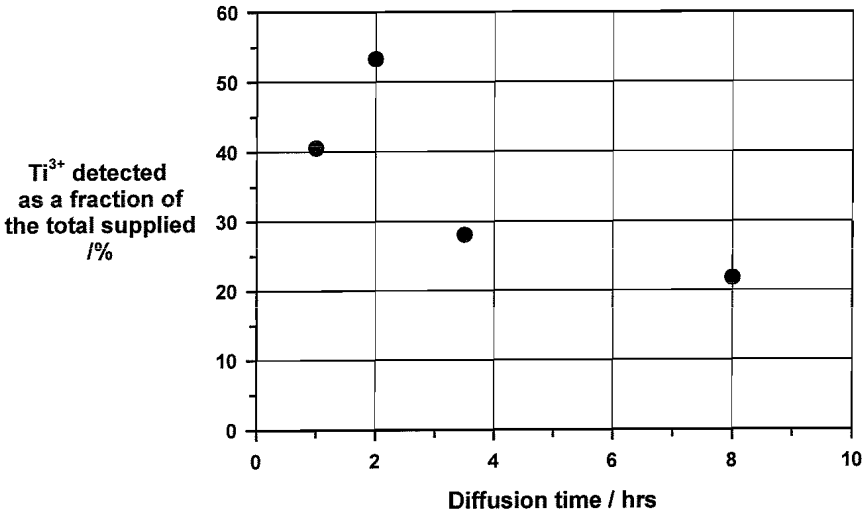

Figure 4.15:- The percentage of Ti^{3+} detected by fluorescence imaging compared to the total amount of Ti supplied in the diffusion source.

The total Ti^{3+} detected by the fluorescence imaging technique for each of the sample, calculated by integrating the area under the curves shown in Figure 4.14, is given in Figure 4.15. In each case, the Ti^{3+} detected is significantly less than that supplied by the diffusion source. These results support the observation that the change in Ti^{3+} distribution with diffusion time does not follow a simple relationship and also indicate that an optimum diffusion time of 2 hours exists for incorporating fluorescent Ti^{3+} ions.

S137 was selected for further analysis of the total-Ti concentration using SIMS. The depth profile was obtained by carrying out a series of SIMS measurements on a section beveled at approximately 0.5° through the diffused region. The results are shown in Figure 4.16, in comparison to the measured Ti^{3+} distribution.

In contrast to the earlier results for the slow cooled sample, Figure 4.16 shows a good correlation between the total-Ti and Ti^{3+} distributions for similar conditions, except for a rapid cool from the diffusion temperature. Unfortunately, modeling the exact form of the total-Ti concentration profile, particularly within the first 10μm of the surface, is complicated by the size of the error bars and the scarcity of analysis points. However, it is clear that the near surface region (<2μm) is depleted in Ti compared to depths of 4-10μm. The location of the peak concentration cannot be conclusively identified from this data.

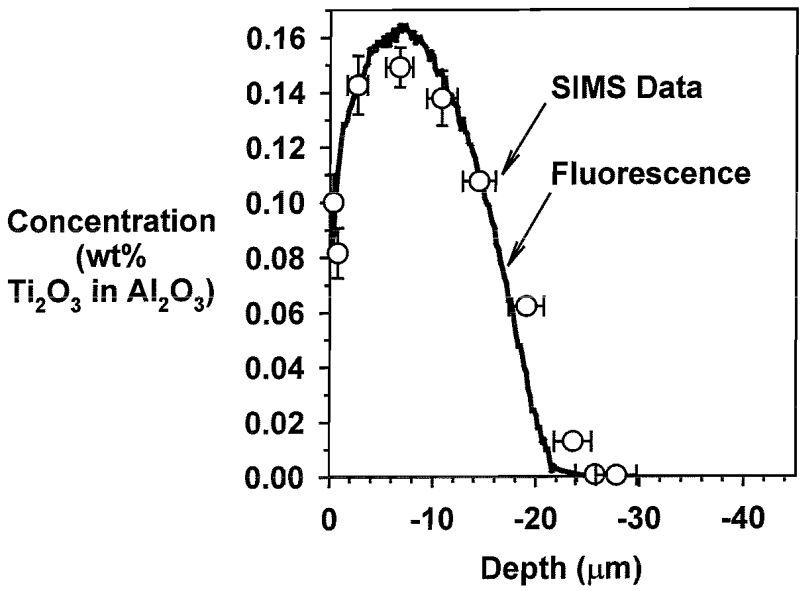

Figure 4.16:- Total titanium concentration illustrated in comparison to the Ti^{3+} distribution obtained following a 2 hour diffusion from a 41nm thick diffusion source at 1950 ℃ and rapidly cooled.

The total-Ti distribution shows a close comparison to the Ti^{3+} distribution obtained for the same sample, which is also illustrated in Figure 4.16. Both the peak concentrations and diffusion depths for the total-Ti and Ti^{3+} distributions are comparable within the error of each measurement technique. In the near surface region, the depletion of Ti observed within 2μm of the surface cannot be compared to the rising Ti^{3+} distribution, without correcting for the resolution of the imaging system.

4.5.3 Discussion of the effect of the cooling rate on diffusion characteristics

The effect of the cooling rate on the diffused Ti^{3+} distribution is shown in Figure 4.17, in which the Ti^{3+} distributions for S130 and S133 are compared with those obtained for S133 and S139.

For the 2 hour diffusion, the Ti^{3+} distributions are distinctly different. For S130 it is known that only half of the diffused Ti is present as the fluorescent Ti^{3+} ion. By cooling rapidly, the concentration of fluorescent Ti^{3+} increases and is in good agreement with the total-Ti distribution. Therefore, it seems that by cooling rapidly, the proportion of Ti included as the fluorescent Ti^{3+} ion is significantly increased.

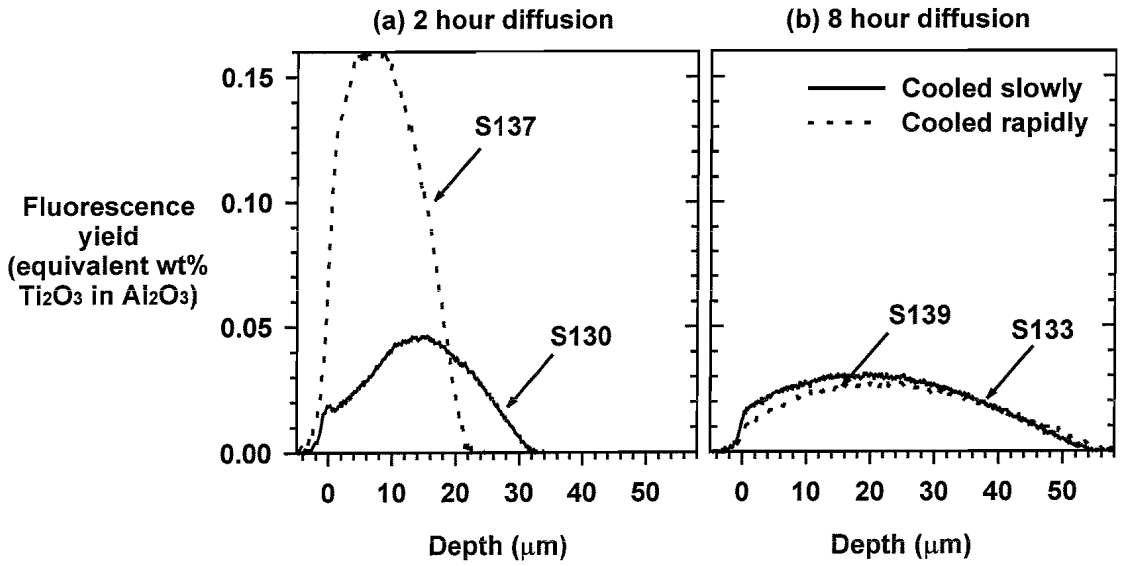

Figure 4.17:- Comparison of Ti^{3+} distribution for rapidly cooled samples and slowly cooled samples, (a) diffused for 2 hours at 1950°C and (b) diffused for 8 hours at 1950°C with a 41nm thick diffuison source.

In contrast, for a longer diffusion time of 8 hours, distinct similarities are observed in the Ti^{3+} distribution for the slowly cooled and rapidly cooled conditions. For example, Figure 4.17 shows that for an 8-hour diffusion time, the peak Ti^{3+} concentrations are both about 0.03wt%, located about 20μm beneath the surface. The diffusion depths, defined as 1/e of the peak Ti^{3+} concentration are again similar, at about 47μm. These similarities are seen in the calculation of total amount of Ti^{3+} detected by the fluorescence analysis technique, at 22% and 24% for the slow and fast cooling regimes respectively. Therefore, for the longer diffusion times at 1950°C, it seems that the amount of Ti^{3+} incorporated is insensitive to the cooling rate. Further SIMS analysis of the total-Ti distribution in samples S139 and S133 could be carried out to confirm this observation.

The mechanism responsible for the change in Ti fluorescence with cooling rate cannot be clearly identified from these results. Considering that the effect appears most pronounced for the shortest diffusion times, it may be related to either the presence of a reaction product between the diffusion source and substrate, or high concentrations of titanium in the near surface region. The change in spectroscopy during cooling may be due to the movement of defects in the lattice, perhaps allowing changes in the Ti valence state and/or the formation of clusters, precipitates or other phases of Ti-doped Al_2O_3.

In summary, for diffusion times of 1 and 2 hours, a rapid cool has significantly increased the concentration of Ti^{3+} incorporated in the sapphire. In the case of the 2-hour diffusion, the Ti^{3+} distribution is in close agreement with the total-Ti distribution. For diffusions over times of 3.7 and 8 hours the cooling conditions appear to have little affect on the diffused Ti^{3+} distribution.

4.5.4 Diffusion at 1950°C with a decreased source thickness

To investigate the effect of reducing the source thickness on the Ti distribution following diffusion at 1950°C, a series of samples S124, S125, S128 and S53 were prepared. The fabrication conditions were similar to those used for series S130-S134, except that the thickness of the diffusion source thickness was reduced to 27nm for S124, S125 and S128, and 25nm for S53. The diffusions were carried out at 1950°C for times between 0.2 and 8 hours. Heating to, and cooling from the diffusion temperature followed the slow regime, controlled over a 32-minute period. For S53, the thin film diffusion source was patterned such that only half of the surface was covered. The Ti^{3+} distribution following diffusion was investigated by fluorescence imaging and the total-Ti concentration in the near surface region (d<2μm) was characterised using SIMS.

4.5.4.1 Diffused Ti^{3+} distribution

Figure 4.18 illustrates the fluorescent Ti^{3+} distribution observed following diffusion at 1950°C for times up to 8 hours from a 25-27nm thick diffusion source. With increasing

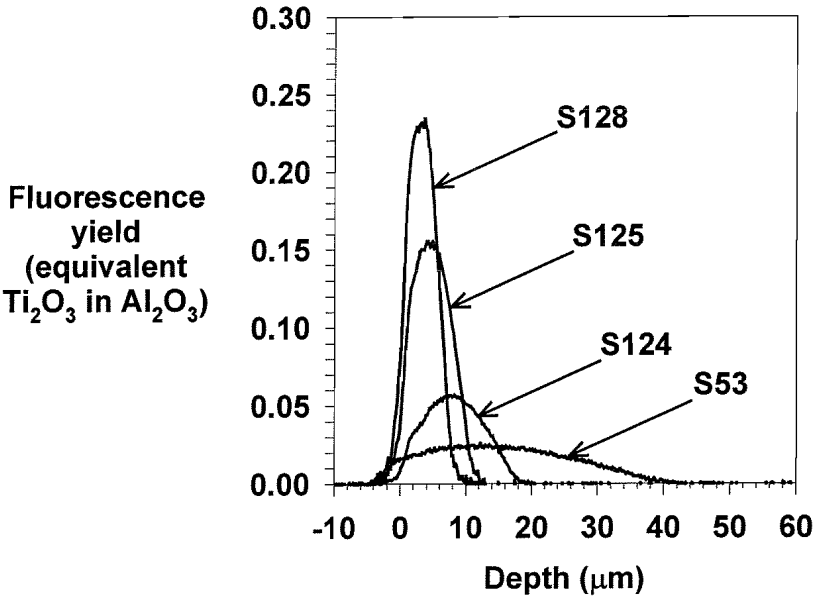

Figure 4.18:- Ti^{3+} distributions following diffusion at 1950°C for times between 0.2 and 8 hours from a 25-27nm diffusion source.

S128 {Slow heat, slow cool, 27nm, 0.2 hr, 1950°C} S125 {Slow heat, slow cool, 27nm, 1 hr, 1950°C} S124 {Slow heat, slow cool, 27nm, 3.7hrs, 1950°C} S53 {Slow heat, slow cool, 25nm, 8 hrs, 1950°C}

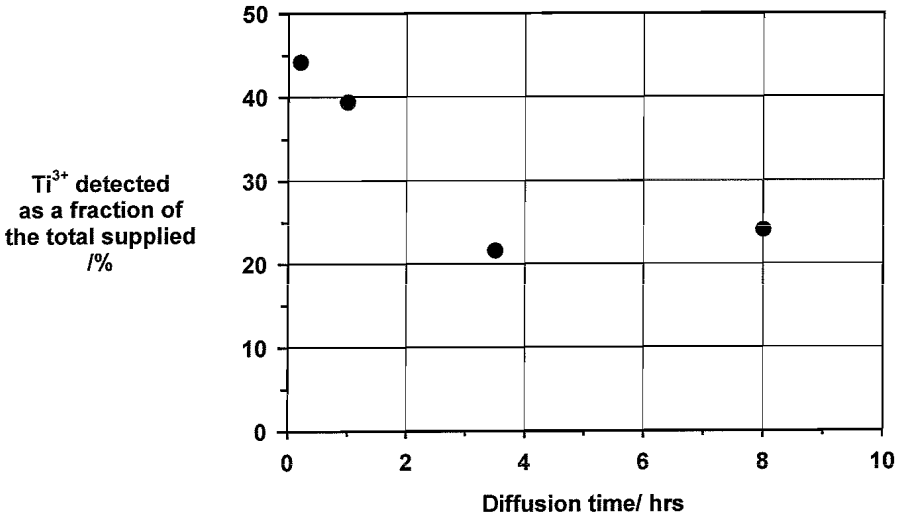

Figure 4.19:- Percentage Ti^{3+} detected by fluorescence imaging compared to total Ti supplied.

diffusion time, the Ti^{3+} peak concentration decreases and the depth of Ti^{3+} inclusion increases. The peak concentration of Ti^{3+} is located at increasing depths beneath the surface with increasing diffusion time, although for the shortest diffusion time, the observation of a peak beneath the surface is inconclusive as the profile is limited by the resolution of the imaging system. Since these samples are cooled slowly from the diffusion temperature, some non-fluorescent Ti may also be present, in varying proportions as a function of diffusion time. This complicates the quantitative interpretation of the trends in the diffusion profile with time.

The total Ti^{3+} detected as a fraction of the Ti supplied is shown in Figure 4.19, calculated by integrating the area under the curves shown in Figure 4.18. It seems that the total Ti^{3+} content is decreasing with diffusion time and that in each case, the amount of Ti^{3+} detected is less than half of the total supplied. It is interesting to see that the Ti^{3+} content tends towards about 25% after an 8 hour diffusion, similar to the observations discussed in the previous section.

4.5.4.2 Total Ti concentration

The total-Ti concentration included in the near surface region of samples S128, S125 and S53 has been measured by SIMS. The data was taken using SIMS in a continuous depth profiling mode, etching a single deep crater in the surface. The total-Ti concentration measured as a function of depth is shown in Figure 4.20.

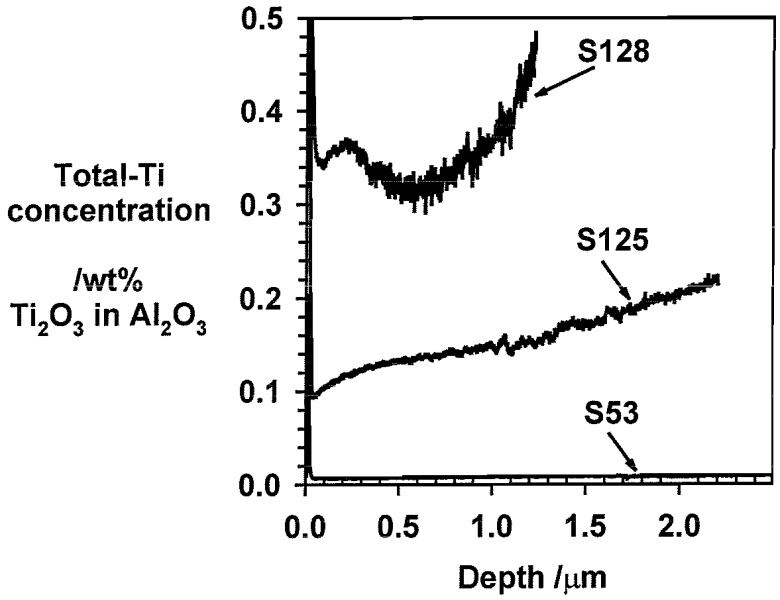

Figure 4.20:- Total-Ti distribution measured by SIMS following diffusion from a 25-27nm continuous thin film source for times up of 0.2, 1 and 8 hours at 1950°C.

In each case the SIMS depth profile shown in Figure 4.20 shows the total-Ti concentration increasing for depths up to 2μm beneath the surface. Whilst not typical of a diffusion process, this trend is a consistent feature of the diffused total-Ti concentration profiles measured by SIMS.

4.5.5 Discussion of the effect of reducing the source thickness

Some comments on the effect of reducing the diffusion source thickness may be made by considering the Ti^{3+} distributions for S134, S131 and S133 in comparison with those obtained for S125, S124 and S53 respectively. The former series were fabricated with a diffusion source of thickness 41nm and the latter a source thickness of 25-27nm, for diffusion times of 1, 3.5-3.7 and 8 hours under otherwise similar conditions. All the samples were cooled slowly, which complicates comparison of fluorescence imaging data since differing amounts of non-fluorescent Ti may be present.

For ease of comparison, Figure 4.21 (a), (b) and (c) replicate the Ti^{3+} distributions obtained for the samples under discussion, grouped for the 1, 3.5-3.7 and 8 hour diffusions respectively.

Following the one-hour diffusion, the peak concentration of included Ti^{3+} is significantly enhanced for the lesser source thickness. The discrepancy is reduced for the 3.5-3.7 hour

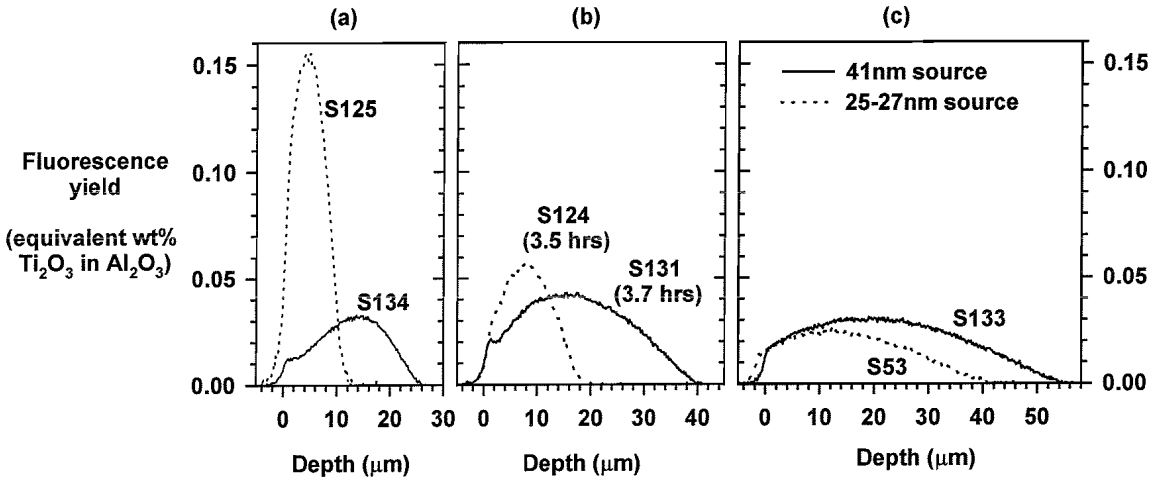

Figure 4.21:- Comparison of Ti^{3+} distributions obtained following diffusion from a 41nm and 25-27nm thin film diffusion source for (a) 1 hour diffusion, (b) 3.5-3.7 hour diffusion and (c) 8 hour diffusion.

diffusions and then reversed for the 8 hour diffusion, although such small differences are subject to limitations in the relative error of the measurements. In each case, the penetration of Ti into the lattice is less for the lesser source thickness. These results indicate that the concentration of Ti^{3+} included as a function of depth is dependent on the amount of source supplied, as well as the diffusion time and cooling conditions.

The observation that the inclusion depth depends on the amount of source, is consistent with a rapid reaction between the Ti(O) diffusion source and sapphire substrate in addition to diffusion into the lattice. The reaction will continue as long as the supply of reactants continues, so that the thickness of the reaction layer will depend on the amount of source supplied. The system of a reaction and diffusion has yet to be modeled for the inclusion of Ti in sapphire. Alternatively, the dependence of diffusion depth on source thickness may be explained by a concentration dependent diffusion rate. Further investigation is required to identify the processes contributing to the transport of Ti into sapphire at 1950°C.

4.5.6 Titanium diffusion at a lower temperature of 1750°C

A series of samples were fabricated to investigate the Ti diffusion characteristics at a lower temperature of 1750°C. Samples S153, S154, S155 and S156 were prepared with a 27nm diffusion source, deposited by evaporation from a powdered Ti_2O_3 source and diffused for times of 1, 2, 3.5 and 8 hours respectively at a temperature of 1750°C. The heating and cooling cycles were controlled over a period of 26 minutes, following the regime reported in

S134 {Slow heat, slow cool, 41nm, 1 hr, 1950°C} *S125 {Slow heat, slow cool, 27nm, 1 hr, 1950°C}*
S131 {Slow heat, slow cool, 41nm, 3.7hrs, 1950°C} *S124 {Slow heat, slow cool, 27nm, 3.5 hrs, 1950°C}*
S133 {slow heat, slow cool, 41nm, 8 hrs, 1950°C} *S53 {Slow heat, slow cool, 25nm, 8 hrs, 1950°C}*

§4.2.4. Following diffusion, the Ti^{3+} distributions were characterised by fluorescence imaging.

4.5.6.1 Diffused Ti^{3+} distribution

Figure 4.22 presents the Ti^{3+} distribution obtained for samples S153–S156 using fluorescence imaging.

In each case Ti^{3+} is observed to have diffused into the sapphire substrate, attaining depths in excess of 40μm after an eight-hour diffusion. The peak concentration of Ti^{3+} incorporated shows a large range, from 0.4wt% for the shortest diffusion time (1 hour), decreasing to 0.02wt% following a 2 hour diffusion. For samples S154-S156, the peak Ti^{3+} concentration is located approximately 15μm beneath the sapphire surface, whilst the resolution of the location of the peak Ti^{3+} concentration for S153 is limited by the system response of the measurement technique.

The changes in the Ti^{3+} distribution with time do not follow the trend expected by standard diffusion theory. The rapid change in diffused Ti^{3+} profile between S153, S154 and S155 is unexpected and may be related to a characteristic change in the transport process. For example, the factor of 10 decrease in the peak Ti^{3+} concentration between S153 and S154 may be related to the end point of a reaction between source and substrate.

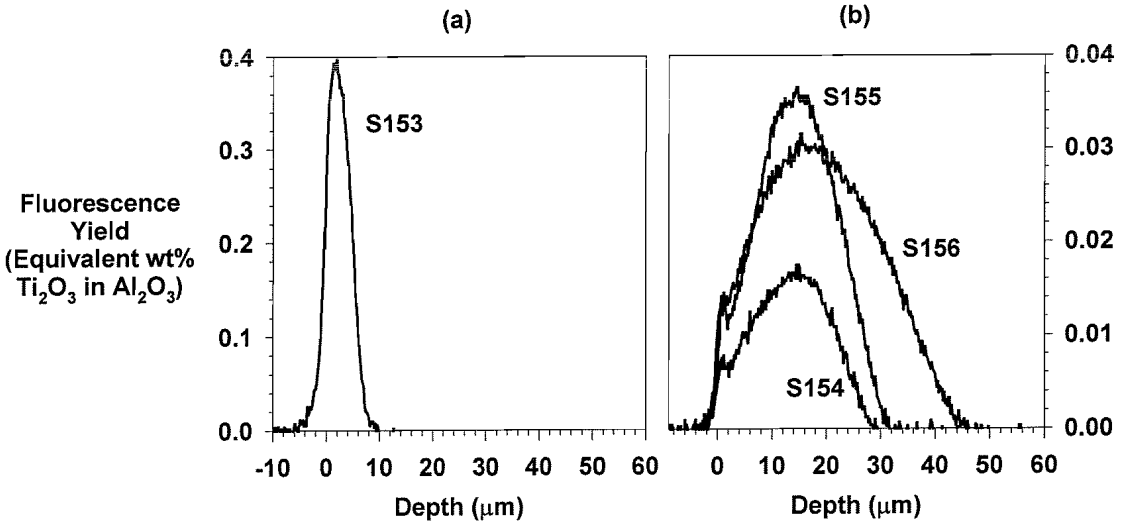

Figure 4.22:- Fluorescence distribution after diffusion from a 27nm continuous thin film source at a temperature of 1750 °C. (a) for a diffusion time of 1 hour and (b) for diffusion times of 2, 3.5 and 8 hours.

S153 {Slow heat, slow cool, 27nm, 1 hr, 1750 °C} S154 {Slow heat, slow cool, 27nm, 2 hr, 1750 °C}
S155 {Slow heat, slow cool, 27nm, 3.5hrs, 1750 °C} S156 {Slow heat, slow cool, 27nm, 8 hrs, 1750 °C}

Further complicating the interpretation of these trends is the expectation that some non-fluorescent Ti may be present, since these samples were cooled slowly from the diffusion temperature.

4.5.7 Discussion of the effect of reducing the temperature

Comparing the Ti^{3+} distribution measured for S125, S124 and S53 with S153, S155 and S156, some comment may be made on the effect of lowering the diffusion temperature from 1950°C to 1750°C. Figure 4.23 compares the Ti^{3+} distribution for these samples.

The reduction in temperature does not show a simple trend in Ti^{3+} distribution for increasing diffusion times between 1 and 8 hours. Following the ideal diffusion theory discussed in chapter 3, a reduction in temperature should lead to a lower diffusion rate and a decrease in the maximum concentration at the surface. These trends are not observed in Figure 4.23, although interpretation of the diffusion profiles is complicated by the unknown proportion of non-fluorescent Ti for each sample, considering all were cooled slowly from the diffusion temperature.

In conclusion, a reduction in the diffusion temperature does not lead to a trivial change in the diffused Ti^{3+} distribution. These results however, do demonstrate that it is possible to incorporate Ti^{3+} to depths of tens of microns, within a time scale of hours, at a temperature of 1750°C.

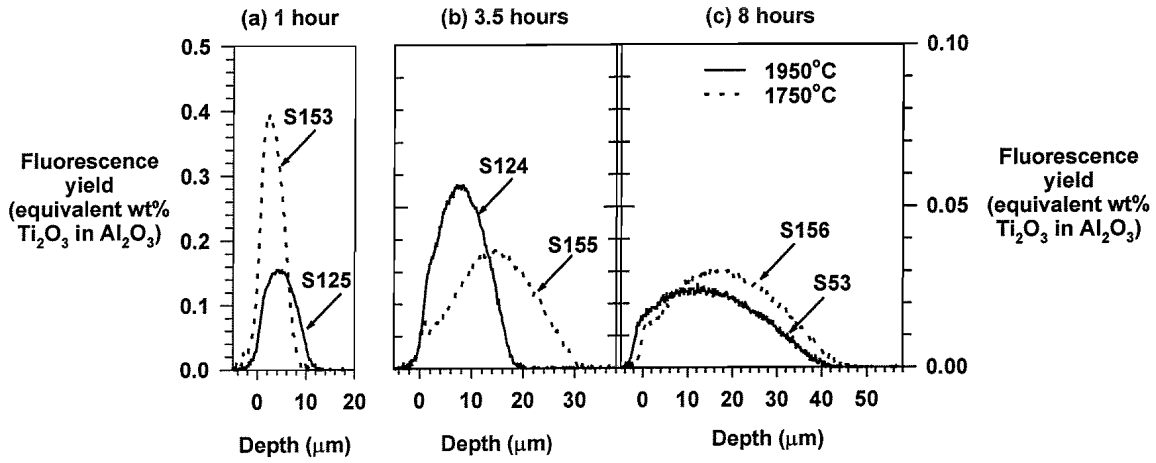

Figure 4.23:- Comparison of Ti^{3+} distribution observed for diffusion at 1950°C and 1750°C under otherwise similar conditions, (a) 1 hour, (b) 3.5 hours and (c) 8 hours.

S153 {Slow heat, slow cool, 27nm, 1 hr, 1750°C} S154 {Slow heat, slow cool, 27nm, 2 hr, 1750°C}
S155 {Slow heat, slow cool, 27nm, 3.5hrs, 1750°C} S156 {Slow heat, slow cool, 27nm, 8 hrs, 1750°C}

4.5.8 Summary of diffusion characteristics observed for a diffusion from a continuous thin film source

The diffusion of titanium into sapphire to depths in excess of 50μm and in concentrations as great as 0.4wt% into sapphire has been demonstrated. Diffusions were carried out at temperatures of 1750°C and 1950°C, for times between 0.2 and 8 hours, from continuous thin films of thickness between 25 and 41nm, for various cooling conditions. The titanium distribution following diffusion was investigated using fluorescence imaging technique which is sensitive to Ti^{3+} ions incorporated with a spectroscopy appropriate for the development of an optical gain medium, and by SIMS, a technique insensitive to the spectroscopy of the diffused titanium. By considering trends in the total-Ti and/or fluorescent Ti^{3+} distribution as a function of fabrication conditions, a number of comments may be made about the incorporation of titanium into sapphire.

At a temperature of 1950°C, diffusing from a 41nm thick diffusion source and under conditions of slow cooling, Ti^{3+} has been incorporated with peak concentrations of the order of 0.04wt% to increasing depths with diffusion time. In each case, the peak concentration is located at depths between 10 and 20μm beneath the surface and the profiles were not consistent with standard diffusion theory. Further investigation of the total-Ti concentration for the sample diffused for 2 hours revealed that the total-Ti content was significantly greater than the fluorescent Ti^{3+} content. The form of the diffused total-Ti profile was closer to that predicted by standard diffusion theory, although the immediate surface region, up to depths of 2μm, was depleted in titanium. An estimate of the diffusion rate appropriate for the inclusion of titanium to the depths observed was of the order of $10^{-14}m^2s^{-2}$.

The effect of the cooling conditions on the total-Ti and Ti^{3+} distribution following diffusion was investigated by fabricating further samples under nominally similar conditions, except that the cooling rate was increased. For short diffusion times (1 and 2 hours) a significant increase in the peak Ti^{3+} concentration was observed for the rapid cooling rate. For the sample diffused for two hours, the Ti^{3+} distribution was in close agreement with the measured total-Ti distribution. Again, a depletion of Ti in the near surface region was observed. The effect of the more rapid cool on the Ti^{3+} distribution observed for the longer diffusion times (3.7 and 8 hours) was less marked and differences in the peak Ti^{3+} concentration and depth were minimal.

A reduction in the diffusion source thickness to 25-27nm, resulted in a significant increase in the peak Ti^{3+} concentration following a one-hour diffusion. After longer diffusion times, the differences were less marked, although in all comparisons, it appears that the reduction in source thickness may have led to an overall reduced diffusion rate.

Reducing the diffusion temperature to 1750°C and diffusing from a 27nm thick diffusion source, Ti^{3+} was incorporated into the sapphire with peak concentrations of 0.4wt%, after a 1 hour diffusion and to depths in excess of 40μm after an eight hour diffusion. The peak Ti^{3+} concentration recorded following the one-hour diffusion is approximately an order of magnitude greater than that recorded for the samples diffused for longer times at 1750°C. The trend in the evolution of the diffused Ti^{3+} profile as a function of diffusion time is not typical of a standard diffusion and interpretation is difficult without further information on the total-Ti distribution.

Following the conclusions of chapter 3, the transport process is expected to include a reaction between the source and substrate followed by a diffusion of Ti^{3+} into the sapphire lattice. The observation that the depth of Ti^{3+} inclusion is dependent on the source thickness and that a simple relation does not hold for a reduction in temperature lends support to a reaction/diffusion model. For example, a greater source thickness will lead to a larger reaction layer so that the diffusion process commences from a greater depth beneath the substrate. In addition, the composition of the reaction product and the rate of formation will vary with diffusion temperature, leading to complex trends in the observed concentration profile.

In addition, the discussion in chapter 3 indicated that evaporation of titanium from the sample surface might occur during the high temperature treatment. Evaporation of titanium during the diffusion process would explain the small fractions of Ti detected in each analysis. For example, after a 2 hour diffusion at 1950°C from a 41nm thick source, only half of the supplied Ti was detected by SIMS analysis, and after 8 hours, only a quarter of the supplied Ti was detected by fluorescence imaging.

The dominance of each mechanism (reaction, diffusion and evaporation) on the overall Ti profile will depend on the diffusion time, temperature and source thickness. Further work is required to establish the kinetics of each mechanism and allow a model of the transport

process to be developed; however a fundamental study of the diffusion mechanism in sapphire is not the principle aim of this work.

In conclusion, Ti^{3+} with a spectroscopy appropriate for optical gain may be included in sapphire by thermal diffusion. Concentrations as great as 0.4wt% may be incorporated and depths of tens of microns achieved within hours at temperatures of 1750°C and 1950°C. The proportion of Ti present as the fluorescent Ti^{3+} ion may be affected by the cooling rate so, for a maximum Ti^{3+} yield, a rapid cool from the diffusion temperature is appropriate. The concentration and depth of Ti^{3+} following a diffusion anneal is dependent on the diffusion time, temperature and source thickness.

Having demonstrated that the active ion Ti^{3+} may be introduced by thermal diffusion, the potential for spatially defining doped regions across the substrate was investigated by diffusing from a patterned diffusion source.

4.6 Diffusion from a patterned source

Diffusing from a photolithographically patterned diffusion source offers control over the spatial distribution of a diffusant across a substrate. This will allow the realisation of a localised gain medium and/or a channel waveguide.

In this work, diffusion from a series of stripes was investigated for temperatures between 1480°C and 1950°C, with diffusion sources of thicknesses ranging up to 270nm. The diffusions were all carried out with a rapid cool from the diffusion temperature, to ensure as much Ti as possible is introduced as the fluorescent Ti^{3+} ion. The mask used in most studies comprised of sets of 14 stripes between 3 and 16μm wide, with each set separated by a 100μm wide marker stripe, with further details given in §4.2.2. Using fluorescence imaging, the distribution of Ti^{3+} both immediately beneath the stripes and in the intervals between stripes were investigated to identify the distribution of diffused Ti^{3+} ions. In addition, considering the diffused profile immediately beneath the 100μm marker stripe, characteristics of the diffusion in the depth direction were obtained for a range of source thicknesses, diffusion temperatures and diffusion times. These results complement the investigation of diffusion from a continuous thin film described in the previous section.

4.6.1 Lateral diffusion at 1750°C and 1950°C

The distribution of diffused Ti^{3+} was investigated for a series of samples fabricated at temperatures of 1750°C and 1950°C, with a patterned diffusion source, 114nm thick. After diffusion, the original location of the stripes could be identified under an optical microscope, identified as regions of increased roughness. This enabled fluorescence imaging to be performed at the original location of the stripe source and in the regions between the stripe sources, to investigate the extent of any lateral diffusion.

For S165, diffused for 1 hour at 1750°C, a significant amount of Ti^{3+} was detected in the region midway between the stripe sources. This is illustrated in Figure 4.24, which shows the Ti^{3+} distribution measured at the location of stripe 15 and at a location between stripes 14 and 15. Since no source was supplied between the original stripes, a significant lateral diffusion must have occurred, to explain the presence of Ti^{3+} between the stripe sources. The extent of this lateral spread is unexpected, considering the stripes are separated by 100μm, and as shown in Figure 4.24, the diffusion depth in a direction perpendicular to the surface is no greater than 10μm.

The full widths at 1/e of the peak concentration are similar for each profile, although caution must be exercised as the profiles may be limited by the resolution of the imaging system. It is interesting to note that the forms of the diffused profiles are similar to those measured for S153 (Figure 4.22), diffused under similar conditions, except for the patterned source and cooling rate.

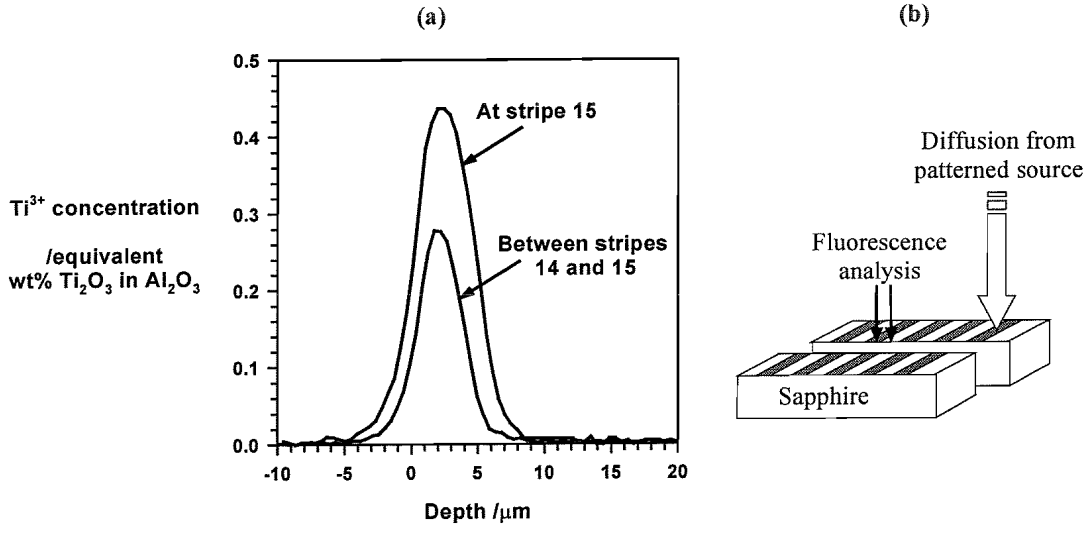

Figure 4.24:- Diffused Ti^{3+} distribution measured at stripe 15 and in the region between stripes 14 and 15, on S165, diffused at 1750°C for 1 hour with a 114nm source.

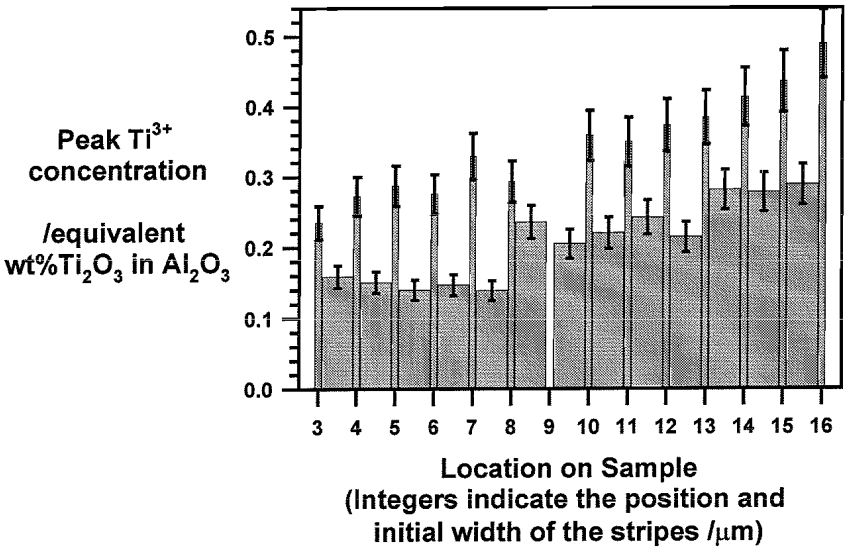

Figure 4.25:- Peak Ti^{3+} concentration measured at locations immediately below a stripe source and in the region between stripe sources on sample S165.

The character of the diffusion from the different stripes on S165 is shown in Figure 4.25, which plots the peak detected Ti^{3+} concentration measured at, and between, the location of the initial stripe source. As the stripe decreases in width, the peak concentration both beneath, and between, the stripe source decreases. The peak concentration between stripes is on average 57% that of the adjacent stripes.

By increasing the diffusion temperature to 1950°C, a similar lateral diffusion is observed. The region between the stripes is filled with fluorescent Ti^{3+}, with an example of the diffused profiles for an intermediary position between stripes 14 and 15, and beneath stripe 15, shown in Figure 4.27. At the higher diffusion temperature, Ti^{3+} has diffused to a greater depth, compared with S165 and the Ti^{3+} peak concentrations are lower. It is interesting to compare these diffused profiles with those obtained for S135 (see Figure 4.14), diffused under similar conditions, except that the diffusion source was a continuous thin film, 41nm thick. With the continuous thin film source, the Ti^{3+} was detected at depths up to 20μm, with a slightly lower peak concentration. These results indicate that that the diffusion from the continuous thin film was more advanced than that observed for the patterned source on S168.

Figure 4.26 shows the peak Ti^{3+} concentration observed at different positions across the surface of S168. The peak concentrations are lower than those measured for S165, diffused at the lower temperature of 1750°C. The contrast in peak concentration measured beneath

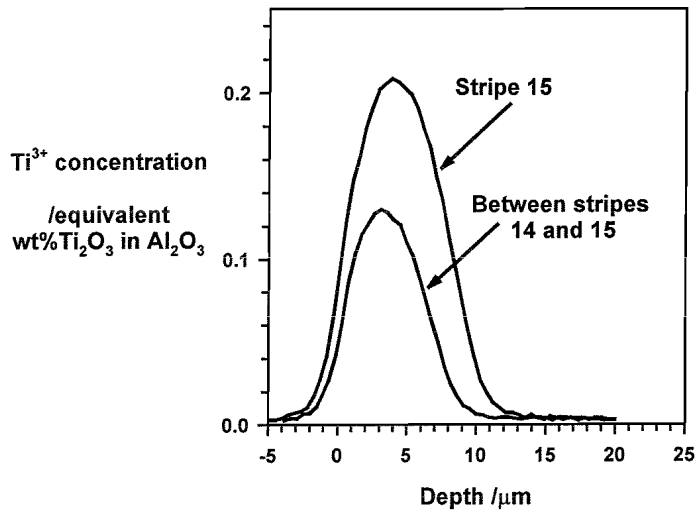

Figure 4.27:- Ti^{3+} distribution beneath stripe 15, and in between stripes 14 and 15 measured on S168, diffused for 1 hour at 1950°C with a 114nm source.

the stripes and at intermediary locations is slightly lower than before, with the peak concentration between stripes an average 66% of the peak concentration beneath the stripes.

In summary, diffusion from a stripe source occurs in directions perpendicular and parallel to the surface. The diffusion rate parallel to the surface is great enough so that the 100μm wide region between stripes is filled with diffused Ti^{3+}, whilst in the depth direction Ti^{3+} is not detected at depths beyond 10μm, for the samples discussed. The cause of the large anisotropy in diffusion is unknown; previous studies of diffusion in sapphire have not led to

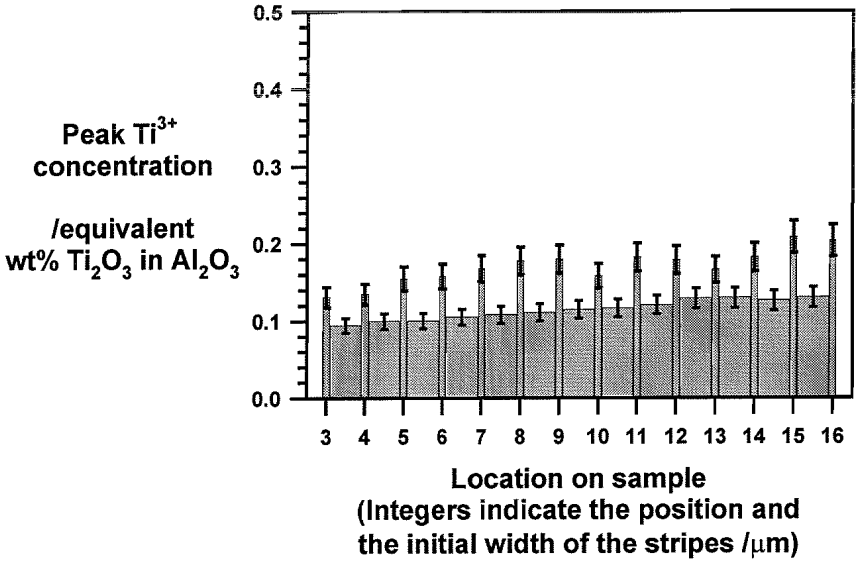

Figure 4.26:- Peak Ti^{3+} concentration measured at locations immediately beneath stripe sources and in between stripe sources on S168, diffused for 1 hour at 1950°C from a 114nm source.

observations of anisotropy in the lattice diffusion rates[11,12]. However, the diffusion rate is expected to be dependent on the defect structure of the sapphire, which may be inhomogeneous, leading to an apparent anisotropy in the observed diffusion rate. Alternatively, the unbound surface may provide a fast diffusion route. Further work is necessary to investigate the cause of the lateral diffusion and to determine how it may be controlled.

4.6.2 Variation in diffused profile as a function of source thickness

The total amount of source available for diffusion is a function of stripe width and height. For example, between the 3μm and 15μm stripe, the amount of source increases by 5-fold. Previously, differences in the diffused Ti^{3+} profiles were observed for a differing source thickness in the study of a continuous thin film, although interpretation of the results were complicated by the use of a slow cool in the fabrication of samples. Therefore for samples diffused from a patterned source, variation in diffused concentration and depth is expected as a function of stripe width and diffusion source thickness. An aspect of this has already been observed in Figure 4.25 and Figure 4.26, which showed an increase in peak Ti^{3+} concentration with stripe width. In this section, trends in the diffused Ti^{3+} concentration are discussed further for diffusion from striped sources of increasing thickness at a temperature of 1750°C, and cooled rapidly.

Figure 4.28 shows the peak Ti^{3+} concentration measured by fluorescence imaging for samples S161, S165 and S147. These samples were fabricated under similar conditions,

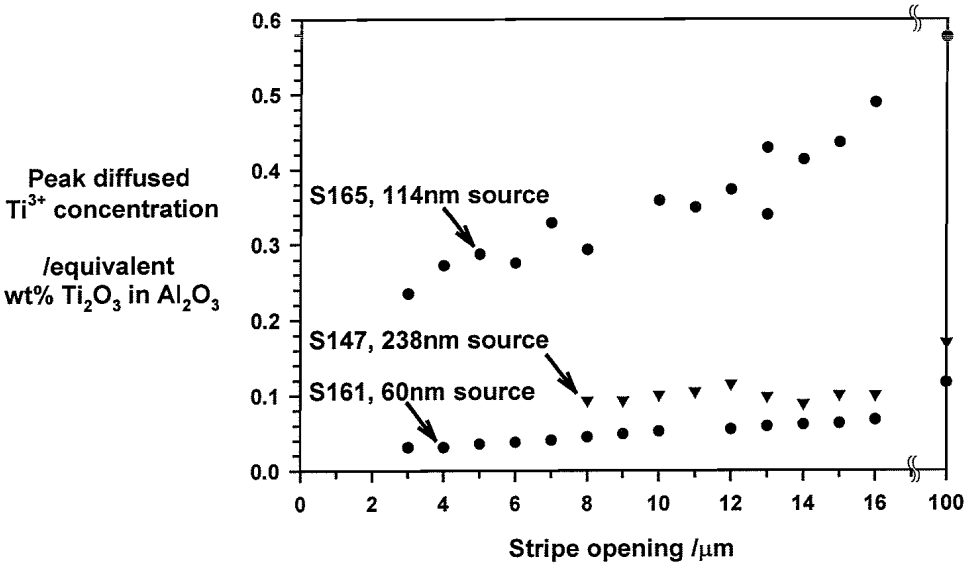

Figure 4.28:- Peak diffused Ti^{3+} concentration for samples diffused under similar conditions, but with differing source thickness.

with striped diffusion sources of 60nm, 114nm and 238nm respectively, with the exception that S147 was also heated to the diffusion temperature rapidly. These samples were diffused at a temperature of 1750°C for a period of 1 hour.

Figure 4.28 shows that with increasing stripe width, and with increasing the source thickness from 60nm to 114nm, the peak Ti^{3+} concentration increases. However, for a further increase in source thickness, to 238nm, the peak Ti^{3+} concentration decreases. This attribute may be related to the change in heating rate for S147, and/or the slightly reduced time at elevated temperature due to the rapid heating, or may be related to the change in source thickness.

The change in the diffused Ti^{3+} profile between S165 and S147 is shown in Figure 4.29, measured beneath the 100μm marker stripe. The decrease in peak concentration for S147 is clear. The profile of S165 is fairly close to that expected for a diffusion profile, with the resolution of the near surface region limited by the resolution of the imaging technique. For S145, the peak is located about 10μm beneath the surface, a feature that cannot be attributed to limitations in the measurement technique. This could be explained by loss of Ti by evaporation, however, it is more likely that some non-fluorescent Ti is present in the near surface region, considering an increase in the surface roughness at the location of the stripe is observed after diffusion. These results indicate that the peak concentration and diffusion depth of Ti^{3+} is closely related to the amount of diffusion source supplied.

In summary, non-ideal trends in the diffused Ti^{3+} distribution have been observed for samples fabricated under similar conditions, with varying diffusion source thickness. For the

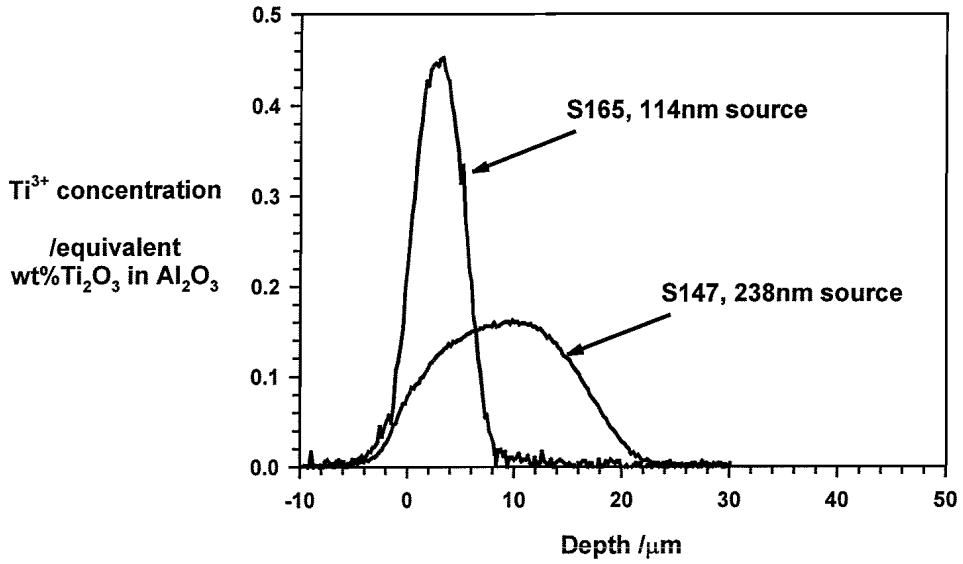

Figure 4.29:- Diffused Ti^{3+} distribution beneath the 100μm stripe on samples S165 and S147.

greatest thickness, 238nm, it appears that not all of the incorporated Ti is present as the fluorescent Ti^{3+} ion, despite the rapid cool.

4.6.3 Diffusion at 1950°C with a 270nm thick source

The effect of increasing the diffusion source thickness has been discussed at a temperature of 1750°C. A further study at 1950°C, for a series of samples, S175, S176 and S146, diffused for 0.2, 1 and 2hr respectively, illustrates other interesting features observed for the thicker diffusion source. The source thickness used for S175 and S176 is 270nm, whilst for S146, the diffusion source thickness is slightly reduced at 238nm. These samples are heated and cooled rapidly to the diffusion temperature. Therefore the diffused profile for the 0.2 hrs (10 minutes total time at elevated temperature) records the early stages of the Ti transport process.

Figure 4.30 shows the Ti^{3+} distribution measured beneath a 100μm stripe on each of the samples. It is interesting to see that the diffused Ti^{3+} penetrates about the same distance in each of the samples, despite the difference in diffusion time. The extent of diffusion of Ti^{3+} for the 10 minute anneal is remarkable; previously, a diffusion to depths of about 10μm was observed for a similar time at 1950°C, for a 27nm continuous thin film source (see Figure 4.18). The relation between peak Ti^{3+} concentration and diffusion time is not simple, and may be related to the small difference in source thickness used for S146 compared to S175 and S176. In each case, the peak Ti^{3+} concentration is some distance beneath the sample surface. This is most pronounced for the shortest diffusion time.

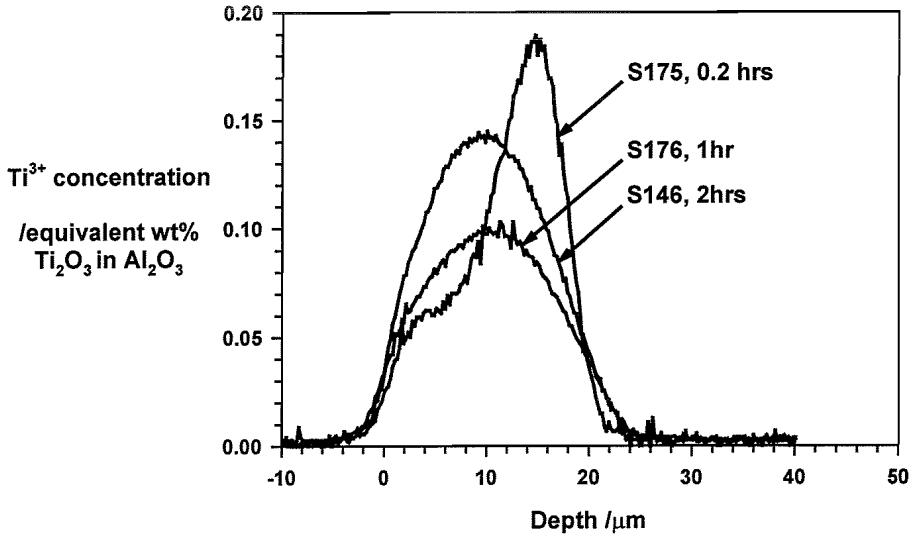

Figure 4.30:- Diffused Ti^{3+} distribution beneath the 100μm stripe following diffusion at 1950°C for times between 0.2 and 2 hours.

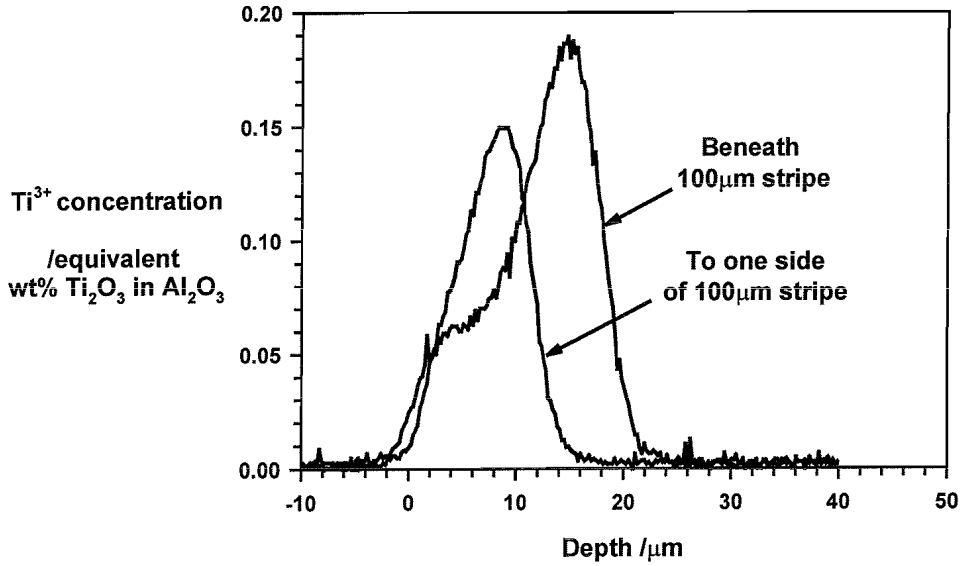

Figure 4.31:- Variation in Ti^{3+} distribution in the locality of a 100μm stripe on S175

Interpretation of these results is complicated by the lateral diffusion from the stripe, and its progression with diffusion time, which has not been analysed in detail for these samples. Similarly to S147, discussed in the previous section, these samples have been heated rapidly to the diffusion temperature, and the effect of this has not been characterised in detail. These profiles indicate that despite the rapid cool some non-fluorescent Ti is present after diffusion.

The profile observed for S175 was obtained for a location directly beneath a 100μm stripe diffusion source. Immediately to the side of the 100μm stripe a distinct change in the profile was observed, as shown in Figure 4.31. The form of the profile obtained to one side of the 100μm stripe is very similar to the deeper section of the profile beneath the centre of the stripe source. This may indicate that an intermediary compound, containing non-fluorescent Ti has formed immediately beneath the stripe source, from which diffusion has occurred into the substrate, and laterally away from the source. The surface at the original location of the 100μm stripe, is rough compared to unannealed sapphire, but does not show any significant swelling. These results support the model of a rapid reaction between the diffusion source and substrate, in addition to diffusion of Ti^{3+} into the sapphire lattice.

In summary, the diffused Ti^{3+} concentration in the vicinity of a 100μm stripe source has been investigated following diffusion at 1950°C for times between 0.2 and 2 hours. The observed trend in the diffused profile with time is not ideal. For the shortest diffusion time it appears that significant non-fluorescent Ti has been incorporated.

4.6.4 Summary of diffusion from a patterned source

A lateral diffusion parallel to the sapphire surface occurs from the patterned diffusion source, which is significantly faster than the diffusion rate perpendicular to the surface. After diffusion at 1750°C, for a time of 1 hour, concentrations of Ti^{3+} as high as 0.4wt% Ti_2O_3 in Al_2O_3 of Ti^{3+} are observed, which is significantly greater than that used in Ti:sapphire laser crystals. Increasing the diffusion temperature to 1950°C, the peak concentrations detected are lower and the diffusion depth greater, as may be expected if the net transport rate increases with temperature. By increasing the source thickness from 114nm to 238nm, a significant change in the diffused profile is observed. The peak concentration of Ti^{3+} appears about 10μm beneath the surface and is less than expected. These results indicate that despite the rapid cool, some non-fluorescent Ti has been incorporated during the diffusion. Therefore obtaining a high quality locally defined gain medium is a function of diffusion source thickness as well as diffusion time and temperature. The dimensions of the gain region will also be limited by the extent of the lateral diffusion. However, the results do show that high quality gain regions may potentially be formed from a patterned source by thermal diffusion.

4.7 Observations of diffusion under range of conditions

The results presented so far indicate that the diffusion process at temperatures of 1750°C and 1950°C contain many features. The results show that diffusion to depths of tens of microns is possible within a time scale of hours and that a large range of concentrations is possible. The diffusion process is far from ideal and a more detailed study would be required to identify each contributory mechanism.

In this section, a series of studies are discussed which have explored some of the features further. For example, the fast diffusion rates observed indicate that lower temperatures may be used. Slower transport rates at lower temperatures may offer greater control over the diffused Ti^{3+} distribution, so the characteristics of samples diffused for an hour at temperatures of 1480°C and 1700°C are presented. One of these samples, S169, was later used to realise a channel waveguide laser. The investigation of diffusion at temperatures as low as 1480°C also offers the possibility of using different furnaces, and the effect of a change in diffusion atmosphere is studied briefly. Characteristics of diffusion from a Ti

metal film are discussed and the possibility of loss of Ti by evaporation is investigated for a bulk doped sample annealed at high temperature. Spatial variation in the diffusion profile has been observed for a patterned source, however, a significant change in the diffused profile is also seen near the edge of the sapphire sample for a continuous thin film.

4.7.1 Diffused Ti^{3+} distribution at temperatures between 1480°C and 1950°C

Numerous further samples were prepared to investigate the diffusion characteristics from a patterned source, with source thickness' ranging from 27nm to 270nm, at temperatures between 1480°C and 1950°C for times between 0.2 and 8 hours. The trend observed for a range of temperatures, following a 1 hour diffusion from a patterned source ranging from 238nm – 270nm, is shown in Figure 4.32.

Figure 4.32 shows that the trend in the peak Ti^{3+} concentration and the diffusion depth is not a simple function of temperature. Sample S169, diffused for 1 hour at a temperature of 1700±60°C shows the greatest Ti^{3+} concentration, with the diffusion doping confined to the surface 10μm. The greater error in diffusion temperature has arisen from an error in the alignment of the optical pyrometer, which monitors the furnace temperature for this sample. The diffused region beneath the 3μm stripe on S169 was selected for laser experiments, reported in chapter 6.

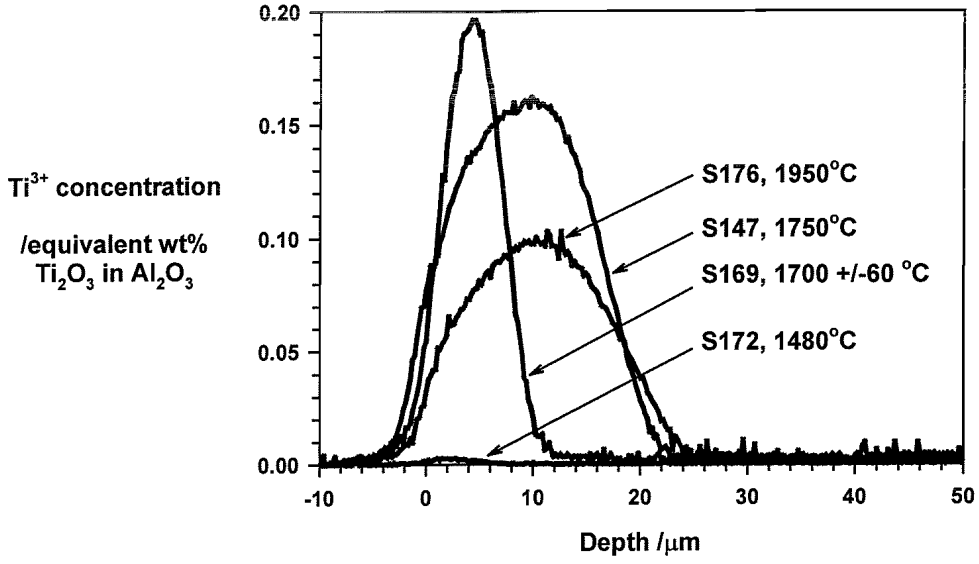

Figure 4.32:- Ti^{3+} distribution beneath the 100μm marker stripe, following diffusion for 1 hour at temperatures between 1480 °C and 1950 °C.

S172{Rapid heat, rapid cool, P270nm, 1hr, 1480 °C} S169{Rapid heat, rapid cool,P270nm,1hr, 1700 °C}
S147{Rapid heat, rapid cool, P238nm, 1hr, 1750 °C} S176{Rapid heat, rapid cool, P238nm, 1hr, 1950 °C}

4.7.2 Diffused Ti^{3+} distribution at 1480°C, in different furnaces

Although initial effort has concentrated on diffusion at temperatures in excess of 1700°C, it is attractive to investigate Ti diffusion at lower temperatures, where the choice of diffusion furnace is greater. The use of an alternative furnace would allow more flexibility over diffusion atmosphere and sample size. To investigate this, a series of samples were fabricated at diffusion temperatures of 1480°C and 1500°C in the usual carbon resistance furnace and a ceramic tube furnace respectively. The tube furnace consists of tungsten heating elements surrounding a high purity alumina tube. During diffusion, argon gas is flushed through the tube in an attempt to maintain an inert atmosphere. However, it is thought that a small partial pressure of oxygen will exist in the tube at temperatures of 1500°C.

A series of samples, S172, S173 and S174 were diffused in the usual carbon resistance furnace at a temperature of 1480°C for times of 1, 4 and 8 hours respectively. In each case, the diffusion source was patterned with stripes, of thickness 270nm. The diffused Ti^{3+} distributions measured in the location of one of the 100μm stripes is shown in Figure 4.33(a). In Figure 4.33(b), the Ti^{3+} distribution beneath the 100μm stripe is shown (note the factor of 10 difference of scale on the y-axis) for samples SL5 and SL6. These samples were diffused for 8 and 16 hours respectively in a ceramic tube furnace at a temperature of 1500°C, from a 264nm thick Ti(O) diffusion source, patterned as stripes.

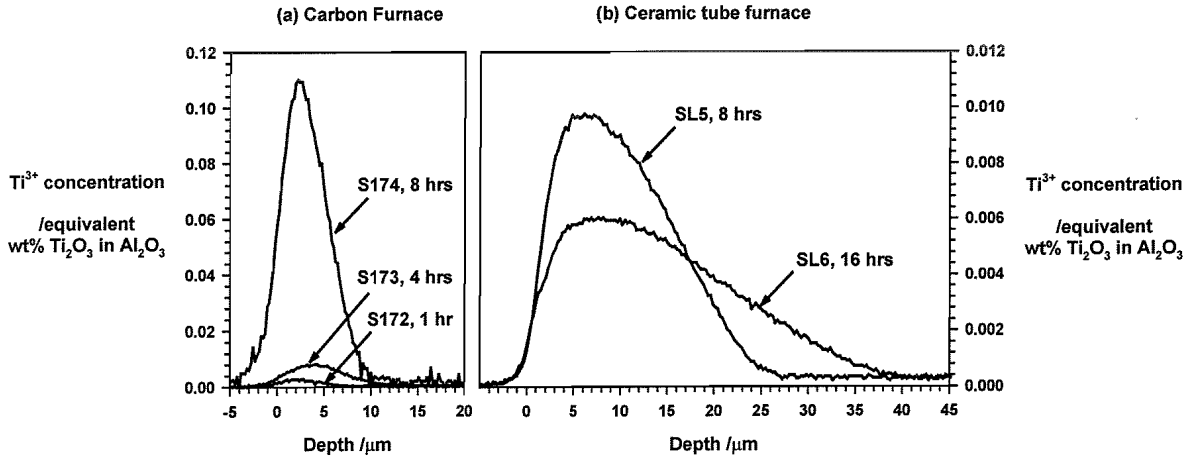

Figure 4.33:- Ti^{3+} distribution beneath a 100μm stripe following diffusion in (a) a carbon furnace and (b) a ceramic tube furnace at temperatures of 1480°C and 1500°C respectively.

S172{Rapid heat, rapid cool, P270nm, 1hr, 1480°C} SL5{Quick heat and cool, P264nm, 8hr,1500°C}
S173{Rapid heat, rapid cool, P270nm, 4hr, 1480°C} SL6{Quick heat and cool, P264nm, 16hr, 1500°C}
S174{Rapid heat, rapid cool, P270nm, 8hr, 1480°C}

Comparing Figure 4.33(a) and (b) it is clear that the choice of furnace has affected the diffused Ti^{3+} distribution. In the carbon resistance furnace, the peak Ti^{3+} concentration increases with diffusion time and the maximum depth of diffusion is of the order of 10μm following an 8 hour diffusion. In the ceramic tube furnace, for similar diffusion conditions, the concentration of Ti^{3+} is about an order of magnitude lower, and the diffused Ti^{3+} extends to depths in excess of 20μm. On increasing the diffusion time further to 16 hours, the peak concentration decreases and the diffusion depth increases.

The change in furnace has clearly affected the Ti diffusion characteristics. It may be that the presence of small amounts of oxygen in the ambient atmosphere affects the Ti valency, the progression of any reaction between the source and substrate, or the defect structure of the sapphire. A change in the valency of the Ti, bulk-doped in sapphire has been previously reported for heating in differing partial oxygen pressures atmospheres[13].

4.7.3 Diffusion from a Ti thin film source

Whilst a Ti_2O_3 thin film source is attractive in that it remains solid at temperatures up to 1840°C, the films are hard to deposit with reproducible composition[3] and thickness by thermal evaporation. The varied composition may have implications for the progression of a reaction between the source and substrate, and may be a contributory factor in the non-ideal diffusion characteristics observed so far. The use of a Ti metal film would be preferred, as the properties of vacuum deposited thin films are expected to be consistent for given set of deposition conditions. The results of preliminary studies into the use of a Ti diffusion source are discussed below, illustrating some of the characteristics of the diffusion at temperatures just below, and above the melting point of the Ti source, 1660°C.

Samples S54, S2 and S4 were diffused for a period of 8 hours at temperatures of 1620°C, 1750°C and 1950°C respectively, with slow heating and cooling regimes. For S54, the film thickness was 25nm, and for S2 and S4 the film was in excess of 100nm. In each case, the surface after diffusion showed distinct features, which are illustrated in Figure 4.34. In each case there is clearly some interaction between the thin film and the substrate.

For diffusion temperatures above the melting point of Ti the interaction appears to be localised. The features seen in Figure 4.34(b) were analysed using energy dispersive spectrometry[14] and were found to have a high Ti content, indicating that these features are

S172{Rapid heat, rapid cool, P270nm, 1hr, 1480°C} *SL5{Quick heat and cool, P264nm, 8hr,1500°C}*
S173{Rapid heat, rapid cool, P270nm, 4hr, 1480°C} *SL6{Quick heat and cool, P264nm, 16hr, 1500°C}*
S174{Rapid heat, rapid cool, P270nm, 8hr, 1480°C}

characteristic of a Ti-rich residue. At the higher temperature of 1950°C, distinct hexagonal pits and associated raised sections are observed. Further investigation would be required to establish whether the surface features form on cooling, or whether they are representative of a localised interaction at the diffusion temperature. A similar beading of thin metal films on sapphire has been observed[15,16] for the metals Pd and Cu, albeit at significantly lower temperatures (<1000°C).

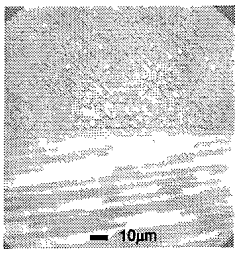

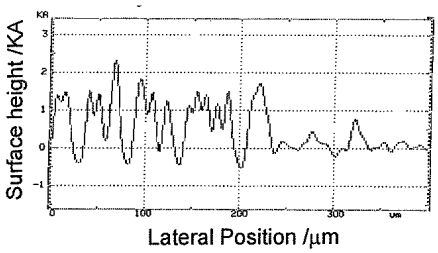

(a) Sapphire 54 after an ***8 hour anneal at 1620°C using a 25nm thick Ti film.*** The photograph shows a pattern on the surface due to some Ti residue. The surface profile on the right is taken in the direction of the arrow.

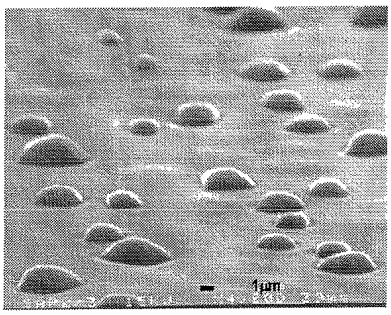

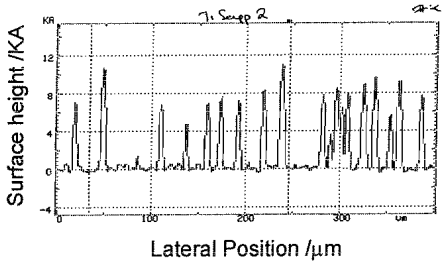

(b) Sapphire 2 after an ***8 hour anneal at 1750°C using a Ti source of thickness > 100nm***. The features range up to 1200nm in height, shown in the surface profile on the right. Compositional analysis of the features indicate a high Ti content.

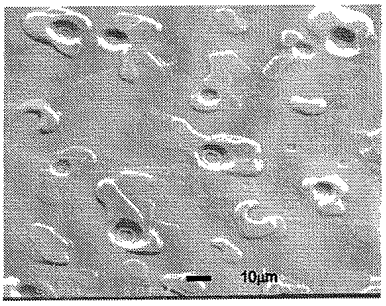

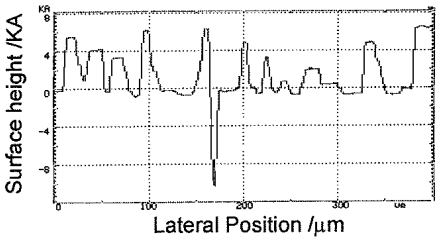

(c) Sapphire 4 after an ***8 hour anneal at 1950°C using a Ti source thickness > 100nm.*** The photograph reveals deep pits and raised regions, which are identifiable in the surface profile on the right.

Figure 4.34:- Surface quality following diffusion from a Ti source at temperatures of (a) 1620°C, (b) 1750°C and (c) 1950°C

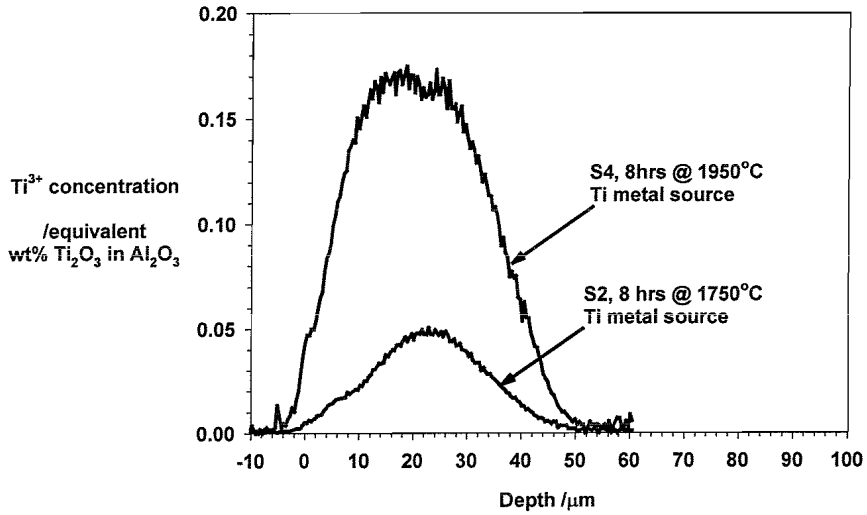

Figure 4.35:- Ti^{3+} distribution measured for samples diffused from a Ti diffusion source at temperatures of 1750°C and 1950°C.

Despite the surface roughness, the diffused Ti^{3+} distribution was investigated for these samples and the results illustrated in Figure 4.35. During the 8 hour diffusion, Ti^{3+} has been incorporated to significant depths, although the profiles are not ideal. The appearance of the peak Ti^{3+} concentration beneath the surface in each case may indicate that some non fluorescent Ti has been incorporated, which may be expected under slow cooling conditions. The presence of a Ti rich residue on S2 may also affect the diffused distribution of fluorescent ions.

In comparison with S156 and S53 (Figure 4.23(c)), diffused under comparable conditions to S2 and S4 respectively, except for the composition and thickness of the diffusion source, the thicker Ti metal diffusion source has led to the incorporation of higher Ti^{3+} concentrations.

These results are encouraging since they indicate that Ti^{3+} may be introduced into sapphire from a Ti metal source, at temperatures above the melting point of Ti. Ti metal is a more attractive diffusion source than Ti_2O_3, as in practice the deposition of Ti is expected to be more reproducible than the deposition of a Ti_2O_3 film. With further development, it is expected that roughness of the surface after diffusion may be reduced.

4.7.4 Movement of Ti in a bulk doped sample

In many of the studies so far, the amount of Ti detected during analysis is significantly less than the total amount supplied in the diffusion source. For example, for diffusion from a continuous thin film source, only 25% of the supplied Ti is detected during fluorescence imaging. This may indicate that either there is an error in the calculation of the amount of

source supplied or that Ti has been lost during the high temperature treatment. An error in the calculation of the amount of Ti content is possible, since it is assumed that the deposited diffusion source is stoichiometric Ti_2O_3, rather than a mixture of lower oxides of Ti as reported by other authors for this deposition technique. However, it is unlikely this would lead to a four-fold over estimate. Therefore, to investigate the movement of Ti at the diffusion temperature of 1950°C, the movement of Ti^{3+} in a bulk doped Ti:sapphire crystal was considered.

Two sapphire samples BD10 and BD5, doped throughout with Ti_2O_3 at 0.11wt% were annealed at 1950°C for two hours. BD10 was cooled slowly from the diffusion temperature to room temperature, whilst BD5 was cooled rapidly. SIMS and fluorescence imaging was used to characterise the distribution of Ti^{3+} and total-Ti after diffusion. Changes in the total-Ti and Ti^{3+} distribution on both the top face of the crystal (exposed to the ambient environment) and the bottom face of the crystal (in contact with a tantalum foil) were investigated.

Figure 4.36 shows the Ti^{3+} distributions measured for BD5 and BD10, with respect to depth from the top and bottom faces of the crystal. In each case, the measured Ti^{3+} concentration is greater on the bottom face, at a level greater than the nominal crystal doping. On the top face, the Ti^{3+} content is at a minimum at the surface, increasing with depth into the crystal. Little difference in the form of the Ti^{3+} distribution is observed for the differing cooling rates.

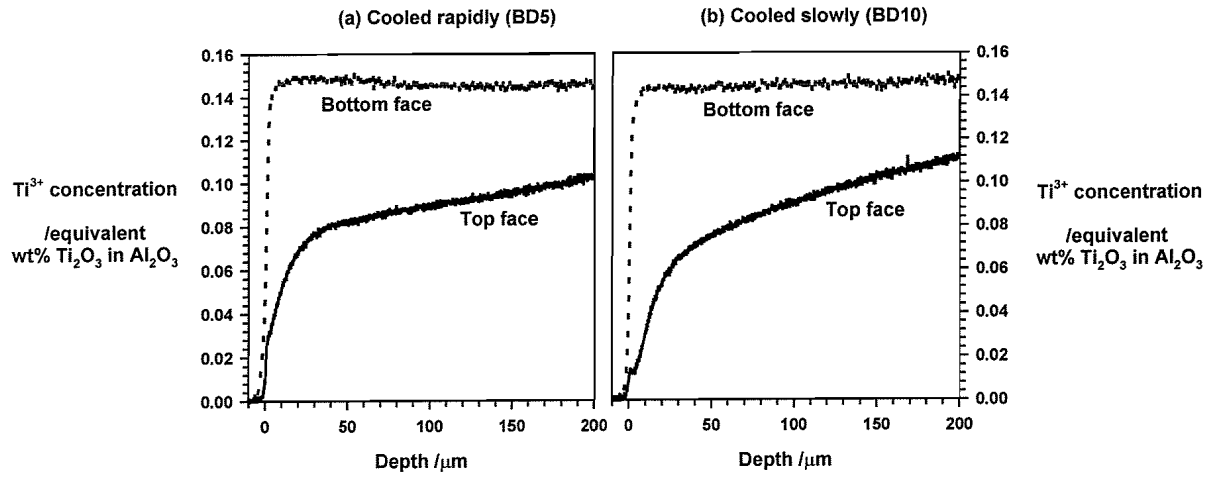

Figure 4.36:- Ti^{3+} distribution after a high temperature anneal for a bulk doped Ti:sapphire crystal nominally doped at 0.11wt%. (a) BD5 cooled rapidly from the anneal temperature, and (b) BD10 cooled slowly from the anneal temperature.

BD5 {Slow heat, rapid cool, bulk doped at 0.1wt%, 2hr, 1950°C}
BD10 {Slow heat, slow cool, bulk doped at 0.1wt%, 2hr, 1950°C}

The increase in Ti^{3+} fluorescence on the bottom face is significant. It may indicate a real increase in the Ti content, which is hard to explain, or it may indicate that the anneal has increased the proportion of fluorescent Ti^{3+}. This latter interpretation would affect the quantitative Ti^{3+} measurements made on all diffused samples, increasing the concentrations by a factor of 0.13/0.11. The increase in Ti^{3+} content of a bulk doped Ti:sapphire laser crystal after a high temperature anneal in a reducing atmosphere has been reported previously[17].

The total-Ti concentration within 2μm of the top and bottom faces of BD5 was investigated using SIMS. Over the first 2μm depth from the top face, the total-Ti distribution is in close agreement with the fluorescence imaging results, with the total-Ti concentration rising from 0.02 to 0.04 wt% Ti_2O_3 in Al_2O_3. Therefore the trend in Ti^{3+} concentration observed as a function of depth from the top face of BD5 by fluorescence imaging is most likely to be due to a depletion of total-Ti concentration, rather than a change in the spectroscopy. Depletion of Ti from the top face may be due to either evaporation from the top face, or diffusion towards the back face of the sample, contributing to the higher levels of Ti detected, both by fluorescence imaging and SIMS. In the light of previous results for Ti-diffused samples, it is considered more likely that the depletion is due to evaporation from the top surface.

On the bottom face the Ti content increases to levels of 0.13wt% Ti_2O_3 in Al_2O_3 within 2μm of the surface, in apparent agreement with the high Ti^{3+} concentrations measured by fluorescence imaging. This increase of total Ti on the lower face of the crystal is hard to explain, and this result should be treated with caution without further investigation. For example, the total-Ti concentration could be measured over a greater depth range by polishing a 0.5° bevel on the sample and carrying out a series of point analyses.

In summary, the movement of Ti in a bulk doped sample following an anneal at 1950°C provides some interesting results. It seems that the amount of Ti on the upper surface has decreased. This loss of Ti may be related to the low levels of Ti detected in diffused samples, compared with the amount of source supplied.

4.7.5 Spatial deviation in the diffused Ti^{3+} distribution

Variation in the diffused Ti^{3+} distribution has been observed after diffusion from a patterned source. It is also interesting to note that variation in the diffused profile is also observed in

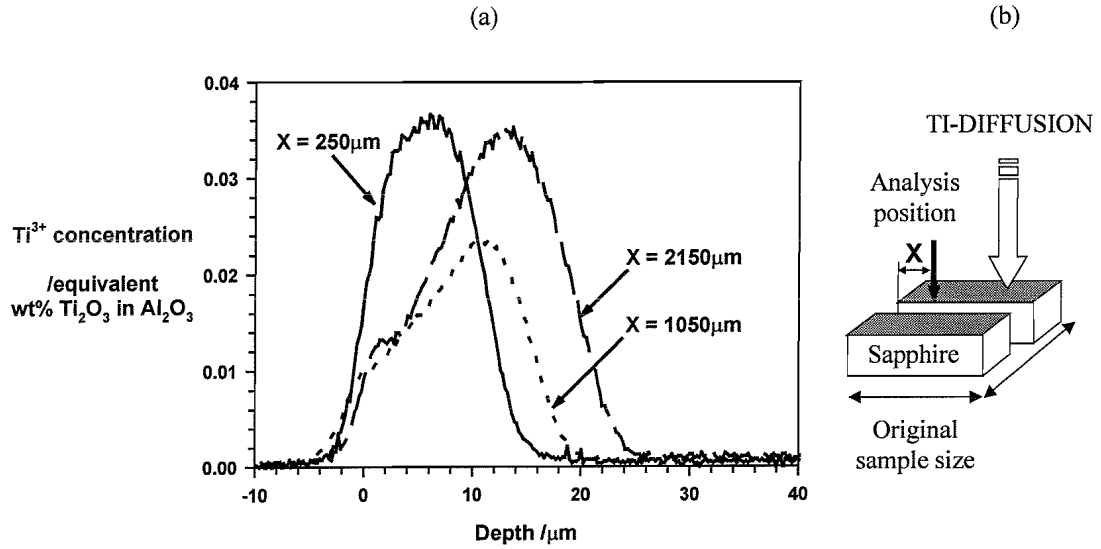

Figure 4.37:- (a) Distribution of diffused Ti^{3+} in the proximity of the sample edge, following the geometry illustrated in (b).

the proximity of the sample edge following diffusion from a continuous thin film. For example, the Ti^{3+} distributions measured at positions within about 2mm of the original sample edge are shown in Figure 4.37, for sample S134. This sample has been discussed earlier (see §4.5.1) and was diffused at 1950°C, for 1 hour and cooled slowly from the diffusion temperature. The diffused distribution is seen to change significantly in peak concentration and depth of diffusion as a function of distance from the edge. For distances greater than 2mm, little further change in profile is observed. Changes in the profile may be related to differences in cooling rate at the edges of the sample or perhaps a local difference in temperature at the edge compared to the more central regions of the sample. This feature of the diffusion means that the outer most 2mm of the sample should be removed before the diffused region is used as an optical device, to ensure uniformity of Ti doping.

4.8 Conclusions

Experimental methods for diffusing and characterising the diffusion of Ti into sapphire have been presented. The results of the experimental studies show that Ti^{3+} may be incorporated into sapphire at temperatures between 1480°C and 1950°C over diffusion times between 0.2 and 8 hours, achieving depths in excess of 50μm and peak Ti^{3+} concentrations greater than 0.4wt% Ti_2O_3 in Al_2O_3. The characteristics of the diffused Ti are highly sensitive to the fabrication conditions, and indicate that more than one mechanism contributes to the

transport process. These results comprise the first demonstration of Ti^{3+} diffusion into sapphire with a view to making an active optical device.

At 1950°C, for diffusion times up to 2 hours with a 41nm Ti(O) source, the proportion of Ti^{3+} included is sensitive to the cooling rate. After a fast cool the Ti^{3+} profile is close to the total-Ti concentration profile, whilst only half of the Ti is present as the fluorescent Ti^{3+} ion after a slow cool. It seems that during the cooling, either defects in the lattice or the Ti ions have sufficient mobility to move to form a non-fluorescent configuration.

Trends in the diffused profile as a function of time, temperature and source thickness indicate that more than one mechanism contributes to the diffusion process. Very high Ti^{3+} concentrations may be incorporated, for example 0.4wt% after 1 hour at 1750°C from a 27nm diffusion source. After 2 hours the peak concentration reduces by more than an order of magnitude. These results are not easily explained by standard diffusion theory, but the observation of high Ti^{3+} concentrations is encouraging for the future development of a laser medium.

From a patterned diffusion source, a very fast lateral diffusion is observed, to the extent that a continuous band of Ti^{3+} is found between the stripe sources. For example, following diffusion at 1750°C for 1 hour, the diffusion depth is less than 10μm whilst the Ti^{3+} has diffused at least 50μm laterally. The Ti^{3+} concentration beneath the stripe source and between stripes varies with temperature, diffusion time and source thickness. Increasing the source thickness does not necessarily lead to higher concentrations of Ti^{3+}. For the thickest diffusion source and short diffusion times, it is thought that some non-fluorescent Ti is present in the near surface region, despite the fast cool. Therefore, the distribution of Ti following diffusion from a patterned source is a function of the source thickness, the temperature and the diffusion time. A fast lateral diffusion will affect the spatial definition of the diffused region.

At a temperature of 1700°C, a peak Ti^{3+} concentration of about 0.2wt% was observed beneath a 100μm marker stripe and the diffused Ti^{3+} contained within 10μm of the surface.

At the lowest temperature investigated, 1480°C, Ti diffusion was observed, with a peak Ti^{3+} concentration of the order of 0.1wt% incorporated after 8 hours. At these temperatures, other furnaces are available, which would allow the use of larger samples and a greater range

of ambient atmospheres. However, the diffusion characteristics of the Ti are affected by the change to a ceramic tube furnace, with a peak Ti^{3+} concentration about an order of magnitude lower for otherwise similar conditions. It seems that the Carbon resistance furnace provides an atmosphere appropriate for diffusing the Ti^{3+} ion.

Ti^{3+} may also be incorporated in sapphire by diffusion from a Ti metal film, at temperatures above the melting point of the titanium. Some degradation of the surface quality was observed, although this may be related to the large source thicknesses used and the presence of a residue after the diffusion anneal. With further development, the use of a Ti metal source may prove an attractive source for diffusion processes.

Annealing a sample of bulk doped Ti:sapphire crystal at 1950°C shows a depletion in the Ti concentration in the near surface region on the top face of the crystal. The loss of Ti from the surface may explain why only a fraction of the supplied Ti is detected after diffusion. On the bottom face of the sample, no such depletion in the Ti concentration is observed. In contrast, an increase in the Ti^{3+} fluorescence is seen, which may indicate that the high temperature treatment has increased the proportion of Ti in the fluorescent state. If so, this would indicate the standard Ti:sapphire crystal used to obtain the quantitative information from the fluorescence imaging technique may contain a proportion of non-fluorescent Ti. This would mean that the reported diffused Ti^{3+} concentrations are consistently underestimated by a small fraction.

Therefore, a Ti^{3+} doped region may be formed in a commercial sapphire wafer by thermal diffusion from either a Ti(O) or Ti metal film at temperatures between 1480°C and 1950°C. The proportion of Ti present as the fluorescent Ti^{3+} ion may be maximised by cooling the sample rapidly and optimising the amount of source supplied. The depth, concentration and spatial distribution of Ti^{3+} may be controlled by varying the temperature, diffusion time and pattern of the source.

Locally doping the sapphire with Ti is the first stage in the realisation of the miniature Ti:sapphire laser. Waveguides to confine and steer radiation through the gain medium will allow the diffused Ti^{3+}:sapphire region to be exploited in the integrated optic format. The realisation of slab and channel waveguides in the Ti-diffused sapphire is presented in chapter 5.

4.9 References to chapter 4

1. H W Gutsche, J W Moody, "**Polishing of sapphire with colloidal silica**"; *J. Electrochem. Soc., **125** (1978), pp136-138*
2. Ecoclear, supplied by Logitech Ltd, Glasgow
3. H K Pulker, G Paesold, E Ritter "**Refractive indices of TiO_2 films produced by reactive evaporation of various titanium-oxygen phases**"; *Appl. Opt., **15** (1976), pp 2986-2991*
4. P F Moulton, "**Spectroscopic and laser characteristics of Ti:Al_2O_3**"; *J. Opt. Soc. Am. B, **3** (1986), pp125-133*
5. B Henderson, G F Imbusch, "**Optical spectroscopy of inorganic solids**"; *Clarendon Press, 1989*
6. S P Smith, R G Wilson, "**SIMS depth profiling and implantation profiles in crystalline Al_2O_3**"; *Publication from Charles Evans and Associates, Redwood City, USA*
7. C Grattepain, E G Moya, D Juvé, D Tréheux, M Acouturier, F Moya, "**Depth profiling for copper diffusion in α-alumina single crystals**"; *SIMS VIII, pp 343-348*
8. E Levin, "**Phase diagrams for ceramists**"; *2nd ed., pub Am. Ceram. Soc., 1964, fig 316 and fig 4376*
9. E G Moya, F Moya, A Sami, D Juvé, D Tréheux, C Grattepain, "**Diffusion of chromium in alumina single crystals**"; *Phil. Mag. A, **2** (1995), pp 861-870*
10. E G Moya, F Moya, private communication
11. I K Lloyd, H K Bowen, "**Iron tracer diffusion in aluminium oxide**"; *J. Am. Ceram. Soc., **64** (1981), pp 744-747*
12. V S Stubican, J W Osenbach, "**Grain-boundary and lattice diffusion of ^{51}Cr in alumina and spinel**"; *Advances in Ceramics, ed. Kingery, 1984, vol 10, p 406*
13. S K Mohapatra, F A Kröger, "**Defect structure of alpha-Al_2O_3 doped with titanium**"; *J. Am. Ceram. Soc., **60** (1977), pp 381-387*
14. P Goodhew, F Humphreys, "**Electron microscopy and analysis**"; *pub. London, Taylor and Francis, 2nd Ed., 1988*
15. R Raj, A Pearce, C M Kennefick, "**Thin films of transition metals on oxides**"; *Acta. Metall. Mater., **39** (1991), pp 3187-3191*
16. C M Kennefick, R Raj, "**Copper on sapphire: stability of thin films at 0.7 T_m**"; *Acta. Metall. Mater., **37** (1989), pp 2947-2952*

17. M R Kokta, "**Processes for enhancing fluorescence of tunable titanium-doped oxide laser crystals**"; *US Patent No 4,988,402*

CHAPTER 5

TITANIUM DIFFUSED WAVEGUIDES IN SAPPHIRE

5.1 Introduction

The realisation of a locally doped Ti^{3+}:sapphire region by thermal diffusion presents a significant step in the realisation of a miniature Ti:sapphire waveguide laser. However, the advantage of the localised gain medium may only be fully exploited if the pump and fluorescence radiation is coincidentally confined in a waveguide configuration. To form a waveguide, the sapphire refractive index needs to be increased over sufficient depth to confine the radiation. Often in integrated optic devices, this is achieved by thermal diffusion of an impurity into the lattice. For example, the thermal diffusion of Ti is one of the best known methods for forming low loss waveguides in $LiNbO_3$[1]. With a large range of Ti concentrations and a broad range of diffusion depths reported in chapter 4, the formation of optical waveguides in Ti-diffused sapphire was investigated and the results reported in this chapter. These results represent the first realisation of diffused waveguides in sapphire.

The first section provides a review of the properties that might be expected for waveguides formed in a diffused, graded refractive index medium. The model presented, uses the WKB method to evaluate the effective refractive index of waveguide modes. The intention is to provide a qualitative overview of the trends that may be expected as a function of fabrication conditions. §5.3 describes the experimental techniques used to characterise waveguide properties, such as the elevation of the modal effective refractive index above that of the substrate, field intensity mode profiles and spectral attenuation in the waveguide. In §5.4, the characteristics of a series of slab waveguides are discussed, formed by diffusion from a continuous thin film source. Trends in the waveguide properties are observed as a function of fabrication conditions and related to the model of waveguide properties developed. Further quantitative analysis of the waveguide characteristics lead to a reconstruction of the refractive index profile, which is compared to the Ti distribution, with reference to chapter 4. An estimate of the relationship between the refractive index change and Ti concentration is

$$\int_0^{Xb} k_o \sqrt{n(x)^2 - n(X_b)^2}\, dx - \left(p + \frac{3}{2}\right)\pi = 0 \qquad \textit{Eqn. 5-5}$$

Assuming the refractive index change for a Ti-diffused waveguide in sapphire is proportional to the concentration of Ti, trends in the n_{eff} will be related to trends in the diffusion profile. In the following sections, the solutions to the diffusion equation presented in §3.3 are used to identify the trends in n_{eff} expected for a slab waveguide formed by diffusion.

5.2.2 Waveguide formed from an infinite diffusion source

For an infinite diffusion source, the diffused refractive index profile, *n(x),* will be given by *Eqn. 5-6*, where Δn_{peak} is the peak refractive index change at the surface due to the Ti doping, n_{sap} is the substrate refractive index, D is the diffusion rate, and t is the diffusion time; $2\sqrt{Dt}$ defines the effective diffusion depth. This relation assumes the refractive index change is proportional to the concentration of Ti.

$$n(x) = \Delta n_{peak}\, erfc\left(\frac{x}{2\sqrt{Dt}}\right) + n_{sap} \qquad \textit{Eqn. 5-6}$$

For Δn_{peak} of 0.001 and n_{sap} of 1.8, the effective refractive indices of modes supported at a wavelength of 633nm calculated for diffusion depths up to 40μm are shown in Figure 5.2.

For diffusion depths less than about 3μm, the graded index does not support a guided mode at this wavelength. With increasing diffusion depth, the effective refractive index of the p=0

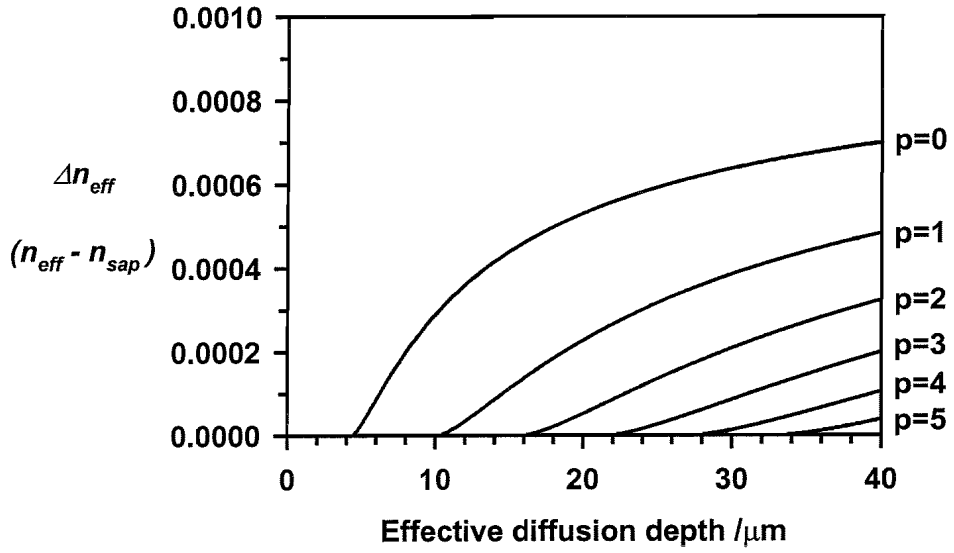

Figure 5.2:- Effective refractive indices for waveguide modes supported by the diffused structure, assuming a peak refractive index of 0.001

mode increases towards the limiting value of 0.001, which is the peak surface refractive index. Higher order modes are supported at increasing effective diffusion depths. These trends are in good agreement with those reported by Hocker in reference 3.

5.2.3 Waveguide formed by diffusion from an instantaneous diffusion source

The trends in the effective refractive index for a waveguide formed by diffusion from an instantaneous diffusion source differ significantly. In this system, the peak Ti concentration will decrease with diffusion time as the effective diffusion depth increases, according to *Eqn. 5-7*. T is a constant, defining the area under the refractive index distribution, with units of meter, n_{sap} is the refractive index of the sapphire substrate, whilst D, t and $2\sqrt{Dt}$ are the diffusion rate, diffusion time and effective diffusion depth, as before. The effective refractive index of modes supported by this structure at a wavelength of 633nm, for $T = 1.5 \cdot 10^{-8}$m and n_{sap}=1.8 are shown in Figure 5.3.

$$n(x) = \frac{T}{\sqrt{\pi}2\sqrt{Dt}} \exp\left(-\frac{x^2}{4Dt}\right) + n_{sap} \qquad \textit{Eqn. 5-7}$$

For shallow diffusion depths (<1μm), no waveguide is supported by the graded index region at this wavelength. For depths greater than about 1μm, a $p=0$ waveguide mode is supported.

The elevation of the modal effective refractive index above the substrate index (Δn_{eff}) reaches a maximum of about 0.0006, before decreasing with increasing diffusion depth.

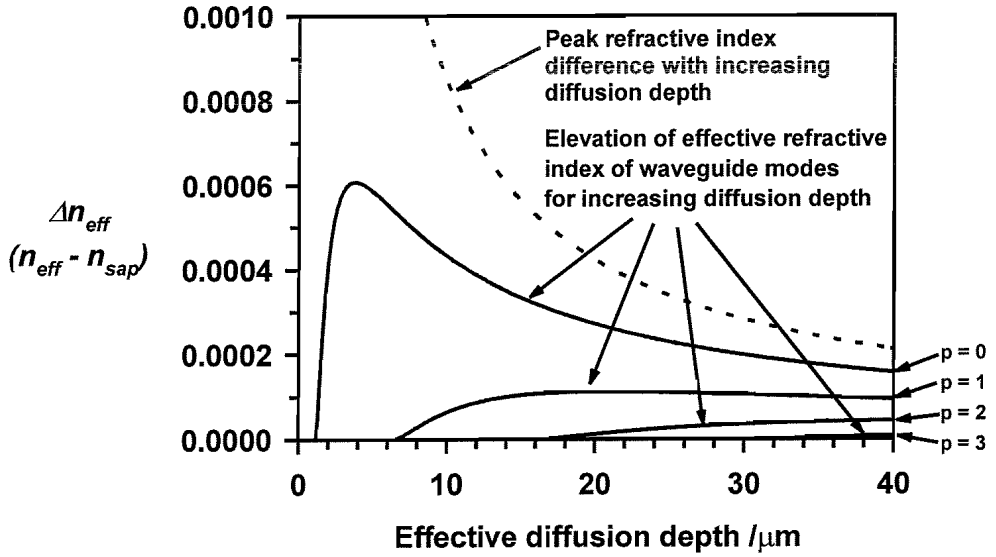

Figure 5.3:- Effective refractive index of waveguide modes supported by a graded refractive index region diffused from an instantaneous source, for effective diffusion depths up to 40μm.

Further modes appear at diffusion depths of about 6μm, 16μm and 30μm. However, considering the elevation of the modal effective index as a fraction of the peak refractive index change at the surface Δn_{peak}, it can be seen that these trends are a characteristic of the decreasing peak refractive index. This feature is clearly illustrated in Figure 5.4, which shows the effective refractive index elevation of the mode, normalised to the peak refractive index of the graded index. Higher order modes appear at increasing diffusion depth, as expected.

5.2.4 Summary of diffused slab waveguide characteristics

The characteristics of slab waveguides formed in a diffused graded refractive index region have been briefly discussed. Assuming the change in refractive index is proportional to the diffused concentration of impurity, trends in the modal effective refractive index for ideal diffused profiles have been presented using the WKB method. In each case, waveguides are not supported until the diffusion depth has exceeded a critical value. With increasing diffusion depth, the effective refractive index of the mode tends towards the peak refractive index at the surface. The number of modes supported by the diffused region increases with effective diffusion depth.

5.3 Experimental waveguide characterisation techniques

The diffusion of Ti into sapphire has been discussed in chapter 4, for a broad range of conditions that lead to the incorporation of Ti^{3+} to depths of tens of microns, with a range of

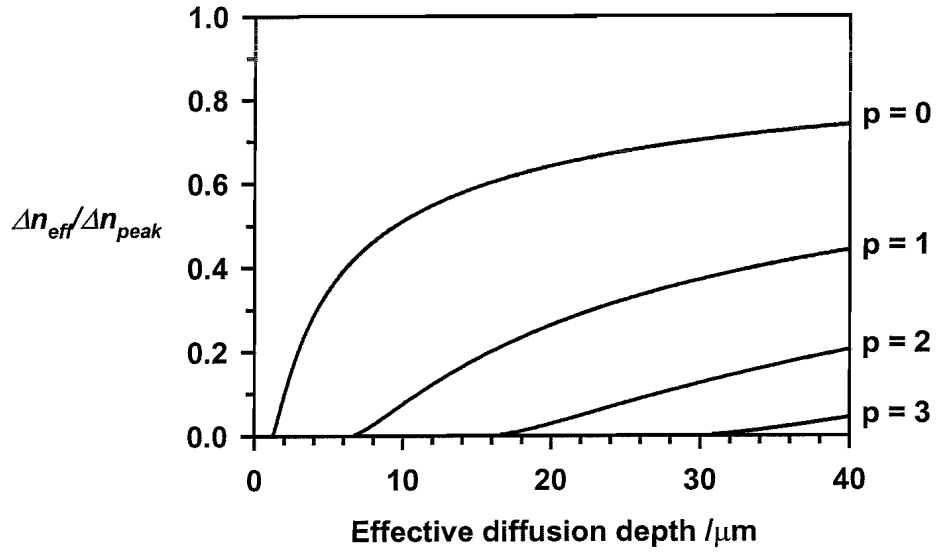

Figure 5.4:- Effective refractive index of waveguide mode normalised to the change in peak refractive index of graded index structure as a function of effective diffusion depth.

$$\frac{\partial^2}{\partial x^2}E(x) + k_x(x)^2 E(x) = 0 \qquad \textit{Eqn. 5-2}$$

In terms of refractive index, k_x is given by *Eqn. 5-3.*

$$k_x(x) = k_o\sqrt{n(x)^2 - n_{eff}{}^2} \qquad \textit{Eqn. 5-3}$$

The effective refractive index of the mode may be found by determining the depths X_a and X_b where the ray turns through the parallel to the surface. At these depths, $k_x = 0$ so that $|\boldsymbol{k}(x)| = k_z$ and hence $n(X_a) = n(X_b) = n_{eff}$. The WKB method may be used to estimate the depths X_a and X_b and so find n_{eff} for a given refractive index distribution.

5.2.1 Trends in n_{eff} for diffused slab waveguides by the WKB method

Following the WKB method, the effective refractive index of a guided mode supported by a known refractive index distribution may be estimated[2,3]. Whilst this method does not lead to exact solutions for n_{eff}, it is attractive because solutions may be readily found using current computational software, allowing the expected trends in waveguide properties for a diffused graded index medium to be evaluated.

The geometry described in Figure 5.1 is maintained for the following calculations. For a graded index region formed by diffusion, the peak refractive index change will occur at the surface so that $X_a=0$, and the problem reduces to locating the lower turning point, X_b, since $n(X_b) = n_{eff}$. The depth X_b may be found by considering that the total phase shift in a complete period of the ray model must be an integer multiple of 2π. This relation is given in *Eqn. 5-4*, where $2\Phi_a$ and $2\Phi_b$ represent the phase shift at the boundaries presented by the turning points X_a and X_b and p is an integer, defining the order of the mode.

$$2\int_0^{X_b} k_x(x)dx + 2\Phi_a + 2\Phi_b = 2p\pi \qquad \textit{Eqn. 5-4}$$

To maintain simplicity, the values of $2\Phi_a$ and $2\Phi_b$ may be approximated to $-\pi$ and $-\pi/2$, respectively following reference 3. This assumption removes the distinction between TE and TM modes, but will still allow trends in the effective refractive index to be observed as a function of diffused index profiles.

Substituting for $k_x(x)$, $2\Phi_a$ and $2\Phi_b$, the depth of the turning point, X_b, may be found by solving for the roots of *Eqn. 5-5*, where $n(X_b) = n_{eff}$.

$$\int_0^{Xb} k_o \sqrt{n(x)^2 - n(X_b)^2}\, dx - \left(p + \frac{3}{2}\right)\pi = 0 \qquad \textit{Eqn. 5-5}$$

Assuming the refractive index change for a Ti-diffused waveguide in sapphire is proportional to the concentration of Ti, trends in the n_{eff} will be related to trends in the diffusion profile. In the following sections, the solutions to the diffusion equation presented in §3.3 are used to identify the trends in n_{eff} expected for a slab waveguide formed by diffusion.

5.2.2 Waveguide formed from an infinite diffusion source

For an infinite diffusion source, the diffused refractive index profile, *n(x),* will be given by *Eqn. 5-6*, where Δn_{peak} is the peak refractive index change at the surface due to the Ti doping, n_{sap} is the substrate refractive index, D is the diffusion rate, and t is the diffusion time; $2\sqrt{Dt}$ defines the effective diffusion depth. This relation assumes the refractive index change is proportional to the concentration of Ti.

$$n(x) = \Delta n_{peak}\, erfc\left(\frac{x}{2\sqrt{Dt}}\right) + n_{sap} \qquad \textit{Eqn. 5-6}$$

For Δn_{peak} of 0.001 and n_{sap} of 1.8, the effective refractive indices of modes supported at a wavelength of 633nm calculated for diffusion depths up to 40μm are shown in Figure 5.2.

For diffusion depths less than about 3μm, the graded index does not support a guided mode at this wavelength. With increasing diffusion depth, the effective refractive index of the p=0

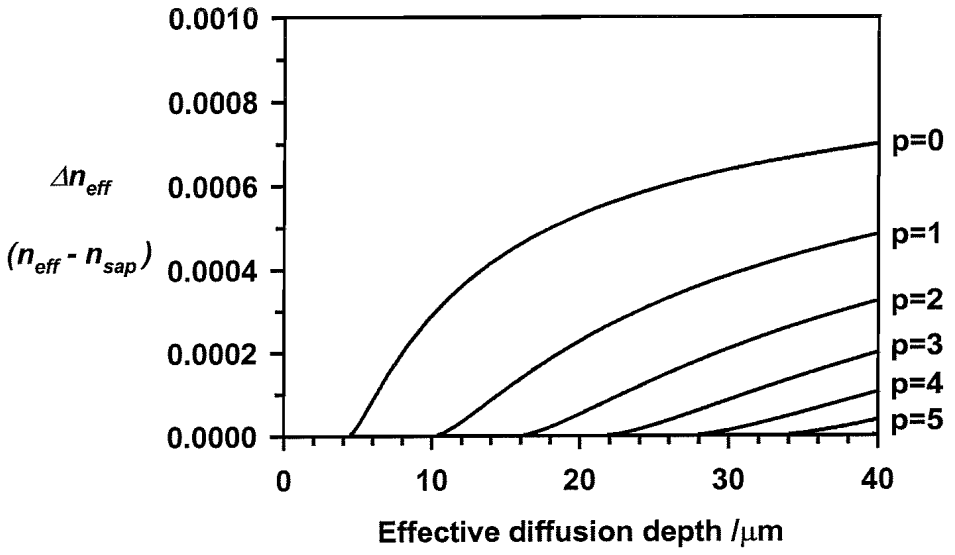

Figure 5.2:- Effective refractive indices for waveguide modes supported by the diffused structure, assuming a peak refractive index of 0.001

concentrations. The diffused regions of many samples were investigated for optical waveguides, leading to the demonstration of both slab and channel waveguides in sapphire for the first time.

The experimental techniques used to characterise the waveguides are outlined in this section. The methods allowed the evaluation of Δn_{eff}, the difference between the effective refractive index of a waveguide mode and that of the substrate, waveguide intensity profiles and spectral attenuation characteristics.

5.3.1 Determination of difference between modal effective index and substrate index

Excitation of waveguide modes by phase matched prism coupling is a well-established technique and enables the determination of the modal effective refractive index[2-5]. However, for early waveguides fabricated by thermal diffusion, the effective refractive index of the modes was close to the substrate refractive index, and experimental errors often led to the evaluation of modal indices less than that of the sapphire host. This is not possible for a guided mode, and so a method was developed which measures the difference between the waveguide effective refractive index and the substrate refractive index to be measured, Δn_{eff}.

5.3.1.1 Experimental method

The experimental configuration is shown schematically in Figure 5.5. Radiation from a He-Ne laser is incident on the oblique face of a rutile prism, having passed through a series of apertures and polarisation controlling components. The rutile prism is clamped to the

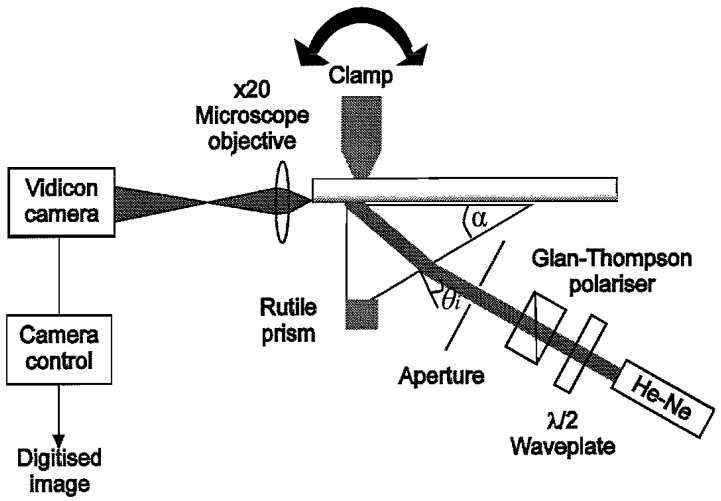

Figure 5.5:- Experimental configuration for excitation of waveguide by prism coupling and determination of Δn_{eff}.

titanium diffused surface of a sapphire sample, separated by a thin film of index matching fluid ($n = 1.72 < n_{sap}$). Precision positioning components ensured the point of closest contact between the prism and sample was coincident with the axis of a motorised rotation stage and the incident radiation. The rotation stage could be adjusted in small increments to enable coupling of radiation into the waveguide and with further movement, refraction of radiation into the sapphire substrate. The spatial distribution of radiation emerging from the polished endface of the sample was imaged on to a vidicon camera (Hamamatsu C1000-02) which was interfaced with software for image scanning and data collection.

The effective refractive index of the waveguide mode was calculated from the incident angle at which the peak power was coupled into the waveguide mode. The substrate refractive index was evaluated under the same experimental constraints by considering the progression of the refracted radiation through the substrate once the conditions for phase-matched waveguide excitation were surpassed.

5.3.1.2 Evaluation of waveguide effective refractive index

Excitation of the waveguide occurs when the evanescent field extending beneath the rutile prism at the point of a total internal reflection, overlaps the waveguide region and its propagation constant matches that of a mode supported by the waveguide. For an incident plane wave the phase- matched condition would be satisfied by a discrete angle of incidence. However, radiation from the He-Ne laser has a characteristic Gaussian wavefront and power may be coupled into the waveguide over a range of angles, limited by the divergence of the incident radiation. This is illustrated in Figure 5.6, for coupling into a TE_0 waveguide mode supported in the diffused region of S128. The effective refractive index is calculated from the incident launch angle using *Eqn. 5-8*, which relates the external angle of incidence to the phase matching conditions, assuming Snell's law of refraction at the prism boundary. n_p is the refractive index of the prism, θ_i is the external angle of incidence, α the base angle of the prism, as marked in Figure 5.5. The modal effective refractive index is taken as the point of peak coupled power and may be identified to within $5 \cdot 10^{-5}$.

$$n_{eff} = n_p \cdot \sin\left[\arcsin\left(\frac{\sin\theta_i}{n_p}\right) + \alpha\right] \qquad \textit{Eqn. 5-8}$$

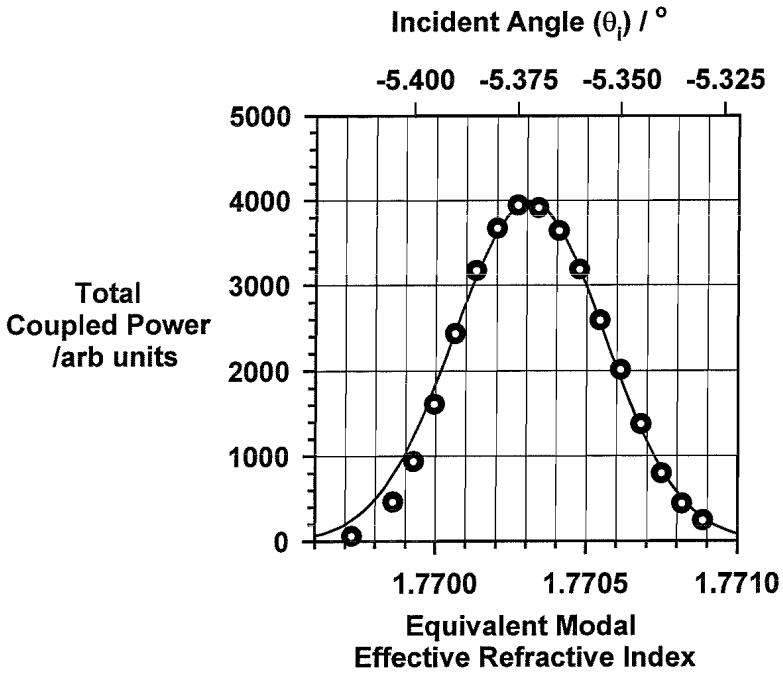

Figure 5.6:- Power coupled into waveguide as a function of incident angle and equivalent effective index. The data was obtained during investigation of the diffused region of S128.

For a double or multiple moded waveguide, the resolution of each mode will be limited by the divergence of the illuminating radiation. Under the experimental conditions used, the coupled power is typically close to a Gaussian distribution with a full width at half maximum of $6 \cdot 10^{-4}$ in the effective index domain. Modes separated by less than this are hard to resolve independently and the uncertainty in the location of the peak coupled power increases to about $1 \cdot 10^{-4}$.

5.3.1.3 Evaluation of substrate refractive index

Once conditions for total internal reflection at the base of the prism are surpassed, radiation is refracted through the gap between the prism and sample, through the waveguide region and into the sapphire substrate. The rate of movement of the radiation through the depth, d, of the substrate (at the polished endface) as a function of incident angle will depend on the refractive index of the substrate, following *Eqn. 5-9*.

$$n_{sap} = \frac{\sqrt{d^2 + l^2}}{l^2} \cdot n_p \cdot \sin\left[\arcsin\left(\frac{\sin\theta_i}{n_p} \right) + \alpha \right] \qquad \textit{Eqn. 5-9}$$

The substrate refractive index may be determined from a series of measurements, as shown in Figure 5.7. The experimental data is modeled using *Eqn. 5-9*, to solve for n_{sap} and l, the distance between the coupling spot and the polished end face. Good agreement is seen

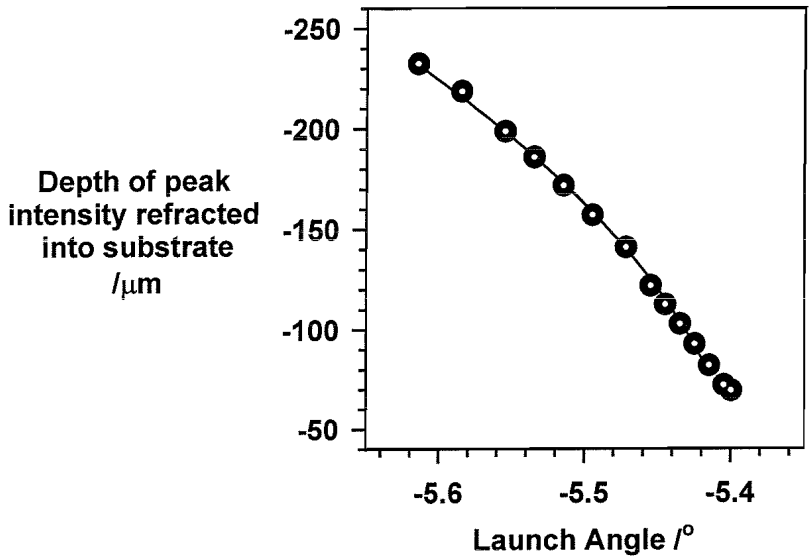

Figure 5.7:- Example of refraction of light into the substrate as a function of incident angle. The data illustrated was obtained during the investigation of TE_0 modes in S128.

between the experimental and theoretical curve considering depths greater than about 70μm. At lesser depths, only a fraction of the incident beam is refracted into the substrate (a proportion related to the divergence of the incident beam). By this technique, the refractive index of the sapphire may be obtained under comparable experimental constraints to those under which the effective refractive index of the waveguide mode was obtained, with an uncertainty of about $1 \cdot 10^{-4}$.

5.3.1.4 Summary

In summary, an experimental technique has been outlined that enables the difference between the effective refractive index of a waveguide mode and the substrate refractive index to be measured under similar experimental conditions. This allows small differences in Δn_{eff} to be measured.

5.3.2 Characterisation of waveguide mode profiles

Evaluating mode intensity profiles at one or more wavelengths yields significant information on the character of the waveguide. At a single wavelength, a spatial mode profile may be interpreted in terms of refractive index profile if the modal effective refractive index is known. At a range of wavelengths, a decrease in confinement may be observed as the waveguide approaches cut-off. For a waveguide laser, tightly confined waveguide modes, with a good overlap will lead to lower pump power thresholds.

5.3.2.1 Experimental method for characterising waveguide mode profiles

The experimental configuration is similar to that shown in Figure 5.5, with waveguides typically excited by phase-matched prism coupling. The modal intensity distribution emerging from the excited waveguide is imaged onto the vidicon camera, which is later calibrated for the magnification used. For slab waveguides, the mode intensity profile is recorded in the depth direction using a line scan function. For channel waveguides, an area function enabled characterisation of the waveguide in both breadth and depth. In each case, the image plane and surface location was obtained by prior illumination of the waveguide end face with a white light source. Waveguides were characterised at wavelengths of 633nm, 488nm and 750-800nm using He-Ne, argon-ion and Ti:sapphire lasers respectively as radiation sources.

An example of an intensity mode profile obtained for a 7μm channel waveguide on S165 at λ=488nm is shown in Figure 5.8. The uncertainty in the location of the sample surface is ±2μm, and the origin of the scale in the breadth direction has been centered with respect to the symmetry of the mode. In this work, the mode size is defined as the full width at 1/e of the peak intensity. For the waveguide mode illustrated, the mode depth and breadth would be approximately 6μm and 13μm respectively.

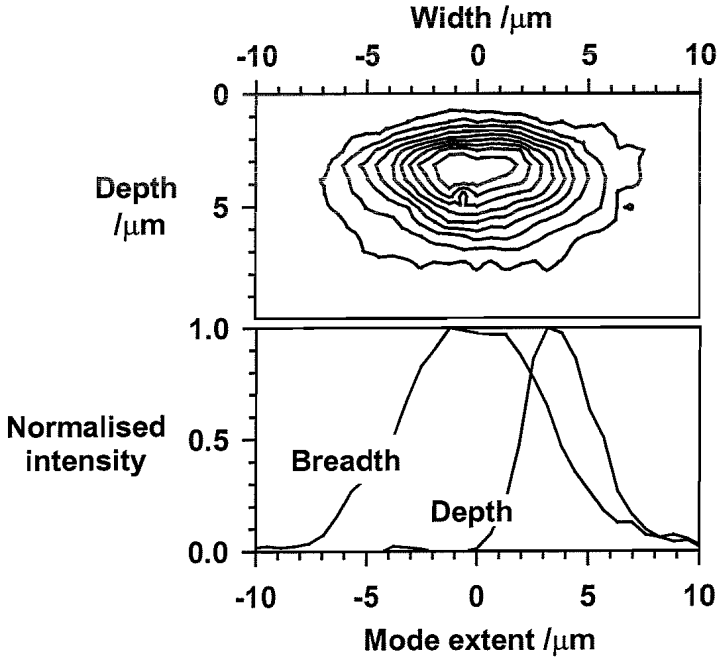

Figure 5.8:- (a) Example of contour plot showing mode intensity profile for a channel waveguide. (b) Sections through the contour plot to show the intensity profile in the depth and width dimensions. The data shown is for the 7μm channel waveguide on S165 at λ=488nm.

5.3.3 Spectral attenuation in waveguides

Spectral changes in waveguide throughput allows a detailed assessment of the waveguide confinement and material characteristics over the wavelength range of interest. For example, the waveguide cut-off would be marked by a rapid increase in loss, as the light is scattered into substrate radiation modes. For the Ti-diffused waveguides, a broad absorption in the blue-green would be characteristic of the Ti^{3+} ion and an absorption in the near infra-red, characteristic of Ti^{3+}-Ti^{4+} pairs. Away from known absorption wavelengths, an estimate of the combined waveguide propagation and waveguide insertion loss may be obtained.

A schematic of the experiment configuration is shown in Figure 5.9. To achieve optimum waveguide coupling efficiency and alignment of the optical components, radiation from a He-Ne laser is launched into a fibre and aligned with the waveguide under investigation. The waveguide output is collected with a x10 microscope objective and focussed at the entrance slit of a monochromator. Prior to the monochromator, the radiation passes through a Glan-Thompson polariser, to enable independent evaluation of TE and TM modal properties. During the alignment phase, the monochromator is set to transmit at 633nm and a silicon detector is aligned immediately behind the exit slit.

To carry out the spectral attenuation measurement, the He-Ne radiation source is replaced with a high power, 1000W tungsten lamp. The fibre delivery system facilitates this change and ensures neither the optical alignment nor waveguide coupling is disturbed. The broad

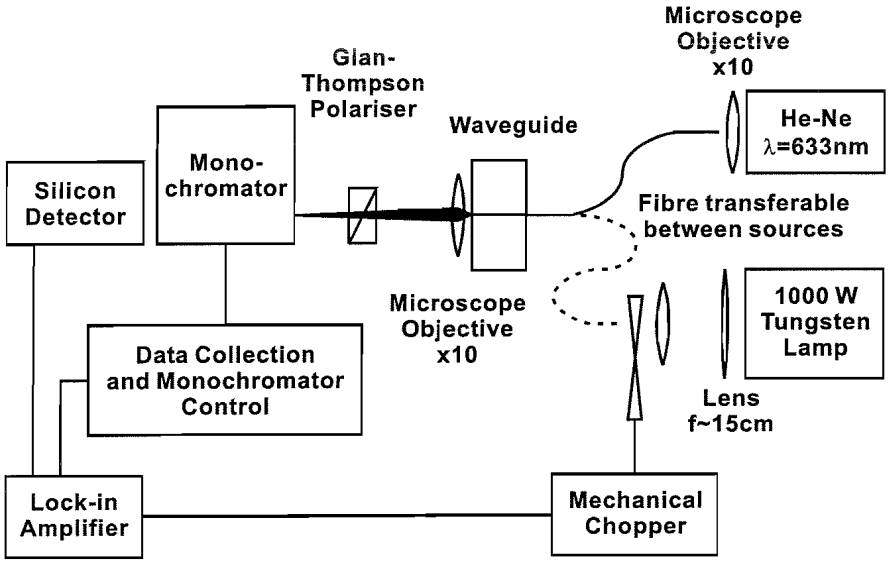

Figure 5.9:- Experimental configuration used for measuring the spectral attenuation in a waveguide.

band radiation from the white light source is focussed into the fibre, having passed through a mechanical chopper. The chopper enables good signal-to-noise ratio to be achieved using lock-in amplification of the signal from the silicon detector. Both the monochromator grating movement and the data collection are controlled remotely using PC software.

Using the configuration described, spectral measurements may be obtained over the wavelength range 450nm to 1050nm. The upper limit is defined by the spectral response of the silicon detector and the lower limit by a combination of reduced output from the tungsten lamp and reduced sensitivity of the detector. Within this wavelength range, two gratings are available for use in the monochromator. One is blazed at 600 lines/mm and is more efficient for wavelengths less than about 650nm compared to the second that is blazed at 1000 lines/mm. For each configuration and each polarisation, the data is corrected for the system response by comparison with the spectrum obtained without the waveguide in place.

An example of the spectral attenuation characteristics measured by this experimental technique is presented in Figure 5.10. The data shown was obtained in the TM polarisation for a channel waveguide diffused from a 7μm stripe on sample S167. The break in the data at around 650nm is due to the change in grating and the small offset in the attenuation is characteristic of the error in the measurement. The data also illustrates some of the waveguide features that may be identified in such a measurement. For example, the increase

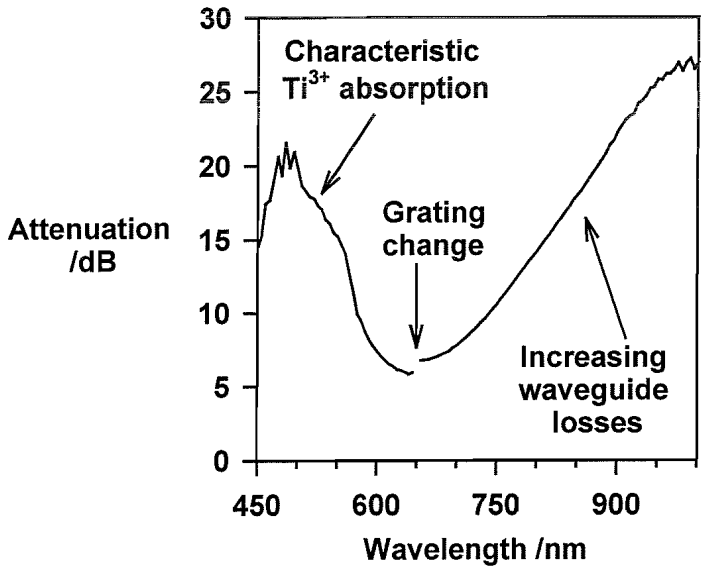

Figure 5.10:- Example of spectral attenuation measured for a Ti-diffused channel waveguide over the wavelength range 450-1000nm. The data illustrated was obtained for a 7μm channel waveguide in S167 in the TM polarisation.

in attenuation in the blue-green is characteristic of an absorption of the Ti^{3+} ion, and the rising losses in the near infra-red show the waveguide tending towards cut off. The minimum waveguide insertion and propagation loss is about 6dB, assuming there is no material absorption over the wavelength range 600-650nm.

In summary, a technique for measuring the waveguide transmission over the wavelength range 450 to 1000nm has been described. The results are corrected for system response and enable features such as absorption and waveguide cut off to be observed.

5.3.4 Summary of experimental methods for waveguide characterisation

A series of experimental techniques have been outlined which allow the characterisation of waveguides using readily available optical components and laboratory equipment. Using prism excitation of the waveguides, the effective refractive index of the mode may be obtained relative to the refractive index of the substrate. Mode intensity profiles are forthcoming by imaging the waveguide output onto a camera interfaced with image scanning and recording software. Spectral attenuation of waveguides allows characterisation of material absorption and waveguide losses over wavelengths in the visible and near infra-red regions.

5.4 Ti-diffused slab waveguides in sapphire

The formation of slab waveguides in the Ti-diffused region of a sapphire substrate has been investigated. The number of waveguide modes, the modal intensity profile and the relative elevation of the modal effective refractive index, Δn_{eff} were investigated for the following series of samples;

- Diffused at 1950°C from a 27nm continuous thin film source
- Diffused at 1950°C from a 41nm continuous thin film source
- Diffused at 1750°C from a 27nm continuous thin film source

The characteristics of the diffused Ti and Ti^{3+} concentrations were discussed for the same samples in chapter 4.

These results comprise the first realisation of waveguides in sapphire by thermal diffusion of an impurity, to the best of my knowledge

5.4.1 Slab waveguides formed by diffusion at 1950°C from a 27nm source

At a wavelength of 633nm, TE_0 and TM_0 waveguide modes were excited by prism coupling in a series of Ti-diffused sapphire samples. The samples, S128, S125 and S124 were fabricated by diffusion at 1950°C from a 27nm continuous thin film source over times of 0·2, 1 and 3.5 hrs respectively. An additional sample S53, diffused for a longer period of 8 hours, was also investigated, but no waveguide confinement was observed.

Figure 5.11 shows the measured difference in modal effective refractive index between the waveguide mode and substrate refractive index (Δn_{eff}), obtained using the prism coupling technique described earlier. The greatest effective refractive index difference at 2.4×10^{-4} is observed for the shortest diffusion time of 0.2 hrs and with increasing diffusion time, the effective refractive index decreases. After an 8 hour diffusion, a waveguide mode may not be excited in the diffused region by prism coupling. Whilst the errors bars are significant in magnitude, the effective refractive index of the TM mode is consistently less than that of the corresponding TE mode. This trend would be expected if the diffusion of Ti causes no additional birefringence in the refractive index.

The trend of decreasing effective refractive index with diffusion time is consistent with the model described in §5.2.3 for waveguides formed by diffusion from an instantaneously depleted diffusion source. Under these conditions, the peak refractive index decreases as the diffusion depth increases.

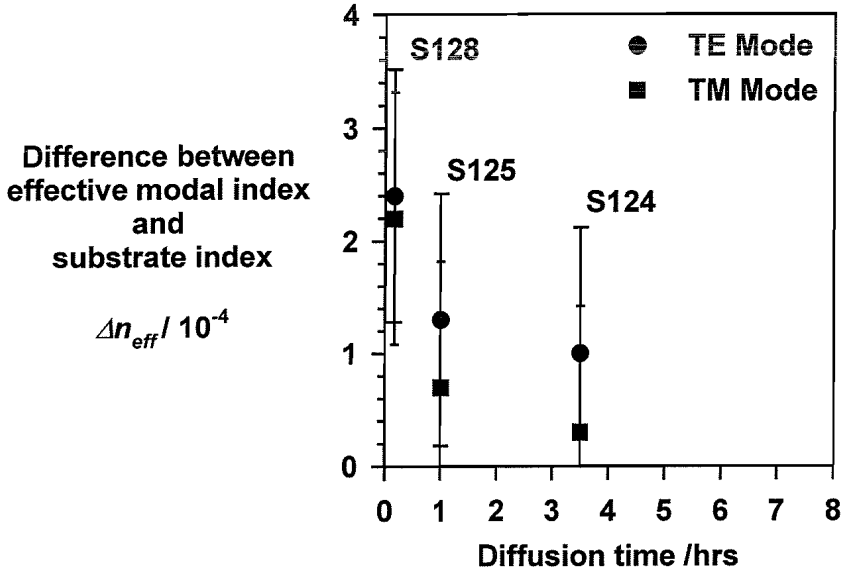

Figure 5.11:- Elevation of effective refractive indices of waveguide modes above the substrate index, following diffusion at 1950 °C with a 27nm thick diffusion source.

S128 {Slow heat, slow cool, 27nm, 0.2hr, 1950°C} S125 {Slow heat, slow cool, 27nm, 1hr, 1950°C}
S124 {Slow heat, slow cool, 27nm, 3.7hrs, 1950°C} S53 {Slow heat, slow cool, 25nm, 8hrs, 1950°C}

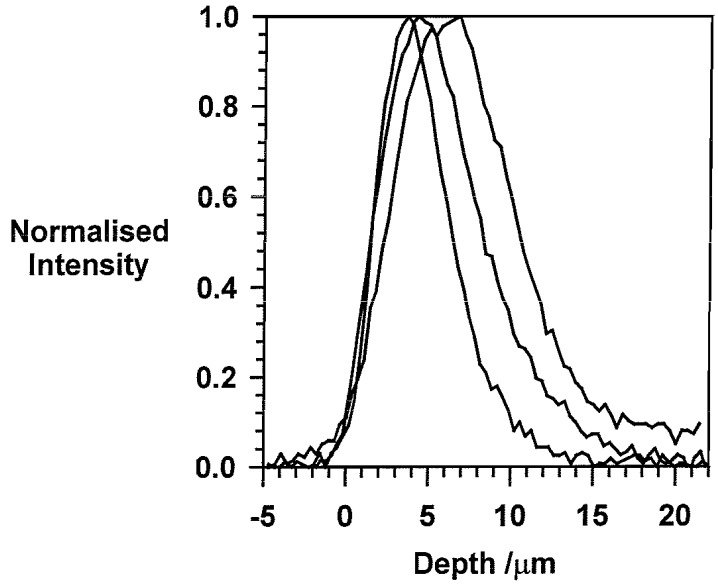

Figure 5.12:- Intensity profiles recorded for waveguide modes supported following diffusion from a 27nm thick source at 1950°C for times between 0.2-3.7 hrs.

The modal intensity distribution in the depth direction for each of the TE_0 modes in S128, S125 and S124 are illustrated in Figure 5.12. With increasing diffusion time, the modal width, defined as the full width at 1/e of the peak intensity, increases from about 9 to 14μm.

In summary, single mode slab waveguides are formed at a wavelength of 633nm following diffusion at 1950°C for times of 0.2, 1 and 3.7 hours from a 27nm source. With increasing diffusion time, the effective refractive indices of the waveguide modes decrease and the mode size increases. The effective refractive index of the TM mode appears consistently less than that of the TE mode.

5.4.2 Characteristics of slab waveguides diffused from a 41nm source at 1950°C

Multi-mode slab waveguides were excited in the Ti-diffused region of samples S134 and S130, fabricated by diffusion from a 41nm source at a temperature of 1950°C for times of 1 and 2 hours respectively. Samples S131 and S133, diffused for longer periods of 3.7 and 8 hours were also investigated for waveguide properties. For S133, there was no evidence of a waveguide at 633nm, and for S131, the observations were inconclusive, with weak, multi-mode guidance observed on a single occasion.

Figure 5.13 shows the elevation of the effective refractive indices for waveguide modes supported in S134 and S130. The individual waveguide modes were distinct for the shorter diffusion time, of 1 hour. Following a 2 hour diffusion, the effective refractive indices of

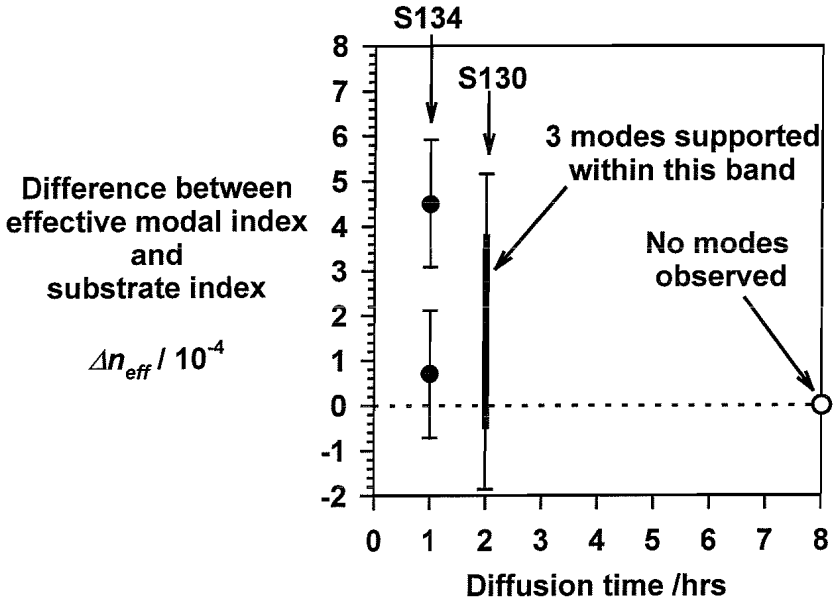

Figure 5.13:- Elevation of effective refractive indices of waveguide modes above the substrate index, following diffusion at 1950°C from a 41nm thick diffusion source

three supported modes are within $4 \cdot 10^{-4}$ of the substrate refractive index. The effective indices of the individual modes could not be distinguished by this technique and the presence of three modes was inferred from the waveguide intensity profiles observed for S130, and shown in Figure 5.14.

Figure 5.14 shows an example of the TM_0 mode and the linear combination of higher order modes observed for waveguides supported by the diffused region of S130, excited by prism coupling. The intensity profiles extend to depths greater than 20μm beneath the surface of

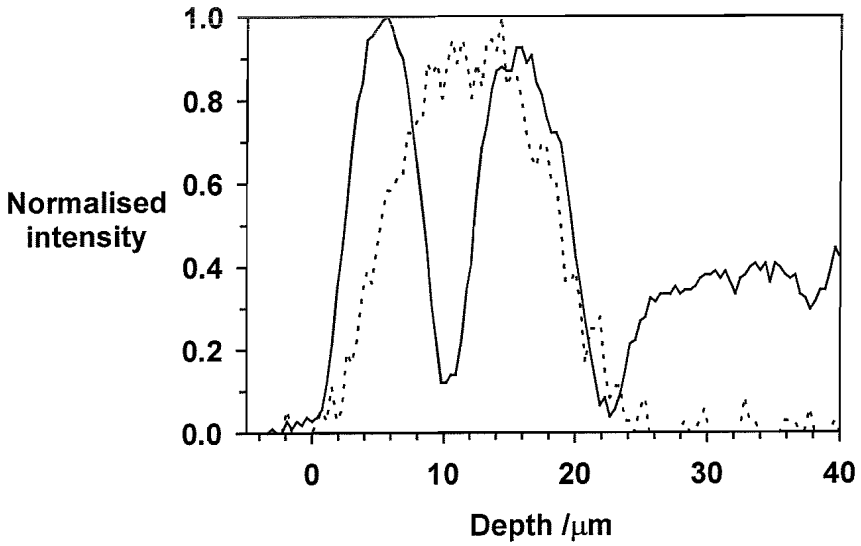

Figure 5.14:- Normalised mode intensity distributions in the TM_0 and TM_1 modes supported by S130.

the substrate. The form of the TM_0 mode is as expected with the radiation confined to a central region in the waveguide with the radiation decaying into the superstrate and the substrate. With continued rotation of the prism coupling apparatus, the mode profile develops minima at approximately 10 and 20μm depths. The occurrence of the minima is consistent with the intensity profile resulting from the linear combination of TM_0, TM_1 and TM_2 modes.

In summary, the diffused regions of S134 and S130 are able to support multi-mode waveguides at λ=633nm. The effective refractive indices of the modes are within $5 \cdot 10^{-4}$ of the substrate refractive index. The modes supported by S134 could be independently characterised, whereas the modes supported by S130 could not be separated by the prism coupling technique. The presence of three modes in the waveguide supported in S130 was inferred from the intensity profiles obtained.

5.4.3 Characteristics of slab waveguides diffused from a 27nm source at 1750°C

Single and dual order slab waveguides were excited at a wavelength of 633nm in the Ti-diffused region of the series of samples S153, S154, S155. The samples were fabricated by diffusion from a 27nm continuous thin film diffusion source at a temperature of 1750±30°C for times of 1,2 and 3.5 hours respectively. For sample S156, diffused for a longer period of 8 hours, there was no evidence of a waveguide in the diffused region. The distribution of diffused Ti^{3+} has been discussed for these samples in chapter 4.

Figure 5.15 shows the elevation of the effective refractive indices measured for the waveguides excited in the Ti-diffused regions of S153, S154 and S155 in the TM polarisation. For the shortest diffusion time, the waveguide supports a single mode. For the longer diffusion times of 2 and 3.5 hrs, a second waveguide mode is supported. After 8 hours, no waveguide is observed by prism coupling, indicated by a zero value of Δn_{eff}. The measured values of Δn_{eff} indicate that the effective index of the fundamental mode is decreasing with diffusion time, and that the index of the first order mode approaches that of the fundamental mode. This trend is consistent with that described in §5.2 for waveguides formed by diffusion from a source that is rapidly depleted.

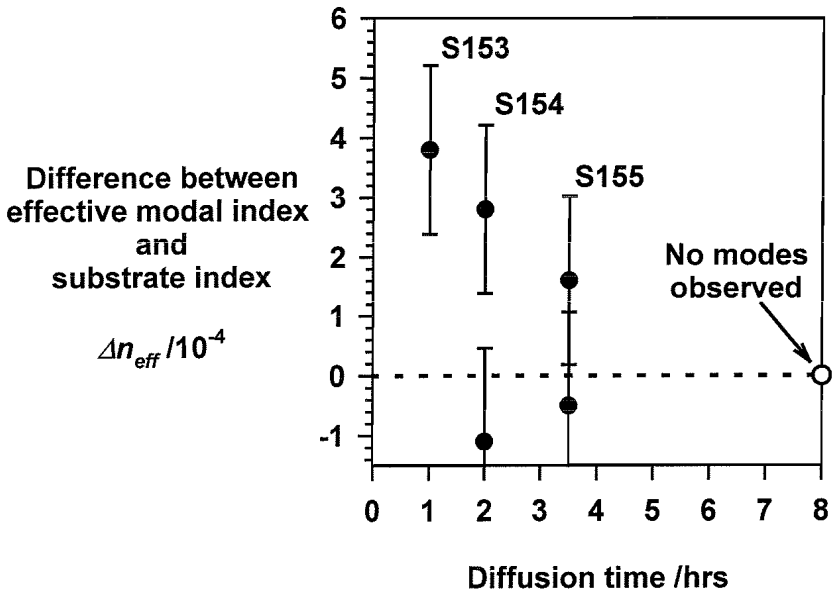

Figure 5.15:- Elevation of effective refractive index of waveguide modes above the substrate index following diffusion at 1750 ℃ with a 27nm thick diffusion source.

For S154 and S155, the measured effective refractive index of the first order modes appears to be less than that of the substrate refractive index. The error in the measurement has been previously discussed and the uncertainty does overlap the region of positive effective refractive index. The error bars indicate that the Δn_{eff} for the first order modes of S154 and S155 are less than $4 \cdot 10^{-5}$ and $1.1 \cdot 10^{-4}$ respectively.

The intensity mode profiles obtained for conditions of maximum coupled power into the waveguide are illustrated in Figure 5.16. The single mode character of S153 is clear. The

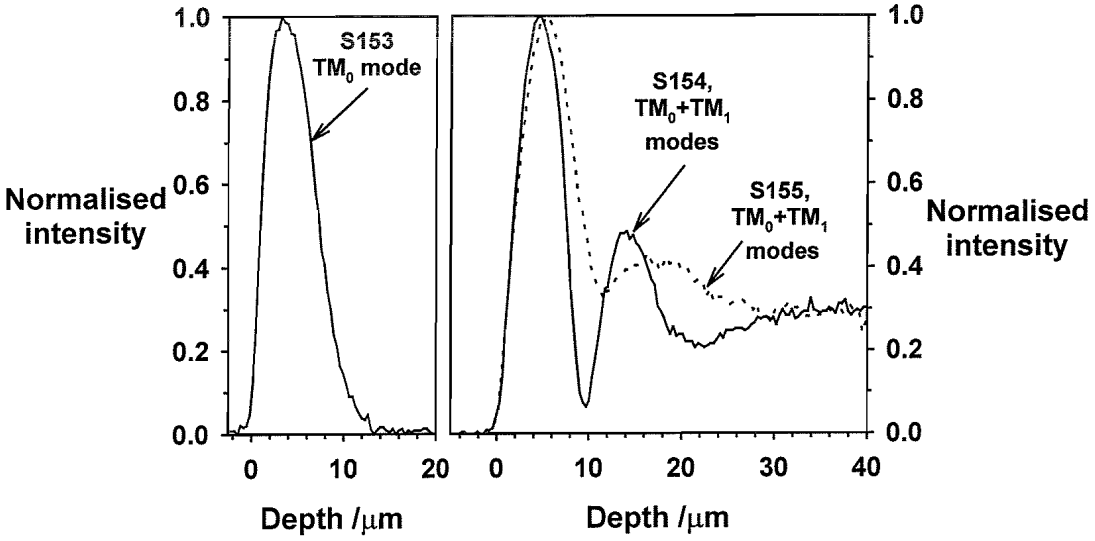

Figure 5.16:- Intensity profiles observed for waveguides supported following diffusion at 1750 ℃ for 1-3.5 hrs from a 27nm thick source.

intensity decays rapidly at the step index change at the substrate surface and decays more slowly in the diffused graded index region. The image will be affected by the limited resolution of the imaging system, which will be similar to that discussed in §4.3.2 for the fluorescence imaging technique.

For the dual order waveguides supported in S154 and S155, a linear combination of the TM_0 and TM_1 modes is observed, when the maximum power is coupled into the waveguide. The intensity distributions extend to depths greater than 15μm, with minima at depths of about 10 and 12μm respectively. The fields are not observed to decrease to zero at extended depths as a proportion of the incident radiation (due to divergence) is refracted into the substrate.

In summary, single and dual slab waveguides are observed in the TM polarisation following diffusion from a 27nm source at temperature of 1750°C, for times between 1 and 3.5 hours. A single mode waveguide was formed after a 1 hour diffusion, dual mode waveguides were observed for 2 and 3.5 hour diffusions, whilst no waveguide mode was supported following an 8 hour diffusion. The effective refractive index of the zeroth order mode decreases with diffusion time, whilst that of the first order mode increases.

5.4.4 Summary of slab waveguide characteristics

Slab waveguides have been realised in Ti-diffused regions of a sapphire substrate, at a wavelength of 633nm. Single mode waveguides were formed following diffusion from a 27nm source for times of 0.2, 1 and 3.7hrs at a temperature of 1950°C, and for 1 hour at 1750°C. Multi-mode waveguides were supported by regions diffused from a 27nm source for times of 2 and 3.5 hours at 1750°C and regions diffused from a 41nm source for times of 1 and 2 hours at 1950°C. Waveguides were not observed following diffusion for times of 8 hours at 1750°C or 1950°C, with either a 27nm or 41nm source.

These results indicate that waveguides may be formed in a Ti-diffused sapphire substrate at a wavelength of 633nm and that properties of the waveguide vary with diffusion conditions. For the design of further waveguide devices, the refractive index change due to the Ti-doping needs to be evaluated, in addition to developing a complete model of the transport process.

5.5 Refractive index change due to Ti-doping

An estimate of the refractive index change due to Ti-doping of sapphire may be obtained by comparing the measured waveguide characteristics to the known Ti concentration. Two approaches to this are considered in this section.

The first approach considers the waveguide properties measured for S128, S125 and S124. For these samples, the waveguide modal effective refractive indices and intensity distributions have been measured. These properties are related to the refractive index profile following *Eqn. 5-2* and *Eqn. 5-3* presented earlier in the chapter. The peak refractive index may be compared to the total-Ti concentration measured by SIMS within 2μm of the surface (see §4.5.4).

The second approach to estimating the relation between refractive index change and Ti concentration uses the data gathered for S130. As discussed in chapter 4, a series of SIMS measurements were carried out on a bevel polished through the diffused region, to characterise the total Ti distribution as a function of depth. Assuming the refractive index change is proportional to the measured Ti distribution, a model describing the waveguide characteristics may be established. Comparing the modeled waveguide characteristics to the measured characteristics allows the refractive index change with Ti concentration to be estimated.

For the samples discussed, it is known that both fluorescent and non-fluorescent phases of Ti have been incorporated into the sapphire during the diffusion process. These calculations assume that the diffused Ti concentration contributes equally to the refractive index change. Therefore, these estimates should be treated with caution, until further experimental data becomes available.

5.5.1 Reconstruction of the diffused refractive index profile

The refractive index profile that supports the series of single mode waveguides formed in samples S128, S125 and S124 may be reconstructed[6] from the intensity mode profiles shown in Figure 5.12 and the effective refractive index data presented in Figure 5.11. These are related by *Eqn. 5-10*, which combines *Eqn.'s 5-2* and *5-3*.

$$\frac{\partial^2 E(x)}{\partial x^2} = k_0{}^2\left[n_{eff}{}^2 - (\Delta n(x) + n_{sap})^2\right]E(x) \qquad \textit{Eqn. 5-10}$$

$E(x)$ is given by the square root of the normalised intensity mode profiles, k_0 is the wave vector for propagation in a vacuum, n_{eff} is the modal effective refractive index, n_{sap} is the substrate refractive index and $\Delta n(x)$ is the change in refractive index due to the Ti as a function of depth.

Prior to the index reconstruction, the raw data recorded for the intensity mode profiles required smoothing to remove high spatial frequencies, which otherwise erroneously dominate the differentiated signal. The smoothing was carried out in the frequency domain of $E(x)$, using a Gaussian function to selectively remove high spatial frequencies. The filter was adjusted to ensure the peak field was maintained at greater than 98% of the measured value; however this procedure has not yet been optimised.

Figure 5.17 shows reconstructed refractive index profiles for samples S128, S125 and S124, using the effective refractive indices and measured intensity mode profiles presented in Figure 5.11 and Figure 5.12 respectively. The periodic fluctuations are an artifact of the filter used to smooth the raw data. The location of the peak refractive index is at a finite distance beneath the surface. This is most likely due to the limited resolution of the imaging system and the Gaussian filtering of the raw data, although it is also possible that the location of a peak beneath the surface is a feature of the transport process.

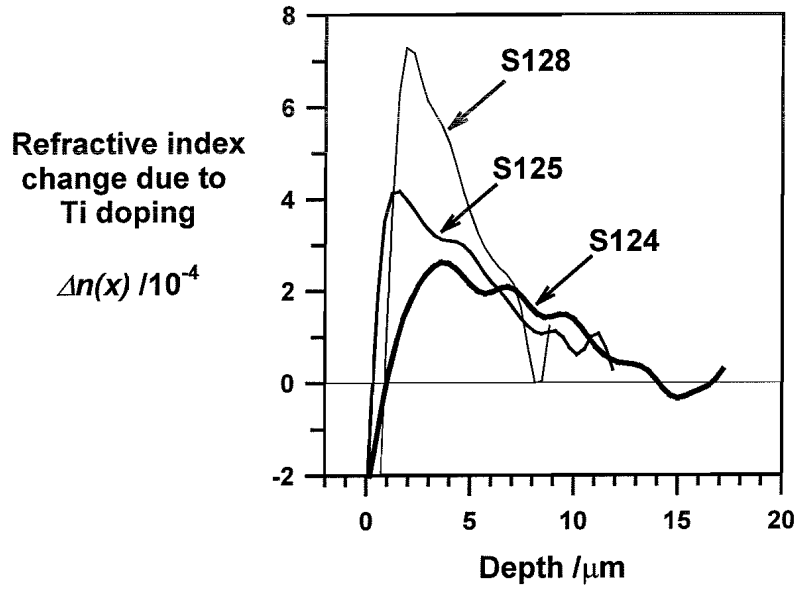

Figure 5.17:- Computed refractive index profiles obtained for the series of single mode waveguides S128, S125, and S124

The depth of the refractive index profiles, defined as 1/e of the peak index are approximately 5, 7 and 9μm for S128, S125 and S124 respectively. The increasing depth and decreasing peak refractive index change would be consistent with diffusion from a finite diffusion source which is depleted during the anneal time.

By comparison with the surface Ti concentrations measured for S128 and S125, the relationship between Ti content and refractive index change may be estimated. As illustrated in Figure 5.18, peak refractive index changes of approximately $7 \cdot 10^{-4}$ and $4 \cdot 10^{-4}$ are observed for Ti concentrations of, (referring to §4.5.4) 0.35±0.03wt% and 0.16±0.03wt% respectively. This corresponds to a refractive index change of $(2.3 \pm 0.6) \cdot 10^{-3}$ per wt% Ti_2O_3 in Al_2O_3.

In summary, the refractive index profiles have been reconstructed for S128, S125 and S124, based on the mode intensity distributions of the TE_0 modes supported by the graded index region. The peak refractive index was observed to decrease and the depth of the profile increase, for increasing diffusion time. Assuming the refractive index change is directly proportional to the titanium concentration, the increase in index per wt% Ti_2O_3 in Al_2O_3 is $(2.3 \pm 0.6) \cdot 10^{-3}$.

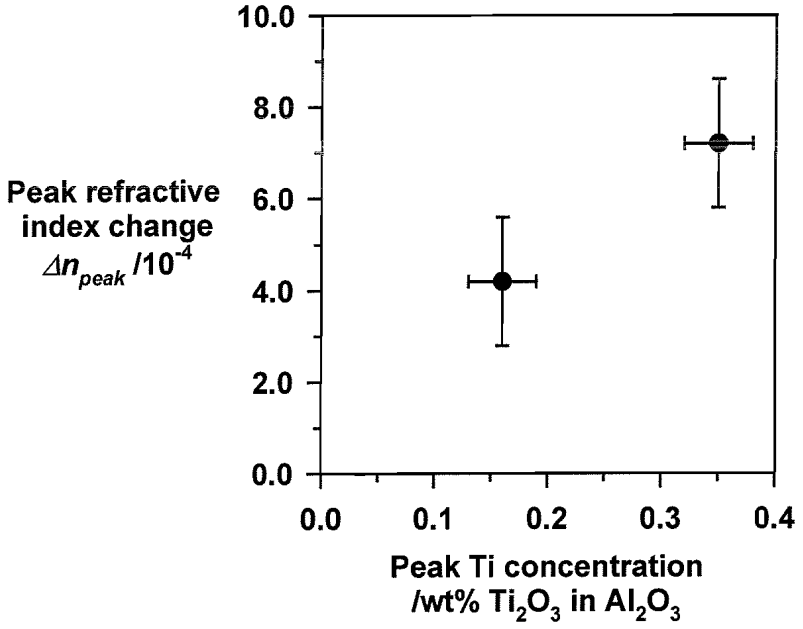

Figure 5.18:- Calculated peak refractive index change as a function of average measured Ti concentration within 2μm of the surface, for S128 and S125

5.5.2 Diffused Ti distribution and waveguide properties of S130

The distribution of total Ti diffused into S130 has been measured by SIMS and discussed in chapter 4. Therefore, assuming the refractive index change is proportional to the Ti concentration, the refractive index of the waveguide region in S130 is given by *Eqn. 5-11*, where Δn_{peak} is the peak refractive index change due to 0.1wt% Ti_2O_3 in Al_2O_3 and n_{sap} is the refractive index of the undoped sapphire substrate.

$$n(x) = \frac{\Delta n_{peak}}{1 + \exp\left[-26 \cdot 10^4 (22 \cdot 10^{-6} - x)\right]} + n_{sap} \qquad \textit{Eqn. 5-11}$$

The effective refractive index of waveguide modes supported by this graded index region may be solved for a range of Δn_{peak}, using the WKB method as before. However, a transfer matrix method[7] was used to determine the effective refractive indices, which was carried out by G R Quigley (ORC Southampton). The method involves the approximation of the graded index structure into a series of step index layers (50 in this case) and solving for the electric field at each of the boundaries. For a peak refractive index, Δn_{peak}, in the range 0-10·10^{-4}, the effective refractive index of each supported waveguide mode was calculated and the results are shown in Figure 5.19.

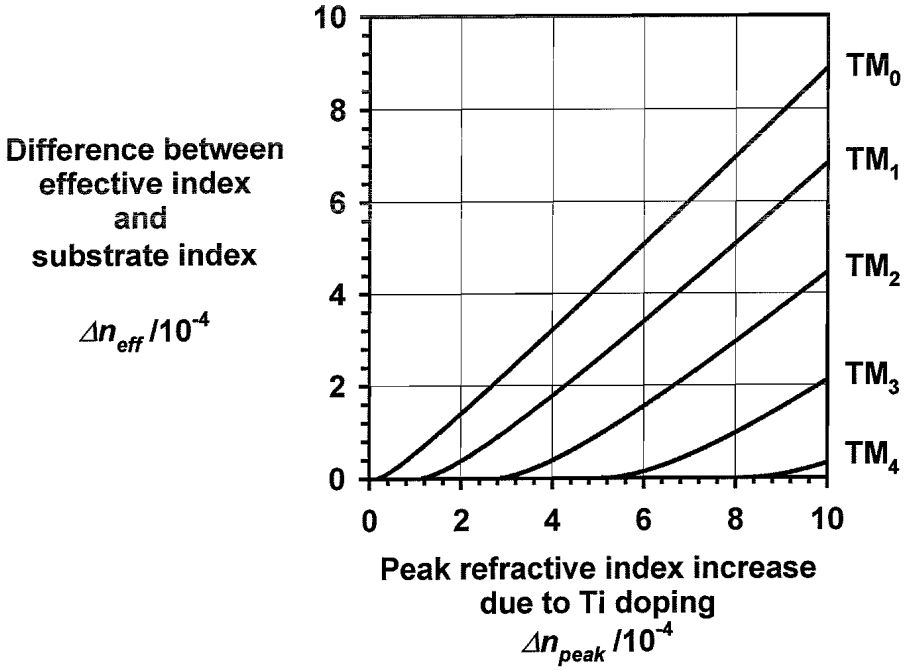

Figure 5.19:- Elevation of the effective refractive index of waveguide modes supported by the graded index region described by Eqn. 5-11 for a range of peak refractive indices, Δn_{peak}.

The results show that as Δn_{peak} increases, the number of waveguide modes that may be supported by the graded index region increases. S130 was observed to support three guided modes, which would correspond to a peak refractive index change between 3 and $5 \cdot 10^{-4}$. The graph also shows that the effective refractive indices of the three modes would be less than $4 \cdot 10^{-4}$. This is in good agreement with the measured effective refractive indices of the modes supported by S130 (see Figure 5.13).

Figure 5.19 indicates that for $\Delta n_{peak} = 4 \cdot 10^{-4}$, the elevation of the modal effective refractive indices would be, $3 \cdot 10^{-4}$, $2 \cdot 10^{-4}$ and $0.4 \cdot 10^{-4}$ for the TM_0, TM_1 and TM_2 modes respectively. The electric field profiles for these modes and the intensity distribution for a linear combination of the fields is illustrated in Figure 5.20. The combined intensity profile compares favorably with the measured profile, which was presented in Figure 5.14.

Therefore, the properties of a waveguide supported by a graded refractive index distribution proportional to the total Ti distribution, with $\Delta n_{peak} = (4 \pm 1) \cdot 10^{-4}$ compare well to those measured for S130. This would lead to an estimate of the refractive index change per wt% Ti_2O_3 in Al_2O_3 of $(4 \pm 1) \cdot 10^{-3}$. This figure is somewhat higher than that of $(2.3 \pm 0.6) \cdot 10^{-3}$ estimated in the previous section. However this discrepancy may be due to the filtering used to smooth the data in the first technique and the limited resolution of the imaging technique.

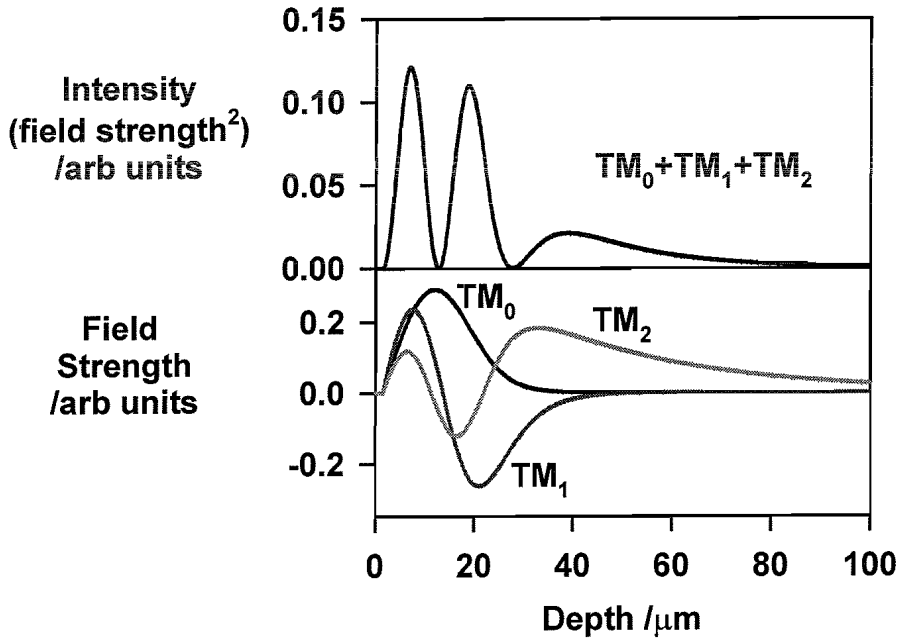

Figure 5.20:- Computed waveguide intensity profiles for TM_0, TM_1 and TM_2 modes and the intensity distribution of the linear combination of modes. The fields were computed for the refractive index profile given in Eqn. 5-11.

5.6 Ti-diffused channel waveguides in sapphire

The potential for forming channel waveguides in samples diffused from a patterned source was investigated. As discussed in chapter 4, the Ti^{3+} distribution in these samples is far from ideal as a fast lateral diffusion occurs from the stripe source. However, the peak Ti^{3+} concentration is higher immediately beneath the stripes compared to between the stripe sources so that a lateral refractive index gradient will occur. Therefore for appropriate fabrication conditions, channel waveguides may be formed.

A series of samples were fabricated in the temperature range 1480°C to 1950°C for times up to 8 hours and with source thickness between 27 and 270nm. The characteristics of the waveguide were qualitatively investigated using prism coupling at a wavelength of 633nm. Those that exhibited some lateral confinement were selected for further characterisation by spectral attenuation measurements and mode intensity profiling at prospective pump and lasing wavelengths.

5.6.1 Qualitative summary of channel waveguide characteristics

In brief, the following trends in the waveguide properties were observed as a function of fabrication conditions. At each temperature investigated (1480°C, 1700°C, 1750°C, 1950°C), channel waveguides with varying degree of lateral confinement could be formed. At the highest temperatures the lateral confinement diminishes rapidly with diffusion time and the waveguide tends towards that of a slab waveguide. This process is accelerated with a lesser diffusion source. In a similar manner to the slab waveguides reported earlier, the waveguides properties are lost if the diffusion time is too great for a given source thickness. At the lowest temperature of 1480°C, well-confined channel waveguides were formed after an 8 hour diffusion, with cut off at wavelengths just beyond 633nm. For shorter diffusion times, the diffusion was insufficiently advanced to support a channel waveguide.

Therefore at each temperature investigated, a limited fabrication window (defined in terms of diffusion time and source thickness), exists for which well confined channel waveguides may be formed. The characteristics of waveguides on S165 and S169 are discussed in greater detail in the following sections. A 3μm channel waveguide on S169 was later selected for the realisation of a channel waveguide laser.

5.6.2 Channel waveguides by diffusion at 1750°C from a 114nm source

The diffused Ti^{3+} distribution of S165, described in chapter 4 is able to support a series of waveguides in the Ti doped regions. This sample was diffused for 1 hour at 1750°C from a 114nm patterned diffusion source. The peak Ti^{3+} concentration beneath the 16μm stripe is just under 0.5wt%, decreasing to about 0.2wt% for the 3μm stripe. Between each stripe Ti^{3+} was observed at concentrations decreasing from 0.3 to 0.1wt%. In all regions, the diffusion depth of Ti^{3+} perpendicular to the surface is less than 10μm. The properties of waveguides supported by this structure were investigated at wavelengths in the visible and near infra-red.

An example of the waveguide modes supported by the structure diffused from the 11μm stripe at a wavelength of 488nm is shown in Figure 5.21. A well-confined TM_{00} mode may be excited by prism coupling, centered in the highest index region. As the incident angle is adjusted, waveguide modes with a lower effective refractive index are excited and the mode is observed to extend further into the titanium-rich region between the original stripe sources. For the broader stripes, where the measured Ti^{3+} concentration increases both between and beneath the stripes, the lateral mode structure becomes more complex. These results confirm the earlier observation of significant lateral spread of titanium from the stripe sources.

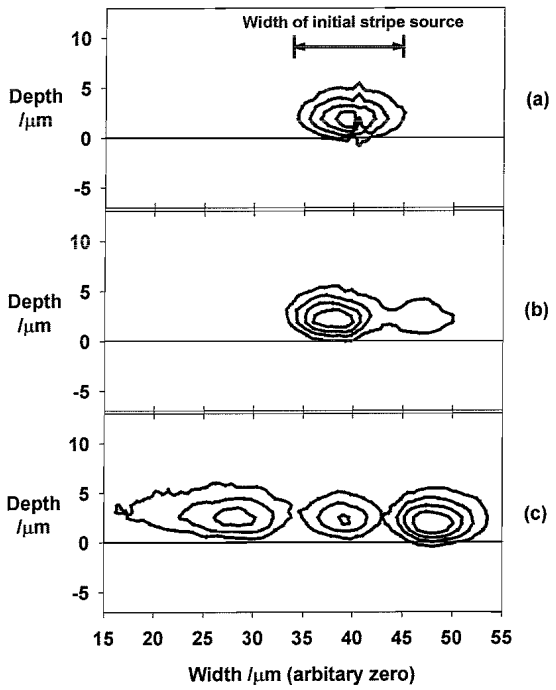

Figure 5.21:- (a), (b) and (c) Contour plots of waveguide intensity mode profiles excited by prism coupling in the region beneath the 11μm stripe on S165 at a wavelength of 488nm. The effective refractive indices of the modes decrease from (a) to (c).

In the near infra-red at a wavelength of 800nm, the complex lateral structure is not observed for the 11μm stripe and a single TE_{00} and TM_{00} may be excited by prism coupling. The mode size (defined as 1/e of the peak intensity) in the depth direction measured as a function of stripe width is shown in Figure 5.22. At this wavelength, the mode sizes of waveguides diffused from the narrower stripe widths are seen to extend further into the substrate and become cut-off. Also shown in Figure 5.22, are the TM_{00} mode depths measured at a wavelength of 488nm, as a function of stripe width. As expected, the mode size (in the depth direction) is smaller at the shorter wavelength. These observations of changing waveguide properties with stripe width are consistent with the earlier observation (Figure 4.25) that the diffused peak Ti^{3+} concentration decreases with stripe width, leading to a lower peak refractive index.

Losses in the waveguides were investigated over wavelengths in the visible and near infra-red, using the spectral attenuation technique described in §5.3.3, and the results are illustrated in Figure 5.23. The attenuation will include coupling losses, propagation losses and absorption losses; the sample length is 5.5mm. The high losses at wavelengths less than 600nm correspond to the Ti^{3+} absorption. Consistent with the previous measurements of lower peak Ti^{3+} concentrations, the narrower channels also exhibit lower absorption at wavelengths in the blue-green. For the 11μm channel waveguide, the peak absorption is aproximately16dB, which would correspond to an average modal Ti^{3+} concentration of just

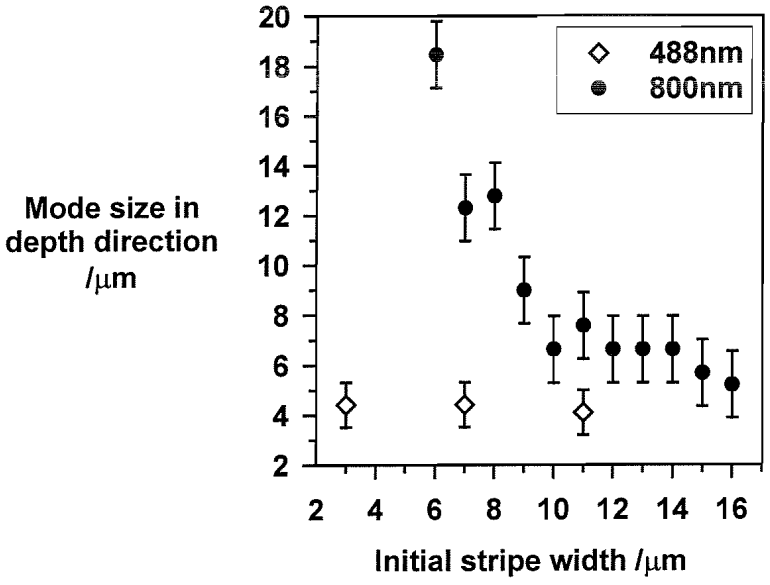

Figure 5.22:- Waveguide mode size in the depth direction, as a function of stripe width for S165.

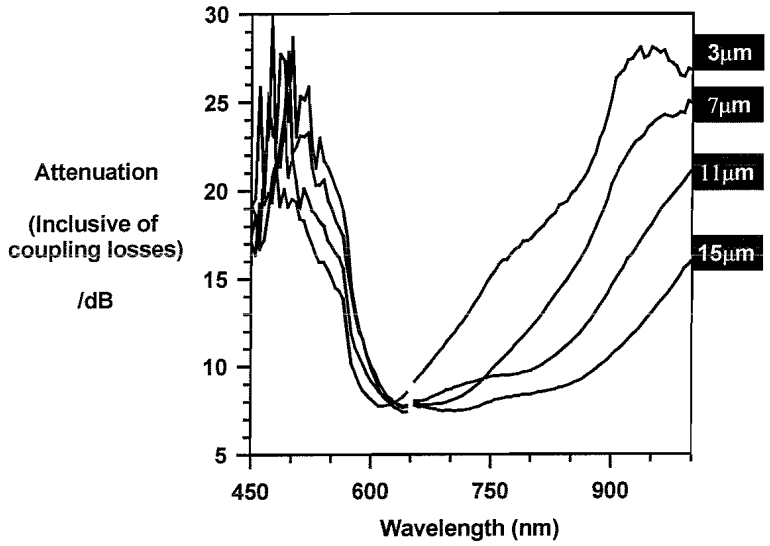

Figure 5.23:- Spectral attenuation in channel waveguides on S165.

under 0.3wt%. Again, this is consistent with the fluorescence imaging results presented in Figure 4.25.

At a wavelength of 600nm, a minimum loss of about 8dB is measured for each channel. The high losses at a wavelength of 800nm for the 3μm and 7μm channel waveguides indicate they are poorly confined at this wavelength, and are approaching cut off. This observation is consistent with the intensity mode size shown in Figure 5.22 for the 7μm channel waveguide. The channel waveguide diffused from the broader stripe sources cut-off at longer wavelengths.

The small increase in loss around a wavelength of 750nm is of interest, as this would affect the performance of a channel waveguide laser. A broad absorption these wavelengths would be consistent with the presence of Ti^{3+}-Ti^{4+} pairs in the lattice. From the results shown, it is inconclusive whether this is an artifact of the experimental technique, due to changes in propagation loss, or due to an absorption in the waveguide.

Comparing the waveguide properties at a wavelength of 488nm and 800nm, it seems that the broader stripes on this sample may be suitable for laser experiments. These waveguides are single mode at the peak of the Ti^{3+} gain band (λ=800nm), although are fairly close to cut off. At the pump wavelength, the fundamental mode may be independently excited, although in the lateral direction, higher order modes can exist. Based on these observations, a further sample was fabricated, using a thicker diffusion source, with the aim of increasing the peak refractive index of the diffused region

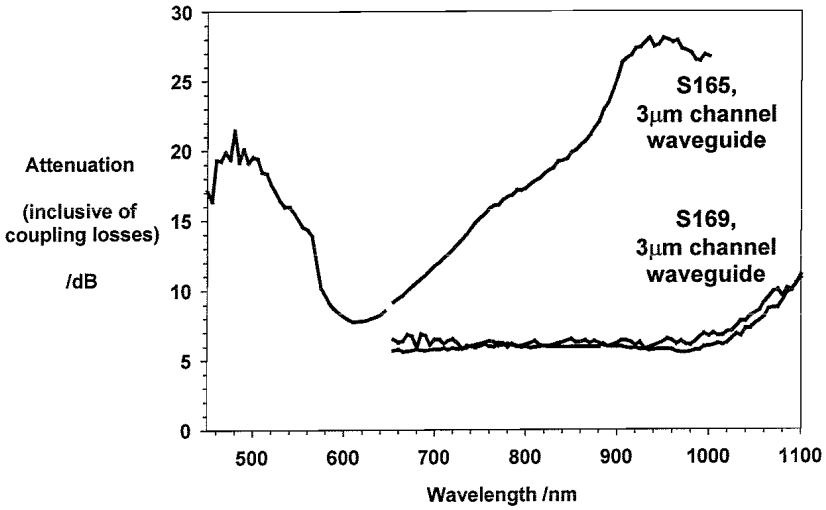

Figure 5.24:- Spectral attenuation for TM polarisation in 3μm channel waveguides on S165 and S169.

5.6.3 3μm channel waveguides by diffusion at 1700°C from a 270nm source

S169 was diffused with a 270nm source, for a time of 1 hour at 1700°C. The aim in the fabrication of this sample was to produce a channel waveguide with a more tightly confined intensity mode profile and a cut-off further in the infra-red, compared with S165.

Figure 5.24 shows the spectral attenuation measured in a 3μm channel waveguide formed on S169, in comparison with the attenuation measured for a similar channel in S165. The spectral attenuation measurement indicates that the cut-off wavelength has been extended to beyond 1000nm for the 3μm channel waveguide in S169. With this result, a 3μm channel waveguide on S169 was investigated in a laser configuration; these results are discussed in chapter 6.

5.7 Conclusions

Waveguides in the Ti-diffused region of a sapphire substrate have been realised for the first time. Characteristics of the waveguides, such as the effective refractive index, the mode intensity profile and the spectral attenuation have been presented. These have led to estimates of the relation between Ti concentration and refractive index change and the selection of a channel waveguide for subsequent laser experiments.

Trends in the properties of waveguides formed in an ideal diffused graded index region were investigated using the WKB method to determine the modal effective refractive index. As expected, the effective refractive index of each supported mode tends towards the peak,

surface refractive index with increasing diffusion time. However, for an instantaneous diffusion source, the decreasing peak refractive index can lead to an overall decrease in modal effective index with increasing diffusion time.

The characteristics of slab waveguides formed following diffusion from a continuous film diffusion source 27nm and 41nm thick, at temperatures of 1750°C and 1950°C were investigated. Single mode and multimode waveguides were observed at a wavelength of 633nm for the shorter diffusion times. Trends in the effective refractive indices of these modes were close to those expected for waveguides formed in a graded index region diffused from an instantaneously depleted source. For longer diffusion times, waveguide modes could not be excited in the Ti-doped region by prism coupling at a wavelength of 633nm.

A quantitative comparison between the measured waveguide properties and the known total Ti concentration was possible for some samples. This led to two independent estimates of the refractive index change per wt% Ti_2O_3 in Al_2O_3, of $(2.3\pm0.6)\cdot10^{-3}$ and $(4\pm1)\cdot10^{-3}$. These calculations assume that the increase in refractive index is proportional to the concentration of Ti, irrespective of the phase of the diffused Ti:Al_2O_3. Results presented in chapter 4 indicate that both fluorescent and non-fluorescent Ti exists in the diffused region of the samples used in the quantitative analysis, which may explain the discrepancy in estimated values.

Following the realisation of slab waveguides in Ti-diffused sapphire, the properties of waveguides formed by diffusion from a patterned source were investigated. At each temperature considered, a limited range of conditions existed for which well-confined channel waveguides were formed at a wavelength of 633nm. The spectral attenuation and mode intensity profiles for 2 samples were discussed in greater detail, and S169 selected for laser experiments.

5.8 References to chapter 5

1. M N Armenise, "**Fabrication techniques of lithium niobate waveguides**"; *IEE Proc, 135 Pt. J (1988), pp 85-91*
2. General reference to this section, D L Lee, "**Electromagnetic principles of integrated optics**"; *pub. John Wiley & Sons, 1986*

3. G B Hocker, W K Burns, "**Modes in diffused optical waveguides of arbitrary index profile**"; *IEEE J. Quant. Electron., **QE-11** (1975), pp 270-276*
4. R Syms, J Cozens, "**Optical guided waves and devices**"; *pub. McGraw-Hill Int. Ltd., 1992*
5. R Ulrich, R T Torge, "**Measurement of thin film parameters with a prism coupler**"; *Appl. Opt., **12** (1973), pp 2901-2908*
6. The preliminary reconstruction of the refractive index profile from the raw data was carried out by J S Wilkinson, whilst at Politecnico di Torino as part of a British Council Anglo-Italian grant, 1997
7. A K Ghatak, K Thyagarajan, M R Shenoy, "**Numerical analysis of planar optical waveguides using matrix approach**"*; J. Lightwave Tech., **LT-5** (1987), pp 660-667*

CHAPTER 6

TI-DIFFUSED CHANNEL WAVEGUIDE LASER IN SAPPHIRE

6.1 Introduction

Significant progress towards the realisation of a Ti:sapphire waveguide laser has been presented so far. Chapter 4 described the diffusion of Ti^{3+} into sapphire, with the diffused region exhibiting spectroscopic properties identical to that of the known Ti:sapphire gain medium. Chapter 5 discussed the formation of slab and channel optical waveguides in Ti-diffused sapphire. Under appropriate conditions the diffused Ti presents good spectroscopic properties and forms a channel waveguide with good confinement of radiation at wavelengths in the visible and near infra-red regime. Such a diffused region presents an ideal candidate for the realisation of a Ti:sapphire channel waveguide laser.

In this chapter, the realisation of a laser in such a channel waveguide is presented. The experimental techniques used to characterise the laser are presented and the spectral, power, modal and temporal behaviour of the laser output is presented for two cavity configurations. This work comprises the first realisation of a channel waveguide laser fabricated by the thermal diffusion of Ti into sapphire.

6.2 Realisation of a waveguide laser

The operation of a laser in a waveguide configuration requires similar components to the more traditional bulk configuration. For the case of the Ti:sapphire system, the transition is optically pumped and the cavity is formed by directly butting dielectric mirrors to the polished endface of the sapphire substrate. With increasing absorbed pump power, guided spontaneous emission and stimulated emission levels build within the laser cavity until the

gain at the emission wavelength compensates for the round trip cavity losses and the threshold for laser emission is achieved.

The simple model developed in chapter 2 indicated that the performance of a Ti:sapphire waveguide laser is dependent on the effective modal area and the total optical loss in the laser cavity. Lowest pump power threshold would occur for small waveguide modes with good overlap at the pump and signal wavelengths, lowest optical loss, maximum doping, and maximum feedback into the cavity. Under these conditions, an optimum sample length exists for lowest threshold operation. The model indicates that pump power thresholds of the order of tens of mW may be achievable, although the model is approximate, as discussed.

In the remainder of §6.2, the characteristics of the waveguide selected for laser experiments are reviewed, the spectral properties of the mirrors used to form the laser cavity are presented and the experimental technique used to characterise the laser operation is presented.

6.2.1 Characteristics of the selected waveguide

The channel waveguide selected for laser experiments was diffused from a 3μm stripe on S169. S169 was diffused for 1 hour at a temperature of 1700°C, from a 270nm thick, patterned diffusion source. The diffused Ti^{3+} distribution measured at a location beneath the 100μm stripe peaked at about 0.2wt% Ti_2O_3 in Al_2O_3 and extended about 10μm beneath the sapphire surface. A similar diffusion depth may be expected for diffusion from the 3μm stripe, although the peak Ti^{3+} concentration is expected to be slightly lower[1]. Subsequent measurements of the average Ti^{3+} absorption in the 3μm waveguide at wavelengths in the blue-green, indicate the average modal concentration of Ti^{3+} is 0.13 ± 0.02wt%. This would correspond to a maximum absorption of 9.2 ± 1.1dB along the 0.6cm waveguide length. This calculation assumes the peak absorption is 2.7cm^{-1} for a crystal doped at 0.1wt% Ti^{3+}, following the results reported by Moulton[2].

The spectral characteristics of the channel waveguide were briefly discussed in chapter 5. Spectral attenuation measurements indicate that the TM mode cuts off at a wavelength beyond 1000nm. The measurements also indicate that the total coupling and waveguide propagation loss was less than 6dB for the 3μm waveguide under the experimental conditions used. In the analysis of the waveguide laser performance, the waveguide

propagation loss is estimated to be between 0 and 2dB/cm, ie. 1±1dB/cm at the pump and signal wavelengths. Further experimental work would enable the loss to be more accurately established.

Based on these characteristics, the optimum waveguide length would be about 0.2cm. Laser experiments, however, were successfully carried out with the full 0.6cm length.

6.2.2 Characteristics of the cavity mirrors

The characteristics of the mirrors that form the laser cavity, providing feedback into the gain medium, strongly affect the laser performance. For example, the wavelength at which the laser first reaches threshold and is able to operate, occurs when the optical gain equals the round trip cavity loss. Particularly for the broad gain band of Ti:sapphire, spectral variation in the power reflectivity of the cavity mirrors will influence the wavelengths that may reach threshold.

Laser experiments were carried out with two cavity configurations using two mirrors of differing spectral reflectivity. The mirrors consisted of a dielectric multi-layer coating commercially deposited on a thin glass substrate. The coatings were designed with a high transmission at the pump wavelength and high power reflectivity for a defined region near the peak of the Ti:sapphire gain band. The power reflectivities of the reflective coating were measured using an optical spectrum analyser over the wavelength range 770 to 830nm and

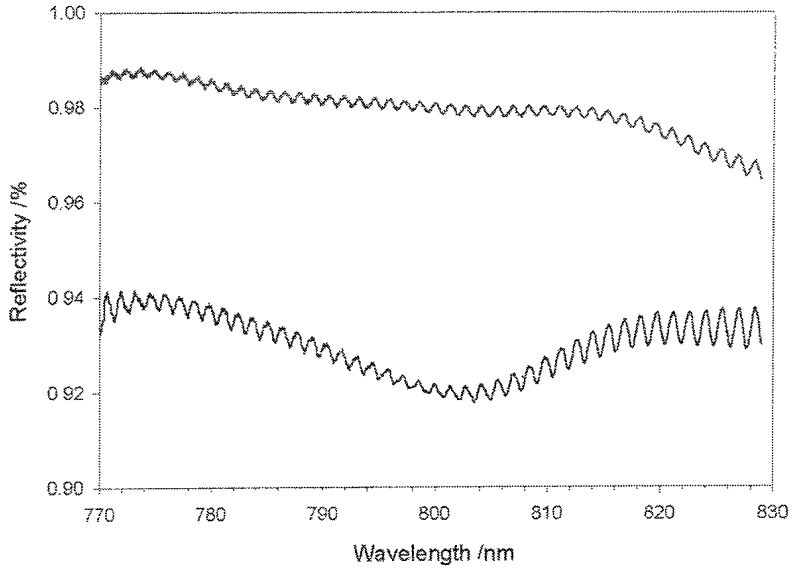

Figure 6.1:- Power reflectivity of the dielectric cavity mirrors, corrected for reflections from the glass substrate, by reference with an uncoated substrate.

are illustrated in Figure 6.1. The influence of reflections at the surface of the substrate material was reduced by normalising to the reflectivity measured for an uncoated substrate. The oscillations in the reflectivity would correspond to the modes of a Fabry-Perot etalon of about 130μm thick, which would match the thickness of the uncoated substrate and indicate a small error in the normalisation.

Based on these results, the mirrors were designated "high reflectivity", with 98±0.5% reflectivity and "lower reflectivity" with a reflectivity of 93±1%. A mirror placed on the output end of the waveguide is referred to as an output coupler, and the characteristics defined in terms of transmission, at 2% and 7% respectively.

In the laser experiments, the cavity was formed by directly butting the coated side of two mirrors to the polished endfaces of the waveguide. The mirrors were initially held in place by the surface tension of a drop of fluorinert FC-70, a fluorinated oil, before being fixed firmly with UHU, an acetone-soluble, quick drying adhesive. This method has the potential for aligning the reflective coating parallel to the polished waveguide endface, with minimal gap between the mirror and waveguide. A gap between the reflective coating and the waveguide endface would reduce the levels of feedback into the waveguide and may form an additional Fabry-Perot etalon inside the main laser cavity. The presence of an additional Fabry-Perot etalon would lead to modulation of the spectral losses in the laser cavity and would affect the laser output spectrum.

6.2.3 Experimental method

Figure 6.2 shows the experimental configuration used to identify the onset of lasing and to investigate the characteristics of the laser emission. A water-cooled argon ion laser was used as a pump source, operating multi-line at a series of wavelengths between 456nm and 515nm. The pump radiation was vertically polarised (parallel to sapphire c-axis or TM waveguide excitation) so as to access the greater Ti^{3+} absorption cross section[2]. The pump radiation was mechanically chopped using a blade with an on:off ratio of 1:19, designed to reduce the average pump power incident on the input cavity mirror. The chopping speed was adjusted to give a pump pulse of duration 0.8ms. The pump radiation was launched into the waveguide, through the input cavity mirror, using a x10 or x6.3 microscope objective.

At the waveguide output, unabsorbed pump radiation was separated from lasing wavelengths using a "cold" mirror which reflects radiation of a wavelength shorter than 700nm, whilst

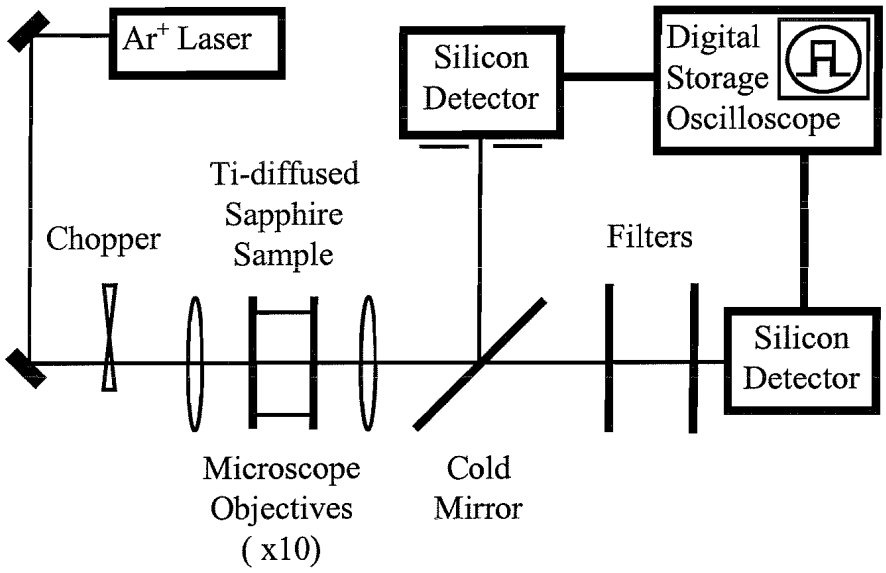

Figure 6.2:- Schematic of apparatus used in laser experiments

transmitting longer wavelengths. The reflected unabsorbed pump radiation was directed through an aperture and was incident on a calibrated silicon detector, with the power levels displayed on a digital storage oscilloscope. Radiation due to waveguide laser operation was transmitted by the cold mirror and was incident on a second calibrated silicon detector whose output was also displayed on the oscilloscope. The response time of the detector was sufficiently fast to enable temporal power fluctuations during the lasing pulse to be investigated.

For spectral analysis of the waveguide laser output, the silicon detector was replaced with an optical spectrum analyser. The minimum integration time of the spectrum analyser was of the order 30ms, and so the recorded spectrum represents the spectral characteristics over approximately two cycles of the chopped pump radiation.

Waveguide mode profiles at the pump and lasing wavelengths were recorded using a silicon vidicon camera, calibrated for the appropriate magnification.

Following the laser characterisation, the transmission through each of the optical components was measured to enable the coupling efficiency into the waveguide to be estimated from the levels of unabsorbed pump power, considering a $1\pm1 dBcm^{-1}$ waveguide propagation loss and a 9.2 ± 1.1dB pump absorption. The value for the waveguide propagation loss is estimated, whilst the pump absorption was experimentally determined

and assumes that the transition is not bleached for the pump powers investigated. From the estimate of the coupling efficiency, the pump power levels launched into the waveguide could be calculated from the measured output power of the argon laser providing the pump radiation.

6.3 Ti-diffused waveguide laser with 2% output coupling

Laser operation was observed for a 3μm Ti-diffused channel waveguide on sample S169 using two high reflectivity mirrors to form the laser cavity. In this configuration, the output coupling is 2%. The power, spectral and temporal characteristics of the waveguide laser are presented in the following sections.

6.3.1 Power, threshold and slope efficiency of the waveguide laser

The laser output power as a function of launched pump power is presented in Figure 6.3 for a 3μm Ti-diffused channel waveguide in S169. The coupling efficiency into the channel waveguide is calculated to be 41±12% and the launched pump power threshold is 1.2±0.4W.

Power extracted from the laser is of the order of tens of μW for a launched pump power of 800mW above threshold pump power, corresponding to a slope efficiency of 0.01%.

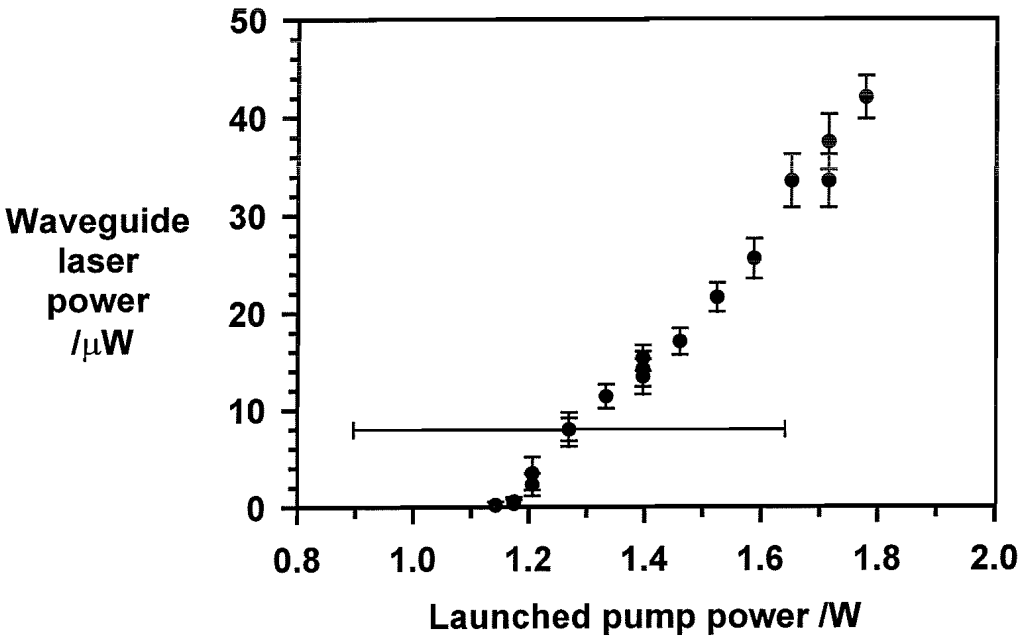

Figure 6.3:- Output power characteristics of the Ti:sapphire waveguide laser with 2% output coupling

The error in the measurement is shown by the errors bars in Figure 6.3, although only a single error bar is shown for the launched pump power to maintain overall clarity. In the laser output power, the data represents the average and standard deviation of the laser output power during the pump pulse. The error in the launched pump power is significant, at about 30% of the recorded value. This represents the combined uncertainty in the Ti^{3+} absorption, waveguide propagation loss, waveguide coupling loss, and the ratio of incident to unabsorbed pump power. With further characterisation of the waveguide, uncertainties in the Ti^{3+} absorption and waveguide propagation loss could be reduced.

The threshold pump power of the waveguide laser in this configuration is about 2 orders of magnitude greater than expected with reference to the model described in chapter 2. The discrepancy is discussed further in §6.5.

6.3.2 Spectral characteristics of the waveguide laser

Figure 6.4 shows an example of the waveguide laser output spectrum, for a launched pump power 700mW above threshold.

Four distinct groups of lasing wavelengths are observed, although it is expected that each of these groups consist of a series of longitudinal cavity modes allowed by the 6mm Fabry-Perot etalon, whose spectral spacing would be about 0.03nm. Each group of cavity modes is about 0.5nm wide at 1/e of the peak intensity, and the resolution of the spectrum analyser is

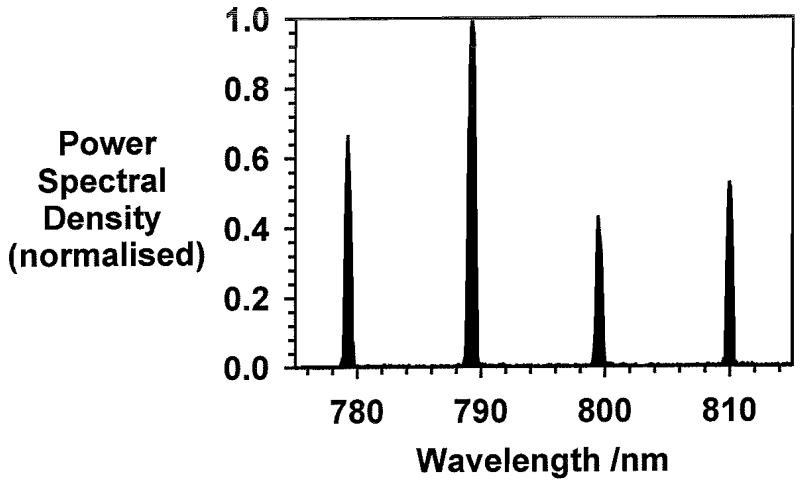

Figure 6.4:- Spectral characteristics of the waveguide laser operating at a launched pump power 0.7W above threshold.

better than 0.12nm. The groups of cavity modes are spaced by about 10nm, which would correspond to the characteristics of a Fabry-Perot etalon with a spacing of the order of 15μm. A small gap between one of the cavity mirrors and the waveguide endface may allow such a cavity to form and contribute accordingly to the spectral cavity characteristics.

On reducing the pump power, the group of cavity modes centred near 810nm cease to lase first, followed by the groups centred at 790nm, 780nm and finally 800nm. The changes in the waveguide laser spectra with pump power are related to the spectral characteristics of gain and loss in the waveguide cavity.

6.3.3 Temporal stability of the waveguide laser

The spectral characteristics of the waveguide laser during the pump pulse were investigated using a fast silicon detector and a series of filters, and an example of the results is shown in Figure 6.5.

For a launched pump power 0.7W above threshold, sharp fluctuations in output power are observed during the laser emission, when viewed through a broad band pass filter with high transmission for wavelengths between 770nm and 830nm. The origin of these fluctuations was investigated by inserting an additional 10nm narrow band pass filter, centred at 810nm,

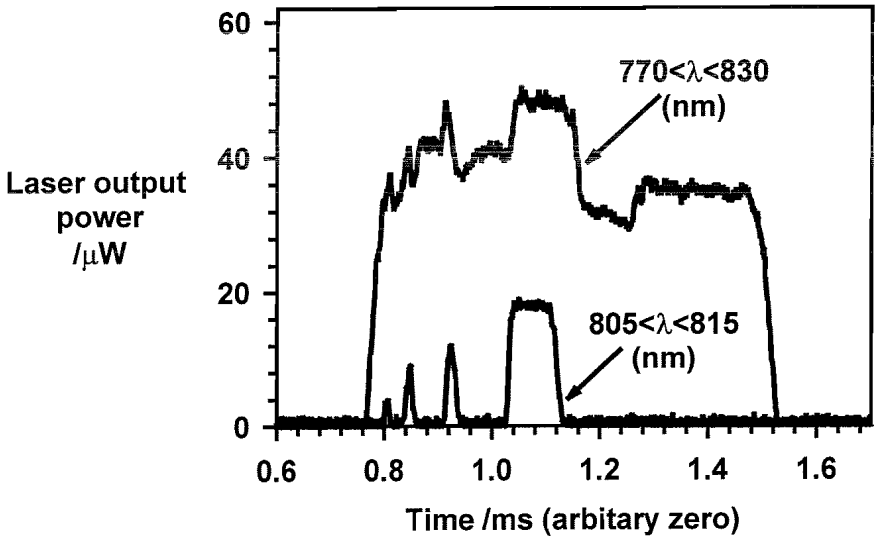

Figure 6.5:- Temporal fluctuations in the laser output power during the pump pulse, for a launched pump power 0.7W above threshold pump power, viewed through broad and narrow band pass filters.

to select the power of one of the groups of lasing modes observed in Figure 6.4. The results indicate that the 810nm group of lasing wavelengths occurs during a fraction of the lasing pulse. Using a series of narrow band pass filters, similar observations are made for the other groups of lasing wavelengths, with the character of the switching between lasing wavelengths sensitive to the launched pump power. These results indicate that there is a temporal instability in the ratio of gain to loss in the cavity, during the pump pulse. This may be related to heating of the waveguide, gain medium, or cavity mirrors.

During the course of one day, the spectral characteristics were repeatable for a given launched pump power, except that the centre wavelength of the groups of oscillating modes were observed to drift by approximately 4nm. This drift is likely to be due to a variation in the spectral characteristics of the Fabry-Perot etalons that influence the laser spectrum. For example, the variation may be due to a small movement of a cavity mirror.

6.3.4 Summary of laser characteristics with 2% output coupling

A Ti:sapphire channel waveguide laser has been realised with a laser cavity formed between high reflectivity mirrors directly butted to the waveguide endfaces. With a chopped pump source operating around 500nm, the launched pump power threshold was measured to be 1.2±0.4W and the slope efficiency, 0.01%. Laser emission was observed at a series of wavelengths between 780 and 810nm for a launched pump power 700mW above threshold. The emission wavelengths formed a series of distinct groups, separated by 10nm, with a full width at 1/e of 0.5nm. Switching between oscillating modes was observed during the lasing pulse.

6.4 Ti-diffused waveguide laser with 7% output coupling

The laser experiments reported in §6.3 were repeated for a 7% output coupler using the same 3μm channel waveguide on S169. The following power, spectral and modal characteristics of the laser were observed.

6.4.1 Power, threshold and slope efficiency

Figure 6.6 illustrates the power characteristics obtained for a 3μm Ti-diffused channel waveguide laser with a 7±1% output coupler. The launched pump power threshold was calculated to be 1.2±0.4W, assuming a 48±14% coupling efficiency. The enhanced coupling

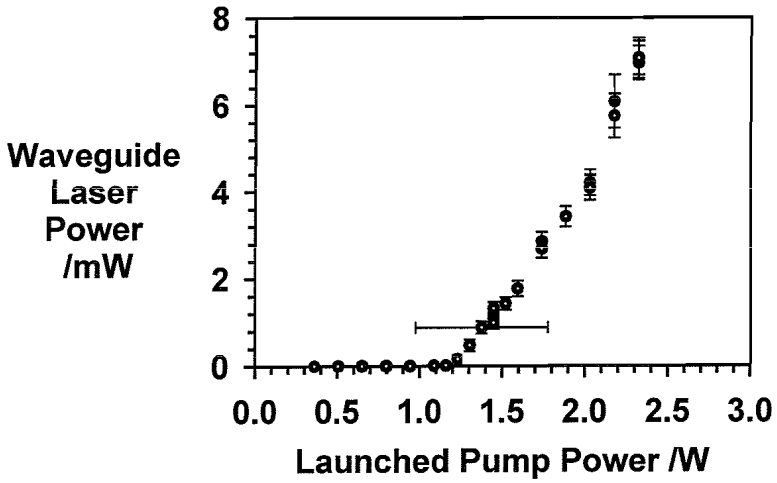

Figure 6.6:- Output power characteristics for a Ti:sapphire waveguide laser with 7±1% output coupling.

efficiency compared to the results described in §6.3 is consistent with a change in the waveguide excitation optics from a x10 microscope objective to a x6.3 microscope objective.

Power levels extracted from the waveguide laser was of the order of mW for launched pump powers approximately 1W above threshold, corresponding to a slope efficiency of 0.5%. Therefore, by increasing the output coupling from 2% to 7%, the slope efficiency has increased by 50 times.

The error in the laser output power is given by the standard deviation of the laser output power during the pump pulse. The error in the launched pump power is calculated from the combined uncertainty in the Ti^{3+} absorption, waveguide propagation loss, waveguide coupling loss, and the ratio of incident to unabsorbed pump power.

6.4.2 Spectral characteristics

The output spectrum of the waveguide laser measured for a launched pump power 1W above threshold is shown in Figure 6.7. The spectrum analyser used integrated the signal over approximately two pump pulse cycles.

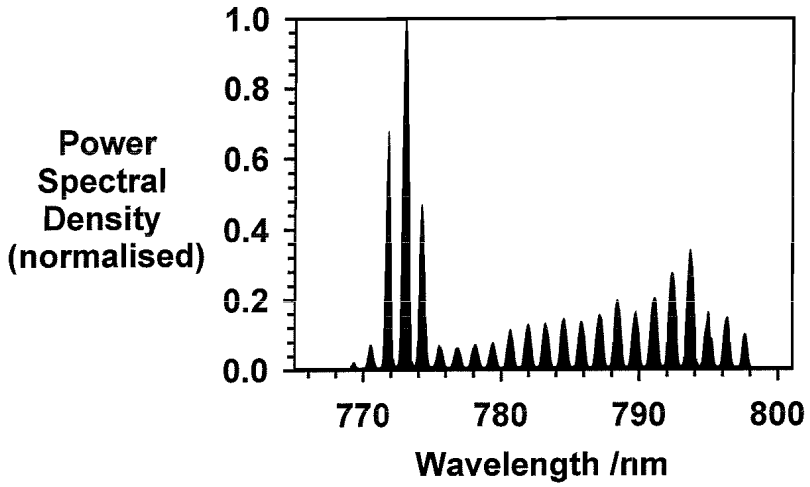

Figure 6.7:- Spectral characteristics of the waveguide laser at a launched pump power 1.0W above threshold

The recorded spectra show laser emission over about 30nm centred at 785nm with a distinctive periodic power density. The period is approximately 1.3nm and the full width at 1/e of the peak of each group, is 0.6nm. The resolution of the spectrum analyser is better than 0.12nm. It is expected that the spectra will also contain a fine structure, characterised by the Fabry-Perot etalon formed by the 0.6cm cavity. These modes would be separated by about 0.03nm, and cannot be resolved using this spectrum analyser.

As the launched pump power is decreased, wavelengths near the centre of the emission spectra at around 775-780nm cease to lase first, followed by the groups of modes operating beyond 790nm and subsequently the modes at 770nm. At a pump power just above threshold, the laser operates at wavelengths between 780 and 785nm. Such a pattern in the spectral characteristics would be related to the spectral dependence of gain and losses within the laser cavity.

Using a fast silicon detector and a series of narrow band pass filters, switching between lasing wavelengths was observed during the laser pulse. This characteristic is similar to the laser characteristics observed for the 2% output coupler cavity configuration.

The periodic nature of the power density spectrum in presented in Figure 6.7 indicates that the fluctuations may be caused by a Fabry-Perot etalon with a characteristic spacing of about 130μm. This is close to the thickness of the mirror substrate, indicating that the small variations in feedback provided by the boundaries of the mirror substrate may be sufficient to modulate the spectral losses in the laser cavity. This behaviour was not observed for the

2% output coupler, although it is believed that a small separation existed between the mirror and the waveguide endface and dominated the spectral characteristics. In contrast, it is expected that for the 7% output coupler, good contact was achieved between the cavity mirrors and the waveguide.

6.4.3 Intensity mode profiles for laser and unabsorbed pump radiation

The intensity mode profiles for unabsorbed pump radiation and lasing wavelengths were obtained whilst the waveguide laser was operating with 7% output coupling. Contour plots showing the imaged intensity profiles are given in Figure 6.8.

The intensity mode profile obtained at the pump wavelengths exhibits a double lobed structure in the depth dimension, whilst in the breadth direction, features a structure that extends along the surface. The structure represents the sum of the unabsorbed power distributed in the waveguide modes excited at each of the wavelengths that comprise the pump radiation. The extension of the mode profile along the near surface region is consistent with the lateral diffusion of Ti^{3+} from the stripe source, discussed in chapter 4. Further characterisation of the waveguide properties at each of the pump wavelengths individually would be needed to characterise the absorption of the pump and the distribution of excited Ti^{3+} ions.

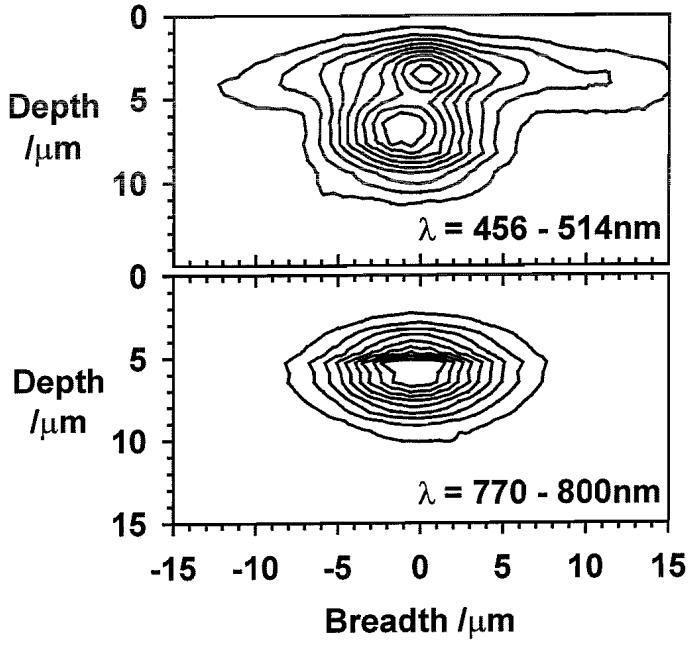

Figure 6.8:- Waveguide mode intensity profiles obtained for unabsorbed pump and laser radiation. The waveguide excitation is optimised for maximum laser output power.

At the lasing wavelengths, the mode exhibits TM_{00} character mode, with a full width at 1/e of the peak intensity of approximately 5μm and 10μm in directions of depth and breadth respectively.

The waveguide laser model developed in chapter 2 indicated that the pump power threshold would decrease with approximately the square of the pump and signal mode sizes. Reducing the mode size and optimising the overlap would lead to a significant reduction in the pump power threshold of the Ti:sapphire waveguide laser.

6.4.4 Summary of laser characteristics with 7% output coupling

Laser operation was observed in a 3μm Ti-diffused channel waveguide in sapphire, with a 7% output coupler. With a chopped pump source operating at wavelengths around 500nm, the launched pump power threshold was 1.2±0.4W and the slope efficiency 0.5%. This represents a 50-fold increase in the power output compared to the power output with the 2% output coupler.

Lasing was observed at a series of wavelengths between approximately 770 and 800nm with a characteristic periodic power density spectrum. The period was approximately 1.3nm with a full width at 1/e of 0.6nm and is likely to be due to modulations in feedback provided by the mirror substrate. These characteristics differ from those observed for the laser operating with a 2% output coupler, and are attributed to small differences in the separation of the cavity mirrors and the waveguide endface.

The mode intensity profile obtained for the laser radiation shows a TM_{00} mode structure. The mode size (measured as 1/e of the peak intensity) is 5x10μm for the depth and breadth dimensions respectively. At the pump wavelengths, a more complex mode structure is observed for the unabsorbed power.

6.5 Discussion and quantitative interpretation of laser performance

The performance of a waveguide laser is related to the geometry of the waveguide, losses in the cavity, the characteristics of the gain medium and the laser cavity configuration. Following the simple model for a Ti:sapphire waveguide laser described in chapter 2, the indication was that a waveguide laser with a pump power threshold of the order of tens of mW can be achieved. These calculations assumed that the waveguide supported circularly

symmetric Gaussian modes of size about 3μm, losses were of the order 1dB/cm at the pump and signal wavelengths, the gain medium doped at 0.1wt%, the waveguide optimised in length, an output coupling of 5%, a quantum efficiency of 0.5 and fluorescence lifetime of 3.2μs

In practice, a waveguide laser with a pump power threshold about two orders of magnitude greater has been realised, for two cavity configurations. For the laser realised, the waveguide mode at the signal wavelength is asymmetric with dimensions 5x10μm (§6.4.3), the propagation loss is known to be less than 6dB over the 6mm device length (§5.6) at the signal wavelength, the average modal concentration of Ti^{3+} is 0.13wt% (§6.2.1), output couplers of 2% and 7% have been used and the quantum efficiency and lifetime of the laser transition have not been measured.

Aspects of the experimental results are discussed in the following section to highlight some of the reasons that contribute to the difference between the projected laser performance and that measured.

6.5.1 Waveguide geometry

The geometry of the waveguide used for the laser experiments was not optimised in terms of waveguide mode size or waveguide length for low pump power threshold. With any losses in the waveguide, an optimum length will exist for optimum laser operation. For the waveguide used, the optimum length is estimated to be 0.2cm, and it is expected that a lower pump power threshold will be achieved if the device is reduced to this length.

In the model presented in chapter 2, the pump power threshold increases with approximately the square of the mode size. Therefore, it is expected that the pump power threshold is greater for the diffused channel waveguide, with a mode of dimensions 5x10μm at the signal wavelength. Assuming the pump mode is also 5x10μm, leading to a perfect overlap of power at the pump and signal wavelengths, and that the power can be described by a Gaussian distribution, this would lead to 5-fold increase in the pump power threshold compared to respective 3x3μm modes.

These differences in waveguide geometry explain some of the discrepancies between the projected laser performance and that measured.

6.5.2 Loss in the laser cavity

Losses in the waveguide cavity will increase the pump power threshold. Sources of optical loss include scattering at the pump and signal wavelengths, absorption at the signal wavelength and loss at the cavity mirrors. The observation of a higher pump power threshold for the waveguide laser compared to the simple model may indicate that the total round trip cavity losses are higher in practice than expected. The total round trip cavity losses can be estimated by considering the slope efficiency of the laser.

Referring to chapter 2, the slope efficiency, *SE*, is given by *Eqn. 6-1*. λ_p and λ_s are the wavelengths of the pump and signal modes, η is the quantum efficiency, describing the fraction of absorbed photons that contribute to radiative decay, T is the transmission of the output coupler and *RTL* is the total round trip loss, expressed in the same dimensions as T.

$$SE = \frac{\lambda p}{\lambda s}\eta\frac{T}{RTL} \qquad \textit{Eqn. 6-1}$$

Assuming λ_p, λ_s and η are 500nm, 800nm and 0.5 respectively, the total loss in the cavity can be estimated for each of the laser cavity configurations. The value of 0.5 assumed for the quantum efficiency is speculative. If in practice a lower quantum efficiency is achieved in the diffused gain medium, the calculated round trip cavity loss will be overestimated. For 2% output coupling, a slope efficiency of 0.01% was measured, which would correspond to a total round trip cavity loss of 23dB. For the 7% output coupling a slope efficiency of 0.5% was measured, indicating that the total round trip cavity loss is about 6dB. These figures indicate that the loss in the cavity is significant, and would in part explain the discrepancy between projected and observed laser performance.

The large difference in loss between the two experiments can be related to the different spectral characteristics of each laser. The laser spectrum observed for the 2% output coupling indicated that a separation of about 15μm occurred between the waveguide endface and the cavity mirror. This would reduce the levels of feedback into the waveguide and in part, will account for the difference in loss observed for the two cavity configurations.

Sources of loss that will contribute to the 6dB round trip loss estimated for the laser operating with a 7% output coupler, include waveguide propagation loss and absorption at the lasing wavelength. For a single pass through the waveguide, this has been measured to be less than 6dB (§5.6), including coupling loss into the waveguide. Further work would be

required to establish the independent propagation, absorption loss and coupling loss. It is expected that these losses may be controlled by the waveguide fabrication conditions, and optimised devices may be realised with further investigation of the diffusion process and waveguide characterisation.

In addition to the waveguide losses, any misalignment in the polished endfaces with respect to the waveguide axis, or in terms of parallelism would reduce the efficiency of feedback into the waveguide and gain medium. Similarly, rounding of the waveguide endface during the polishing procedure would add to the round trip cavity losses. These loss contributions may be reduced in future devices by optimising the polishing technique and developing schemes that ensure accurate alignment. For example, mirrors could be directly deposited on the polished waveguide endfaces.

6.5.3 Heating in the waveguide

Heating in the waveguide will affect the properties of the waveguide and the gain medium. In addition, heating of the reflective coatings and mirror substrate may cause distortions to the plane mirror and affect the power reflectivity. Changes in the mirror properties that reduce the feedback into the waveguide will increase the pump power threshold. In future devices, the materials used for the reflective coating could be optimised for high power densities, and deposited directly onto the polished endface.

6.5.4 Physical properties of the diffused gain medium

The model presented in chapter 2 assumed that the gain medium exhibited spectroscopic properties comparable to a bulk doped Ti:sapphire crystal. For the diffused medium, experimental results (§4.4) indicate that the lifetime and fluorescence spectrum are in excellent agreement with those of a high quality bulk doped Ti:sapphire laser crystal. However, the spectroscopic properties of the diffused region used as the gain medium for the waveguide laser have not been investigated directly. Deviations, from the values used in the model would contribute to the discrepancy between the laser performance observed and that projected. For example, if in practice a quantum efficiency less than 0.5 is achieved, the projected pump power threshold of the waveguide laser would increase.

6.5.5 Summary

The measured performance of the Ti:sapphire waveguide laser has been discussed in comparison with the simple model developed in chapter 2. The observation of higher pump power thresholds than expected may be related to the difference in waveguide geometry, the occurrence of higher round trip cavity losses, heating in the waveguide and discrepancies in the spectroscopic properties of the diffused gain medium.

Further characterisation of the current device is possible, particularly to determine the origin of the 6dB round trip cavity loss estimated for the laser operating with 7% output coupling. In addition, optimising the length of the waveguide should lead to the realisation of a waveguide laser with a lower pump power threshold.

6.6 Conclusions

A Ti:sapphire channel waveguide laser has been realised for the first time. The waveguide and the gain medium were formed in a low cost, high quality, commercially available sapphire wafer, by the thermal diffusion of titanium. The channel waveguide laser has been demonstrated and characterised for two cavity configurations. These results clearly illustrate the feasibility of this approach to the realisation of an integrated optic Ti:sapphire waveguide laser.

With a 2% output coupler and a chopped argon ion pump source operating at wavelengths between 456 and 514nm, a pump power threshold of 1.2±0.4W was achieved with a slope efficiency of 0.01%. Well above threshold, laser emission was observed over 30nm between approximately 780 and 810nm, in four distinct groups of cavity modes separated by approximately 10nm. The spectral characteristics are believed to be dominated by the occurrence of an additional 15μm Fabry-Perot etalon between a mirror and polished endface of the waveguide. The centre wavelength of each group of modes drifted over about 4nm during the course of a day. Within each laser cycle, switching between groups of cavity modes was observed.

For the 7% output coupler, under otherwise similar experimental conditions, the waveguide laser operated with a pump power threshold of 1.2±0.4W and slope efficiency of 0.5%. Well above threshold, laser emission was observed over approximately 30nm, between approximately 770 and 800nm. The characteristics of the emission spectra are thought to be

dominated by a wavelength variation in the feedback into the cavity caused by the reflections from the boundaries of the mirror substrates. Switching between emission wavelengths occurred during the laser cycle.

A quantitative interpretation of the laser characteristics for this first-generation device indicates that the observation of higher pump power thresholds than expected will be related to the waveguide mode size, device length and higher than expected round trip losses. In addition, heating in the waveguide and deviation from ideal spectroscopic properties of the gain medium may contribute to differences between the projected performance and that measured. A reduction in the pump power threshold for this device may be achieved by optimising the length of the waveguide. Further development of the waveguide laser model, and further characterisation of the Ti-diffused waveguide and gain medium should allow the discrepancy between the model and experiment to be reduced.

Switching of the emission wavelength through the laser cycle indicates a temporal and spectral variation of the cavity losses. Such dynamics indicate high sensitivity of the laser characteristics to instabilities in the laser cavity, which may in the future be exploited to provide integrated tuning and control of the laser emission.

In conclusion, this first demonstration of a Ti:sapphire laser in a planar waveguide geometry by diffusion of titanium into a readily available sapphire wafer clearly illustrates the feasibility of this approach for the realisation of a compact, broadly tunable waveguide laser.

6.7 References to chapter 6

1. L M B Hickey, J S Wilkinson, "**Characterisation of Ti-diffused channel waveguides in sapphire**"; *Proc. 8th Europ. Conf. Int. Opt., Sweden, Stockholm, 1-4 Apr. 1997, paper EWB1, pp 40-43*
2. P F Moulton, "**Spectroscopic and laser characteristics of Ti:Al_2O_3**";*J. Opt. Soc. Am. B, 3 (1986), pp 125-133*

CHAPTER 7

CONCLUSIONS

7.1 Introduction

This thesis describes the first realisation of a Ti:sapphire channel waveguide laser. Both the gain medium and optical waveguide are formed by the thermal diffusion of Ti into a commercially available sapphire wafer, for the first time. These results clearly illustrate the feasibility of this approach to forming a miniature Ti:sapphire laser on a sapphire chip.

In this chapter, key aspects in the development of the waveguide laser are reviewed and directions for future work proposed.

7.2 Summary of work reported

Interest in developing waveguide devices in sapphire has been increasing, with effort concentrated on realising rare-earth doped devices in Al_2O_3 waveguides, and on realising transition metal ion based lasers in single crystal sapphire. Recent successes include the realisation of optical amplification in Er-doped Al_2O_3 waveguides[1] and the realisation of a Ti:Al_2O_3 slab waveguide laser grown by pulsed laser deposition[2]. Many fabrication techniques have been reported with a varying degree of success. However, prior to this work, there were no reports of optical devices formed by thermal diffusion in sapphire. The technique of thermal diffusion offers the flexibility in the design of a doped region and has proven successful in the development of integrated optic devices in $LiNbO_3$[3].

In chapter 2, the properties of sapphire and Ti-doped sapphire were reviewed, to highlight the potential for a Ti:sapphire waveguide laser. The origins of the spectroscopic properties of Ti-doped sapphire that provide the basis for the broadly tunable laser were discussed. To realise a localised gain medium, the Ti needs to be introduced substitutionally on the Al lattice in the Ti^{3+} valence state. A simple model was developed for a Ti:sapphire laser and trends in the pump power threshold and the laser slope efficiency were discussed as a

function of the waveguide geometry, intracavity losses and cavity configuration. In conclusion, it was estimated that a waveguide laser with a pump power threshold less than 100mW is achievable.

In chapter 3, the dynamics of impurity diffusion into a substrate were discussed, with models illustrated for ideal diffusion conditions. The effect of competitive diffusion rates along extended defects was discussed, in addition to other mechanisms that lead to deviation from the simple diffusion model. Previous studies of metal diffusion in sapphire were reviewed, to identify the range of diffusivities and diffusion mechanisms observed. Based on this review, it was proposed that initial diffusion studies be carried out at temperatures of 1750°C and 1950°C.

The diffusion technique developed for diffusing Ti into sapphire at temperatures up to 1950°C was outlined in chapter 4. Techniques developed to analyse the diffused Ti^{3+} and diffused total Ti distribution were described. Experimental results for diffusion from a continuous film source and a patterned diffusion source were presented. Diffusion temperatures between 1480°C and 1950°C, diffusion times up to 8 hours and diffusion source thickness between 27nm and 270nm were considered. Peak concentrations as great as 0.5wt% Ti_2O_3 in Al_2O_3 and diffusion to depths of 50μm have been observed. The proportion of diffused Ti incorporated as the fluorescent Ti^{3+} ion depends on the cooling conditions from the diffusion temperature; a rapid cool was observed to increase the yield of diffused Ti^{3+}. The results indicated that Ti^{3+} ions with a spectroscopy appropriate for a localised gain medium could be introduced by thermal diffusion. The diffused profile is related to the diffusion temperature, diffusion time, source thickness and distribution of the source. These results comprise the first realisation of a locally doped sapphire wafer with Ti^{3+} by thermal diffusion.

In chapter 5, the characteristics of slab and channel waveguides formed in the Ti-diffused region of sapphire wafers were presented. A simple model of waveguides formed in a diffused graded index region was described, using the WKB method to calculate modal effective refractive indices[4]. The trends observed for waveguides formed in a graded index region diffused from an instantaneously depleted diffusion source were similar to those observed for a series of slab waveguides in Ti-diffused sapphire. Comparing the measured waveguide characteristics to the total diffused concentration, estimates of the relation

between Ti and refractive index change were obtained. The characteristics of channel waveguides formed by diffusion from a patterned source were discussed and a waveguide identified for laser experiments. The results reported comprise the first realisation of optical waveguides in sapphire, formed by thermal diffusion.

The realisation of a Ti:sapphire channel waveguide laser was reported in chapter 6. The waveguide laser was formed in a commercial sapphire wafer by the thermal diffusion of Ti to form both the gain medium and the optical waveguide. The laser was demonstrated with two cavity configurations, with 2% and 7% output coupling. With the 2% output coupler, the pump power threshold was of 1.2±0.4W, with laser operation characterised by a high intracavity loss. The high loss is likely to be due to inefficient feedback at one of the cavity mirrors. With the 7% output coupler, a pump power threshold of 1.2±0.4W was achieved, with an estimated round trip cavity loss of 6dB. Laser output was observed at wavelengths between 770nm and 810nm. Rapid switching between wavelengths was observed on a sub-millisecond timescale, indicating some temporal instability within the laser cavity. By optimising the waveguide length, a lower pump power threshold is expected for the same channel waveguide.

In summary, the results reported in this thesis illustrate that an optical gain medium and optical waveguides may be formed in a commercial sapphire wafer by thermal diffusion of Ti. This has led to the realisation of a channel waveguide laser. Further development of the waveguide, gain medium and the addition of intracavity control components, may lead to the realisation of monolithically integrated broadly tunable Ti:sapphire waveguide laser.

7.3 Future directions

Pursuing the aim of realising a fully integrated Ti:sapphire waveguide laser, requires activity on many fronts. The model of the waveguide laser needs to be developed further, schemes need to be devised for integrating control components on the sapphire chip and the diffusion dynamics of Ti in sapphire require greater experimental investigation.

7.3.1 Development of model describing Ti:sapphire waveguide laser

The current model of a Ti:sapphire waveguide laser indicates that a pump power threshold of less than 100mW may be achieved under ideal conditions. The model indicated that for low threshold operation, the waveguide losses and the waveguide mode sizes should be

minimised. Under these conditions, an optimum waveguide length will exist. For given distributed losses, the optimum length decreases as the doping level increases. Development of this model should include the effect of heating in the waveguide and changes in the material parameters, such as quantum efficiency and figure of merit as a function of Ti concentration. The model should also include the solution of waveguide mode sizes at the pump and signal wavelengths, calculation of the effective interaction area and the overlap of the waveguide modes with the Ti^{3+} distribution that provides the gain. In addition, with further investigation of the diffusion process, the model may be expressed in terms of the diffusion temperature, diffusion time and source thickness, to relate the characteristics of the waveguide laser directly to the fabrication conditions to yield an optimised waveguide laser.

The model may indicate that the use of Ti to form both the gain medium and the waveguide restricts the properties of the laser. In future devices, the properties of the waveguide and gain medium may be decoupled, by introducing a second ion to determine the waveguide properties. The introduction of a second ion will allow the development of passive waveguides, selectively doped with the active ion Ti^{3+} to form the gain medium as required. The choice of second ion is discussed further below.

7.3.2 Integration of control components

The attraction of the Ti:sapphire waveguide laser is the potential for broad tunability over 400nm at wavelengths in the near infra-red. In the planar waveguide geometry, intracavity components may be incorporated on the same sapphire chip, to control the laser operation. This would significantly enhance the ease of operation of the Ti:sapphire laser, and open the way for a host of novel applications. Integrated control has been achieved for other integrated optic lasers.

The laser output wavelength is determined by the ratio of intracavity loss and gain. Therefore, by introducing an externally tuned spectral loss, the wavelength of the laser may be controlled. Wavelength selection may be achieved by design of appropriate coupled cavity devices, and wavelength tuning by modulation of the waveguide path length. For example, the refractive index of a waveguide section may be increased by heating the waveguide. Models of the waveguide selection and control components may be developed and incorporated with the waveguide laser model.

7.3.3 Refinement of Ti-diffusion dynamics

The Ti diffusion characteristics described in this thesis indicate that several mechanisms are contributing to the overall transport process. In particular, a fast lateral diffusion from a patterned source results in a limited fabrication window for the realisation of channel waveguides. Further experimental work is required to establish the origin of the lateral diffusion and to allow each of the contributing mechanisms to be characterised. This is necessary to enable optimised waveguide lasers to be developed.

Further experimental work is proposed, considering the diffusion from a thick Ti-metal film, half covering a sapphire substrate. Characterisation of the diffused Ti^{3+} and total Ti distribution both beneath the original film and on the initially uncovered half of the substrate will allow the characteristics of the depth and lateral diffusion to be established. The influence of a preanneal on the extent of the lateral diffusion may be investigated. The use of other surface analysis techniques may allow an insight to the progression of a reaction between the diffusion source and substrate. In samples where a single Ti species is present in the diffused region, further estimates of the relationship between Ti concentration and refractive index change may be achieved.

In conclusion, further experimental work on the diffusion of Ti into sapphire is proposed so that a model describing the transport process can be established. The model will aid the realisation of optimised waveguides and gain regions, and the development of a low threshold Ti:sapphire waveguide laser.

7.3.4 Characterisation of the Ti-diffused gain medium

The spectroscopic properties of the diffused Ti may be investigated further. For example, the quantum efficiency, fluorescence lifetime and the figure of merit of the diffused region may be characterised as a function of Ti concentration and distribution. These studies would aid the development of the waveguide laser model and indicate the scope of the diffused Ti:sapphire as a gain medium.

7.3.5 Development of passive waveguides

The use of Ti to form both the waveguide and the gain medium presents an elegant one-step process to fabricate a waveguide laser in sapphire. However, the characteristics of the gain medium are coupled to those of the waveguide, which limits the design of the laser.

Introducing a second ion, to form a passive waveguide will allow greater flexibility of design. This route has been pursed in the development of active devices in $LiNbO_3$ hosts[5].

A second ion needs to display complementary spectroscopic properties to the active Ti^{3+} ion, and complementary redox characteristics, to ensure the diffused Ti remains as Ti^{3+} on an Al lattice site. For example the introduction of a divalent ion, such as Mg, would increase the solubility of Ti in the 4+ valence state[6]. Metal ions that may be complementary include Ga^{3+}, Y^{3+} and Cr^{3+}. Ga is a metal in the same group as Al in the periodic table and the phase diagram shows a finite solubility in the sapphire lattice[7]. Y is a transition metal ion and in the 3+ valence has no d-shell electrons and is so expected to be transparent to wavelengths in the visible and near infra-red. However, the solubility of Y^{3+} is reported to be low[8], which may limit the maximum refractive index change and the formation of optical waveguides. In contrast, Cr^{3+} is highly soluble in sapphire. However, Cr-doped Al_2O_3 is a well-known laser medium, with a broad absorption in the blue-green and emission at over narrow wavelength bands at around 690nm[9]. The introduction of Cr^{3+} as a second ion to form the waveguide, would have some effect on the Ti:sapphire laser performance, as it would not form a passive waveguide. The advantage of the independent control over waveguide and gain characteristics would have to be considered in balance with the degradation in the Ti:sapphire laser performance.

In summary, these developments would build on the progress achieved to date in the development of a miniature waveguide laser. The realisation of a broadly tunable Ti:sapphire waveguide laser would present a novel source for a host of remote and portable instrumentation for use in optical sensing and spectroscopy.

7.4 References to chapter 7

1. G N van den Hoven, E Snoeks, A Polman, C van Dam, J W M van Uffelen, M K Smit, "**Optical gain in erbium-implanted Al_2O_3 waveguides**"; *Proc. 7th Europ. Conf. Int. Opt., 3-6 April 1995, Delft, Holland, pp 229-232*

2. A A Anderson, R W Eason, L M B Hickey, M Jelinek, C Grivas, D S Gill, N A Vainos, "**A Ti:sapphire planar waveguide laser grown by pulsed laser deposition**"; *Opt. Lett., **22** (1997), pp 1556-1558*
3. M Kondo, "**$LiNbO_3$ waveguide devices**"*; J. Ceram. Soc. Jpn., **101** (1993), pp38-42*
4. G B Hocker, W K Burns, "**Modes in diffused optical waveguides of arbitrary index profile**"*; IEEE J. Quant. Electron., **QE-11** (1975), pp 270-276*
5. J Amin, "**Integrated optical devices in rare-earth doped $LiNbO_3$**"; *PhD Thesis, University of Southampton, November 1996*
6. S K Roy, R L Coble, "**Solubilities of magnesia, titania and magnesium titanate in aluminium oxide**"; *J. Am. Ceram. Soc., **51** (1968), pp 1-6*
7. E Levin, "**Phase diagrams for ceramists**"; *2^{nd} ed., pub. Am. Ceram. Soc., fig. 310, 1964*
8. J D Cawley, J W Halloran, "**Dopant distribution in nominally yttrium-doped sapphire**"; *J. Am. Ceram. Soc., **69** (1986), C195-196*
9. A Yariv, "**Quantum Electronics**"*; pub. John Wiley & Sons, 1989, pp 202-207*

CONFERENCE AND JOURNAL PUBLICATIONS

OBTAINED DURING THE COURSE OF THIS THESIS

1. L M B Hickey, E Martins, W S Brocklesby, J S Wilkinson, F Moya, "**Spectroscopic characteristics of Ti-indiffused sapphire**"; *12th UK National Quantum Electronics Conference, 4-8th September 1995, Southampton, UK, paper P3-33*

2. L M B Hickey, E Martins, J E Roman, W S Brocklesby, J S Wilkinson, "**Fluorescence of Ti^{3+} ions thermally diffused into sapphire**"; *Optics Letters, 21 (1996), pp 597-599*

3. L M B Hickey, J E Roman, J S Wilkinson, E G Moya, F Moya, "**Thermal diffusion of Ti^{3+} into sapphire for active integrated optical devices**"; *XX International Quantum Electronics Conference, 14-19 July 1996, Sydney, Australia, paper WD5*

4. A A Anderson, R W Eason, M Jelinek, L M B Hickey, C Grivas, C Fotakis, K Rogers, D Lane, "**Waveguiding and crystallographic properties of single crystal Ti:sapphire layers produced by pulsed laser deposition**" ; *Conference on Lasers and Electro-Optics Europe, 8-13th September 1996, Hamburg, Germany, paper CTuG8, p 79*

5. L M B Hickey, A A Anderson, J S Wilkinson, "**Titanium diffused waveguides in sapphire**" ; *Conference on Lasers and Electro-Optics Europe, 8-13th September 1996, Hamburg, Germany, paper CFH4, p 346*

6. L M B Hickey, J S Wilkinson, "**Titanium diffused waveguides in sapphire**"; *Electronics Letters, 32 (1996), pp 2238-2239*

7. L M B Hickey, J S Wilkinson, "**Characterisation of Ti:diffused channel waveguides in sapphire**" ; *8th European Conference on Integrated Optics, 2-4th April 1997, Stockholm, Sweden, paper EWB1, pp 40-43*

8. L M B Hickey, A A Anderson, J S Wilkinson, "**Ti-sapphire channel waveguide laser by thermal diffusion of titanium into sapphire**" *; 8th European Conference on Integrated Optics, 2-4th April 1997, Stockholm, Sweden, post-deadline paper PD6*

9. A A Anderson, R W Eason, M Jelinek, C Grivas, D Lane, K Rogers, L M B Hickey, C Fotakis, "**Growth of Ti:sapphire single crystal thin films by pulsed laser deposition**"*; Thin Solid Films, **300** (1997), pp 68-71*

10. A A Anderson, R W Eason, L M B Hickey, M Jelinek, C Grivas, D S Gill, N A Vainos, "**Ti:sapphire planar waveguide laser grown by pulsed laser deposition**" *; Optics Letters, **22** (1997), pp 1556-1558*